Imperial College
London

# Aeroelastic Modelling and Control of Very Flexible Air Vehicles using a Nonlinear Modal Formulation

Yinan, Wang

Supervised by Dr. Rafael Palacios
Dr. Andrew Wynn

Imperial College London
Department of Aeronautics

This thesis is submitted for the degree of
Doctor of Philosophy and the Diploma of Imperial College London.

February 2015

# Declaration

I hereby declare that the contents of this thesis are of my own work and that references or quotations from other works are fully acknowledged. No parts of this thesis has been submitted as part of another degree.

Yinan Wang

To my parents

## Acknowledgements

A special thanks goes to my two supervisors. Dr Rafael Palacios was not only a supervisor on academic matters but also an instructor for sharing wisdoms in all aspects of life, offering more than knowledge and experience but new ways to think. Dr Andrew Wynn awes me with his insightful mathematical wizardry and taught me to be rigorous with true Britishness. I always enjoyed the intelligent discussions with both of them and they are the best supervisors that I had ever known. I would also like to thank Dr Paul Goulart who repeatedly offered very helpful advice in areas that I have had little experience in.

I would like to gratefully acknowledge the sponsor of my PhD, the UK Engineering and Physical Sciences Research Council (EPSRC). I must also thank the education I received along the way. The teachers at No.8 Middle School did not teach how to dream big, but instead taught me how to excel and educated me with things that helped me to this day. Prof Pete Nellist and Prof Peter Wilshaw at Oxford provided the support and guidance that allowed me to choose my own path.

I am very thankful to fellow PhD students throughout my time in the Aeronautics Department for brightening me up when I had been working on a project that was almost entirely to myself. My high school classmates were always a source of both support and aspiration. I am also grateful to the very special friends in 63483199 and ICAS who helped me to stay open and positive, and opened up the world's treasures when I was the most oblivious.

There is nothing quite like the unwavering support from my loving parents and I must dedicate this work to them for creating a peaceful environment that often spared me the hardships of life, so that I could focus on the better things. Thank you all!

# Abstract

We present the development of a nonlinear reduced-order formulation for the simulation of geometrically-nonlinear responses of flexible aircraft and other aeroelastic systems. The theoretical foundation of the formulation will be presented first, based on a modal projection of the intrinsic description for beams, coupled with a 2-D unsteady aerodynamic description. We will then investigate the preservation of conservation laws in the proposed method and develop the numerical details in a practical implementation of the method in MATLAB. In this work we also developed a method of obtaining coeffcients of the nonlinear modal beam equations by means of a condensation process, based on the direct application of Guyan reduction of a high-fidelity 3D FE model. Structural and aeroelastic simulations will be presented to verify the implementation of the method against theory and published results, as well as demonstrating the numerical properties of the approach. Static trim, stability analysis and open-loop nonlinear flight simulations using the framework will be demonstrated on a highly-flexible flying wing and compared with published results, as well as carrying out control design and closed-loop nonlinear simulations to demonstrate the capabilities of the proposed reduced-order method.

# List of Figures

# List of Tables

# List of Symbols

Bold upper case indicates matrix, bold lower case indicates vector. Normal font indicates a scalar or an element.

$\mathcal{A}$: Linear operator in unsteady aerodynamic formulation

$A_j^{AE}$: Coefficient in unsteady aerofoil theory

$A_w$: The entire sectional area of a beam

$\mathbf{A}$: Linear modal coefficient matrix containing $\mathbf{A}_1$ and $\mathbf{A}_2$

$\overline{\delta\mathcal{A}}$: Boundary integral in Hamilton's equation

$a$: Distance of aerodynamic centre to structural reference axis normalised with semi-chord

$\mathbf{B}$: Reference frame

$b$: Semi-chord of an aerofoil

$b_j^{AE}$: Coefficient in unsteady aerofoil theory

$\mathbf{b}$: Unit vectors along axes of a reference frame

$C$ (subscript): Boundary (surface) of $S_N$

$C_D$: Aerofoil drag coefficient

$C_{D0}$: Aerofoil drag coefficient at zero angle of attack

$C_k$: Theodorsen's function

$C_L$: Aerofoil lift coefficient

$C_{L0}$: Aerofoil lift coefficient at zero angle of attack and zero control surface deflection

$C_{L\alpha}$: Aerofoil lift coefficient derivative with angle of attack

$C_{L\delta}$: Aerofoil lift coefficient derivative with control surface deflection

$C_M$: Aerofoil moment coefficient

$C_{M0}$: Aerofoil moment coefficient at zero control surface deflection

$C_{M\delta}$: Aerofoil moment coefficient derivative with control surface deflection

$\mathbf{C}$: Beam sectional compliance matrix

$D_a$: Aerodynamic drag evaluated at structural axis

$D_{AE}$: Aerodynamic drag evaluated at aerodynamic centre

$E$: Free ends of the beam assembly $S$

$\mathbf{E}$: The constant matrix $\mathcal{L}_1(\begin{bmatrix} \mathbf{e}^\top & \mathbf{k}_0^\top \end{bmatrix}^\top)$

$\mathbf{e}$: The constant vector $\begin{bmatrix} 1 & 0 & 0 \end{bmatrix}^\top$

$\mathcal{E}$: Total kinetic and potential energy

$F_{a2}$: In-plane aerodynamic force on an aerofoil

$F_{a3}$: Out-of-plane aerodynamic force on an aerofoil

$\mathbf{F}_a$: Collection of forces and moments on an aerofoil

$\mathbf{f}$: Beam sectional force resultant

$\mathbf{f}_A$: The collection of externally applied force and moment

$\hat{\mathbf{f}}_A$: Externally applied $\mathbf{f}_A$ under static equilibrium

$\mathbf{f}_E$: Externally applied force

$\mathbf{f}_K$: Nodal force induced by stiffness matrix $\mathbf{K}_a$

$\mathbf{f}_T$: Collection of applied thrusts

$\mathcal{G}$: Linear operator that staggers two constant vectors $\mathbf{g}_0$

$g_w$: Change in mass density due to curvature strain

$\mathbf{g}$: Gravity vector in local frame

$\mathbf{g}_0$: The constant gravity vector $\begin{bmatrix} 0 & 0 & 9.81 \end{bmatrix}^\top$

$\mathbf{H}_g$: Gravity load coupling coefficients

$\mathbf{H}_T$: Thrust load coupling coefficients

$\mathbf{H}_1$: Quasi-steady aerodynamic coupling coefficients

$\mathbf{H}_{13}$: A collection of $\mathbf{H}_1$ and $\mathbf{H}_3$ coefficients

$\mathbf{H}_2$: Induced aerodynamic coupling coefficients

$\mathbf{H}_3$: Control surface-related aerodynamic coupling coefficients

$\mathbf{h}$: Beam sectional angular momentum

$I_T$: Temporal integral of structural intensity

$\mathbf{I}$: Identity matrix of appropriate size

$i$: Structural intensity

$\mathbf{i}_t$: Beam sectional inertia

$J$: Average $I_T$ in the limit of infinity

$\mathbf{K}$: $\mathcal{H}_\infty$ controller dynamics

$\mathbf{K}_a$: Stiffness matrix of a reduced FE model

$\mathbf{K}_g$: Stiffness matrix of a full FE model

$\mathcal{K}$: Kinetic energy of system

$k_r$: Reduced frequency in unsteady aerofoil theory

$\mathbf{k}$: Curvature of the reference axis

$L_a$: Aerodynamic lift evaluated at structural axis

$L_{AE}$: Aerodynamic lift evaluated at aerodynamic centre

$\mathcal{L}$: Linear transformation

$M_a$: Aerodynamic moment evaluated at structural axis

$M_{AE}$: Aerodynamic moment evaluated at aerodynamic centre

$\mathbf{M}$: Beam sectional mass matrix

$\mathbf{M}_g$: Mass matrix of a reduced FE model

$\mathbf{M}_g$: Mass matrix of a full FE model

$\mathbf{M}_L$: Lumped mass matrix

$\mathbf{m}$: Beam sectional moment resultant

$\mathbf{m}_E$: Externally applied moment

$\mathbf{m}_K$: Nodal force induced by stiffness matrix $\mathbf{K}_a$

$m_s$: Beam sectional mass

$N_a$: Number of (analysis) nodes in a beam structure

$N_{AE}$: Number of aerodynamic states retained in the RFA of unsteady aerofoil theory

$N_C$: Number of modes with their full dynamics retained, as opposed to being residualised

$N_M$: Total number of modes retained in the modal system

$\mathbf{N}$: Projection matrix between local (FE) and global modes

$\mathbf{N}_D$: Linear operator on $\mathbf{T}$ for displacement integration

$\mathbf{N}_R$: Linear operator on $\mathbf{T}$ for rotation integration

$\mathbf{P}_1$: Constant matrix to reshape vec-

tors
$\mathbf{P}_2$: Constant matrix to reshape vectors
$\mathbf{p}$: Beam sectional momentum
$p_j$: The coefficient $b_j^{AE}/b$
$\mathbf{q}$: Collection of all states
$\mathbf{q}_a$: Modal aerodynamic states
$\mathbf{q}_H$: High-frequency part of structural states
$\mathbf{q}_L$: Low-frequency part of structural states
$\mathbf{q}_1$: Velocity in modal coordinates (modal amplitude)
$\mathbf{q}_1*$: Gust-modified velocity in modal coordinates
$\mathbf{q}_{1g}$: Gust-induced velocity component in modal coordinates
$\mathbf{q}_2$: Sectional force resultants in modal coordinates (modal amplitude)
$\mathbf{R}$: Coordinate transformation matrix
$\mathcal{R}$: Operator that diagonally staggers two 3×3 rotation matrices
$\mathbf{r}$: Spatial coordinate along beam reference line
$\mathbf{r}^*$: Spatial coordinate of an arbitrary point on a particular beam cross-section
$S$ (subscript): The collection of all beam reference axes
$\mathbf{S}$: The linearised state-space system matrix
$S_N$ (subscript): An infinitesimal part of $S$ around a lumped mass node
$\mathbf{s}$: Distance along the beam reference axis (in the original configuration)
$k_r$: Reduced time in unsteady aerofoil theory
$T$: Period of an oscillation
$\mathbf{T}$: The coordinate transformation matrix $\mathbf{R}^{at}$
$\mathbf{T}_L$: The coordinate transformation matrix $\mathbf{R}^{0a}$
$\mathbf{T}_v$: The collection of $\mathbf{T}$ matrices re-arranged into vector form
$\mathbf{t}$: Time
$\mathcal{U}$: Potential energy of system
$\mathbf{u}$: Displacement vector
$\mathbf{u}_c$: Control input to linear state-space system
$V_2$: In-plane velocity of aerofoil against still air evaluated at the aerodynamic centre
$V_3$: Out-of-plane velocity of aerofoil against still air evaluated at the aerodynamic centre
$V_\infty$: Freestream velocity
$v_2$: In-plane velocity of aerofoil against still air evaluated at the structural axis
$v_3$: Out-of-plane velocity of aerofoil against still air evaluated at the structural axis
$\mathbf{v}$: Velocity vector
$\hat{\mathbf{v}}$: Gust-induced relative velocity against local airflow
$\overline{\delta\mathcal{W}}$: Variation of external work in Hamilton's equation
$\mathbf{W}$: Block matrix containing $\mathbf{W}_D$
$\mathbf{W}_D$: Diagonal matrix containing eigenvalues of the structural system
$\mathbf{W}_H$: Part of $\mathbf{W}$ containing high-frequency eigenvalues

$\mathbf{W}_L$: Part of $\mathbf{W}$ containing low-frequency eigenvalues

$\mathbf{w}_d$: External disturbance of linear state-space system

$\mathbf{w}_t$: Sectional warping field

$\mathbf{x}_a$: Part of $\mathbf{x}_g$ to be retained

$\mathbf{x}_g$: Displacement and rotation DOFs on an FE model

$\mathbf{x}_r$: Part of $\mathbf{x}_g$ to be removed

$\mathbf{x}_1$: Local velocity and angular velocity

$\mathbf{x}_2$: Local sectional force and moment resultants

$\mathbf{x}_0$: Global (linear) displacement and rotation

$\hat{\mathbf{x}}_2$: The value of $\mathbf{x}_2$ at a static equilibrium under an applied $\hat{\mathbf{f}}_A$

$\mathbf{Y}$: Coefficient matrix in transformation between local (FE) and global modes

$\mathbf{y}_c$: Control objective of linear state-space system

$\mathbf{y}_m$: Measurements taken from the linear state-space system

$\mathbf{Z}$: Coefficient matrix in transformation between local (FE) and global modes

$\mathbf{z}$: $\mathcal{H}_\infty$ controller states

$\alpha_T$: Angle of attack

$\mathbf{\Gamma}$: Structural nonlinear coupling coefficients containing $\mathbf{\Gamma}_1$ and $\mathbf{\Gamma}_2$

$\mathbf{\Gamma}_H$: Part of $\mathbf{\Gamma}$ containing high-frequency components

$\mathbf{\Gamma}_L$: Part of $\mathbf{\Gamma}$ containing low-frequency components

$\mathbf{\Gamma}_1$: Structural nonlinear coupling coefficients

$\mathbf{\Gamma}_2$: Structural nonlinear coupling coefficients

$\boldsymbol{\gamma}$: Force strain

$\delta$: Control surface deflection

$\delta_{ij}$: Dirac delta notation

$\boldsymbol{\eta}$: External load in modal coordinates containing $\boldsymbol{\eta}_1$

$\boldsymbol{\eta}_g$: Gravity load in modal coordinates

$\boldsymbol{\eta}_H$: High-frequency contributions of $\boldsymbol{\eta}$

$\boldsymbol{\eta}_L$: Low-frequency contributions of $\boldsymbol{\eta}$

$\boldsymbol{\eta}_T$: Thrust load in modal coordinates

$\boldsymbol{\eta}_1$: External load $\mathbf{f}_A$ in modal coordinates

$\boldsymbol{\eta}_{1a}$: Aerodynamic load in modal coordinates

$\boldsymbol{\theta}$: Linearised rotation vector

$\boldsymbol{\kappa}$: Curvature strain

$\boldsymbol{\kappa}_{AE}$: Constant vector in the evaluation of aerodynamic states

$\mathbf{\Lambda}$: Linear modal coupling coefficient matrix containing $\mathbf{\Lambda}_1$ and $\mathbf{\Lambda}_2$

$\mathbf{\Lambda}_1$: Linear modal coupling coefficient matrix

$\mathbf{\Lambda}_2$: Linear modal coupling coefficient matrix

$\lambda_j$: Aerodynamic state in unsteady aerofoil theory

$\boldsymbol{\mu}_1$: Local (FE) modes in $\mathbf{x}_1$

$\boldsymbol{\mu}_2$: Local (FE) modes in $\mathbf{x}_2$

$\boldsymbol{\xi}$: Position vector on the beam cross-section relative to the beam reference axis at that location

$\rho$: Air density

$\rho_m$: Mass density

$\mathbf{\Phi}_0$: Mode shapes in $\mathbf{x}_a$
$\mathbf{\Phi}_g$: Mode shapes in $\mathbf{x}_g$
$\boldsymbol{\phi}$: Modal basis
$\hat{\boldsymbol{\phi}}$: Modal basis around loaded equilibrium
$\boldsymbol{\phi}_1$: Modal basis in $\mathbf{x}_1$
$\boldsymbol{\phi}_2$: Modal basis in $\mathbf{x}_2$
$\boldsymbol{\phi}_0$: Continuous modal basis in displacements and rotations
$\varphi_1$: Linear interpolation function
$\varphi_2$: Piecewise-constant interpolation function
$\boldsymbol{\varphi}_1$: Local (FE) basis in $\mathbf{x}_1$
$\boldsymbol{\varphi}_2$: Local (FE) basis in $\mathbf{x}_2$
$\mathbf{\Psi}$: Cartesian rotation vector
$\boldsymbol{\psi}_1$: The momentum mode $\mathbf{M}\boldsymbol{\phi}_1$
$\boldsymbol{\psi}_2$: The strain mode $\mathbf{C}\boldsymbol{\phi}_2$
$\omega$: Angular velocity of a 2D aerofoil
$\omega^*$: Angular frequency in frequency-domain analysis of unsteady aerodynamics
$\boldsymbol{\omega}$: Angular velocity vector
$\omega_j$: Angular frequency (of the $j$-th mode)
$\hat{\omega}_j$: Angular frequency around a loaded equilibrium (of the $j$-th mode)

$\bullet'$: Derivative w.r.t. $s$ (length along the undeformed beam)
$\dot{\bullet}$: Derivative w.r.t. $t$ (time)
$\hat{\bullet}$: Equilibrium value of a variable
$\tilde{\bullet}$: The cross-product operator operating on a vector
$\bullet_0$: A local quantity in the initial (possibly bent) configuration, in the undeformed local axes
$\bullet_t$: A local quantity in the deformed configuration, in the deformed local axes
$\bullet_{t,a}$: A local quantity in the deformed configuration, in the inertial axes. i.e. when the quantity is not represented in its local frame

A non-bold variable represent a particular element from the corresponding bold variable.

# Contents

# 1 Introduction

## 1.1 Context and motivation

High-altitude, long-endurance (HALE) aircraft are a class of air vehicles designed to operate for extended periods at high altitudes. The ability to remain on station for days or even months opens the possibilities for potential missions including long-range communication relay, aerial survey or general atmospheric research. Some of these tasks are currently carried out by satellites that are far more expensive to operate, service or replace than aircraft. Advances in sensor and communication technology resulted in an interest in developing aircraft for such tasks, often unmanned due to their mission profile, in recent years [10].

As a result of their mission requirement, HALE aircraft need to be made as efficient as possible to minimise power requirements, thus an important aspect of their design is maximising aerodynamic efficiency. Henderson and Holmes [11] indicated that for most subsonic aircraft configurations, induced drag contributes about 50 percent of the total drag of the aircraft throughout its flight profile. Due to the presence of wing-tip vortices, the lift-to-drag ratio of a finite wing reduces to that of the aerofoil section for an infinite aspect ratio [12] with the induced drag being inversely proportional to aspect ratio at low aspect ratios [13]. Thus, aircraft designed for very long endurance tend to feature wings with a very high aspect ratio. Another result of the endurance requirements means that wings on HALE aircraft should be made as light as possible, resulting in a reduction in stiffness. Consequently, large deformations of the wings during flight is common, as can be seen in Figure 1(a). A review of these non-conventional aircraft and many other configurations can be found in the work by Livne and Weisshaar [14].

Solar power provides an alternative power source to these types of aircraft without the endurance being limited by fuel storage, as power can be replenished during daytime flight. However the amount of sunlight that can be captured by on-board solar cells also means the design must be particularly efficient, as indicated by Noth [15]. An example of such aircraft is the Helios prototype UAV (unmanned aerial vehicle), shown in Figure 1(a) which represents an attempt to use solar power to power continued flight lasting for days. Other aircraft or proposed designs with similar targets include the QinetiQ Zephyr, shown in Figure 1(b) and the DARPA Vulture and Aurora programmes. Boeing is also exploring the use of liquid hydrogen as a source of power in their Phantom Eye programme. Finally, there is also a rapidly growing commercial interest in this class of aircraft. Ascenta, recently acquired by facebook, is developing HALE UAVs that would function as aerial survey platforms and communication relays in less-developed areas

(a) The Helios Prototype. Source: http://en.wikipedia.org/wiki/NASA_Helios

(b) The QinetiQ Zephyr. Source: https://www.flickr.com/photos/qinetiq/4638654958

Figure 1: Experimental solar-powered HALE aircraft.

at the time of writing (Jan 2015). Google also acquired Titan Aerospace, a maker of ‘atmospheric satellites’ with an intended application in similar areas. The trend towards slender and lighter wings are not limited to UAV designs. The push to design more environment-friendly airliners and obvious economic gains has also resulted in the wings of commercial airliners becoming more slender and less stiff. Such design philosophy is already applied to some extent on the Boeing 787, whose wingtip will experience a static deflection of 10 feet (3 metres) during normal flight, meanwhile Thiede [16] indicated that 1% drag reduction on the Airbus A340 could save 400000 litres of fuel per year and 5000kg emission.

The development of HALE aircraft was not always smooth. The large dynamic deflections experienced by slender and lightweight wings are geometrically-nonlinear and could lead to behaviours not captured by linear design tools or not anticipated by linear control designs. It is generally acknowledged that such effects contributed to the loss of Helios airframe in 2003. The airframe was lost due to unstable dynamic oscillations arising from a gust disturbance following a prior change in payload distribution, subsequently causing structural failure. The report into the loss of the Helios airframe highlighted the need to [17]:

“Develop more advanced, multidisciplinary (structures, aeroelastic, aerodynamics, atmospheric, materials, propulsion, controls, etc) ‘time-domain’ analysis methods appropriate to highly flexible, ‘morphing’ vehicles.”

The lack of a fundemental understanding into their combined effect has prompted research into the nonlinear aeroelastic and flight dynamic behaviour of very flexible airframes, as well as the modelling and control of these structures. A review of research in this field will be presented in the following sections.

In summary, despite the significant progress made by various experimental designs of HALE aircraft, geometrical nonlinearities remains a very real challenge in the development of these very flexible airframes. The creation of new computational tools is necessary to address this question and enable these aircraft to serve in practical roles. In addition, geometrically nonlinear aeroelastic systems also appear in other closely related fields. These include flapping wing aircraft [18, 19], where elastic deformations as well as large rigid-body rotations are experienced by the wings during operation. Helicopter and wind turbine blades also feature slender rotor blades whose rotation also brings about nonlinear effects [20, 21]. These areas face similar challenges in modelling the geometrically nonlinear behaviour of their respective structures and will also benefit from research in this area.

## 1.2 Review of the State-of-the-Art in Flexible Aircraft Dynamics Modelling

In this section we will try to provide a brief overview of recent developments in the aeroelastic modelling of very flexible aircraft. Structural and aerodynamic models of various fidelities as applied to flexible aircraft modelling will be reviewed first. Among the range of structural models, the use of geometrically-nonlinear beam formulations is very common in the modelling of slender airframes and is treated in more detail. We will also review the techniques, e.g. homogenisation, to obtain the structural property definitions used in such a nonlinear beam model of the airframe. The review of the aerodynamic models will focus on 3D potential flow and 2D models, as full 3D CFD methods are not normally used in modelling dynamic aeroelastic interactions on slender airframes with geometrically-nonlinear deformations. We will subsequently examine existing flexible aircraft dynamics modelling frameworks, noting their choice of modelling fidelities for their particular applications and the associated advantages and drawbacks. Finally we will make a brief review of both linear and nonlinear active control methodologies that have been investigated for flexible aircraft applications. This will also include the application of linear and nonlinear model order reduction methods in flexible aeroelastic systems that are carried out for the purpose of control design.

### 1.2.1 Geometrically-Nonlinear Structural Modelling

Here we are concerned about geometric nonlinearities in structural models which exist due to the presence of large displacements and finite rotations, and are the primary source of nonlinearity in a very flexible slender structure. The incorporation of finite rotations in computational structural dynamics has been subject to much research. Modelling flexible-body dynamics using geometrically nonlinear 3D elements is possible and are included in standard FE solvers [22]. It is not the purpose of this work to make a detailed review on geometrically-nonlinear FE methods, however it is generally accepted that such techniques are associated with very high computational costs for models of practical sizes.

Structures that are capable of undergoing large deformations by design commonly have a dominant dimension. For these structures a fidelity reduction is possible in the form of beam and shell theories, where the full 3D degrees of freedom are reduced into a much smaller number of variables describing e.g. sectional strain and stress resultants, with the appropriate cross-sectional properties that describe the linear material property distributions at each section [23]. These theories can accurately capture the dynamics of the full structure down to the length scale of the typical section sizes. Meanwhile the process of obtaining such sectional definitions, called homogenisation, shall be reviewed later.

The beam or plate theories subsequently describe the dynamics of the 3D structure as the dynamics of the reference line / surface in the beam / shell model. Owing to this reduction in fidelity, geometrically-nonlinear beam and shell simulations are much less computationally demanding than a full nonlinear simulation using 3D FE elements of the same structure and suffer much less from the numerical problems associated with nonlinear solid elements. These advantages made beam and shell theories good choices in the modelling of most geometrically-nonlinear aeroelastic systems, and the nonlinear aeroelastic response of very flexible airframes are typically modelled using geometrically nonlinear beam theory [24–31]. In addition, nonlinear beam theory is also used to model helicopter blade dynamics [21] and large (typically off-shore) wind turbine blades [20,32], whereas nonlinear plate and shell theories have found their application in modelling flapping-wing aircraft [18, 19, 33], although beam theory have also been used for this purpose in [34].

In this review we shall limit our discussion to the geometrically-exact composite beam theory. Composite beam theory was developed from the original Euler-Bernoulli beam theory by allowing non-uniform warping of the cross-section within the linear regime (the warping field) [35]. The extension of composite beam theory to include geometrical nonlinearities involves the treatment of beam kinematics in the presence of finite rotations. Overviews of geometrically-nonlinear beam theories can be found in [23,36,37]. Cosserat [38] first described a model for nonlinear analysis of space-curved beams and was subsequently adapted by Love [39] and Reissner [40] into an inertial-frame formulation. Simo and Vu-Quoc [2,41] were then able to generalise the description to full 3D using quaternion representation of finite rotations. In contrast, Geradin and Cardona [1] formulated the problem using cartesian rotation vectors. Another formulation based on rotation matrices has been described by Danielson *et al.* [35] following an analysis of the application of rotations matrices in such setting [42].

As well as representation of rotations, the geometrically-nonlinear composite beam theory has been formulated using a number of different selections of primary variables. Palacios *et al.* [43] provides a detailed review of the range of formulations. Formulations based on nodal displacement are most commonly found in the literature and general-purpose FE implementations [3,23,44], with the advantage of displacement and rotation informations being readily available. In contrast, the three-field mixed variational formulation by Hodges [45] retains internal (local) velocities, strains and rotations all as primary variables. The formulation requires a larger number of variables but with considerably simplified equations, it also easily addresses the issue of rotation objectivity, where a rotation of coordinate systems may generate different results due to the necessary truncation of infinite-order rotational couplings. Finally, Crisfield and Jelenic [46] demonstrated that while many displacement-based implementations violated rotational objectivity, they also showed that numerical schemes can be tailored to be free of this issue.

The strain-based formulation developed by Su and Cesnik [27] uses only the beam's internal strains as primary variables instead of displacements. This provides the advantage of having a constant stiffness matrix which does not require updating, however post-processing is required to reclaim displacement and rotation variables. A two-field intrinsic formulation that uses both internal (local) velocities and stresses was developed by Hodges [47], with Macchelli [48] independently arriving at a similar formulation for the purpose of control design. The formulation doubles the number of variables from the strain-based formulation, however it reduces the nonlinear couplings in the equation to an order of two (i.e. quadratic). The use of local variables such as strains is not limited to beam theory, references [49,50] demonstrated the stability advantage of formulation using local variables in modelling contacts and incompressible solids, Cannarozzi *et al.* [51] also applied a similar formulation to thermoelastic modelling.

Despite being geometrically nonlinear, geometrically-exact beam and shell theories are cast under linear elastic assumption, that although the overall displacements and rotations during deformation can be large, the strains at each location remains small and within the range of linear material behaviour. Structural and material nonlinear effects can also be incorporated into the sectional property definitions to account for material nonlinearities or other effects such as freeplay or wrinkling are also common. For example Su and Cesnik [7] applied a skin wrinkling correction to the modelling of flexible airframes that reduces torsional stiffness at large bending strains. Such corrections however are not within the framework of reduced-fidelity theories and are best captured by full 3D simulations.

At open or constrained ends of a beam, the sectional warping field changes from the interior solutions. This is especially true in torsion, where it is widely known that composite beam theory require a higher-order correction term near ends of the beam to accurately describe the dynamics at these locations and have been implemented in commercial FE software [52]. This correction requires additional parameters and results in higher-order beam theories, a version of which can be found in [53].

The structural equations usually encountered in flexible multibody dynamics are numerically stiff due to the large range of eigenvalues in the system. The stiffness often requires the use of implicit time-marching schemes that are unconditionally stable, most importantly represented by the Newmark family that feature unconditional stability with numerical dissipation at high frequencies. The original Newmark method [54] can be modified to operate on nonlinear problems using Newton-Raphson subiterations, as presented in the book by Geradin and Rixen [55]. Other dissipative methods based on the Newmark scheme with better accuracy for low frequency are reviewed by Fung [56].

When a structure with a uniform section is modelled as a beam, the sectional material properties can be obtained through a cross-sectional analysis, such as the variational asymptotic method [57]. This is a very well-developed theory and cross-sectional/unit-cell analysis tools exist [58–60] that extracts the sectional property definitions from an arbitrary section shape and material distribution. It is often the case that the beam approximates a structure that does not have a uniform section. In order to obtain the equivalent sectional properties on these non-uniform structures, homogenisation methods have been applied to 3D periodic slender structures such as those with regular structural members or lattice structures. Examples of works in this area include [61–63] and more recently that of Dizy *et al.* [64].

### 1.2.2 Unsteady Aerodynamic Modelling of Slender Wings

Nonlinear aeroelastic analysis of very flexible aircraft with the aerodynamics given by direct solutions to the Navier-Stokes (typically RANS approximation) equations have been conducted by a number of authors [65–68]. It is interesting to note that the

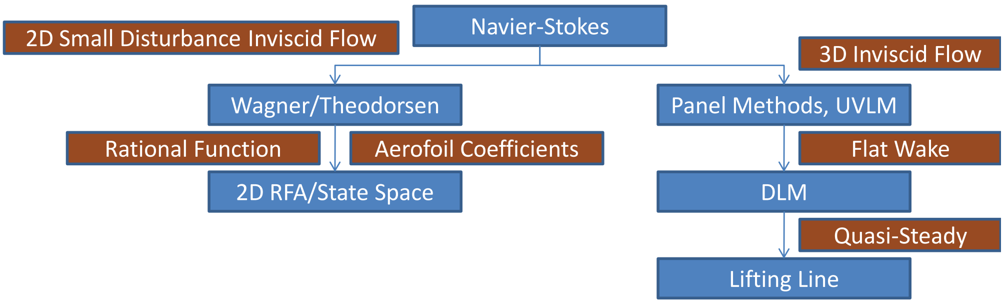

Figure 2: Fidelities of aerodynamic models (blue) and their associated assumptions (red).

examples shown in these works were static solutions. Dynamic CFD simulations are very expensive especially at the relatively low Reynolds number where HALE aircraft typically operates, which corresponds to transitional flow conditions. Additionally when the aerodynamic surfaces encounter large deflections, mesh deformations or re-meshing, also very expensive operations, are required. The acceleration of CFD simulations is an area of very active research and its outside the scope of this work, but despite advances in computing power and algorithms, CFD remains impractical for full-vehicle dynamic simulations with large wing excursions. Research into very flexible dynamic aeroelastic systems have thus focused on the application of low- to medium-fidelity aerodynamic models instead and will be the subject of review in this section. Figure 2 illustrates the range of aerodynamic modelling fidelities that will be reviewed.

The normal operating conditions of flexible aircraft designs that are of interest in this work are associated with low-speed attached flow, this fact makes incompressible potential flow solutions a very attractive alternative. In addition, as drag does not significantly affect the structural dynamic response of flexible airframes, the lack of viscous drag in a potential-flow solution is not critical in this application. Practical potential flow methods for low-speed aerodynamics have been developed extensively and are readily found in standard textbooks [69–71]. The underlying philosophy behind potential flow methods is that the governing equation for incompressible potential flow can be formulated as a boundary-value problem. Rather than solving the entire flow field by discretising the entire volume, the linear governing equations can be solved by finding a superposition of singularities, or elementary solutions, which satisfies the boundary conditions in the problem. The boundary conditions are typically non-penetration conditions on lifting surfaces that enforces zero normal velocity at selected collocation points, and the Kutta-Joukowski condition to enforce uniqueness of solution. The use of singularities lead to a much lower number of unknowns in the problem than FE discretisations, however as each singularity solution interacts with each other, the resulting numerical system requires inversion of fully populated matrices as compared to very sparse matrices that normally results from FE-type methods. The associated reduction in computational cost in potential flow methods enabled them to be used widely in aircraft design and analysis, transforming the aircraft design process at times when computing power is still very limited [72]. Apart from modelling traditional wing designs, the effectiveness of the UVLM method was also demonstrated on delta wings, however the method functions less well when the separation point is not easily known, including situations such as stall [69].

Among the many choices of singularity elements, the Doublet Lattice Method (DLM) [73,74] is the standard method used in the aircraft industry and stands out as a frequency-domain description of potential flow. The method uses doublet panels with a fixed, flat wake and the frequency-domain solution is obtained by assuming a flat wake history that is convected downstream at the constant freestream velocity. The DLM can also account for small, dynamic deformations normal to the local lifting surface and is very efficient for flutter predictions. However accounting for in-plane motion is difficult in the DLM framework and is a known problem in the analysis of T-tail flutter [75]. Additionally the assumption of a flat wake precludes any wake roll-up, as well as being unable to model large nonlinear deformations of the airframe due to the method's linear boundary condition assumptions. Detailed reviews of the DLM method can be found in the works by Blair [76] and Rodden [77].

The vortex lattice method (VLM) is similar to DLM but with doublet panels replaced by vortex panels. The use of the alternative singularity element enables modelling of the effect of in-plane motions of the aerodynamic surfaces which DLM fails. An extension to the VLM is the unsteady vortex lattice method, or UVLM. It is a time-domain method that assumes the trailing wake is free and convects with the local flow velocity, that is not necessarily the freestream velocity as is the case in DLM and VLM. This enables the modelling of wake roll-up and wake interactions with other aerodynamic surfaces, such as the study on an X-29 type configuration in [78, 79]. The UVLM is not limited to small changes in geometry of either the aerodynamic surfaces or wake, in fact it is possible to introduce geometrically-nonlinear deformations to the lifting surface in an UVLM description. The UVLM formulation is reviewed in detail in the book by Katz and Plotkin [69].

In UVLM, the existence of a free wake opens the possibility of wing/wake panels intersecting with each other. As the singularity elements produce influences approaching infinity close to the elements themselves, such intersections may lead to numerical instability in the method. Furthermore, the number of wake panels in a UVLM description increases linearly as simulation time progresses, making long simulations much more costly due to the increasing size of influence coefficient matrices. Voutsinas [80] described the use of subgrids and regularisation methods to address the stability issues, while Willis *et al.* [81] applied the fast multipole method from multibody dynamics to reduce the number of computations required for influence coefficients.

Although panel methods represent a significant reduction in problem size from CFD methods, the high number of wake panels can still produce a large model that includes a fully populated influence coefficient matrix. The Lifting Line theory is a quasi-steady singularity element method that makes further simplifications regarding the wake and the wing. Rather than modelling the wake history as a series of singularity elements convected downstream, the lifting line theory assumes the wake to be infinitely-long horseshoe vortices that are not dependent on previous history. In addition, the wing is also modelled as a single line. This leads to a further, significant reduction in the number of variables in the problem due to the removal of the wake history while still retaining the 3D interactions between different parts of the wing and the wake, however the simplification also limits the method to modelling very low reduced-frequency responses using extensions to unsteady flow by e.g. James [82] and also by Ahmadi and Widnall [83].

Owing to the need to further reduce the computational cost from panel methods and the problem associated with lifting-line theories, we make the observation that attached, laminar flow over slender wings is largely 2D [43]. Thus by completely ignoring spanwise interactions, another way to reduce the fidelity of aerodynamic model further is to model the response of each aerofoil section individually. This method presents the advantage that 2D aerofoil properties are usually known to great detail, including viscous effects and models and data of their post-stall behaviour.

The problem of unsteady aerodynamic loads on an inviscid, small-angle pitching and heaving flat aerofoil section has been solved analytically in widely known works by Wagner [84] in time-domain and Theodorsen [85] in frequency-domain, using singularity solutions (2D free, point vortices in this case). Such a response for a thick aerofoil with a free wake can be computed numerically using Vortex Methods [69] (the 2D version of the UVLM). Rational-function approximations and state-space fitting of these models have been developed by works including [86–88]. In particular, the inflow model [88–90] modified the original problem of a fixed aerofoil in freestream flow to an equivalent problem of a moving aerofoil in still air, the model described the aerodynamic forces on the aerofoil's local frame of reference as a function of the aerofoil's inertial velocities in still air and removes the explicit definition of a freestream velocity.

As stated previously, the advantage of 2D aerofoil models over potential flow solutions is the ease of applying aerodynamic coefficients (lift, drag, moment) corresponding to the particular aerofoil, as well as incorporating nonlinear aerodynamic effects, most notably stall. In contrast, stall becomes more problematic to include in the 3D potential flow solutions reviewed above, although the inclusion of stall within lifting line theory [28] and UVLM [29] is still possible. For 2D aerofoils, ONERA [91, 92] is a widely-used semi-empirical 2D dynamic stall model and another model described Leishman and Beddoes [93]. Additionally [94] developed a method to project nonlinear reduced-order models to 2D inviscid solutions and also 2D CFD solutions, so that the accuracy of higher-fidelity results can be achieved without incurring the penalty in their associated high computational cost.

A well-known problem associated with 2D aerodynamic models is the tip effects that arises from a finite wing. The existence of the wing tip introduces 3D interactions in the adjacent region, in general this leads to a loss of lift compared to 2D predictions, as well as modifying the aeroelastic eigenvalues. As the tip effect diminishes as aspect ratio increases, this effect is disregarded on slender wings in works such as [8]. It is also common to apply a correction factor in the tip region to achieve a better match the 3D predictions [12]. Despite these advances, effects such as wake-tail interference are still modelled much more easily using a 3D aerodynamic model.

### 1.2.3 Aeroelasticity of Very Flexible Aircraft

In the above sections we have reviewed the range of structural and aeroelastic fidelities in flexible aircraft modelling. We shall now review coupled frameworks for flexible aircraft simulations. There have been a number of simulation frameworks created to model the aeroelastic and flight dynamic responses of very flexible aircraft. This section will try to provide an account of the range of full-vehicle modelling fidelities used in these frameworks.

Van Schoor and von Flotow's work [95] was one of the earliest to use a nonlinear structural model in aeroelastic analysis of aircraft with high-aspect ratio wings. Static nonlinear solutions were obtained using the nonlinear structural model coupled with 2D strip theory, subsequent linearisation around the static solution enabled stability and linear unsteady analysis of full aircraft models.

Geometrically-nonlinear beam models are very commonly used as the structural model of nonlinear aeroelastic frameworks. Patil and Hodges [96, 97] applied the mixed variational beam formulation and a 2D finite-state aerodynamics theory from Peters [89] with an additional static stall model in their framework, later named NATASHA. The authors used the framework to predict stability about nonlinear static equilibrium and post-flutter behaviour including onset of limit-cycle oscillations. Their results demonstrated the change in natural frequency, stability and LCO behaviour, including chaotic response, for different static equilibria due to the structural (geometric) nonlinearity, the initiation of an LCO on an stable equilibrium under a large transient disturbance is also demonstrated. They conclude that a stall model is necessary to capture LCO behaviours and structural nonlinearity modifies them. The authors subsequently applied their model to a free-flying airframe and again demonstrated changes in flight dynamics behaviour due to wing flexibility and nonlinearity, and later [8] to model the trim stability and flight dynamics of a Helios-like flying-wing configuration. In this work the authors also implemented a simple nonlinear elastic behaviour in the structural model in the form of reduced sectional stiffness at large sectional strains due to (nonlinear) skin wrinkling effects.

Modelling studies by [98, 99] used the UM/NAST flexible aircraft modelling framework [24, 99] that consists of a strain-based nonlinear beam model and also a 2D finite-state aerodynamic formulation. The framework is applied to a variety of full aircraft configurations, including joined-wing configurations and the high aspect ratio flying wing previously modelled by Patil. In modelling the flying wing, a tip correction on the 2D aerodynamic model is applied to capture the tip effects of a finite wing. As well as trim, stability and flight dynamics studies, the authors also investigated control methods for flight control, stabilisation and load alleviation, simulating closed-loop responses. These developments were followed up by the X-HALE project [100] that is designed to provide experimental validation to the simulation results, as well as a test platform for control strategies.

An implementation of the UVLM aerodynamic model is found in the SHARP framework developed by Palacios *et al.* [3, 44, 101, 102]. The framework couples the aerodynamic model to a displacement-based nonlinear beam model and is used by the authors to obtain nonlinear trim, stability and flight dynamic results on very flexible airframes. The authors demonstrated the capability of the framework in modelling wake roll-up, wake-tail interactions and transient loads experienced by the aircraft flying through the wake of another similar aircraft. Murua [75] later applied the model to investigate the

T-tail flutter problem in which in-plane motions of lifting surfaces become important and also developed techniques to linearise the UVLM solution and obtained reduced-order 3D aerodynamic models [103].

Drela developed the ASWING integrated simulation environment [28] by coupling the 3D quasi-steady lifting-line theory with an additional static stall model with displacement-based geometrically-nonlinear beam elements. The framework is capable of finding nonlinear trim equilibrium on full aircraft models and, by linearising about the equilibrium, perform linear time- and frequency-domain analysis very efficiently for preliminary design studies. Love *et al.* [104] subsequently used the framework to analyse the coupled aeroelastic and flight dynamic characteristics of the Sensorcraft configuration, a high aspect-ratio swept-wing concept.

Wang *et al.* [29] developed the NANSI framework using a tightly coupled UVLM and intrinsic beam model, also including a stall model adapted to the UVLM solution. This framework was demonstrated using the flying wing case from Patil, on which trim and nonlinear gust responses were computed. The method combined UVLM's full 3D fidelity with stall models and provides an important extension to the standard UVLM technique. Zhao and Ren [30] also used nonlinear displacement-based beam model with the ONERA aerofoil stall model to study various aspects of control design and closed-loop behaviour of flexible airframes. The authors investigated limit-cycle oscillations, flight control and active flutter suppression on a flexible full-aircraft model using their method.

In the framework that Meirovitch and Tuczu [31] used, quasi-steady strip theory was coupled with a nonlinear beam model to simulate full aircraft responses. They proposed the separation of the coupled nonlinear unsteady dynamics into a nonlinear flight dynamic component and a perturbation-based elastic/rigid body dynamic component. This separation leads to a reduction in computational cost of the dynamic response, while the associated reduction in accuracy is justified by the eventual goal of implementation in on-board control systems.

The use of geometrically-nonlinear structural models other than the beam formulation is also possible. Tang *et al.* [105] investigated flutter and LCO behaviour using a nonlinear shell model coupled with a (fixed-wake) vortex lattice model and, importantly, validated their results with experimental studies using a cantilever wing setup. They found good agreement for flutter predictions and for small-amplitude LCOs. At larger amplitudes the theoretical predictions began to diverge from experimental data and the authors concluded that nonlinear aerodynamic models are needed to capture large LCO accurately.

Finally, Demasi and Livne [106, 107] coupled a 3D linear unsteady modal formulation of aerodynamic loads onto a full-order 3D nonlinear structural model using a set of deformation shape vectors. Their approach was demonstrated using a joined-delta wing configuration where limit-cycle oscillations can arise due to structural nonlinearities. Their method has the advantage of being applicable to any aerodynamic description as long as it is linearised and written into a modal form. In works where the beam formulation is used to model the wing structure, the aerofoil section is generally assumed to be unchanged despite structural deformations. However as this work uses plate elements, it effectively incorporates aerofoil warping effects on the aerodynamic forces.

### 1.2.4 Aeroelastic Control

***Linear and Nonlinear Model Reduction***

Many structural and aerodynamic methods reviewed previously are developed as a low-order representation of complex aeroelastic systems to facilitate long time-domain simulations, however they can still require considerable computational effort. Especially for the purpose of control system design, a model of very low order is often required. Here we will review first some methods that have been used in the literature to obtain reduced-order linear or nonlinear models on a geometrically-nonlinear aeroelastic systems of varying levels of complexity.

Model reduction on linear systems is very well-developed out of the aforementioned necessity of using low-order models in linear control design. A general-purpose reduction method that has been applied widely on aeroelastic systems, especially for the purpose of control design, is the balanced model reduction method [108]. The method involves first a balancing step using the observability and controllability Gramians (balancing) and subsequently a singular value decomposition (SVD) on the projected linear system. This transforms the system into a form where the modes with the most significant contributions to the system's input-output behaviour can be identified. By retaining only the modes with the greatest contributions (and any mode that is unstable), the method arrives at a reduced system with the most similar input-output behaviour as the original system. For very large problems, Krylov subspace techniques can be used to obtain a reduced system without needing to decompose the entire full system [109].

In some CFD problems where direct linearisation is not readily available, reduced-order models still can be obtained via proper orthogonal decomposition (POD) on a set of snapshots of the flow field (in fact, POD is a special case of SVD). This method is very commonly used to obtain reduced-order models in CFD problems with examples including those in Refs. [110–112].

By comparison, nonlinear model reduction is much more problem-dependent. Methods that take advantage of the particular structure of the nonlinearities are used as well as more general-purpose nonlinear model reduction techniques. For example, by identifying the nature of the nonlinearity, Hesse *et al.* [3] demonstrated the use of linear elastic modes at the same time retaining nonlinear gyroscopic couplings in the rigid-body modes only to account for large rigid-body rotations. The methodology is demonstrated to work best in cases where rigid-body rotations contribute to the majority of the nonlinearity in the system. Similarly Demasi [106,107] used a 3D nonlinear structural model and assumed that the aerodynamic forces from the linear 3D aerodynamic model at each point rotated with the structure's local frame of reference.

The methods described above separates "important" contributors to nonlinear behaviour using first principles, e.g. by isolating rigid-body rotations, aerodynamic nonlinearities, or material nonlinearities. In problems where the source of nonlinearity is complex and a separation of "important" contributors to nonlinear interactions using first principles, as used in the cases above, is difficult, more general methods of nonlinear model reductions have been used. These methods are extensions to the linear model reduction techniques into the nonlinear regime, generally incorporating nonlinear interactions as higher-order couplings between the linear states, or modifications to the linear dynamics. The application of balancing as applied to nonlinear systems were used by works including [113–115], where the nonlinear terms are incorporated via Galerkin projections on the reduced linear system. Da Ronch *et al.* [116] used a general-purpose method, which projected the nonlinear system through a series expansion onto a small basis of eigenvectors representative of the full-order dynamics, subsequently obtaining a reduced-order description of the CFD solution of 2D aerofoils. The choice of various bases on which the nonlinear dynamics is projected onto are reviewed in detail in [117] and [118]. Finally, Amsallem and Farhat [119] applied a reduced-order model (ROM) adaptation technique, modifying the ROM dynamically during operation and effectively making their approach another nonlinear reduction technique.

The methods described in this part serves to reduce the problem to a manageable size. Once this is complete a control system can be designed with the knowledge of this reduced-order system. In the following part we will review control methods commonly applied to aeroelastic systems.

### ***Linear and Nonlinear Control Methods for Aeroelastic Systems***

Classic PID (proportional-integral-derivative) control methods have been applied widely to control aeroelastic systems, especially in the role of flutter suppression and flutter boundary extension [120–123]. However it is often the case that aeroelastic systems are MIMO (multiple-input, multiple-output) problems. The application and tuning of the classic control methods (PID, pole placement etc.) to MIMO systems can become cumbersome and sometimes dangerous due to a lack of theoretical frameworks that guarantees good controller performance [124]. Optimal control methods are a more attractive option in the control of MIMO systems because rather than focusing on particular measures, optimal control theory takes an heuristic approach that is concerned about minimising the total transfer of energy-like measures from the combination of inputs to all outputs. Silvestre and Paglione [125] applied the $\mathcal{H}_\infty$ robust control method in the role of control augmentation on a flexible aircraft, the authors modelled the rigid-body motions of the aircraft while treating the elastic deformations as input disturbances. Cook *et al.* [126] also applied an $\mathcal{H}_\infty$ controller to both linearised and nonlinear model of a flexible aircraft to achieve gust load alleviation. Dillsaver *et al.* [98] used an LQG (linear-quadratic regulator) optimal controller to achieve load alleviation on a flexible airframe under external gust influence, also demonstrating a technique to enforce a hard limit on structural deflection. The LQG and $\mathcal{H}_\infty$ methods use different norms in casting the optimisation problem in their control synthesis. Although LQG has no guaranteed stability margin [127] (an issue which the $\mathcal{H}_\infty$ method was developed precisely to address, thus called a robust controller), this is only a real problem in rare pathological cases. The robustness aspect of robust controllers also make them attractive in controlling nonlinear systems, this is because the nonlinearity in the system serves to modify the linear behaviour during operation and can be regarded as deviations from the ideal linearised system.

While the linear control theory reviewed above is very well-developed, only a patchwork of nonlinear control methods exist and each serves particular classes of nonlinear systems. Examples of nonlinear control methods include feedback linearisation, passivity theory and sliding mode control theory, methods which are reviewed in textbooks including that by Slotine and Li [128] and a more specialised description of nonlinear control as applied to structural problems can be found in the book by Wagg and Neild [129]. Although it is outside the scope of this work to review recent developments of advanced control strategies, it is interesting to mention the control of flexible aeroelastic systems using the MPC (model-predictive control) method, which is an extension of LQG-type approaches applicable to nonlinear systems in general. Rather than casting an analytical optimisation problem using a linear state-space model over an infinite horizon as done in LQG, MPC casts the optimisation problem over a finite horizon with the distinction that the optimisation is now solved at discrete times using a model of the system. This allows the controller to account for nonlinear effects in the model, however current constraints in computation power limits the method to using very small (reduced-order) models of the system in order to run in real-time. Simpson *et al.* [130] applied a MPC controller to achieve gust load alleviation on a cantilever wing model, noting the MPC's advantage in accounting for control saturation over an LQG controller. Giesseler *et al.* [131] also demonstrated gust load alleviation using a model of a realistic aircraft. In this case, lidar information of incoming gust disturbance was available and MPC was able to utilise this information to its advantage. Raghavan and Patil [26] demonstrated a multistep nonlinear dynamic inversion controller for the purpose of path-following on a flexible flying-wing, using an internal model of the nonlinear flight dynamic system. The authors also noted its superior performance to linear controllers used in the same role. However, there is currently no clear dominant strategy in the literature on the use of nonlinear controllers for nonlinear aeroelastic problems.

## 1.3 Open Problems and Research Questions

A variety of structural and aerodynamic modelling fidelities have been presented showing their application to modelling the nonlinear dynamic responses of flexible airframes. It was seen in general that reduced-fidelity descriptions capture the low-frequency dynamics of these problems with good accuracy. Beam descriptions that take advantage of the slenderness in the wing of typical HALE aircraft designs are found to offer an adequate accuracy and improved computational efficiency. Similarly, 3D potential flow and 2D strip theories can capture aerodynamic effects that are of interest in HALE aircraft and provide an alternative to full CFD solutions using a tractable level of computational power and are also linearised and reduced more easily.

Sectional and unit-cell homogenisation represent powerful tools in the application of beam theory to tackle complex structural problems. These methods require the specification or construction of a separate, tailored model for the sole purpose of extracting the sectional stiffness properties from the structure. However in industrial settings, it is often the case that a high-fidelity linear FE model already exists for linear load analysis and this linear model could be used to our advantage.

Despite using reduced-fidelity models, model reduction is still necessary from a control design or concept iteration point of view. In applying model reduction on geometrically-nonlinear aeroelastic models, problem-specific nonlinear reduction techniques have used displacement-based descriptions. A review of beam formulations already highlighted the complexities of using displacement-based beam formulations in modelling geometrical nonlinearities and it is desirable to explore other beam formulations in this application. In particular, the intrinsic beam formulation offers a simple description of the nonlinear effects in an geometrically nonlinear beam problem. However this is a less-explored formulation with limited literature on the subject and further investigation into the properties of this formulation is needed.

Based on the summary above, the main objectives of this research will be as follows,

1. Developing an aeroelastic modelling framework using the intrinsic modal theory and a suitable aerodynamic formulation.
2. Identifying the properties, advantages and drawbacks of the intrinsic beam theory as the basis for nonlinear flexible aircraft dynamic modelling (and more generally for flexible multibody dynamics simulations), especially when cast in a modal form.
3. Developing a method to extract beam sectional properties, or otherwise arrive at a nonlinear beam formulation directly from a 3D model of a structure with a non-uniform and non-periodic structure.
4. Understanding whether the modal formulation of the intrinsic beam theory serve as a good basis for nonlinear model reduction and control design on nonlinear aeroelastic systems.

## 1.4 Outline of Thesis

The subsequent chapters of this thesis will be arranged as follows,

Chapter 2 outlines the intrinsic beam theory and the unsteady 2D aerodynamic model in the form used in the current work. The derivation of intrinsic formulation using Hamilton's principle is adapted from [47], whereas the derivation of unsteady 2D aerodynamic loads starts from Wagner's solution of a heaving and pitching flat aerofoil in inviscid flow [84] and transforms it into the aerofoil's local coordinate system following Peter's description [90].

Chapter 3 formulates the structural and aerodynamic models into a coupled modal framework. The aerodynamic forces are projected onto the structural model by means of a Galerkin projection in a nonlinear state-space form that is easily linearised about any equilibrium condition. As part of the eventual goal of control design, the process of linearising the modal aeroelastic system and the process of creating an $\mathcal{H}_\infty$ robust controller based on the linearised modal aeroelastic system will also be discussed.

Chapter 4 outlines the numerical methods and discretisations leading to the implementation of the modal aeroelastic framework, as outlined in the first objective of the research. Time-marching and optimisation of numerical procedure used in the numerical implementation will also be discussed, as well as investigating the conservation properties of the intrinsic structural formulation, as stated in the second objective of this research.

Chapter 5 addresses the third research objective and describes the development of a static condensation method for extracting a nonlinear intrinsic modal system using a linear FE model. Rather than attempting to arrive at sectional properties via homogenisation from cross-section or unit cell definitions, the method described in this section arrives directly at a nonlinear intrinsic modal description of the structure based on a reduced set of nodes, using Guyan reduction on the linear elastic response of the full 3D model.

Chapter 6 provides numerical results to verify the structural part of the simulation framework. Some numerical details regarding convergence and conservation on the intrinsic modal formulation will also be demonstrated.

Chapter 7 presents coupled aeroelastic simulation results using the framework developed in this work. First a linear analysis will be conducted on the onset of flutter of a cantilever wing, then a flexible flying wing configuration will be used to demonstrate trim, stability analysis, control design and closed-loop flight simulation. The two results chapters will address the fourth research objective.

Finally, Chapter 8 provides a summary of the findings and achievements in this work, as well as discussing potential areas to explore in future works.

# 2 Background Theories

The formulations in this work will rely heavily on the intrinsic beam formulation and the 2D unsteady strip theory, therefore it is necessary to provide a detailed introduction to these existing formulations for completeness. In this chapter, we first present the full derivation of the intrinsic beam formulation, based on the works by Hodges [45, 47] and Palacios [43]. We will then develop the 2D unsteady aerodynamic formulation described in aerofoil local coordinates, as in Peters' inflow model [90]. These two descriptions provide the theoretic foundation on which the coupled aeroelastic framework is eventually constructed.

## 2.1 Intrinsic Beam Formulation

The intrinsic beam theory is a total Lagrangian formulation which describes beam dynamics using velocity, strain, momentum and sectional force, together with their rotational counterparts as primary variables. This derivation first seeks to express the equations of motion of beams, starting from Hamilton's principle, using these intrinsic variables, then completes a closed-form description by deriving additional compatibility relations and constitutive relations.

### 2.1.1 Problem Description

An initially undeformed, i.e. without internal stresses, but curved and twisted beam assembly resides in a global inertial reference frame $a$ so that any point on the reference line of the undeformed beam is only a function of its position along the beam ($s$) and not of time. The variable $s$ defines the position of a point along the beam's reference line as well as a material cross-section of the beam located at that point. At each point along the reference line, a position $\mathbf{r}_0(s)$ from the origin, a local coordinate system, $\mathbf{B}_0$ is formed using the unit vectors $\mathbf{b}_{0,1}$, which is tangential to the reference line, with $\mathbf{b}_{0,2}$ and $\mathbf{b}_{0,3}$ which are both orthogonal to $\mathbf{b}_{0,1}$. Here it is thus assumed that the local cross-section is always taken perpendicular to the reference line in this initial configuration. For any point on the cross-section at $s$, its position in a global reference frame could be written as a combination of the cross-section location and its local position on the section, $w_2$ and $w_3$, as

$$\mathbf{r}_0^* = \mathbf{r}_0 + w_2\mathbf{b}_{0,2} + w_3\mathbf{b}_{0,3}. \tag{2.1}$$

As all variables in this section are a function of the same variable $s$, the symbol will be omitted from the following discussion.

Similarly, consider the same beam under deformation, where for a point on the beam $\mathbf{r}_t^*$ lying on the now-deformed cross-section $\mathbf{r}_t$,

$$\mathbf{r}_t^* = \mathbf{r}_t + \mathbf{R}(w_2\mathbf{b}_{t,2} + w_3\mathbf{b}_{t,3} + \mathbf{w}_t), \tag{2.2}$$

where $\mathbf{R}$ is a transformation matrix between the initial and current local coordinate framed described in the following paragraph, and $\mathbf{w}_t(s, w_2, w_3)$ is a sectional warping field that deforms the initial cross-section. Along the reference line, $\mathbf{r}_t$ and $\mathbf{r}_0$ are related by a displacement vector $\mathbf{u}$ in the global reference frame,

$$\mathbf{r}_{t,a} = \mathbf{r}_{0,a} + \mathbf{u}. \tag{2.3}$$

Here the subscripts $\bullet_t$ and $\bullet_0$ will be used to denote quantities of the final (current) and initial configuration expressed in their respective local reference frames respectively, whereas $\bullet_a$ denotes a global inertial reference frame. Unless stated otherwise, in the following part of this chapter displacement and rotation vectors without subscripts are also defined in the global reference frame, whereas other vector quantities without explicit subscripts, such as $\mathbf{v}$, are implied to have been defined in the local reference frame in the final configuration ($\bullet_t$). Variables with one explicit subscript, for example $\mathbf{k}_t$, denotes quantities in that particular configuration defined in their respective local frames, those with two explicit subscripts, such as $\mathbf{u}_{0,t}$, define variables in one configuration expressed in the reference frame of the second subscript.

### Rotation Matrix Definition

Here we define the convention of rotation matrix used in this work. In matrix notation, if $\mathbf{B}_0$ and $\mathbf{B}_t$ are two local coordinate systems in a global inertial axis system, with their three axes $\mathbf{b}_{0,1}, \mathbf{b}_{0,2}, \mathbf{b}_{0,3}$ and $\mathbf{b}_{t,1}, \mathbf{b}_{t,2}, \mathbf{b}_{t,3}$, where in component form,

$$\mathbf{B}_0 = \begin{pmatrix} b_{0,1x} & b_{0,2x} & b_{0,3x} \\ b_{0,1y} & b_{0,2y} & b_{0,3y} \\ b_{0,1z} & b_{0,2z} & b_{0,3z} \end{pmatrix} \tag{2.4}$$

and

$$\mathbf{B}_t = \begin{pmatrix} b_{t,1x} & b_{t,2x} & b_{t,3x} \\ b_{t,1y} & b_{t,2y} & b_{t,3y} \\ b_{t,1z} & b_{t,2z} & b_{t,3z} \end{pmatrix}, \tag{2.5}$$

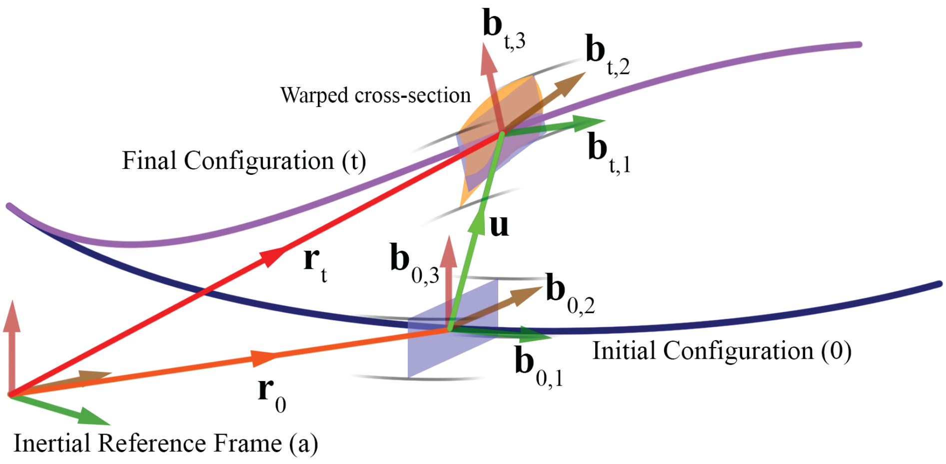

Figure 3: Illustration of the beam problem definition with relevant vector quantities indicated.

or in general, $\mathbf{B} = \begin{bmatrix} \mathbf{b}_1 & \mathbf{b}_2 & \mathbf{b}_3 \end{bmatrix}$. The rotation matrix $\mathbf{R}$ is defined as a matrix that transforms the coordinate system from one set of reference frame to another, i.e. expressing a given vector quantity in another set of coordinates.

For a transformation of an arbitrary vector from frame $\mathbf{B}_0$ into $\mathbf{B}_t$, the matrix $\mathbf{R}^{t0}$, i.e. the transformation from the $\mathbf{B}_0$-basis into the $\mathbf{B}_t$-basis, is used and can be expressed as:

$$\mathbf{r}_t = \mathbf{R}^{t0}\mathbf{r}_0, \tag{2.6}$$

with the transformation matrix $\mathbf{R}^{t0}$ defined formally in matrix notation as

$$\mathbf{R}^{t0} = \mathbf{B}_0^\top \mathbf{B}_t. \tag{2.7}$$

Note that in general the transpose of the coordinate transformation matrix is also its inverse and represents an inverse transformation from the final frame to the initial frame, or

$$(\mathbf{R}^{t0})^\top = (\mathbf{R}^{t0})^{-1} = \mathbf{R}^{0t} \tag{2.8}$$

and it follows from simple argument that successive transformations are equivalent to one transformation from the starting frame into the finishing frame, for example

$$\mathbf{R}^{t0}\mathbf{R}^{0a} = \mathbf{R}^{ta}. \tag{2.9}$$

Furthermore it should also be noted that

$$\frac{\partial \mathbf{R}^{t0}}{\partial s}\mathbf{R}^{0t} = -\mathbf{R}^{t0}\frac{\partial \mathbf{R}^{0t}}{\partial s} \tag{2.10}$$

as

$$\frac{\partial \mathbf{R}^{t0}}{\partial s}\mathbf{R}^{0t} + \mathbf{R}^{t0}\frac{\partial \mathbf{R}^{0t}}{\partial s} = \frac{\partial}{\partial s}(\mathbf{R}^{t0}\mathbf{R}^{0t}) = \frac{\partial \mathbf{I}}{\partial s} = \mathbf{0}, \tag{2.11}$$

this relation also holds if $s$ is changed to $t$ and the rotation matrix relates two arbitrary frames.

**Cross Product Operator Definition**

For convenience, we also define the cross product operator as a linear operator acting on a (3-element) vector

$$\tilde{\mathbf{a}} = \begin{pmatrix} 0 & -a_3 & a_2 \\ a_3 & 0 & -a_1 \\ -a_2 & a_1 & 0 \end{pmatrix}. \tag{2.12}$$

When the resulting matrix multiplies another vector, it is the equivalent of computing a cross product of the original vector with that vector

$$\tilde{\mathbf{a}}\mathbf{r} = \mathbf{a} \times \mathbf{r}. \tag{2.13}$$

The following identities hold and can be proven with minimal effort:

$$\tilde{\mathbf{z}}^\top = -\tilde{\mathbf{z}}, \tag{2.14a}$$

$$\tilde{\mathbf{z}}\mathbf{z} = \mathbf{0}, \tag{2.14b}$$

$$\tilde{\mathbf{z}}\mathbf{y} = -\tilde{\mathbf{y}}\mathbf{z}, \tag{2.14c}$$

$$\mathbf{y}^\top\tilde{\mathbf{z}} = -\mathbf{z}^\top\tilde{\mathbf{y}}, \tag{2.14d}$$

$$\tilde{\mathbf{y}}\tilde{\mathbf{z}} = \mathbf{z}\mathbf{y}^\top - \mathbf{I}\mathbf{y}^\top\mathbf{z}, \tag{2.14e}$$

$$\widetilde{\tilde{\mathbf{y}}\mathbf{z}} = \tilde{\mathbf{y}}\tilde{\mathbf{z}} - \tilde{\mathbf{z}}\tilde{\mathbf{y}} \tag{2.14f}$$

The definitions made in this section will be used in the following derivation of the intrinsic beam equations.

### 2.1.2 Hamilton's Equation

Hamilton's equation is written as

$$\int_{t_1}^{t_2} \left( \int_S \left( \delta(\mathcal{K} - \mathcal{U}) + \overline{\delta \mathcal{W}} \right) \, ds \right) dt = \overline{\delta \mathcal{A}} \tag{2.15}$$

which for the intrinsic beam problem we will seek to express using intrinsic variables. The $\delta$ indicates variations of a quantity and an overline in this equation indicates that the quantity is a path function and therefore only exists as a variation in here. The kinetic energy $\mathcal{K}$, potential energy $\mathcal{U}$ and external work variation $\overline{\delta \mathcal{W}}$ terms will be described in the following paragraphs in sequence. The $\overline{\delta \mathcal{A}}$ is an action term and introduces the eventual boundary conditions of the problem. It will be case-dependent. The symbol $S$ here denotes an integration along all beam segments.

#### Potential Energy Component

The potential energy $\mathcal{U}$ in the case of a beam is the strain energy and will be written in terms of intrinsic variables in the spirit of the derivation of the intrinsic formulation. These intrinsic variables are the local force strains $\boldsymbol{\gamma}$ and moment strains $\boldsymbol{\kappa}$, the variations of these variables multiplying the sectional forces $\mathbf{f}$ and moments $\mathbf{m}$ respectively, also expressed in local frame. We eventually seek to write the variation on potential energy as variations on displacement and rotation in order to relate it to variation on kinetic energy.

First we provide the definition of the terms in the potential energy. The moment strain in the local frame of reference is represented directly as the rate of change with respect to space ($\frac{\partial}{\partial s}$, indicated by $\bullet'$) in the local reference frame (thus the additional transformation from global to current local frame using $\mathbf{R}^{at}$) in terms of position along the beam. i.e.

$$\tilde{\mathbf{k}}_t = -\mathbf{R}^{ta\prime}\mathbf{R}^{at} = \mathbf{R}^{ta}\mathbf{R}^{at\prime}, \tag{2.16a}$$

$$\tilde{\mathbf{k}}_0 = -\mathbf{R}^{0a\prime}\mathbf{R}^{a0}, \tag{2.16b}$$

making use of (2.10). In the following discussion, the variation operator $\delta$ takes precedence over space and time derivatives and transpose operations, i.e. $\delta\mathbf{R}' = (\delta\mathbf{R})'$.

The moment strain is by definition the difference between the local curvatures of starting and ending configurations, written as

$$\boldsymbol{\kappa} = \mathbf{k}_t - \mathbf{k}_0. \tag{2.17}$$

Written as a pseudo-vector, the moment strain is defined in the form of

$$\boldsymbol{\kappa} = \begin{bmatrix} \kappa_1 & \kappa_2 & \kappa_3 \end{bmatrix}^\top \tag{2.18}$$

and in the local element's frame corresponds to the moment strain in twisting and two bending directions.

Using rotation matrix identities and the product rule, we obtain

$$\begin{aligned} \tilde{\mathbf{k}}_t &= -\mathbf{R}^{ta\prime}\mathbf{R}^{at} = -(\mathbf{R}^{t0}\mathbf{R}^{0a})'\mathbf{R}^{at} = -\mathbf{R}^{t0\prime}\mathbf{R}^{0t} - \mathbf{R}^{t0}\mathbf{R}^{0a\prime}\mathbf{R}^{a0}\mathbf{R}^{0t} \\ &= -\mathbf{R}'\mathbf{R}^\top + \mathbf{R}\tilde{\mathbf{k}}_0\mathbf{R}^\top, \end{aligned} \tag{2.19}$$

where $\mathbf{R} = \mathbf{R}^{t0}$.

The strain, by definition, is the rate of change of position vectors in their respective local reference frames expressed as

$$\boldsymbol{\gamma} = \mathbf{R}^{ta}\mathbf{r}'_{t,a} - \mathbf{R}^{0a}\mathbf{r}'_{0,a}. \tag{2.20}$$

Similar to the moment strain, the simplified force strain defined as a vector is

$$\boldsymbol{\gamma} = \begin{bmatrix} \gamma_1 & \gamma_2 & \gamma_3 \end{bmatrix}^\top. \tag{2.21}$$

When expressed in the local element's frame this corresponds to the force strain in the axial and two shear directions.

Again using rotation matrix identities and changes of reference frames we obtain

$$\begin{aligned} \boldsymbol{\gamma} &= \mathbf{R}^{t0}\mathbf{R}^{0a}(\mathbf{R}^{a0}\mathbf{r}'_{t,0} + \mathbf{R}^{a0\prime}\mathbf{r}_{t,0}) - \mathbf{R}^{0a}(\mathbf{R}^{a0}\mathbf{r}'_{0,0} + \mathbf{R}^{a0\prime}\mathbf{r}_{0,0}) \\ &= \mathbf{R}^{t0}(\mathbf{r}'_{t,0} + \tilde{\mathbf{k}}_0\mathbf{r}_{t,0}) - (\mathbf{r}'_0 + \tilde{\mathbf{k}}_0\mathbf{r}_0). \end{aligned} \tag{2.22}$$

For an initially undeformed beam, we can always define the direction and distance along the reference line so that $\mathbf{R}^{0a}\mathbf{r}'_a = [1, 0, 0]^\top = \mathbf{e}$ which we assign a constant vector $\mathbf{e}$ as a shorthand. This follows from the fact that the $\mathbf{b}_1$ axis of the local reference frame is always tangent to the reference line in the undeformed configuration and that $s$ is by definition the arc length along the reference line.[1] By definition we have

$$\mathbf{r}_{t,0} = \mathbf{r}_0 + \mathbf{u}_0, \tag{2.23}$$

which we then substitute into (2.22) to obtain

$$\boldsymbol{\gamma} = \mathbf{R}(\mathbf{e} + \mathbf{u}_0' + \tilde{\mathbf{k}}_0 \mathbf{u}_0) - \mathbf{e}. \tag{2.24}$$

From now on, we shall make the definition that when shown without superscripts,

$$\mathbf{R} = \mathbf{R}^{t0}. \tag{2.25}$$

Now that we have the force and moment strains, $\boldsymbol{\gamma}$ and $\boldsymbol{\kappa}$ respectively, expressed in terms of displacements $\mathbf{u}$ and rotations $\mathbf{R}$, we are able to compute the variations on the moment and force strains expressed as variations on $\mathbf{u}$ and $\mathbf{R}$. Since $\mathbf{k}_0$ is fixed as the initial condition,

$$\delta\boldsymbol{\kappa} = \delta\mathbf{k}_t. \tag{2.26}$$

First we post-multiply (2.19) by $\mathbf{R}$ and obtain

$$\mathbf{R}' = \mathbf{R}\tilde{\mathbf{k}}_0 - \tilde{\mathbf{k}}_t\mathbf{R}. \tag{2.27}$$

Now we define a *virtual rotation* $\delta\boldsymbol{\Psi}_t$ in the $t$-frame (final configuration) as

$$\delta\tilde{\boldsymbol{\Psi}}_t = \mathbf{R}\delta\mathbf{R}^\top = -\delta\mathbf{R}\mathbf{R}^\top. \tag{2.28}$$

This variable is introduced because despite the rotation matrix $\mathbf{R}$ having 9 elements, it has only 3 degrees-of-freedom due to the implicit constraints imposed on a valid rotation matrix. This is evident from the axis-angle or Euler angle representations of rotations, both containing only three variables. Using this definition of virtual rotation is essentially a change of variable from taking variations on rotation matrix directly ($\delta\mathbf{R}$) and makes the following derivations easier to follow. The variation in rotation or virtual rotation is one variable in a pair of independent variables in the variation on potential energy $\mathcal{U}$ and also kinetic energy $\mathcal{K}$, the other one being variation on displacement. Note that such a definition of infinitesimal rotation using the tilde notation is valid as the matrix

---

[1] If for some particular reason there is a need to define a non-zero initial strain, the $\mathbf{R}^{0a}\mathbf{r}_a'$ term is retained in place of the $\mathbf{e}$ term and the term $\mathbf{e} + \boldsymbol{\gamma}_0$ will replace $\mathbf{e}$ in subsequent derivations where $\boldsymbol{\gamma}_0$ is the initial tensile and shear deformation. An example of one such reason is that the aerodynamic model used in this work could impose constraints on how such a local reference frame is defined.

expression is always anti-symmetric due to

$$\mathbf{R}\delta\mathbf{R}^\top + (\mathbf{R}\delta\mathbf{R}^\top)^\top = \mathbf{R}\delta\mathbf{R}^\top + \delta\mathbf{R}\mathbf{R}^\top = \delta(\mathbf{R}\mathbf{R}^\top) = \delta\mathbf{I} = \mathbf{0}. \tag{2.29}$$

In general, an infinitesimal variation on rotation matrix is also always anti-symmetric.

Using (2.28) we can also write

$$\delta\mathbf{R} = -\delta\tilde{\boldsymbol{\Psi}}_t\mathbf{R} \tag{2.30}$$

therefore

$$\delta\tilde{\boldsymbol{\Psi}}_t' = -\delta\mathbf{R}'\mathbf{R}^\top - \delta\mathbf{R}\mathbf{R}^{\top\prime} \tag{2.31}$$

where the tilde and space derivative can be carried out in any order. We now post-multiply (2.27) by $\mathbf{R}^\top$ and take variations to obtain an expression for variation on $\mathbf{k}_t$ (thus $\boldsymbol{\kappa}$) as

$$\delta\tilde{\mathbf{k}}_t = \delta\mathbf{R}'\tilde{\mathbf{k}}_0\mathbf{R}^\top + \mathbf{R}'\tilde{\mathbf{k}}_0\delta\mathbf{R}^\top - \delta\mathbf{R}'\mathbf{R}^\top - \mathbf{R}'\delta\mathbf{R}^\top, \tag{2.32}$$

substituting (2.27) and (2.31) leads to

$$\delta\tilde{\mathbf{k}}_t = [\delta\tilde{\boldsymbol{\Psi}}_t' + \delta\mathbf{R}\mathbf{R}^{\top\prime}] - \mathbf{R}'\delta\mathbf{R}^\top + \delta\mathbf{R}\tilde{\mathbf{k}}_0\mathbf{R}^\top + [\mathbf{R}' + \tilde{\mathbf{k}}_t\mathbf{R}]\delta\mathbf{R}^\top, \tag{2.33}$$

from which we can cancel terms and rearrange into

$$\delta\tilde{\mathbf{k}}_t = \delta\tilde{\boldsymbol{\Psi}}_t' + \delta\mathbf{R}(\mathbf{R}^{\top\prime} + \tilde{\mathbf{k}}_0\mathbf{R}^\top) + \tilde{\mathbf{k}}_t\mathbf{R}\delta\mathbf{R}^\top. \tag{2.34}$$

Further substitutions using (2.28) produces

$$\begin{aligned}\delta\tilde{\mathbf{k}}_t &= \delta\tilde{\boldsymbol{\Psi}}_t' + (-\delta\tilde{\boldsymbol{\Psi}}_t\mathbf{R})(\mathbf{R}^{\top\prime} + \tilde{\mathbf{k}}_0\mathbf{R}^\top) + \tilde{\mathbf{k}}_t\delta\tilde{\boldsymbol{\Psi}}_t \\ &= \delta\tilde{\boldsymbol{\Psi}}_t' - \delta\tilde{\boldsymbol{\Psi}}_t(-\mathbf{R}'\mathbf{R}^\top + \mathbf{R}\tilde{\mathbf{k}}_0\mathbf{R}^\top) + \tilde{\mathbf{k}}_t\delta\tilde{\boldsymbol{\Psi}}_t,\end{aligned} \tag{2.35}$$

a final substitution using (2.19) leads to

$$\begin{aligned}\delta\tilde{\mathbf{k}}_t &= \delta\tilde{\boldsymbol{\Psi}}_t' - \delta\tilde{\boldsymbol{\Psi}}_t\tilde{\mathbf{k}}_t + \tilde{\mathbf{k}}_t\delta\tilde{\boldsymbol{\Psi}}_t \\ &= \delta\tilde{\boldsymbol{\Psi}}_t' + \widetilde{\tilde{\mathbf{k}}_t\delta\boldsymbol{\Psi}_t}.\end{aligned} \tag{2.36}$$

Therefore by removing the tildes altogether, we arrive at

$$\delta\boldsymbol{\kappa} = \delta\mathbf{k}_t = \delta\boldsymbol{\Psi}_t' + \tilde{\mathbf{k}}_t\delta\boldsymbol{\Psi}_t. \tag{2.37}$$

thus expressing variations of moment strains as variations of rotations which we have represented using virtual rotations.

We now seek to express force strain variations as variations of displacements and in this case, also rotations, using a similar process. We start by taking variations on the strain equation (2.24), giving

$$\delta\boldsymbol{\gamma} = \delta\mathbf{R}(\mathbf{e} + \mathbf{u}_0' + \tilde{\mathbf{k}}_0\mathbf{u}_0) + \mathbf{R}(\delta\mathbf{u}_0' + \tilde{\mathbf{k}}_0\delta\mathbf{u}_0) \tag{2.38}$$

Now we define virtual displacement in frame $\mathbf{R}_0$ (initial local frame) in particular, as $\delta\mathbf{u}_0$. We then transform this variation into the final (current) reference frame. By definition the virtual displacement is (from [47])

$$\mathbf{R}\delta\mathbf{u}_0 = \overline{\delta\mathbf{u}_t} \tag{2.39}$$

and it should be noted that this is not equal to taking a variation in final frame as $\delta\mathbf{u}_t = \mathbf{R}\delta\mathbf{u}_0 + \delta\mathbf{R}\mathbf{u}_0$ and is not independent from virtual rotation due to the $\delta\mathbf{R}$ term.

Taking space derivative on the virtual displacement leads to

$$\overline{\delta\mathbf{u}_t}' = (\mathbf{R}\delta\mathbf{u}_0)' = \mathbf{R}'\delta\mathbf{u}_0 + \mathbf{R}\delta\mathbf{u}_0' = \mathbf{R}'\mathbf{R}^\top\overline{\delta\mathbf{u}_t} + \mathbf{R}\delta\mathbf{u}_0', \tag{2.40}$$

$$\mathbf{R}\delta\mathbf{u}_0' = \overline{\delta\mathbf{u}_t}' - \mathbf{R}'\mathbf{R}^\top\overline{\delta\mathbf{u}_t}. \tag{2.41}$$

Substituting (2.38) with (2.27) and (2.41) and also by pre-multiplying (2.24) by $\mathbf{R}^\top$, the variation on local strain can be simplified as

$$\delta\boldsymbol{\gamma} = \delta\mathbf{R}\mathbf{R}^\top(\mathbf{e} + \boldsymbol{\gamma}) + \overline{\delta\mathbf{u}_t}' - \mathbf{R}'\mathbf{R}^\top\overline{\delta\mathbf{u}_t} + \mathbf{R}\tilde{\mathbf{k}}_0\delta\mathbf{u}_0. \tag{2.42}$$

Further substituting with (2.28), (2.39) and again post-multiplying (2.27) by $\mathbf{R}^\top$ produces

$$\begin{aligned}\delta\boldsymbol{\gamma} &= -\delta\tilde{\boldsymbol{\Psi}}_t(\mathbf{e} + \boldsymbol{\gamma}) + \overline{\delta\mathbf{u}_t}' - (\mathbf{R}\tilde{\mathbf{k}}_0\mathbf{R}^\top - \tilde{\mathbf{k}}_t)\overline{\delta\mathbf{u}_t} + \mathbf{R}\tilde{\mathbf{k}}_0\mathbf{R}^\top\overline{\delta\mathbf{u}_t} \\ &= \overline{\delta\mathbf{u}_t}' + \tilde{\mathbf{k}}_t\overline{\delta\mathbf{u}_t} + (\tilde{\mathbf{e}} + \tilde{\boldsymbol{\gamma}})\delta\boldsymbol{\Psi}_t,\end{aligned} \tag{2.43}$$

which describes variations of force strains using variations on displacements and rotations. We have therefore expressed variations of both force and moment strains ($\boldsymbol{\gamma}$ and $\boldsymbol{\kappa}$) as variations of displacements and rotations ($\mathbf{u}$ and $\mathbf{R}$), in order to relate them to variations on velocities ($\mathbf{v}$ and $\boldsymbol{\omega}$) which we will also seek to express in displacements and rotations.

Now we are ready to express the variation on potential energy as variations on force and moment strains starting from the definition of strain energy,

$$\int_S \delta\mathcal{U}\, ds = \int_S (\delta\boldsymbol{\gamma}^\top \mathcal{U}_\gamma + \delta\boldsymbol{\kappa}^\top \mathcal{U}_\kappa)\, ds = \int_S (\delta\boldsymbol{\gamma}^\top \mathbf{f}_t + \delta\boldsymbol{\kappa}^\top \mathbf{m}_t)\, ds, \tag{2.44}$$

then expressing local force and moment strain variations in terms of variations on displacement and rotations,

$$\delta\mathcal{U} = (\overline{\delta\mathbf{u}_t}^{\top\prime} - \overline{\delta\mathbf{u}_t}^{\top}\tilde{\mathbf{k}}_t - \delta\boldsymbol{\Psi}_t^\top(\tilde{\mathbf{e}} + \tilde{\boldsymbol{\gamma}}))\mathbf{f}_t + (\delta\boldsymbol{\Psi}_t^{\top\prime} - \delta\boldsymbol{\Psi}_t^\top\tilde{\mathbf{k}}_t)\mathbf{m}_t. \tag{2.45}$$

Note here that the transpose operation reverses the matrix multiplication order and that identity (2.14a) is also used. The fact that energy conjugates of force and moment strains are strictly the total sectional forces and moments $\mathbf{f}_t$ and $\mathbf{m}_t$ is discussed in detail by Hodges [45] and will not be repeated here.

### Kinetic Energy Component

Similar to potential energy, we now seek to write variations of kinetic energy as variations of displacement and rotation which will enable us to express the potential and kinetic energy using variations on the same variables. The kinetic energy of the entire structure can be written as an integral of the kinetic energy per unit length $s$, $\mathcal{K}$:

$$\int_S \mathcal{K}\, ds = \frac{1}{2}\int_S \iint_{A_w} \rho_m \mathbf{v}^{*\top}\mathbf{v}^* \sqrt{g_w}\, d\boldsymbol{\xi}\, ds \tag{2.46}$$

where the velocity is taken at any point on a cross-section on the beam and $\rho_m$ is the mass density at that point in the strain-free configuration. The $A_w$ indicates an integration over the entire section area $\boldsymbol{\xi}$ where $\boldsymbol{\xi}$ is the location of the point on the particular cross-section,

$$\boldsymbol{\xi} = \begin{pmatrix} 0 \\ w_2 \\ w_3 \end{pmatrix}. \tag{2.47}$$

The $\sqrt{g_w}$ term represents the change in the amount of material per area on the cross-section as a result of initial curvature in the $w_2$ and $w_3$ directions with

$$\sqrt{g_w} = 1 - w_2 k_3 + w_3 k_2. \tag{2.48}$$

We first define angular velocities in terms of rotations in the same spirit as the curvature is defined [39]. As curvature is a change of local coordinates along space, angular velocity is its change in time therefore similar to (2.16) we can define

$$\tilde{\boldsymbol{\omega}}_t = -\dot{\mathbf{R}}^{ta}\mathbf{R}^{at} = \mathbf{R}^{ta}\dot{\mathbf{R}}^{at}, \tag{2.49a}$$

$$\tilde{\boldsymbol{\omega}}_0 = -\dot{\mathbf{R}}^{0a}\mathbf{R}^{a0} = \mathbf{0} \tag{2.49b}$$

with the only difference to moment strain being that $\boldsymbol{\omega}_0 = \mathbf{0}$ by definition. By replacing the space derivative ($\bullet'$) with time derivative ($\frac{\partial}{\partial t}$, indicated by $\dot{\bullet}$) in (2.19) it is trivial to show that

$$\tilde{\boldsymbol{\omega}}_t = -\dot{\mathbf{R}}\mathbf{R}^\top + \mathbf{R}\tilde{\boldsymbol{\omega}}_0\mathbf{R}^\top = -\dot{\mathbf{R}}\mathbf{R}^\top. \tag{2.50}$$

The velocity $\mathbf{v}_t^*$ can be further broken down as a component of centroid velocity and another component caused by rotations about the centre point on the particular cross-section

$$\mathbf{v}_t^* = \mathbf{v}_t + \tilde{\boldsymbol{\omega}}_t\boldsymbol{\xi} \tag{2.51}$$

where $\mathbf{v}_t$ is the local linear velocity of the corresponding point on the reference line. It is important to note that sectional deformations do not affect the validity of this relation as such effects will become part of the sectional inertia, a part of the material description, without appearing explicitly in kinetic energy.

The kinetic energy per unit length $s$ now becomes

$$\begin{aligned}\mathcal{K} &= \frac{1}{2}\iint_{A_w} \rho_m\sqrt{g_w}(\mathbf{v}_t + \tilde{\boldsymbol{\omega}}_t\boldsymbol{\xi}_t)^\top(\mathbf{v}_t + \tilde{\boldsymbol{\omega}}_t\boldsymbol{\xi}_t)\, d\boldsymbol{\xi} \\ &= \frac{1}{2}\iint \rho_m\sqrt{g_w}(\mathbf{v}_t^\top\mathbf{v}_t - 2\boldsymbol{\omega}_t^\top\tilde{\mathbf{v}}_t\boldsymbol{\xi}_t + \boldsymbol{\omega}_t^\top((\boldsymbol{\xi}_t^\top\boldsymbol{\xi}_t\mathbf{I} - \boldsymbol{\xi}_t\boldsymbol{\xi}_t^\top))\boldsymbol{\omega}_t)\, d\boldsymbol{\xi},\end{aligned} \tag{2.52}$$

or

$$\mathcal{K} = \frac{1}{2}(m_s\mathbf{v}_t^\top\mathbf{v}_t - 2m_s\boldsymbol{\omega}_t^\top\tilde{\mathbf{v}}_t\boldsymbol{\xi}_t + \boldsymbol{\omega}_t^\top\mathbf{i}_t\boldsymbol{\omega}_t) \tag{2.53}$$

where the sectional mass $m_s$ and inertia $\mathbf{i}_t$ are given by

$$m_s = \iint_{A_w} \rho_m\sqrt{g_m}\, d\boldsymbol{\xi}, \tag{2.54a}$$

$$\mathbf{i}_t = \iint_{A_w} \rho_m\sqrt{g_m}(\boldsymbol{\xi}^\top\boldsymbol{\xi}\mathbf{I} - \boldsymbol{\xi}\boldsymbol{\xi}^\top)\, d\boldsymbol{\xi}_t. \tag{2.54b}$$

Now we attempt to write variations on kinetic energy $\mathcal{K}$ using variations on virtual displacements and rotations, as we have done with the potential energy component $\mathcal{U}$.

From the definition of $\boldsymbol{\omega}_t$, one can arrive at an almost identical identity as in the spatial case (2.27) by again replacing space with time derivatives,

$$\dot{\mathbf{R}} = -\tilde{\boldsymbol{\omega}}_t \mathbf{R}. \tag{2.55}$$

Therefore we can write variations of local angular velocity as variations of infinitesimal rotations, replacing space by time derivative in (2.37) resulting in

$$\delta \boldsymbol{\omega}_t = \delta \dot{\boldsymbol{\Psi}}_t + \tilde{\boldsymbol{\omega}}_t \delta \boldsymbol{\Psi}_t. \tag{2.56}$$

We define linear velocities similar to the definition of force strains,

$$\mathbf{v}_t = \mathbf{R}^{ta} \dot{\mathbf{r}}_{t,a} = \mathbf{R} \dot{\mathbf{r}}_{t,0}. \tag{2.57}$$

Here an important difference is that $\mathbf{R}^{0a} \dot{\mathbf{r}}_{0,a} = \mathbf{0}$ whereas $\mathbf{R}^{0a} \mathbf{r}'_{0,a} = \mathbf{e}$, as $s$ is defined as distance along beam length while $t$ tracks the same point in time. Thus $\mathbf{e}$ does not appear in the velocity expression in the same way it appears in the strain expression. After a replacement of space by time derivative and removal of the $\mathbf{e}$ term on (2.43), the variation on linear velocity is

$$\delta \mathbf{v}_t = \dot{\overline{\delta \mathbf{u}_t}} + \tilde{\boldsymbol{\omega}}_t \overline{\delta \mathbf{u}_t} + \tilde{\mathbf{v}}_t \delta \boldsymbol{\Psi}_t. \tag{2.58}$$

Now we have the expressions for variations of velocity and angular velocity expressed as variations of displacement and rotation, we can take variations on the kinetic energy expression (2.53) and obtain, similar to (2.45),

$$\begin{aligned} \delta \mathcal{K} &= \delta \mathbf{v}_t^\top \mathbf{p}_t + \delta \boldsymbol{\omega}_t^\top \mathbf{h}_t \\ &= (\dot{\overline{\delta \mathbf{u}_t}} + \tilde{\boldsymbol{\omega}}_t \overline{\delta \mathbf{u}_t} + \tilde{\mathbf{v}}_t \delta \boldsymbol{\Psi}_t) \mathbf{p}_t + (\delta \dot{\boldsymbol{\Psi}}_t + \tilde{\boldsymbol{\omega}}_t \delta \boldsymbol{\Psi}_t) \mathbf{h}_t \end{aligned} \tag{2.59}$$

which is the final form of the variation on kinetic energy of the system expressed as variations of displacements and rotations. The linear and angular momenta can be expressed as

$$\mathbf{p}_t = m_s (\mathbf{v}_t - \tilde{\boldsymbol{\xi}}_t \boldsymbol{\omega}_t), \tag{2.60a}$$

$$\mathbf{h}_t = m_s \tilde{\boldsymbol{\xi}}_t \mathbf{v}_t + i_t \boldsymbol{\omega}_t, \tag{2.60b}$$

or written as a constitutive relation between velocities and momenta using a sectional mass matrix $\mathbf{M}$,

$$\begin{pmatrix} \mathbf{p}_t \\ \mathbf{h}_t \end{pmatrix} = \mathbf{M} \begin{pmatrix} \mathbf{v}_t \\ \boldsymbol{\omega}_t \end{pmatrix}. \tag{2.61}$$

Note that this constitutive relation is derived explicitly for velocities and momenta but does not include any sectional warping effects which will be present in a real structure [53]. This is also the reason a similar analysis for the sectional compliance linking $\mathbf{f}_t$, $\mathbf{m}_t$ to $\boldsymbol{\gamma}$, $\boldsymbol{\kappa}$ is not carried out in detail and in a real structure these will instead be obtained by sectional analysis methods [58–60]. A detailed discussion will be made in Section 2.1.4 which is dedicated to constitutive relations.

### Variational Form of Hamilton's Equation

The external work $\overline{\delta \mathcal{W}}$ is related to the externally applied forces and moments $\mathbf{f}_{E,t}$ and $\mathbf{m}_{E,t}$ by

$$\overline{\delta \mathcal{W}} = \overline{\delta \mathbf{u}_t}^\top \mathbf{f}_{E,t} + \delta \boldsymbol{\Psi}_t^\top \mathbf{m}_{E,t}. \tag{2.62}$$

By collecting the potential and kinetic energy components ((2.45) and (2.59)) as well as external work (2.62) into Hamilton's equation (2.15), we arrive at the variational form of the Hamilton's equation,

$$\begin{aligned} &\int_{t_1}^{t_2} \int_S \{ \overline{\delta \mathbf{u}_t}^\top (\mathbf{f}'_t + \tilde{\mathbf{k}}_t \mathbf{f}_t + \mathbf{f}_{E,t} - \dot{\mathbf{p}}_t - \tilde{\boldsymbol{\omega}}_t \mathbf{p}_t) + \\ &\qquad \delta \boldsymbol{\Psi}_t^\top [\mathbf{m}'_t + \tilde{\mathbf{k}}_t \mathbf{m}_t + (\tilde{\mathbf{e}} + \tilde{\gamma}_t + \tilde{\gamma}_0) \mathbf{f}_t + \mathbf{m}_{E,t} - \dot{\mathbf{h}}_t - \tilde{\boldsymbol{\omega}}_t \mathbf{h}_t - \tilde{\mathbf{v}}_t \mathbf{p}_t] \} \, ds \, dt \\ &\qquad = \int_S [\overline{\delta \mathbf{u}_t}^\top (\mathbf{p}_t(\overline{\delta \mathbf{u}_t}) - \mathbf{p}_t(\mathbf{0})) + \delta \boldsymbol{\Psi}_t^\top (\mathbf{h}_t(\delta \boldsymbol{\Psi}_t) - \mathbf{h}_t(\mathbf{0}))]_{t_1}^{t_2} \, ds - \\ &\qquad \int_{t_1}^{t_2} [\overline{\delta \mathbf{u}_t}^\top (\mathbf{f}_t(\overline{\delta \mathbf{u}_t}) - \mathbf{f}_t(\mathbf{0})) + \delta \boldsymbol{\Psi}_t^\top (\mathbf{m}_t(\delta \boldsymbol{\Psi}_t) - \mathbf{m}_t(\mathbf{0}))]_E \, dt \end{aligned} \tag{2.63}$$

where the $\overline{\delta \mathcal{A}}$ term appears on the RHS as boundary conditions and the evaluation at $E$ indicates evaluation at the free ends of the beam assembly $S$. By requirement of Hamilton's equation $\overline{\delta \mathbf{u}_t}$ and $\delta \boldsymbol{\Psi}_t$ must be zero at the start and end of the time interval ($t_1$ and $t_2$) therefore the first term on the RHS disappears. We are also normally interested in *natural boundary conditions* at the open ends of the beam assembly where

$$\overline{\delta \mathbf{u}_t}^\top \mathbf{f}_t(\overline{\delta \mathbf{u}_t}) = \delta \boldsymbol{\Psi}_t^\top \mathbf{m}_t(\delta \boldsymbol{\Psi}_t) = 0. \tag{2.64}$$

For example, this corresponds to $\overline{\delta \mathbf{u}_t} = \delta \boldsymbol{\Psi}_t = \mathbf{0}$ for a fully clamped end, whereas a free end implies $\mathbf{f}_t = \mathbf{m}_t = \mathbf{0}$ at that end. Therefore by setting the RHS to zero we obtain

$$\mathbf{f}_t' + \tilde{\mathbf{k}}_t\mathbf{f}_t + \mathbf{f}_{E,t} = \dot{\mathbf{p}}_t + \tilde{\boldsymbol{\omega}}_t\mathbf{p}_t, \tag{2.65a}$$

$$\mathbf{m}_t' + \tilde{\mathbf{k}}_t\mathbf{m}_t + \mathbf{m}_{E,t} + (\tilde{\mathbf{e}} + \tilde{\boldsymbol{\gamma}})\mathbf{f}_t = \dot{\mathbf{h}}_t + \tilde{\boldsymbol{\omega}}_t\mathbf{h}_t + \tilde{\mathbf{v}}_t\mathbf{p}_t. \tag{2.65b}$$

The $t$'s can now be dropped as all variables are entirely in one single frame of reference (current configuration). After replacing $\mathbf{k}_t$ by $\boldsymbol{\kappa} + \mathbf{k}_0$ from (2.17), the final form of the Hamilton's equation (momentum conservation equations) becomes

$$\mathbf{f}' + (\tilde{\boldsymbol{\kappa}} + \tilde{\mathbf{k}}_0)\mathbf{f} + \mathbf{f}_E = \dot{\mathbf{p}} + \tilde{\boldsymbol{\omega}}\mathbf{p}, \tag{2.66a}$$

$$\mathbf{m}' + (\tilde{\boldsymbol{\kappa}} + \tilde{\mathbf{k}}_0)\mathbf{m} + \mathbf{m}_E + (\tilde{\mathbf{e}} + \tilde{\boldsymbol{\gamma}})\mathbf{f} = \dot{\mathbf{h}} + \tilde{\boldsymbol{\omega}}\mathbf{h} + \tilde{\mathbf{v}}\mathbf{p}. \tag{2.66b}$$

### 2.1.3 Compatibility Relations

Two sets of variables (velocities and strains, with their rotational counterparts) are used in the equations of motion (2.66), these are in fact not independent as both sets are derivatives of position and rotation, one with time and one with space. This relation leads to the derivation of compatibility relations to complement the equations of motion in order to provide a closed-form description of the dynamics. First consider the definitions of curvatures (2.19),

$$\begin{aligned} \tilde{\boldsymbol{\kappa}} &= -\mathbf{R}'\mathbf{R}^\top + \mathbf{R}\tilde{\mathbf{k}}_0\mathbf{R}^\top - \tilde{\mathbf{k}}_0, \\ \Rightarrow \dot{\tilde{\boldsymbol{\kappa}}} &= -\dot{\mathbf{R}}'\mathbf{R}^\top - \mathbf{R}'\dot{\mathbf{R}}^\top + \dot{\mathbf{R}}\tilde{\mathbf{k}}_0\mathbf{R}^\top + \mathbf{R}\tilde{\mathbf{k}}_0\dot{\mathbf{R}}^\top, \end{aligned} \tag{2.67}$$

and angular velocities (2.49),

$$\begin{aligned} \tilde{\boldsymbol{\omega}} &= -\dot{\mathbf{R}}\mathbf{R}^\top = \mathbf{R}\dot{\mathbf{R}}^\top, \\ \Rightarrow \tilde{\boldsymbol{\omega}}' &= -\dot{\mathbf{R}}'\mathbf{R}^\top - \dot{\mathbf{R}}\mathbf{R}^{\top\prime}. \end{aligned} \tag{2.68}$$

Making use of (2.10) results in

$$\begin{aligned} \tilde{\boldsymbol{\kappa}}\tilde{\boldsymbol{\omega}} &= -\mathbf{R}'\dot{\mathbf{R}}^\top + \mathbf{R}\tilde{\mathbf{k}}_0\dot{\mathbf{R}}^\top, \\ \Rightarrow \tilde{\boldsymbol{\omega}}\tilde{\boldsymbol{\kappa}} &= -\dot{\mathbf{R}}\mathbf{R}^{\top\prime} + \dot{\mathbf{R}}\tilde{\mathbf{k}}_0\mathbf{R}^\top, \\ \Rightarrow \dot{\tilde{\boldsymbol{\kappa}}} &= \tilde{\boldsymbol{\omega}}' + \tilde{\boldsymbol{\kappa}}\tilde{\boldsymbol{\omega}} - \tilde{\boldsymbol{\omega}}\tilde{\boldsymbol{\kappa}} = \tilde{\boldsymbol{\omega}}' + \widetilde{\tilde{\boldsymbol{\kappa}}\boldsymbol{\omega}}, \end{aligned} \tag{2.69}$$

thus

$$\dot{\boldsymbol{\kappa}} = \boldsymbol{\omega}' + \tilde{\boldsymbol{\kappa}}\boldsymbol{\omega} + \tilde{\mathbf{k}}_0\boldsymbol{\omega}. \tag{2.70}$$

A similar relation is found with linear curvatures and velocities starting from velocities (2.57),

$$\begin{aligned} \mathbf{v} &= \mathbf{R}\dot{\mathbf{u}}, \\ \Rightarrow \mathbf{v}' &= \mathbf{R}'\dot{\mathbf{u}} + \mathbf{R}\dot{\mathbf{u}}', \end{aligned} \tag{2.71}$$

and force strains (2.24),

$$\begin{aligned} \boldsymbol{\gamma} &= \mathbf{R}(\mathbf{e} + \mathbf{u}' + \tilde{\mathbf{k}}_0\mathbf{u}) - \mathbf{e} - \boldsymbol{\gamma}_0, \\ \Rightarrow \dot{\boldsymbol{\gamma}} &= \dot{\mathbf{R}}(\mathbf{e} + \mathbf{u}' + \tilde{\mathbf{k}}_0\mathbf{u}) + \mathbf{R}(\dot{\mathbf{u}}' + \tilde{\mathbf{k}}_0\dot{\mathbf{u}}), \end{aligned} \tag{2.72}$$

We also have

$$\begin{aligned} \dot{\mathbf{u}} &= \mathbf{R}^\top\mathbf{v}, \\ \Rightarrow \dot{\boldsymbol{\gamma}} &= \dot{\mathbf{R}}\mathbf{R}^\top(\mathbf{e} + \boldsymbol{\gamma}) + \mathbf{R}\tilde{\mathbf{k}}_0\dot{\mathbf{u}} + \mathbf{R}\dot{\mathbf{u}}', \\ \Rightarrow \mathbf{v}' &= \mathbf{R}'\mathbf{R}^\top\mathbf{v} + \mathbf{R}\dot{\mathbf{u}}', \end{aligned} \tag{2.73}$$

Therefore

$$\begin{aligned} \dot{\boldsymbol{\gamma}} - \dot{\mathbf{R}}\mathbf{R}^\top(\mathbf{e} + \boldsymbol{\gamma}) - \mathbf{R}\tilde{\mathbf{k}}_0\mathbf{R}^\top\mathbf{v} &= \mathbf{v}' - \mathbf{R}'\mathbf{R}^\top\mathbf{v}, \\ \Rightarrow \dot{\boldsymbol{\gamma}} + \tilde{\boldsymbol{\omega}}(\mathbf{e} + \boldsymbol{\gamma}) - \mathbf{R}\tilde{\mathbf{k}}_0\mathbf{R}^\top\mathbf{v} + \mathbf{R}'\mathbf{R}^\top\mathbf{v} &= \mathbf{v}', \\ \Rightarrow \dot{\boldsymbol{\gamma}} - (\tilde{\mathbf{e}} + \tilde{\boldsymbol{\gamma}})\boldsymbol{\omega} - \tilde{\boldsymbol{\kappa}}\mathbf{v} - \tilde{\mathbf{k}}_0\mathbf{v} &= \mathbf{v}', \end{aligned} \tag{2.74}$$

thus

$$\dot{\boldsymbol{\gamma}} = \mathbf{v}' + \tilde{\boldsymbol{\kappa}}\mathbf{v} + (\tilde{\mathbf{e}} + \tilde{\boldsymbol{\gamma}})\boldsymbol{\omega} + \tilde{\mathbf{k}}_0\mathbf{v}. \tag{2.75}$$

### 2.1.4 Constitutive Equations

The beam's material imposes additional constraints on the variables, namely the speed-momentum and stress-strain relations link the variables via material properties,

$$\begin{pmatrix} \boldsymbol{\gamma} \\ \boldsymbol{\kappa} \end{pmatrix} = \mathbf{C} \begin{pmatrix} \mathbf{f} \\ \mathbf{m} \end{pmatrix} \tag{2.76}$$

and

$$\begin{pmatrix} \mathbf{p} \\ \mathbf{h} \end{pmatrix} = \mathbf{M} \begin{pmatrix} \mathbf{v} \\ \boldsymbol{\omega} \end{pmatrix}. \tag{2.77}$$

Here $\mathbf{C}$ and $\mathbf{M}$ are both symmetric matrices of the sectional properties that vary as a function of sectional location $s$ only. (2.60a) provides a simple form of the exact value of the mass matrix $\mathbf{M}$, however it does not account for sectional warping. Although a similar derivation can be made to obtain the exact form of the compliance matrix $\mathbf{C}$, the inherently complex nature of sectional warping makes computation under the prior assumption of planar cross-sections questionable. In practical situations the exact $\mathbf{M}$ and $\mathbf{C}$ matrices often come from a structural homogenisation or sectional analysis on the 3D FE model which inherently incorporates the warping field $\mathbf{w}_t$ [58–60]. In Chapter 5 we will describe an alternative method based on static condensation that does not require the computation of $\mathbf{C}$ and $\mathbf{M}$ explicitly.

### 2.1.5 Strong Form of the Beam Equations

Combining the compatibility relations ((2.70) and (2.75)) and equation of motion (2.66), the closed-form equations of the intrinsic beam theory can now be expressed as (from [47])

$$\overset{\cdot}{\begin{pmatrix}\mathbf{p}\\ \mathbf{h}\end{pmatrix}} - \begin{pmatrix}\mathbf{f}\\ \mathbf{m}\end{pmatrix}' - \begin{pmatrix}\tilde{\mathbf{k}}_0 & \mathbf{0}\\ \tilde{\mathbf{e}} & \tilde{\mathbf{k}}_0\end{pmatrix}\begin{pmatrix}\mathbf{f}\\ \mathbf{m}\end{pmatrix} + \begin{pmatrix}\tilde{\boldsymbol{\omega}} & \mathbf{0}\\ \tilde{\mathbf{v}} & \tilde{\boldsymbol{\omega}}\end{pmatrix}\begin{pmatrix}\mathbf{p}\\ \mathbf{h}\end{pmatrix} + \begin{pmatrix}\mathbf{0} & \tilde{\mathbf{f}}\\ \tilde{\mathbf{f}} & \tilde{\mathbf{m}}\end{pmatrix}\begin{pmatrix}\boldsymbol{\gamma}\\ \boldsymbol{\kappa}\end{pmatrix} = \begin{pmatrix}\mathbf{f}_E\\ \mathbf{m}_E\end{pmatrix}, \tag{2.78a}$$

$$\overset{\cdot}{\begin{pmatrix}\boldsymbol{\gamma}\\ \boldsymbol{\kappa}\end{pmatrix}} - \begin{pmatrix}\mathbf{v}\\ \boldsymbol{\omega}\end{pmatrix}' + \begin{pmatrix}-\tilde{\mathbf{k}}_0 & -\tilde{\mathbf{e}}\\ \mathbf{0} & -\tilde{\mathbf{k}}_0\end{pmatrix}\begin{pmatrix}\mathbf{v}\\ \boldsymbol{\omega}\end{pmatrix} - \begin{pmatrix}-\tilde{\boldsymbol{\omega}} & -\tilde{\mathbf{v}}\\ \mathbf{0} & -\tilde{\boldsymbol{\omega}}\end{pmatrix}\begin{pmatrix}\boldsymbol{\gamma}\\ \boldsymbol{\kappa}\end{pmatrix} = \mathbf{0}, \tag{2.78b}$$

together with the constitutive relations ((2.76) and (2.77)). By substituting the constitutive relations and grouping the variables, one obtain (following [9])

$$\mathbf{M}\dot{\mathbf{x}}_1 - \mathbf{x}_2' - \mathbf{E}\mathbf{x}_2 + \mathcal{L}_1(\mathbf{x}_1)\mathbf{M}\mathbf{x}_1 + \mathcal{L}_2(\mathbf{x}_2)\mathbf{C}\mathbf{x}_2 = \mathbf{f}_A, \tag{2.79a}$$

$$\mathbf{C}\dot{\mathbf{x}}_2 - \mathbf{x}_1' + \mathbf{E}^T\mathbf{x}_1 - \mathcal{L}_1^\top(\mathbf{x}_1)\mathbf{C}\mathbf{x}_2 = \mathbf{0}, \tag{2.79b}$$

which is the final, strong form of the beam equations, with the state variables being $\mathbf{x}_1 = \begin{bmatrix}\mathbf{v}^\top & \boldsymbol{\omega}^\top\end{bmatrix}^\top$ and $\mathbf{x}_2 = \begin{bmatrix}\mathbf{f}^\top & \mathbf{m}^\top\end{bmatrix}^\top$, all defined in the local reference frame.

The $\mathcal{L}$ linear operators operate on 6-element vectors and are defined as

$$\mathcal{L}_1\left(\begin{bmatrix} \mathbf{a} \\ \mathbf{b} \end{bmatrix}\right) = \begin{pmatrix} \tilde{\mathbf{b}} & \mathbf{0} \\ \tilde{\mathbf{a}} & \tilde{\mathbf{b}} \end{pmatrix}, \tag{2.80a}$$

$$\mathcal{L}_2\left(\begin{bmatrix} \mathbf{a} \\ \mathbf{b} \end{bmatrix}\right) = \begin{pmatrix} \mathbf{0} & \tilde{\mathbf{a}} \\ \tilde{\mathbf{a}} & \tilde{\mathbf{b}} \end{pmatrix}, \tag{2.80b}$$

where **a** and **b** are 3-element vectors.

The problem is posed together with boundary conditions that are dependent on the setup of the problem. For example a cantilever setup with the end at $s = 0$ fixed and free at $s = L$ would be

$$\begin{cases} \mathbf{x}_1(s,0) = \hat{\mathbf{x}}_1(s) \\ \mathbf{x}_1(0,t) = [0,0,0,0,0,0]^\top \\ \mathbf{x}_2(L,t) = [0,0,0,0,0,0]^\top \end{cases}. \tag{2.81}$$

The current form of the intrinsic equations is based on the assumption of no structural damping, as in Hodges' original work. It will be very easy to include a damping term but would be of limited use as damping is normally measured experimentally.

It is interesting to note that the $\mathcal{L}$ functions have the properties

$$\mathcal{L}_2^\top(\mathbf{a}) = -\mathcal{L}_2(\mathbf{a}), \tag{2.82a}$$

$$\mathcal{L}_1(\mathbf{a})\mathbf{b} = -\mathcal{L}_2(\mathbf{b})\mathbf{a} = \mathcal{L}_2^\top(\mathbf{b})\mathbf{a}, \tag{2.82b}$$

$$\mathcal{L}_1^\top(\mathbf{a})\mathbf{b} = -\mathcal{L}_1^\top(\mathbf{b})\mathbf{a}, \tag{2.82c}$$

$$\mathbf{b}^\top\mathcal{L}_1^\top(\mathbf{a}) = -\mathbf{a}^\top\mathcal{L}_2^\top(\mathbf{b}) = \mathbf{a}^\top\mathcal{L}_2(\mathbf{b}), \tag{2.82d}$$

$$\mathbf{b}^\top\mathcal{L}_1(\mathbf{a}) = -\mathbf{a}^\top\mathcal{L}_1(\mathbf{b}). \tag{2.82e}$$

The initial beam curvature appears in the local **E** matrix where

$$\mathbf{E} = \mathcal{L}_1(\begin{bmatrix} \mathbf{e}^\top & \mathbf{k}_0^\top \end{bmatrix}^\top). \tag{2.83}$$

### 2.1.6 Displacements and Rotations

In the preceding sections we have detailed the derivation of the strong form of the intrinsic beam formulation following previous work by Hodges [45, 47]. The displacement and rotation at each point along the reference line are not variables in the intrinsic description but can be reclaimed via velocity or strain from their respective definitions. There is more than one way of computing these variables and a method that uses quaternions is described in [43]. In this work we shall use the rotation matrix description as outlined in [47]. From rearranging (2.49) we can obtain

$$\tilde{\boldsymbol{\omega}} = \tilde{\boldsymbol{\omega}}_t = \mathbf{R}^{ta}\dot{\mathbf{R}}^{at}, \tag{2.84}$$

thus pre-multiplying by $\mathbf{R}^{ta}$ produces

$$\dot{\mathbf{R}}^{at} = \mathbf{R}^{at}\tilde{\boldsymbol{\omega}}. \tag{2.85}$$

Similarly, from (2.57) we can obtain

$$\dot{\mathbf{r}}_{t,a} = \mathbf{R}^{at}\mathbf{v}_t = \mathbf{R}^{at}\mathbf{v}, \tag{2.86}$$

which describes the time evolution of the position and rotation of each point in the global reference frame. Similarly from (2.16) and (2.20) it is trivial to show that

$$\mathbf{R}^{at'} = \mathbf{R}^{at}(\tilde{\boldsymbol{\kappa}} + \widetilde{\mathbf{k}_0}) \tag{2.87}$$

and

$$\mathbf{r}'_{t,a} = \mathbf{R}^{at}(\boldsymbol{\gamma} + \mathbf{e}), \tag{2.88}$$

which describe the variations of position and rotation along each beam segment. In subsequent sections we define the local orientation relative to the global coordinate system at a particular point along the beam as $\mathbf{T} = \mathbf{R}^{at}$ and its displacement relative to the origin in global frame $\mathbf{r} = \mathbf{r}_{t,a}$, giving

$$\dot{\mathbf{T}} = \mathbf{T}\tilde{\boldsymbol{\omega}}, \tag{2.89a}$$

$$\dot{\mathbf{r}} = \mathbf{T}\mathbf{v}, \tag{2.89b}$$

$$\mathbf{T}' = \mathbf{T}(\tilde{\boldsymbol{\kappa}} + \widetilde{\mathbf{k}_0}), \tag{2.89c}$$

$$\mathbf{r}' = \mathbf{T}(\boldsymbol{\gamma} + \mathbf{e}). \tag{2.89d}$$

## 2.2 2-D Aerofoil Theory and Aerodynamic Formulation

The standard 2D linear unsteady aerofoil theory relates the aerodynamic forces on an 2-D aerofoil section, subject to a freestream airflow of a constant velocity (airspeed), to the angle-of-attack of the aerofoil via linear relations. The 2D linear aerodynamic assumptions are that the local aerodynamic forces are only dependent upon the local

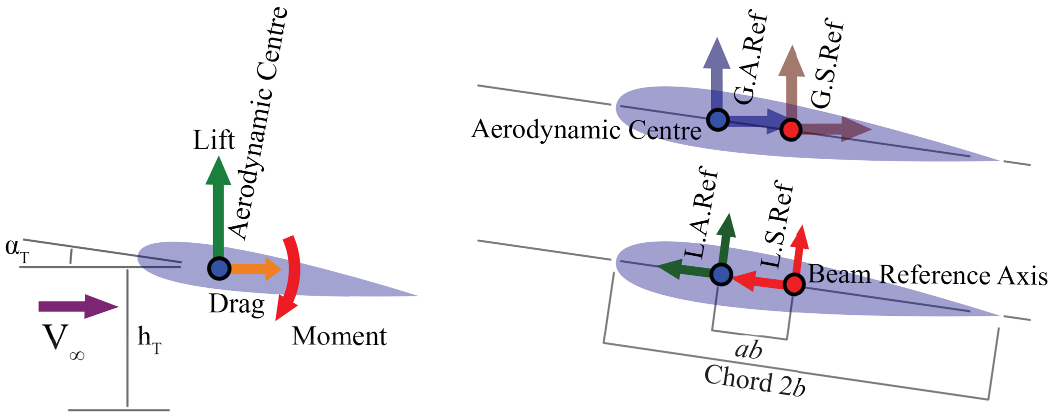

(a) Aerodynamic variable definitions

(b) Reference frame definitions

Figure 4: Illustration of the 2D aerofoil problem. The figure on the right indicates the four reference frames used in this section, which are the global aerodynamic reference frame (blue), global structural reference frame (dark red), local aerodynamic reference frame (green) and local structural reference frame (red).

instantaneous airflow and for the unsteady case, the lift history; has no shockwave movements, stall, other nonlinear phenomena, or 3D aerodynamic interactions. Although the effect of sweep is implied, it is far from accurate as the model does not account for spanwise airflow. The unsteady aerodynamic formulation used in this work will be that obtained via inviscid analysis on a flat 2D aerofoil using the small disturbance approximation (Theodorsen's solution), with the solution then modified to fit actual parameters of the wing shape. These will be reformulated using Peters' [90] inflow model into a description using velocities and forces in the wing's local frame, which will subsequently be coupled onto the intrinsic structural equations using the method described by Palacios *et al.* [9]. This section is a detailed description of the derivation that leads to the result obtained by Palacios *et al.*in [9].

### 2.2.1 Theodorsen's Solution for Inviscid Unsteady Flat-Plate Aerofoil

Theodorsen's solution is a description of 2D unsteady aerodynamic forces. The solution treats the trailing wake shed by an aerofoil as a flat sheet of vortices and integrates their influences on the aerofoil. This produces an exact analytic solution of the time-varying aerodynamic forces on the aerofoil as a function of aerofoil heaving and pitching motions. As a very standard and widely used solution, it is reviewed in detail by Katz and Plotkin [69], among many others, and will not be discussed here in depth. Only the resulting solution will be used.

To set up the 2D unsteady aerofoil problem, the aerofoil in question has a chord of $2b$, vertical (out-of-plane) position in an inertial reference frame $h_T$ and angle of attack (a.o.a.) $\alpha_T$ moving in a freestream velocity $V_\infty$. The lift $L_{AE}$ (positive up) is defined as the total aerodynamic force on the aerofoil section perpendicular to the direction of *airflow*, where drag $D_{AE}$ (positive downstream) is the total aerodynamic force on the aerofoil section parallel to the direction of *airflow*. The moment $M_{AE}$ (positive pitch-up) is defined as the total aerodynamic moment around the aerodynamic centre of the aerofoil. The aerodynamic lift $L_{AE}$, drag $D_{AE}$, moment $M_{AE}$, angle of attack $\alpha_T$ and vertical location $h_T$ are measured in the inertial reference frame at the aerodynamic centre, in this case at quarter-chord, a location where the aerodynamic moment does not depend on the steady-state angle of attack. The above quantities are defined in an inertial reference frame that moves against the oncoming airflow with velocity $V_\infty$, which will subsequently be called the *global aerodynamic reference frame*. In the spirit of Peters' inflow model, we will then transform the description into one that describes local aerodynamic forces at an arbitrary location on the chord using local velocities at that location. Thus we further define another reference frame which we will refer to as the *local aerodynamic reference frame* with the axes local to the aerofoil and origin on the aerodynamic centre. This reference frame treats the air as stationary and the aerofoil moving forward with a velocity $V_\infty$, in which we define the transverse velocity $V_2$ (positive forward) parallel to the chordline, normal velocity $V_3$ (positive up) perpendicular to the chordline and angular velocity $\omega$ around the aerodynamic centre (positive pitch-up). It is worth noting that this could be different from the transverse velocity components $v_2$ and $v_3$ in the structural problem as $V_2$ and $V_3$ are defined with the origin at the aerodynamic centre instead of the structural reference axis, and that the aerofoil's zero-lift direction need not point in an axis of the structural reference frame. Here for the purpose of Theodorsen's solution it is assumed that the aerofoil is flat with zero thickness.

Theodorsen's solution considers this flat plate aerofoil in an inviscid 2D flow with a constant freestream velocity, with the aerofoil undergoing heaving and pitching motions (changes in $h_T$ and $\alpha_T$). The aerodynamic forces on such an aerofoil in frequency-domain can be calculated to be [69]

$$\overline{L}_{AE}(ik_r) = \pi\rho V_\infty 2b C_k(ik_r)[V_\infty \overline{\alpha}_T(ik_r) - \dot{\overline{h}}_T + b\dot{\overline{\alpha}}_T(ik_r)], \tag{2.90a}$$

$$\overline{M}_{AE}(ik_r) = -\frac{1}{2}\pi\rho b^2[V_\infty b\dot{\overline{\alpha}}_T(ik_r)], \tag{2.90b}$$

where an overline indicates a frequency-domain variable of the corresponding variable in time-domain. Here we take the Laplace transform from time- into frequency-domain as

$$\overline{\alpha}_T(ik_r) = \int_0^\infty e^{-ik_r s_r} \alpha_T(s_r). \tag{2.91}$$

The reduced (non-dimensional) time $s_r$ defined as

$$s_r = \frac{tV_\infty}{b}, \tag{2.92}$$

the corresponding reduced frequency $k_r$ is defined as

$$k_r = \frac{\omega^* V_\infty}{b} \tag{2.93}$$

with $\omega^*$ being angular frequency.

Note that only lift and moment are present in this formulation, the drag force is zero as a result of inviscid analysis. $C_k$, the *Theodorsen's function*, is a non-rational function that arises from a convolution integral from the wake vortex sheet model and is written in terms of Bessel functions, which here we will approximate using rational functions (from [9]) in a form that we will benefit from in subsequent analysis,

$$C_k(ik_r) = 1 - \sum_{j=1}^{N_{AE}} \frac{ik_r A_j^{AE}}{ik_r + b_j^{AE}} \tag{2.94}$$

where for a given $N_{AE}$, the sum of coefficients $A_j^{AE}$ always equals 1/2. This approximation is exact in the limit of $N_{AE} \to \infty$.

It is important to note that the form of the solution here does not include the effects of apparent mass, which would give additional terms multiplying $\ddot{\overline{h}}$, $\dot{\overline{\alpha}}$ and $\ddot{\overline{\alpha}}$. These are omitted on purpose due to the low frequency of anticipated dynamics on a HALE aircraft. On more rigid, low aspect-ratio wings the effect of apparent mass is much more pronounced due to dynamics occuring at a higher frequency.

We now make a change of variable from $h_T$ and $\alpha_T$ defined in the global aerodynamic reference frame into $V_2$, $V_3$ and $\omega$ defined in the local aerodynamic reference frame. Using small-angle approximation on $\alpha_T$, we obtain the following relations,

$$V_\infty = V_2/\cos\alpha_T \approx V_2, \tag{2.95a}$$

$$\dot{h}_T = V_3\cos\alpha_T + V_2\sin\alpha_T \approx V_3 + V_2\alpha_T, \tag{2.95b}$$

$$\dot{\alpha}_T = \omega, \tag{2.95c}$$

which results in the following forms of aerodynamic lift and moment,

$$\overline{L}_{AE}(ik_r) = 2\pi\rho V_\infty b\left(1 - \sum_{j=1}^{N_{AE}} \frac{ik_r A_j^{AE}}{ik_r + b_j^{AE}}\right)[-\overline{V}_3(ik_r) + b\overline{\omega}(ik_r)], \tag{2.96a}$$

$$\overline{M}_{AE}(ik_r) = -\pi\rho b^2 V_\infty \cdot \frac{b}{2}\overline{\omega}(ik_r). \tag{2.96b}$$

Note here that we retain $V_\infty$ in the unsteady aerodynamic terms as it will be computed separately later in the formulation. We now make another substitution by defining a set of aerodynamic states $\lambda_j$ corresponding to each coefficient in the Theodorsen's function approximation:

$$\overline{\lambda}_j(ik_r) = \frac{1}{V_\infty}\frac{1}{ik_r + b_j^{AE}}[-\overline{V}_3(ik_r) + b\overline{\omega}(ik_r)] \tag{2.97}$$

and substituting this variable into the aerodynamic lift gives

$$\overline{L}_{AE}(ik) = 2\pi\rho V_\infty b(-\overline{V}_3(ik) + b\overline{\omega}(ik) - V_\infty \sum_{j=1}^{N_{AE}} ikA_j^{AE}\overline{\lambda}_j(ik)). \tag{2.98}$$

Manipulating the definition of $\lambda_j$ and making a Laplace transform into time-domain gives

$$(ik_r + b_j^{AE})\overline{\lambda}_j(ik_r) = \frac{1}{V_\infty}[-\overline{V}_3(ik_r) + b\overline{\omega}(ik_r)], \tag{2.99}$$

$$\frac{d\lambda_j(s_r)}{ds_r} + b_j^{AE}\lambda_j(s_r) = \frac{1}{V_\infty}[-V_3(s_r) + b\omega(s_r)]. \tag{2.100}$$

Since $\frac{d}{ds_r} = \frac{b}{V_\infty}\frac{d}{dt}$,

$$\frac{d\lambda_j(s_r)}{dt} + \frac{b_j^{AE}V_\infty}{b}\lambda_j(s_r) = [-\frac{1}{b}V_3(s_r) + \omega(s_r)], \tag{2.101}$$

or finally

$$\dot{\lambda}_j + \frac{b_j^{AE}V_\infty}{b}\lambda_j = -\frac{1}{b}V_3 + \omega. \tag{2.102}$$

By using (2.99) and the identity $\sum A_j^{AE} = \frac{1}{2}$,

$$ik_r\overline{\lambda}_j(ik_r) = -\, b_j^{AE}\overline{\lambda}_j(ik_r) + \frac{1}{V_\infty}[-\overline{V}_3(ik_r) + b\overline{\omega}(ik_r)]. \tag{2.103}$$

$$\begin{aligned} -V_\infty \sum A_j^{AE} ik_r\overline{\lambda}_j(ik_r) =& V_\infty \sum A_j^{AE} b_j^{AE}\overline{\lambda}_j(ik_r) \\ & - \sum A_j^{AE}[-\overline{V}_3(ik_r) + b\overline{\omega}(ik_r)], \\ =& V_\infty \sum A_j^{AE} b_j^{AE}\overline{\lambda}_j(ik_r) - \frac{1}{2}[-\overline{V}_3(ik_r) + b\overline{\omega}(ik_r)]. \end{aligned} \tag{2.104}$$

This gives

$$\overline{L}_{AE}(ik_r) = 2\pi\rho V_\infty b(\frac{1}{2}(-\overline{V}_3(ik) + b\overline{\omega}(ik_r)) + V_\infty \sum_{j=1}^{N_{AE}} (A_j^{AE} b_j^{AE}\overline{\lambda}_j(ik_r))). \tag{2.105}$$

Transforming the lift and moment expressions results in

$$L_{AE}(s_r) = 2\pi\rho V_\infty b \left[\frac{1}{2}(-V_3(s_r) + b\omega(s_r)) + V_\infty \sum_{j=1}^{N_{AE}} A_j^{AE} b_j^{AE} \lambda_j(s_r)\right], \tag{2.106a}$$

$$M_{AE}(s_r) = -2\pi\rho V_\infty b^2 \cdot \frac{b}{4}\omega(s_r). \tag{2.106b}$$

or simply

$$L_{AE} = 2\pi\rho V_\infty b \left[\frac{1}{2}(-V_3 + b\omega) + V_\infty \sum_{j=1}^{N_{AE}} A_j^{AE} b_j^{AE} \lambda_j\right], \tag{2.107a}$$

$$M_{AE} = -2\pi\rho V_\infty b^2 \cdot \frac{b}{4}\omega, \tag{2.107b}$$

which together with (2.102) provides a complete description of the aerodynamic forces and moments in terms of aerofoil velocities defined in the local aerodynamic reference frame. Figure 5 illustrates the contribution of each aerodynamic state in the 2-state aerodynamic model to the unsteady lift for a change of angle of attack at time zero.

Note again that in this solution, the drag is absent due to the use of an inviscid fluid model. The steady-state lift and moment coefficients, which in reality depend on the exact shape and symmetry of the aerofoil, also assumes the theoretical values $2\pi$ and zero respectively [69] due to the use of flat plate aerofoil in the model. The following part will thus examine the extension of this model to fit actual aerofoil parameters and write the solution in a form that is easily coupled with the intrinsic structural model.

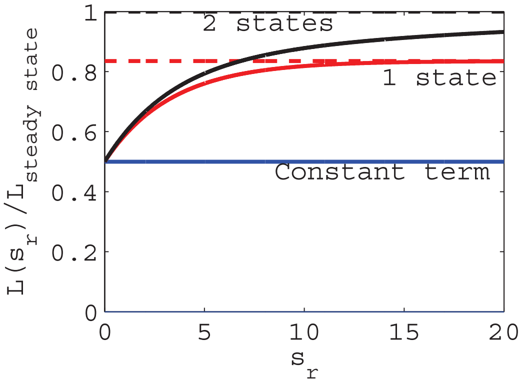

Figure 5: Lift variation against non-dimensional time for an instantaneous change of angle of attack at time zero, normalised by the steady-state value. This figure illustrates the contribution of unsteady aerodynamic terms of the 2-state aerodynamic model to the lift response.

### 2.2.2 Unsteady Aerodynamic Solution using Aerofoil Parameters for Arbitrary Reference Axis

For a thick, cambered aerofoil, the steady-state lift, drag and moment coefficient, $C_L$, $C_D$ and $C_M$ follow these formal definitions from dimensional analysis [69],

$$L_{AE} = \frac{1}{2}\rho V_\infty^2 \cdot 2bC_L, \tag{2.108a}$$

$$D_{AE} = \frac{1}{2}\rho V_\infty^2 \cdot 2bC_D, \tag{2.108b}$$

$$M_{AE} = \frac{1}{2}\rho V_\infty^2 \cdot 2b \cdot 2bC_M, \tag{2.108c}$$

which, in linear aerofoil theory, become

$$C_L = C_{L0} + C_{L\alpha}\alpha_T + C_{L\delta}\delta, \tag{2.109a}$$

$$C_M = C_{M0} + C_{M\delta}\delta, \tag{2.109b}$$

$$C_D = C_{D0}, \tag{2.109c}$$

where $\alpha$ is the angle of attack and $\delta$ is the control surface deflection angle. This means that, in first approximation, the lift/drag/moment coefficients are dependent on various aerofoil parameters and the orientation of the aerofoil and any of its control surfaces. The constant $C_{L\alpha}$ is defined as the slope of steady-state lift coefficient with respect to the angle of attack $\alpha$, whereas $C_{L0}$ is the steady-state lift coefficient at zero angle of attack. The last constant $C_{M0}$ is the steady-state moment coefficient of the aerofoil regardless of the angle of attack (due to the definition of the aerodynamic centre). It is already seen that for a flat plate aerofoil in particular, the aerodynamic centre is at the forward quarter-chord location.The control surfaces introduce additional contributions to the lift and moment coefficient through the $C_{L\delta}$ and $C_{M\delta}$ coefficients particular to the control surface design.

In Theodorsen's solution, the inviscid model on a flat aerofoil produces $C_{L\alpha} = 2\pi$ and $C_{M0} = C_{D0} = 0$. Thus here we will make the assumption, as previous works have done using this model [7, 8], that the same solution applies for a thick and cambered aerofoil with arbitrary aerodynamic coefficients. For this we define another global reference frame with origin *aft* of the aerodynamic centre located with a distance of $ab$ from the a.c. where $a$ is the ratio of this distance to the length of half-chord, a point which we will refer to as the structural axis (a negative $a$ indicates the reference axis is forward of the a.c.). This frame will be referred to as the *global structural reference frame* with the associated aerodynamic loads being $L_a$, $D_a$ and $M_a$. We further define a final reference frame similar to the local aerodynamic reference frame but with the origin at the structural axis. In this reference frame we define the transverse velocity $v_2$ (positive forward) parallel to the chordline, normal velocity $v_3$ (positive up) perpendicular to the chordline and angular velocity $\omega$ around the aerodynamic centre (positive pitch-up), together with associated loads measured at the structural axis being $F_{a2}$, $F_{a3}$ and $M_a$.

We start by modifying the solution of the unsteady aerodynamic forces (2.107) obtained previously using the definitions of aerofoil parameters to obtain

$$L_{AE} = \frac{1}{2}\rho V_\infty \cdot 2b(C_{L\alpha}(\frac{1}{2}(-V_3 + b\omega) + \frac{1}{2}V_\infty \sum_{j=1}^{N_{AE}} 2A_j^{AE} b_j^{AE} \lambda_j) + V_\infty(C_{L0} + C_{L\delta}\delta)), \tag{2.110a}$$

$$D_{AE} = \frac{1}{2}\rho V_\infty^2 \cdot 2bC_{D0}, \tag{2.110b}$$

$$M_{AE} = -\frac{1}{2}\rho V_\infty \cdot 2b \cdot 2bC_{L\alpha}\frac{b}{8}\omega + \frac{1}{2}\rho V_\infty^2 \cdot 2b \cdot 2b(C_{M0} + C_{M\delta}\delta). \tag{2.110c}$$

For simplicity, in the current model we assume that there is no unsteady effects associated with control surface deflection, which would be straightforward to incorporate if necessary. We now transform the aerodynamic forces onto the global structural reference frame according to

$$L_a = L_{AE}, \tag{2.111a}$$

$$D_a = D_{AE}, \tag{2.111b}$$

$$M_a = M_{AE} + L_{AE} \cdot ab, \tag{2.111c}$$

which produces

$$\begin{aligned} M_a = & \frac{1}{2}\rho V_\infty \cdot 2b \cdot 2b(-C_{L\alpha}\frac{b}{8}\omega + V_\infty(C_{M0} + C_{M\delta}\delta)) \\ & + ab\frac{1}{2}\rho V_\infty \cdot 2b(C_{L\alpha}(\frac{1}{2}(-V_3 + b\omega) + \frac{1}{2}V_\infty \sum_{j=1}^{N_{AE}} 2A_j^{AE} b_j^{AE} \lambda_j) + V_\infty(C_{L0} + C_{L\delta}\delta)) \end{aligned} \tag{2.112}$$

with the other two components being identical to their counterparts at the global aerodynamic reference frame.

We then express the velocities defined in the local aerodynamic frame as velocities defined in the local structural frame as

$$V_2 = V_\infty = v_2, \tag{2.113a}$$

$$V_3 = v_3 + ab\omega. \tag{2.113b}$$

Substituting this into the aerodynamic loads ((2.110) and (2.112)) provides a relation between global aerodynamic loads (lift/drag/moment) at the structural axis as a function of local velocities at that point, with the components being

$$L_a = \frac{1}{2}\rho V_\infty \cdot 2b(C_{L\alpha}(\frac{1}{2}(-v_3 + b(1-a)\omega) + \frac{1}{2}V_\infty \sum_{j=1}^{N_{AE}} 2A_j^{AE} b_j^{AE} \lambda_j) + V_\infty(C_{L0} + C_{L\delta}\delta)), \tag{2.114a}$$

$$D_a = \frac{1}{2}\rho V_\infty^2 \cdot 2bC_{D0}, \tag{2.114b}$$

$$\begin{aligned} M_a = & \frac{1}{2}\rho V_\infty \cdot 2b \cdot 2b(-C_{L\alpha}\frac{b}{8}\omega + V_\infty(C_{M0} + C_{M\delta}\delta)) \\ & + ab\frac{1}{2}\rho V_\infty \cdot 2b(C_{L\alpha}(\frac{1}{2}(-v_3 + b(1-a)\omega) + \frac{1}{2}V_\infty \sum_{j=1}^{N_{AE}} 2A_j^{AE} b_j^{AE} \lambda_j) + V_\infty(C_{L0} + C_{L\delta}\delta)). \end{aligned} \tag{2.114c}$$

Finally we transform the global force definitions into the local forces, using

$$F_{a2} = L_a \sin\alpha - D_a \cos\alpha, \tag{2.115a}$$

$$F_{a3} = L_a \cos\alpha + D_a \sin\alpha, \tag{2.115b}$$

$$\sin\alpha = -\frac{v_3}{V_\infty}, \tag{2.115c}$$

$$\cos\alpha = \frac{v_2}{V_\infty}, \tag{2.115d}$$

to produce the following expressions that relate the local velocities at the structural axis to the local aerodynamic loads generated by these velocities:

$$\begin{aligned} F_{a2} = {} & -\frac{1}{2}\rho v_3 \cdot 2b(C_{L\alpha}(\frac{1}{2}(-v_3 + b(1-a)\omega) + \frac{1}{2}V_\infty \sum_{j=1}^{N_{AE}} 2A_j^{AE} b_j^{AE} \lambda_j) + V_\infty(C_{L0} + C_{L\delta}\delta)) \\ & -\frac{1}{2}\rho V_\infty v_2 \cdot 2bC_{D0}, \end{aligned} \tag{2.116a}$$

$$\begin{aligned} F_{a3} = {} & \frac{1}{2}\rho v_2 \cdot 2b(C_{L\alpha}(\frac{1}{2}(-v_3 + b(1-a)\omega) + \frac{1}{2}V_\infty \sum_{j=1}^{N_{AE}} 2A_j^{AE} b_j^{AE} \lambda_j) + V_\infty(C_{L0} + C_{L\delta}\delta)) \\ & -\frac{1}{2}\rho V_\infty v_3 \cdot 2bC_{D0}, \end{aligned} \tag{2.116b}$$

$$\begin{aligned} M_a = {} & \frac{1}{2}\rho V_\infty \cdot 2b \cdot 2b(-C_{L\alpha}\frac{b}{8}\omega + V_\infty(C_{M0} + C_{M\delta}\delta)) \\ & + ab\frac{1}{2}\rho V_\infty \cdot 2b(C_{L\alpha}(\frac{1}{2}(-v_3 + b(1-a)\omega) + \frac{1}{2}V_\infty \sum_{j=1}^{N_{AE}} 2A_j^{AE} b_j^{AE} \lambda_j) + V_\infty(C_{L0} + C_{L\delta}\delta)). \end{aligned} \tag{2.116c}$$

We shall write the above relations in compact form as

$$\mathbf{F}_a = \mathbf{F}_{a,qs} + \mathbf{F}_{a,i} \cdot V_\infty \sum_{j=1}^{N_{AE}} 2A_j^{AE} b_j^{AE} \lambda_j + \mathbf{F}_{a,c}\delta \tag{2.117}$$

with $\mathbf{F}_a = \begin{bmatrix} 0 & F_{a2} & F_{a3} & M_a & 0 & 0 \end{bmatrix}^\top$ and other variables defined similarly. In this form the quasi-steady contribution becomes

$$F_{a2,qs} = \rho b(-C_{D0}v_2^2 + \frac{1}{2}C_{L\alpha}v_3^2 - \frac{1}{2}b(1-a)C_{L\alpha}\omega v_3 - v_2v_3C_{L0}), \tag{2.118a}$$

$$F_{a3,qs} = \rho b((-\frac{1}{2}C_{L\alpha} - C_{D0})v_2v_3 + \frac{1}{2}b(1-a)C_{L\alpha}v_2\omega + v_2^2C_{L0}), \tag{2.118b}$$

$$M_{a,qs} = \rho v_2 b^2((2C_{M0} + aC_{L0})v_2 - \frac{1}{2}aC_{L\alpha}v_3 + \frac{1}{2}b(a - a^2 - \frac{1}{2})C_{L\alpha}\omega), \tag{2.118c}$$

while the induced component is

$$F_{a2,i} = -\frac{1}{2}\rho bC_{L\alpha}v_3, \tag{2.119a}$$

$$F_{a3,i} = \frac{1}{2}\rho bC_{L\alpha}v_2, \tag{2.119b}$$

$$M_{a,i} = \frac{1}{2}\rho ab^2C_{L\alpha}v_2, \tag{2.119c}$$

and finally the control surface contribution being

$$F_{a2,c} = -\rho bC_{L\delta}v_2v_3, \tag{2.120a}$$

$$F_{a3,c} = \rho bC_{L\delta}v_2^2, \tag{2.120b}$$

$$M_{a,c} = \rho b^2(2C_{M\delta} + aC_{L\delta})v_2^2. \tag{2.120c}$$

With a similar change of variables in (2.102), the definition of the aerodynamic state is now

$$\dot{\lambda}_j + \frac{b_j^{AE}V_\infty}{b}\lambda_j = -\frac{1}{b}v_3 + (1-a)\omega. \tag{2.121}$$

We further define the instantaneous sectional velocity state in the local structural reference frame as $\mathbf{x}_1 = \begin{bmatrix} v_1 & v_2 & v_3 & \omega_1 & \omega_2 & \omega_3 \end{bmatrix}^\top$ with $\omega = \omega_1$, identical to the definition of velocity state in the intrinsic beam formulation. We thus arrive at a compact form of the aerodynamic description using matrices that is identical to the description in [9],

$$\mathbf{F}_a = \rho b(\mathcal{A}_1(\mathbf{x}_1)\mathbf{x}_1 + V_\infty\mathcal{A}_2\mathbf{x}_1 \cdot \sum_{j=1}^{N_{AE}} 2A_j^{AE}b_j^{AE}\lambda_j + \mathcal{A}_3(\mathbf{x}_1)\mathbf{x}_1 \cdot \delta), \tag{2.122a}$$

$$\dot{\lambda}_j = \boldsymbol{\kappa}_{AE}^\top\mathbf{x}_1 - \frac{b_j^{AE}V_\infty}{b}\lambda_j, \tag{2.122b}$$

with the definition of the vector $\boldsymbol{\kappa}_{AE}^\top = \begin{bmatrix} 0 & 0 & -1/b & (1-a) & 0 & 0 \end{bmatrix}$ and the linear operators $\mathcal{A}$ being

$$\mathcal{A}_1(\mathbf{x}_1) = \tag{2.123a}$$

$$\begin{pmatrix} 0 & 0 & 0 & 0 & 0 & 0 \\ 0 & -C_{D0}x_2 & \frac{C_{L\alpha}}{2}x_3 - C_{L0}x_2 & -b(1-a)\frac{C_{L\alpha}}{2}x_3 & 0 & 0 \\ 0 & C_{L0}x_2 - (\frac{C_{L\alpha}}{2} + C_{D0})x_3 & 0 & b(1-a)\frac{C_{L\alpha}}{2}x_2 & 0 & 0 \\ 0 & (2bC_{M0} + abC_{L0})x_2 - ab\frac{C_{L\alpha}}{2}x_3 & 0 & b^2(a - a^2 - \frac{1}{2})\frac{C_{L\alpha}}{2}x_2 & 0 & 0 \\ 0 & 0 & 0 & 0 & 0 & 0 \\ 0 & 0 & 0 & 0 & 0 & 0 \end{pmatrix}, \tag{2.123b}$$

$$\mathcal{A}_2 = \begin{pmatrix} 0 & 0 & 0 & 0 & 0 & 0 \\ 0 & 0 & -1 & 0 & 0 & 0 \\ 0 & 1 & 0 & 0 & 0 & 0 \\ 0 & ab & 0 & 0 & 0 & 0 \\ 0 & 0 & 0 & 0 & 0 & 0 \\ 0 & 0 & 0 & 0 & 0 & 0 \end{pmatrix}, \tag{2.124}$$

$$\mathcal{A}_3(\mathbf{x}_1) = \begin{pmatrix} 0 & 0 & 0 & 0 & 0 & 0 \\ 0 & 0 & -C_{L\delta}x_2 & 0 & 0 & 0 \\ 0 & C_{L\delta}x_2 & 0 & 0 & 0 & 0 \\ 0 & (abC_{L\delta} + 2bC_{M\delta})x_2 & 0 & 0 & 0 & 0 \\ 0 & 0 & 0 & 0 & 0 & 0 \\ 0 & 0 & 0 & 0 & 0 & 0 \end{pmatrix}. \tag{2.125}$$

The $V_\infty$ is retained in the $\mathcal{A}_2$ term instead of being replaced by a local $v_2$ in order to keep the aerodynamic description second-order. This leads to an additional assumption that $V_\infty$ changes slowly which is justified under the fidelity of this formulation as the original Theodorsen's solution does not allow changes in $V_\infty$ at all.

To summarise, we have arrived at a description which uses Theodorsen's solution as a starting point and developed a relation between aerodynamic loads on a 2D aerofoil section and its velocities relative to still air, all expressed in a local reference frame. It is important to realise that whereas Theodorsen's solution assumes the small-angle approximation throughout, the subsequent transformation of the aerodynamic loads into the aerofoil's local reference frame regards the angle-of-attack finite and that the lift is not perpendicular to the zero-lift line. As a result, using different levels of approximations or even a different order of transformation could result in formulations that are subtly different than the one described here. Such can be seen when compared to similar work by Patil [8] who used a coordinate system centred at mid-chord rather than the quarter-chord as the starting point of the analysis, which, although equivalent in Theodorsen's solution, produces slightly different terms in the final formulation than those presented here. It should be noted that neither should be regarded as being more correct than the other as the linear (small-disturbance) assumption of Theodorsen's solution is that the lift is always perpendicular to the *incoming airflow direction.* However by also allowing for heaving (and pitching) motions, this direction in fact could not be uniquely defined. In the next section we will describe the projection of this formulation onto structural modes in arriving at a modal aeroelastic formulation of an aircraft.

# 3 Nonlinear Aeroservoelastic System Description in Modal Coordinates

This chapter will describe the projection of the intrinsic structural and aerodynamic equations developed in the previous chapter onto a set of global modes to obtain an intrinsic modal formulation of the structural and aerodynamic systems. This process converts a set of nonlinear PDEs into a set of nonlinear ODEs that can be marched in time more easily and also makes model reduction easier to carry out. The chapter will also describe system linearisation and the process by which a robust linear controller can be created on the system.

## 3.1 Modal Structural Formulation

### 3.1.1 Natural Modes and Orthogonality under Unloaded Equilibrium

In order to obtain the natural modes of the structure, we will use the intrinsic beam equation (2.79) as the starting point of the modal structural formulation. When we assume there is no external force applied and linearise about the unloaded equilibrium of $\mathbf{x}_1 = \mathbf{x}_2 = \mathbf{0}$, the intrinsic equations take the form of

$$\mathbf{M}\dot{\mathbf{x}}_1 - \mathbf{x}_2' - \mathbf{E}\mathbf{x}_2 = \mathbf{f}_A, \tag{3.1a}$$

$$\mathbf{C}\dot{\mathbf{x}}_2 - \mathbf{x}_1' + \mathbf{E}^\top\mathbf{x}_1 = \mathbf{0}. \tag{3.1b}$$

By setting $\mathbf{f}_A$ to zero, one can define the linear natural modes of the system using separation of variables, e.g. assuming $\mathbf{x}_1(s,t) = x_{1T}(t)\mathbf{x}_{1S}(s)$ and solving the equations for $t$ and $s$ separately. Such an approach leads to the following forms,

$$\mathbf{x}_1 = \boldsymbol{\phi}_{1j}(s)\sin(\omega_j t), \tag{3.2a}$$

$$\mathbf{x}_2 = \boldsymbol{\phi}_{2j}(s)\cos(\omega_j t). \tag{3.2b}$$

Note that this is essentially a separation of the natural mode of the system into its real and imaginary components. By substituting (3.2) into the linear equations(3.1) we obtain the equations for solving the space-domain structural modes $\boldsymbol{\phi}_{1j}$ and $\boldsymbol{\phi}_{2j}$ where the $s$ is now omitted,

$$\boldsymbol{\phi}_{1j}' - \mathbf{E}^\top\boldsymbol{\phi}_{1j} = -\omega_j\mathbf{C}\boldsymbol{\phi}_{2j}, \tag{3.3a}$$

$$\boldsymbol{\phi}_{2j}' + \mathbf{E}\boldsymbol{\phi}_{2j} = \omega_j\mathbf{M}\boldsymbol{\phi}_{1j}. \tag{3.3b}$$

These equations form a generalised eigenvalue problem of the form

$$\begin{pmatrix} \frac{\partial}{\partial s} - \mathbf{E}^\top & \mathbf{0} \\ \mathbf{0} & \frac{\partial}{\partial s} + \mathbf{E} \end{pmatrix} \begin{pmatrix} \boldsymbol{\phi}_{1j} \\ \boldsymbol{\phi}_{2j} \end{pmatrix} = \omega_j \begin{pmatrix} \mathbf{0} & -\mathbf{C} \\ \mathbf{M} & \mathbf{0} \end{pmatrix} \begin{pmatrix} \boldsymbol{\phi}_{1j} \\ \boldsymbol{\phi}_{2j} \end{pmatrix} \tag{3.4}$$

whose solutions need to be solved with appropriate boundary conditions numerically, or in simple cases, analytically, as can be found in [43]. As the system lacks damping, the eigenvalues are always real and each positive eigenvalue will have an equal and negative counterpart. For a continuous problem the number of eigenvalues will be infinite, whereas for a discretised problem the total number of eigenvalues will equal to the number of degrees of freedoms in the problem.

We now set out to prove that the natural modes of the system are orthogonal to each other as it will be an important property later in the analysis. Assuming that these solutions are now known, multiplying (3.3) with $\boldsymbol{\phi}_{1i}^\top$ or $\boldsymbol{\phi}_{2i}^\top$ and integrating over the entire $S$ gives

$$\int_S (\boldsymbol{\phi}_{2i}^\top \boldsymbol{\phi}_{1j}' - \boldsymbol{\phi}_{2i}^\top \mathbf{E}^\top \boldsymbol{\phi}_{1j})\, ds = -\omega_j \int_S \boldsymbol{\phi}_{2i}^\top \mathbf{C} \boldsymbol{\phi}_{2j}\, ds, \tag{3.5a}$$

$$\int_S (\boldsymbol{\phi}_{1i}^\top \boldsymbol{\phi}_{2j}' + \boldsymbol{\phi}_{1i}^\top \mathbf{E} \boldsymbol{\phi}_{2j})\, ds = \omega_j \int_S \boldsymbol{\phi}_{1i}^\top \mathbf{M} \boldsymbol{\phi}_{1j}\, ds. \tag{3.5b}$$

Integrating by parts and assuming natural boundary conditions (which makes $\boldsymbol{\phi}_{2i}^\top \boldsymbol{\phi}_{1j}\big|_E = 0$) gives

$$\int_S \boldsymbol{\phi}_{2i}^\top \boldsymbol{\phi}_{1j}'\, ds = \boldsymbol{\phi}_{2i}^\top \boldsymbol{\phi}_{1j}\Big|_E - \int_S \boldsymbol{\phi}_{2i}^{\top\prime} \boldsymbol{\phi}_{1j}\, ds = -\int_S \boldsymbol{\phi}_{1j}^\top \boldsymbol{\phi}_{2i}'\, ds. \tag{3.6}$$

After exchanging $i$ and $j$, we substitute (3.6) into the first equation in (3.5). This results in

$$\int_S (-\boldsymbol{\phi}_{1i}^\top \boldsymbol{\phi}_{2j}' - \boldsymbol{\phi}_{2j}^\top \mathbf{E}^\top \boldsymbol{\phi}_{1i})\, ds = \int_S (-\boldsymbol{\phi}_{1i}^\top \boldsymbol{\phi}_{2j}' - \boldsymbol{\phi}_{1i}^\top \mathbf{E} \boldsymbol{\phi}_{2j})\, ds = -\omega_i \int_S \boldsymbol{\phi}_{2i}^\top \mathbf{C} \boldsymbol{\phi}_{2j}\, ds, \tag{3.7}$$

since the identity $\mathbf{a}^\top \mathbf{C} \mathbf{b} = \mathbf{b}^\top \mathbf{C}^\top \mathbf{a}$ holds for any combination of $\mathbf{a}$, $\mathbf{b}$ and matrix $\mathbf{C}$. Finally we add (3.7) to the second equation of (3.5) and obtain

$$\omega_j \int_S \boldsymbol{\phi}_{1i}^\top \mathbf{M} \boldsymbol{\phi}_{1j}\, ds - \omega_i \int_S \boldsymbol{\phi}_{2i}^\top \mathbf{C} \boldsymbol{\phi}_{2j}\, ds = 0. \tag{3.8}$$

Since $i$ and $j$ are arbitrary, the equation holds equally when $i$ and $j$ are exchanged. Thus we can also show that

$$\omega_i \int_S \boldsymbol{\phi}_{1i}^\top \mathbf{M} \boldsymbol{\phi}_{1j}\, ds - \omega_j \int_S \boldsymbol{\phi}_{2i}^\top \mathbf{C} \boldsymbol{\phi}_{2j}\, ds = 0. \tag{3.9}$$

Provided at least one of $\omega_i$ and $\omega_j$ is non-zero, we will then proceed to multiply (3.8) by $\omega_i$ and (3.9) by $\omega_j$, subtracting between them results in

$$(\omega_i^2 - \omega_j^2) \int_S \boldsymbol{\phi}_{2i}^\top \mathbf{C} \boldsymbol{\phi}_{2j}\, ds = 0 \tag{3.10}$$

which then proves that if $\omega_i \neq \omega_j$, the integral $\int_S \boldsymbol{\phi}_{2i}^\top \mathbf{C} \boldsymbol{\phi}_{2j}\, ds$ must be zero. A similar proof can be made for the $\int_S \boldsymbol{\phi}_{1i}^\top \mathbf{M} \boldsymbol{\phi}_{1j}\, ds$ integral. This condition holds as long as $\omega_i \neq \omega_j$, possible exceptions to this would be if the two modes are both rigid-body modes, which have an eigenvalue of zero, or are members of a set of redundant (i.e. identical) eigenvalues. The reason is that in both cases, any linear combination between $\boldsymbol{\phi}_{1i}$ and $\boldsymbol{\phi}_{1j}$ (and between $\boldsymbol{\phi}_{2i}$ and $\boldsymbol{\phi}_{2j}$) is also a natural mode of the system. However even in these situations it is always possible to prescribe particular linear combinations of the redundant modes in order to make the previous relation hold. If instead $i = j$, then due to $\mathbf{M}$ and $\mathbf{C}$ being symmetrical everywhere, the integrals ($\int_S \boldsymbol{\phi}_{1i}^\top \mathbf{M} \boldsymbol{\phi}_{1i}\, ds$ and $\int_S \boldsymbol{\phi}_{2i}^\top \mathbf{C} \boldsymbol{\phi}_{2i}\, ds$) will be a non-zero positive number, which can be set to unity by scaling the magnitude of $\boldsymbol{\phi}_{1i}$ or $\boldsymbol{\phi}_{2i}$ accordingly. Thus we have demonstrated the orthogonality between the natural modes of the structural system which is written as

$$\int_S \boldsymbol{\phi}_{1i}^\top \mathbf{M} \boldsymbol{\phi}_{1j}\, ds = \delta_{ij}, \tag{3.11a}$$

$$\int_S \boldsymbol{\phi}_{2i}^\top \mathbf{C} \boldsymbol{\phi}_{2j}\, ds = \delta_{ij} \tag{3.11b}$$

where we have also implicitly normalised the magnitudes of individual modes.

### 3.1.2 Natural Modes and Orthogonality under Loaded Equilibrium

The previous section described the linearisation about the unloaded equilibrium where the sectional stresses are zero everywhere. However in practice it is common to operate at an equilibrium condition under external loads, i.e. with the sectional stress $\mathbf{x}_2 = \hat{\mathbf{x}}_2 \neq \mathbf{0}$ and the equilibrium $\hat{\mathbf{x}}_2$ is the solution to the static equilibrium equation by setting $\mathbf{x}_1 = \mathbf{0}$ in (2.79), resulting in

$$-\hat{\mathbf{x}}_2' - \mathbf{E}\hat{\mathbf{x}}_2 + \mathcal{L}_2(\hat{\mathbf{x}}_2)\mathbf{C}\hat{\mathbf{x}}_2 = \hat{\mathbf{f}}_A, \tag{3.12}$$

under the external load distribution $\hat{\mathbf{f}}_A$.

Using the identities in (2.82), the linearised intrinsic equations with a non-zero $\hat{\mathbf{x}}_2$ takes the form of

$$\mathbf{M}\dot{\mathbf{x}}_1 - \mathbf{x}_2' - \mathbf{E}\mathbf{x}_2 + \left(\mathcal{L}_2(\hat{\mathbf{x}}_2)\mathbf{C} - \mathcal{L}_1(\mathbf{C}\hat{\mathbf{x}}_2)\right)\mathbf{x}_2 = \mathbf{0}, \tag{3.13a}$$

$$\mathbf{C}\dot{\mathbf{x}}_2 - \mathbf{x}_1' + \mathbf{E}^\top\mathbf{x}_1 + \mathcal{L}_1^\top(\mathbf{C}\hat{\mathbf{x}}_2)\mathbf{x}_1 = \mathbf{0}. \tag{3.13b}$$

Similar to before, if we assume the solution to the linearised equations has the form of

$$\begin{aligned} \mathbf{x}_1 &= \hat{\boldsymbol{\phi}}_{1j}(s)\sin(\hat{\omega}_j t), \qquad (3.14a)\\ \mathbf{x}_2 &= \hat{\mathbf{x}}_2 + \hat{\boldsymbol{\phi}}_{2j}(s)\cos(\hat{\omega}_j t), \end{aligned}$$

then the natural modes, where we will refer to as $\hat{\boldsymbol{\phi}}_1$ and $\hat{\boldsymbol{\phi}}_2$ to distinguish from the zero-equilibrium ones, will be the solutions to the generalised eigenvalue problem of

$$\begin{aligned} &\begin{pmatrix} \frac{\partial}{\partial s} - \mathbf{E}^\top - \mathcal{L}_1^\top(\mathbf{C}\hat{\mathbf{x}}_2) & \mathbf{0} \\ \mathbf{0} & \frac{\partial}{\partial s} + \mathbf{E} - \left(\mathcal{L}_2(\hat{\mathbf{x}}_2)\mathbf{C} - \mathcal{L}_1(\mathbf{C}\hat{\mathbf{x}}_2)\right) \end{pmatrix} \begin{pmatrix} \hat{\boldsymbol{\phi}}_{1j} \\ \hat{\boldsymbol{\phi}}_{2j} \end{pmatrix} \\ &= \hat{\omega}_j \begin{pmatrix} \mathbf{0} & -\mathbf{C} \\ \mathbf{M} & \mathbf{0} \end{pmatrix} \begin{pmatrix} \hat{\boldsymbol{\phi}}_{1j} \\ \hat{\boldsymbol{\phi}}_{2j} \end{pmatrix}. \end{aligned} \tag{3.15}$$

These natural modes, unlike the unloaded case, are not orthogonal under the definition in (3.11) due to a lack of symmetry induced by the $\hat{\mathbf{x}}_2$ terms. For this reason as well as energy-conservation properties detailed in Section 4.1.3, subsequent parts of this work shall use the natural modes on an undeformed structure as basis if possible.

### 3.1.3 Nonlinear Beam Equation in Modal Coordinates

In this section, we describe the process of using Galerkin projection on the intrinsic structural equation in order to project it into its modal form. Assuming that we have obtained the natural modes of the system according to Section 3.1.1, or that we have otherwise pre-defined a custom set of modes as the modal basis (which are not necessarily natural modes), we can use this complete set of modes to represent an arbitrary configuration of the structure as

$$\mathbf{x}_1 = \sum_{j=1}^{\infty} \boldsymbol{\phi}_{1j}(s) q_{1j}(t), \tag{3.16a}$$

$$\mathbf{x}_2 = \sum_{j=1}^{\infty} \boldsymbol{\phi}_{2j}(s) q_{2j}(t). \tag{3.16b}$$

Here it is possible for $\boldsymbol{\phi}$ to be an arbitrary set of (possibly non-orthogonal) modes, i.e. they are not required to satisfy (3.11). However it is still required that they are linearly independent, i.e. no mode can be obtained from a linear combination of the other modes. Here we still assume the system uses the full number of modes, therefore the total number of modes is again equal to the total number of degrees of freedom in the structure.

We perform the Galerkin projection on the full nonlinear equation by inserting (3.16) into the intrinsic structural equation (2.79), multiplying by $\boldsymbol{\phi}_{1j}$ or $\boldsymbol{\phi}_{2j}$ and integrating, which results in

$$\int_S \boldsymbol{\phi}_{1j}^\top \Bigg[\mathbf{M}\sum_{k=1}^{\infty}\boldsymbol{\phi}_{1k}\dot{q}_{1k} - (\sum_{k=1}^{\infty}(\boldsymbol{\phi}_{2k}' + \mathbf{E}\boldsymbol{\phi}_{2k})q_{2k}) \tag{3.17a}$$

$$+\sum_{k=1}^{\infty}\mathcal{L}_1(\boldsymbol{\phi}_{1k})q_{1k}\mathbf{M}\sum_{l=1}^{\infty}\boldsymbol{\phi}_{1l}q_{1l} + \sum_{k=1}^{\infty}\mathcal{L}_2(\boldsymbol{\phi}_{2k})q_{2k}\mathbf{C}\sum_{l=1}^{\infty}\boldsymbol{\phi}_{2l}q_{2l}\Bigg]\,ds = \int_S \boldsymbol{\phi}_{1j}^\top \mathbf{f}_A\,ds,$$

$$\int_S \boldsymbol{\phi}_{2j}^\top \Bigg[\mathbf{C}\sum_{k=1}^{\infty}\boldsymbol{\phi}_{2k}\dot{q}_{2k} - (\sum_{k=1}^{\infty}(\boldsymbol{\phi}_{1k}' - \mathbf{E}^\top\boldsymbol{\phi}_{1k})q_{1k}) - \sum_{k=1}^{\infty}\mathcal{L}_1^\top(\boldsymbol{\phi}_{1k})q_{1k}\mathbf{C}\sum_{l=1}^{\infty}\boldsymbol{\phi}_{2l}q_{2l}\Bigg]\,ds = 0. \tag{3.17b}$$

We now define a number of coefficients to simplify this pair of equations,

$$\mathrm{A}_{1,jk} = \int_S \boldsymbol{\phi}_{1j}^\top \mathbf{M}\boldsymbol{\phi}_{1k}\,ds, \tag{3.18a}$$

$$\Lambda_{1,jk} = \int_S \boldsymbol{\phi}_{1j}^\top(\boldsymbol{\phi}_{2k}' + \mathbf{E}\boldsymbol{\phi}_{2k})\,ds, \tag{3.18b}$$

$$\Gamma_{1,jkl} = \int_S \boldsymbol{\phi}_{1j}^\top \mathcal{L}_1(\boldsymbol{\phi}_{1k})\mathbf{M}\boldsymbol{\phi}_{1l}\,ds, \tag{3.18c}$$

$$\Gamma_{2,jkl} = \int_S \boldsymbol{\phi}_{1j}^\top \mathcal{L}_2(\boldsymbol{\phi}_{2k})\mathbf{C}\boldsymbol{\phi}_{2l}\,ds, \tag{3.18d}$$

$$\eta_{1,j} = \int_S \boldsymbol{\phi}_{1j}^\top \mathbf{f}_A\,ds, \tag{3.18e}$$

$$\mathrm{A}_{2,jk} = \int_S \boldsymbol{\phi}_{2j}^\top \mathbf{C}\boldsymbol{\phi}_{2k}\,ds, \tag{3.18f}$$

$$\Lambda_{2,jk} = \int_S \boldsymbol{\phi}_{2j}^\top(\boldsymbol{\phi}_{1k}' - \mathbf{E}^\top\boldsymbol{\phi}_{1k}))\,ds, \tag{3.18g}$$

$$\Gamma_{3,jkl} = \int_S \boldsymbol{\phi}_{2j}^\top \mathcal{L}_1^\top(\boldsymbol{\phi}_{1k})\mathbf{C}\boldsymbol{\phi}_{2l}\,ds. \tag{3.18h}$$

Note that the $\Gamma$ coefficients have the properties arising from the forms of the $\mathcal{L}$ operators, described in (2.82), that

$$\Gamma_{3,kjl} = \Gamma_{2,jkl}, \tag{3.19a}$$

$$\Gamma_{1,kjl} = -\Gamma_{1,jkl}, \tag{3.19b}$$

$$\Gamma_{1,jjl} = 0. \tag{3.19c}$$

However for now the $\Gamma_{3,kjl}$ term is retained for clarity. The intrinsic equation under Galerkin projection (3.17) now becomes

$$\sum_{k=1}^{\infty} \mathrm{A}_{1,jk}\dot{q}_{1k} - \sum_{k=1}^{\infty} \Lambda_{1,jk} q_{2k} + \sum_{k=1}^{\infty}\sum_{l=1}^{\infty} \Gamma_{1,jkl} q_{1k} q_{1l} + \sum_{k=1}^{\infty}\sum_{l=1}^{\infty} \Gamma_{2,jkl} q_{2k} q_{2l} = \eta_{1,j}, \tag{3.20a}$$

$$\sum_{k=1}^{\infty} \mathrm{A}_{2,jk}\dot{q}_{2k} - \sum_{k=1}^{\infty} \Lambda_{2,jk} q_{1k} - \sum_{k=1}^{\infty}\sum_{l=1}^{\infty} \Gamma_{3,jkl} q_{1k} q_{2l} = 0, \tag{3.20b}$$

or, using Einstein's notation to imply summing over repeated indices,

$$\mathrm{A}_{1,jk}\dot{q}_{1k} = \Lambda_{1,jk} q_{2k} - \Gamma_{1,jkl} q_{1k} q_{1l} - \Gamma_{2,jkl} q_{2k} q_{2l} + \eta_{1,j}, \tag{3.21a}$$

$$\mathrm{A}_{2,jk}\dot{q}_{2k} = \Lambda_{2,jk} q_{1k} + \Gamma_{3,jkl} q_{1k} q_{2l}. \tag{3.21b}$$

After retaining a finite number of modes, the equation can also be written in vector form so that

$$\mathbf{A}_1\dot{\mathbf{q}}_1 = \boldsymbol{\Lambda}_1\mathbf{q}_2 - \boldsymbol{\Gamma}_1(\mathbf{q}_1)\mathbf{q}_1 - \boldsymbol{\Gamma}_2(\mathbf{q}_2)\mathbf{q}_2 + \boldsymbol{\eta}_1, \tag{3.22a}$$

$$\mathbf{A}_2\dot{\mathbf{q}}_2 = \boldsymbol{\Lambda}_2\mathbf{q}_1 + \boldsymbol{\Gamma}_3(\mathbf{q}_1)\mathbf{q}_2, \tag{3.22b}$$

or

$$\dot{\mathbf{q}}_1 = \mathbf{A}_1^{-1}(\boldsymbol{\Lambda}_1\mathbf{q}_2 - \boldsymbol{\Gamma}_1(\mathbf{q}_1)\mathbf{q}_1 - \boldsymbol{\Gamma}_2(\mathbf{q}_2)\mathbf{q}_2 + \boldsymbol{\eta}_1), \tag{3.23a}$$

$$\dot{\mathbf{q}}_2 = \mathbf{A}_2^{-1}(\boldsymbol{\Lambda}_2\mathbf{q}_1 + \boldsymbol{\Gamma}_3(\mathbf{q}_1)\mathbf{q}_2), \tag{3.23b}$$

where $\mathbf{A}$, $\boldsymbol{\Lambda}$, $\mathbf{q}$ and $\mathbf{Q}$ are matrices or vectors with elements being their counterparts in (3.21) and $\boldsymbol{\Gamma}_1(\mathbf{q}_1)|_{jl} = \sum_k \Gamma_{1,jkl} q_{1k}$. The $\boldsymbol{\Gamma}_2$ and $\boldsymbol{\Gamma}_3$ are defined similarly. We further group the two equations together by defining $\mathbf{q} = \begin{bmatrix} \mathbf{q}_1 & \mathbf{q}_2 \end{bmatrix}^\top$, $\boldsymbol{\eta} = \begin{bmatrix} \boldsymbol{\eta}_1 & \mathbf{0} \end{bmatrix}^\top$ and

$$\mathbf{A} = \begin{bmatrix} \mathbf{A}_1 & \mathbf{0} \\ \mathbf{0} & \mathbf{A}_2 \end{bmatrix}, \quad \boldsymbol{\Lambda} = \begin{bmatrix} \mathbf{0} & \boldsymbol{\Lambda}_1 \\ \boldsymbol{\Lambda}_2 & \mathbf{0} \end{bmatrix}, \quad \boldsymbol{\Gamma}(\mathbf{q}) = \begin{bmatrix} -\boldsymbol{\Gamma}_1(\mathbf{q}_1) & -\boldsymbol{\Gamma}_2(\mathbf{q}_2) \\ \mathbf{0} & \boldsymbol{\Gamma}_3(\mathbf{q}_1) \end{bmatrix}, \tag{3.24}$$

resulting in

$$\dot{\mathbf{q}} = \mathbf{A}^{-1}(\boldsymbol{\Lambda}\mathbf{q} + \boldsymbol{\Gamma}(\mathbf{q})\mathbf{q} + \boldsymbol{\eta}). \tag{3.25}$$

We have thus obtained the modal form of the intrinsic beam equations where the original variables $\mathbf{x}_1$ and $\mathbf{x}_2$ can be reclaimed from (3.16).

If, in particular, we seek to use the natural modes $\boldsymbol{\phi}_1$ and $\boldsymbol{\phi}_2$ in the modal projection, their orthogonality allows us to further simplify the A and $\Lambda$ coefficients using (3.3) and (3.11),

$$\mathrm{A}_{1,jk} = \mathrm{A}_{2,jk} = \delta_{jk}, \tag{3.26a}$$

$$\Lambda_{1,jk} = \omega_j \delta_{jk}, \tag{3.26b}$$

$$\Lambda_{2,jk} = -\omega_j \delta_{jk}, \tag{3.26c}$$

which results in a simpler form of the modal structural equations,

$$\dot{q}_{1j} = \omega_j q_{2j} - \Gamma_{1,jkl} q_{1k} q_{1l} - \Gamma_{2,jkl} q_{2k} q_{2l} + \eta_{1,j}, \tag{3.27a}$$

$$\dot{q}_{2j} = -\omega_j q_{1j} + \Gamma_{3,jkl} q_{1k} q_{2l}, \tag{3.27b}$$

or

$$\dot{\mathbf{q}} = \mathbf{W}\mathbf{q} + \boldsymbol{\Gamma}(\mathbf{q})\mathbf{q} + \boldsymbol{\eta} \tag{3.28}$$

with

$$\mathbf{W} = \begin{bmatrix} \mathbf{0} & \mathbf{W}_D \\ -\mathbf{W}_D & \mathbf{0} \end{bmatrix} \tag{3.29}$$

and $\mathbf{W}_D = diag(\omega_j)$.

### 3.1.4 Modal Equations in Loaded Basis

Similar to expansion on the unloaded equilibrium, the intrinsic beam dynamics can be expanded around a loaded equilibrium $\hat{\mathbf{x}}_2$ by defining

$$\mathbf{x}_1 = \sum_{j=1}^{\infty} \hat{\boldsymbol{\phi}}_{1j}(s) q_{1j}(t), \tag{3.30a}$$

$$\mathbf{x}_2 = \hat{\mathbf{x}}_2 + \sum_{j=1}^{\infty} \hat{\boldsymbol{\phi}}_{2j}(s) q_{2j}(t). \tag{3.30b}$$

This leads to an identical modal system (3.21) but with the *linear* coefficients modified as

$$\Lambda_{1,jk} = \int_S \boldsymbol{\phi}_{1j}^{\top} (\boldsymbol{\phi}_{2k}' + \mathbf{E}\boldsymbol{\phi}_{2k} - (\mathcal{L}_2(\hat{\mathbf{x}}_2)\mathbf{C} - \mathcal{L}_1(\mathbf{C}\hat{\mathbf{x}}_2)\boldsymbol{\phi}_{2k})\, ds, \tag{3.31a}$$

$$\eta_{1,j} = \int_S \boldsymbol{\phi}_{1j}^{\top} (\mathbf{f}_A - \hat{\mathbf{f}}_A)\, ds, \tag{3.31b}$$

$$\Lambda_{2,jk} = \int_S \boldsymbol{\phi}_{2j}^{\top} (\boldsymbol{\phi}_{1k}' - \mathbf{E}^{\top}\boldsymbol{\phi}_{1k} - \mathcal{L}_1^{\top}(\mathbf{C}\hat{\mathbf{x}}_2)\boldsymbol{\phi}_{1k})\, ds, \tag{3.31c}$$

In this case, the $\mathbf{A}$ and $\boldsymbol{\Lambda}$ coefficient matrices are no longer diagonal as the modes are not orthogonal. However as they are still the natural modes of the system, they still hold the property that

$$\mathbf{A}_1^{-1}\boldsymbol{\Lambda}_1 = \mathbf{W}_D, \tag{3.32a}$$

$$\mathbf{A}_2^{-1}\boldsymbol{\Lambda}_2 = -\mathbf{W}_D, \tag{3.32b}$$

a property which the natural modes of the unloaded equilibrium holds trivially.

## 3.2 Unsteady Modal Aerodynamic Description

Previously we have obtained the modal formulation of the intrinsic structural equations (3.21). We are now ready to project the aerodynamic forces onto the structural modes as added couplings in the modal formulation. The starting point of this process is the expression for unsteady aerodynamic forces expressed in the local frame (2.117), which can be regarded as an expression of local aerodynamic loads $\mathbf{F}_a(\mathbf{x}_1)$ in terms of local velocities $\mathbf{x}_1$. As described previously, this aerodynamic system will be coupled with the structural system via the external forcing term.

This aerodynamic projection process has a number of requirements. The first requirement is that the chord of the lifting surface(s) must all be equal and constant in order for the unsteady terms to be projected, if there is a difference between chord lengths of different lifting surfaces and all of which require accurate unsteady models, separate sets of aerodynamic states would be required for each one which could lead to a huge increase in the size of the problem. Another requirement is that the structural axis system ($\mathbf{B}_0$) should coincide with the aerodynamic axis system, namely that the $\mathbf{b}_2$ and $\mathbf{b}_3$ axes should lie in the same plane as the aerofoil section with $\mathbf{b}_2$ pointing in the zero-lift direction. If the axis system is specified differently to above, then subsequent instances of $\mathbf{x}_1$ should be replaced with $\mathcal{R}(\mathbf{R}^{c0})\mathbf{x}_1$ where we define the operator $\mathcal{R}$ as

$$\mathcal{R}(\mathbf{R}^{c0}) = \begin{pmatrix} \mathbf{R}^{c0} & \mathbf{0} \\ \mathbf{0} & \mathbf{R}^{c0} \end{pmatrix} \tag{3.33}$$

and $\mathbf{R}^{c0}$ is the transformation from the local structural (0) frame into the local aerodynamic ($c$) frame defined according to the aforementioned requirement.

We start by substituting (3.16) into (2.117), assuming natural modes are used, we obtain

$$\begin{aligned} \mathbf{F}_a = \rho b(\mathcal{A}_1(\sum_{k=1}^{\infty} \boldsymbol{\phi}_{1k} q_{1k}) \sum_{l=1}^{\infty} \boldsymbol{\phi}_{1l} q_{1l} + V_\infty \mathcal{A}_2 \sum_{k=1}^{\infty} \boldsymbol{\phi}_{1k} q_{1k} \cdot \sum_{l=1}^{N_{AE}} 2A_l^{AE} b_l^{AE} \lambda_l \\ + \mathcal{A}_3(\sum_{k=1}^{\infty} \boldsymbol{\phi}_{1k} q_{1k}) \sum_{l=1}^{\infty} \boldsymbol{\phi}_{1l} q_{1l} \cdot \delta), \end{aligned} \tag{3.34a}$$

$$\dot{\lambda}_j = \boldsymbol{\kappa}_{AE}^{\top} \sum_{k=1}^{\infty} \boldsymbol{\phi}_{1k} q_{1k} - \frac{b_j^{AE} V_\infty}{b} \lambda_j. \tag{3.34b}$$

For the second equation, we further split $\lambda_j$ into components corresponding to each velocity mode $\boldsymbol{\phi}_{1k}$ as

$$\lambda_j = \sum_{k=1}^{\infty} \boldsymbol{\kappa}_{AE}^{\top} \boldsymbol{\phi}_{1k} q_{a,jk}, \tag{3.35}$$

converting the time evolution equation into

$$\dot{q}_{a,jk} = q_{1k} - \frac{b_j^{AE} V_\infty}{b} q_{jk} = q_{1k} - p_j V_\infty q_{a,jk}, \tag{3.36}$$

where $p_j = \frac{b_j^{AE}}{b}$. The first equation in (3.16) is now

$$\mathbf{F}_a = \rho b(\mathcal{A}_1(\sum_{k=1}^{\infty} \boldsymbol{\phi}_{1k} q_{1k}) \sum_{l=1}^{\infty} \boldsymbol{\phi}_{1l} q_{1l} + V_\infty \mathcal{A}_2 \sum_{k=1}^{\infty} \sum_{l=1}^{N_{AE}} \sum_{m=1}^{\infty} \boldsymbol{\phi}_{1k} q_{1k} \cdot 2A_l^{AE} b_l^{AE} \boldsymbol{\kappa}_{AE}^\top \boldsymbol{\phi}_{1m} q_{a,lm} \tag{3.37a}$$

We then insert the aerodynamic forcing into the external forcing term and define the modal aerodynamic forcing as

$$\eta_{1a,j} = \int_S \boldsymbol{\phi}_{1j}^\top \mathbf{F}_A \, ds, \tag{3.38}$$

again using Einstein notation,

$$\eta_{1a,j} = \mathrm{H}_{1,jkl} q_{1k} q_{1l} + V_\infty \mathrm{H}_{2,jkl} q_{1k} q_{a,kl} + \mathrm{H}_{3,jkl,d} q_{1k} q_{1l} \cdot \delta_d \tag{3.39}$$

where

$$\mathrm{H}_{1,jkl} = \int_S \rho b \boldsymbol{\phi}_{1j}^\top \mathcal{A}_1(\boldsymbol{\phi}_{1k}) \boldsymbol{\phi}_{1l} \, ds, \tag{3.40a}$$

$$\mathrm{H}_{2,jklm} = \int_S \rho b \boldsymbol{\phi}_{1j}^\top \mathcal{A}_2 \boldsymbol{\phi}_{1k} \cdot 2A_l^{AE} b_l^{AE} \boldsymbol{\kappa}_{AE}^\top \boldsymbol{\phi}_{1m} \, ds, \tag{3.40b}$$

$$\mathrm{H}_{3,jkl,d} = \int_S \rho b \boldsymbol{\phi}_{1j}^\top \mathcal{A}_{3,d}(\boldsymbol{\phi}_{1k}) \boldsymbol{\phi}_{1l} \, ds. \tag{3.40c}$$

Note here an additional index $d$ is added to the $\mathcal{A}_3$ operators, this is to account for the existence of multiple control surfaces, each of them creating their own set of $\mathcal{A}_3$ operators. Similarly the other aerodynamic coefficients including $C_{L\alpha}$, $C_{M0}$ and $C_{L\delta}$ are now all dependent on $s$ which means the $\mathcal{A}$ operators are also $s$-dependent. We finally combine the modal aerodynamic formulation with the structural equations (3.21) and obtain the final form of the modal aeroelastic system as

$$\begin{aligned} \mathrm{A}_{1,jk} \dot{q}_{1k} =& \Lambda_{1,jk} q_{2k} - (\Gamma_{1,jkl} - \mathrm{H}_{1,jkl} - \mathrm{H}_{3,jkl,d}\delta_d) q_{1k} q_{1l} - \Gamma_{2,jkl} q_{2k} q_{2l} \\ &+ V_\infty \mathrm{H}_{2,jkl} q_{1k} q_{a,kl}, && (3.41a) \\ \mathrm{A}_{2,jk} \dot{q}_{2k} =& \Lambda_{2,jk} q_{1k} + \Gamma_{3,jkl} q_{1k} q_{2l}, && (3.41b) \\ \dot{q}_{a,jk} =& q_{1k} - p_j V_\infty q_{a,jk}, && (3.41c) \end{aligned}$$

or written in vector form by truncating to a finite number of modes,

$$\begin{aligned}
\dot{\mathbf{q}}_1 =& \mathbf{A}_1^{-1}(\boldsymbol{\Lambda}_1\mathbf{q}_2 - (\boldsymbol{\Gamma}_1(\mathbf{q}_1) - \mathbf{H}_1(\mathbf{q}_1) - V_\infty\mathbf{H}_2(\mathbf{q}_a) - \mathbf{H}_{3,d}(\mathbf{q}_1)\delta_d)\mathbf{q}_1 \\
&- \boldsymbol{\Gamma}_2(\mathbf{q}_2)\mathbf{q}_2), \quad (3.42a) \\
\dot{\mathbf{q}}_2 =& \mathbf{A}_2^{-1}(\boldsymbol{\Lambda}_2\mathbf{q}_1 + \boldsymbol{\Gamma}_3(\mathbf{q}_1)\mathbf{q}_2), \quad (3.42b) \\
\dot{\mathbf{q}}_a =& \mathbf{P}_1\mathbf{q}_1 - V_\infty\mathbf{P}_2\mathbf{q}_a, \quad (3.42c)
\end{aligned}$$

where we define the vector form of the aerodynamic states $\mathbf{q}_a$ as

$$\mathbf{q}_a = \begin{bmatrix} \mathbf{q}_{a1} \\ \mathbf{q}_{a2} \\ \cdots \\ \mathbf{q}_{aN_{AE}} \end{bmatrix}, \quad (3.43)$$

with each vector $\mathbf{q}_{ak}|_j = q_{a,jk}$. Similar to the $\boldsymbol{\Gamma}$ operators, the $\mathbf{H}$ operators are defined as

$$\begin{aligned}
\mathbf{H}_1(\mathbf{q}_1)|_{jl} &= \sum_{k=1}^{N_M} \mathrm{H}_{1,jkl}q_{1k}, \quad (3.44a) \\
\mathbf{H}_2(\mathbf{q}_a)|_{jk} &= \sum_{l=1}^{N_{AE}} \sum_{m=1}^{\infty} \mathrm{H}_{2,jklm}q_{a,lm}, \quad (3.44b) \\
\mathbf{H}_{3,d}(\mathbf{q}_1)|_{jl} &= \sum_{k=1}^{N_M} \mathrm{H}_{3,jkl,d}q_{1k}. \quad (3.44c)
\end{aligned}$$

Finally, the $\mathbf{P}_1$ and $\mathbf{P}_2$ matrices take the form of

$$\mathbf{P}_1 = \begin{bmatrix} \mathbf{v} & \mathbf{0} & \dots & \mathbf{0} \\ \mathbf{0} & \mathbf{v} & \dots & \mathbf{0} \\ \dots & \dots & \dots & \dots \\ \mathbf{0} & \mathbf{0} & \dots & \mathbf{v} \end{bmatrix}, \ \mathbf{P}_2 = \begin{bmatrix} \mathbf{P} & \mathbf{0} & \dots & \mathbf{0} \\ \mathbf{0} & \mathbf{P} & \dots & \mathbf{0} \\ \dots & \dots & \dots & \dots \\ \mathbf{0} & \mathbf{0} & \dots & \mathbf{P} \end{bmatrix}, \quad (3.45)$$

with $\mathbf{v}$ is a vector the same size as $\mathbf{q}_1$ with every element being unity and the diagonal matrix $\mathbf{P}|_{jj} = p_j$. Finally the $V_\infty$ value is a global scalar value and could be obtained by computing, for example, the local velocity at any node chosen as a reference node.

We have thus arrived at the closed-form modal aeroelastic formulation of a flexible aircraft structure. The flying wing test case in the numerical results section will illustrate the practical application of this formulation by demonstrating the entire process.

## 3.3 Flight Dynamic Description

The modal aeroelastic system (3.42) describes a flexible structure moving in still air without gravity. In order to create a description that can be used to model full-vehicle flight-dynamics response, additional effects such as gravity, gust and engine thrust must be accounted for and will be described in this section.

### 3.3.1 Displacement and Rotation Tracking

It can be seen from 2.1.6 that the integration of displacements and rotations from the intrinsic variables is a highly nonlinear process. Rather than projecting displacements and rotations onto a modal basis as we have done with the aerodynamic forces, we will retain the integration of displacements and rotations from the intrinsic variables themselves as a post-processing step. Thus starting from (2.89), for each point we have

$$\dot{\mathbf{T}} = \mathbf{T}\tilde{\boldsymbol{\omega}} = \mathbf{T}\sum_{j=1}^{\infty}\tilde{\boldsymbol{\phi}}_{1j}|_{456}q_{1j}, \tag{3.46a}$$

$$\dot{\mathbf{r}} = \mathbf{T}\mathbf{v} = \mathbf{T}\sum_{j=1}^{\infty}\boldsymbol{\phi}_{1j}|_{123}q_{1j} \tag{3.46b}$$

and

$$\mathbf{T}' = \mathbf{T}(\tilde{\boldsymbol{\kappa}} + \tilde{\mathbf{k}}_0) = \mathbf{T}\left(\sum_{j=1}^{\infty}\widetilde{\mathbf{C}\boldsymbol{\phi}_{2j}}|_{456}q_{2j} + \tilde{\mathbf{k}}_0\right), \tag{3.47a}$$

$$\mathbf{r}' = \mathbf{T}(\boldsymbol{\gamma} + \mathbf{e}) = \mathbf{T}\left(\sum_{j=1}^{\infty}(\mathbf{C}\boldsymbol{\phi}_{2j})|_{123}q_{2j} + \mathbf{e}\right) \tag{3.47b}$$

where all variables are a function of $s$. Their $s$ dependence is omitted for clarity in all subsequent equations in this chapter. The time integration equations (3.46) are linear in both rotation $\mathbf{T}$ and velocity state $\mathbf{q}_1$ and therefore there exists linear operators $\mathbf{N}_R$ and $\mathbf{N}_D$ so that

$$\dot{\mathbf{T}}_v = \mathbf{N}_R(\mathbf{T})\mathbf{q}_1, \tag{3.48a}$$

$$\dot{\mathbf{r}} = \mathbf{N}_D(\mathbf{T})\mathbf{q}_1. \tag{3.48b}$$

Here $\mathbf{T}_v$ denotes $\mathbf{T}$ rearranged into a vector form.

### 3.3.2 Effect of Gravity

The gravity force is a constant vector in the global reference frame $a$. Its effect on the intrinsic variables should be computed by transforming this constant vector into the local reference frame using $\mathbf{T}$,

$$\mathbf{g} = \mathbf{T}^\top \mathbf{M} \mathcal{G}(\mathbf{g}_0). \tag{3.49}$$

Here $\mathbf{g}$ is the gravity vector in the local frame, transformed from $\mathbf{g}_0 = [0, 0, -g_0]^\top$, the constant gravity vector in the global frame where $g_0$ is taken to be the gravity acceleration ($9.81ms^{-1}$ at sea level) and with the $z$-axis being the global "up" direction. The linear transformation $\mathcal{G}$ is defined as

$$\mathcal{G}(\mathbf{g}_0) = \begin{pmatrix} \mathbf{g}_0 \\ \mathbf{g}_0 \end{pmatrix}. \tag{3.50}$$

When projected onto the modes, this force influences the $j$-th velocity mode $\mathbf{q}_{1j}$ as a contribution to the external force term,

$$\eta_{g,j} = \int_S \boldsymbol{\phi}_{1j}^\top \mathbf{T}^\top \mathbf{M} \mathcal{G}(\mathbf{g}_0) \, ds. \tag{3.51}$$

This is a linear function of $\mathbf{T}$ thus we can also write the influence of gravity in vector form as $\boldsymbol{\eta}_g = \mathbf{H}_g(\mathbf{T})$ which will appear in the $\boldsymbol{\eta}$ term in (3.55).

### 3.3.3 Effect of Thrust

The thrust vector is modelled as a follower force (since pods move with the local airframe) exerted at the locations $s_n$ on which the engine pods are mounted. It influences velocity modes simply as another constant external force contribution, but defined in the local frame as

$$\eta_{T,j} = \sum_{n=1}^{N_T} \boldsymbol{\phi}_{1j}^\top \Big|_{s=s_n} \mathbf{f}_{t,n}, \tag{3.52}$$

The variable $\mathbf{f}_{t,n} = \mathbf{f}_{t0,n} f_n$ describes a 6-element thrust force/moment vector of magnitude $f_n$ and direction $\mathbf{f}_{t0,n}$ with a total of $N_T$ thrust vectors. In order for changes in thrust to be considered as well, the influence can be written as a vector $\boldsymbol{\eta}_T = \mathbf{H}_T \mathbf{f}_n$ where $\mathbf{f}_n$ is the collection of $f_n$ which will also appear in the $\boldsymbol{\eta}$ term in (3.55).

### 3.3.4 Effect of Gusts

In the aerodynamic model, the aerodynamic loads are computed by assuming that the aerofoil section is moving through still air. In the spirit of this framework, the formulation will model the effect of an external gust, $\mathbf{v}_g(\mathbf{r})$, defined as a spatial gust distribution of gust velocities in the global frame, as causing an additional downwash as a local gust velocity, modifying the local velocity $\mathbf{v}$, and thus a different $\mathbf{q}_1$:

$$\hat{\mathbf{v}} = \mathbf{v} - \mathbf{T}^\top \mathbf{v}_g(\mathbf{r}), \tag{3.53a}$$

$$q_{1j}^* = q_{1j} - \int_S \boldsymbol{\phi}_{1j}^\top|_{123} \mathbf{T}^\top \mathbf{v}_g(\mathbf{r})\, ds, \tag{3.53b}$$

or in vector form,

$$\mathbf{q}_1^* = \mathbf{q}_1 + \mathbf{q}_{1g}, \tag{3.54}$$

This modified $\mathbf{q}_1^*$ affects aerodynamic forces only and is not used in the structural model or displacement integration.

### 3.3.5 Modal Aeroservoelastic System

The final assembled equation of the aeroservoelastic system is written as:

$$\begin{aligned}
\dot{\mathbf{q}}_1 =& \mathbf{A}_1^{-1}(\boldsymbol{\Lambda}_1 \mathbf{q}_2 - \boldsymbol{\Gamma}_1(\mathbf{q}_1)\mathbf{q}_1 - \boldsymbol{\Gamma}_2(\mathbf{q}_2)\mathbf{q}_2 + (\mathbf{H}_{13}(\mathbf{q}_1^*) + V_\infty \mathbf{H}_2(\mathbf{q}_a))\mathbf{q}_1^* \\
&+ \mathbf{H}_g(\mathbf{T}) + \mathbf{H}_T \mathbf{f}_n), && (3.55a)\\
\dot{\mathbf{q}}_2 =& \mathbf{A}_2^{-1}(\boldsymbol{\Lambda}_2 \mathbf{q}_1 + \boldsymbol{\Gamma}_3(\mathbf{q}_1)\mathbf{q}_2), && (3.55b)\\
\dot{\mathbf{q}}_a =& \mathbf{P}_1 \mathbf{q}_1^* - V_\infty \mathbf{P}_2 \mathbf{q}_a, && (3.55c)\\
\dot{\mathbf{T}}_v =& \mathbf{N}_R\left(\mathbf{T}\right) \mathbf{q}_1, && (3.55d)\\
\dot{\mathbf{r}} =& \mathbf{N}_D\left(\mathbf{T}\right) \mathbf{q}_1, && (3.55e)
\end{aligned}$$

with $\boldsymbol{\Gamma}$, $\mathbf{N}$ and $\mathbf{H}$ being linear functions of their respective variables and

$$\mathbf{H}_{13} = \mathbf{H}_1 + \mathbf{H}_{3,d}\delta_d, \tag{3.56a}$$

$$\mathbf{q}_1^* = \mathbf{q}_1 + \mathbf{q}_{1g}. \tag{3.56b}$$

## 3.4 Modal Reduction and Mode Selection

Although (3.55) describes a full, possibly infinite-dimensional model, it is equally valid for a system with a finite number of modes. Our process of modal reduction on the system of ODEs simply involves retaining the modes of interest ($\boldsymbol{\phi}_1$ and $\boldsymbol{\phi}_2$) and truncating the remainder of the modes and associated dynamics. Note that this method removes all information of the truncated modes altogether, a method which retains some information of the removed modes will be described later in Section 4.6.1. It should be noted here that there is no requirement that the structural states $\mathbf{q}_1$ and $\mathbf{q}_2$ should contain the same number of modes in a finite-dimensional system. In this work it is assumed that by using a finite number of natural structural modes in the aeroelastic system of a free-flying airframe, the number of sectional force modes $\boldsymbol{\phi}_2$ will be defined as $N_M$ whereas the number of velocity modes $\boldsymbol{\phi}_1$ will be $N_M + 6$. The retained natural modes of the structural model $\boldsymbol{\phi}_1$ and $\boldsymbol{\phi}_2$ exist in pairs ($\boldsymbol{\phi}_{1,1}$ to $\boldsymbol{\phi}_{1,N_M}$ and $\boldsymbol{\phi}_{2,1}$ to $\boldsymbol{\phi}_{2,N_M}$), the six extra modes in the velocity modes ($\boldsymbol{\phi}_{1,N_M+1}$ to $\boldsymbol{\phi}_{1,N_M+6}$) are due to the existence of three translational and three rotational rigid body velocity modes with no corresponding force modes.

In the process of modal reduction on the nonlinear system, it was previously demonstrated [132] using an isotropic cantilever model that bending modes in the cantilever model only couple with each other via nonlinear coupling with axial modes, thus if no axial modes are included in the reduced-order representation, no nonlinear couplings will occur. This result highlighted that mode type could be an important criterion when trying to select a set of modes to retain in the reduced model. However it should also be noted that the degrees of freedoms in the isotropic cantilever are uncoupled and in a more complex, coupled setup, it will be difficult to discern types of modes or to decide which ones to retain without checking the performance using an actual simulation. Therefore in this work, the selection of the structural modes to retain during modal reduction is based on frequency only, i.e. modes are retained starting from the lowest frequency until a satisfactory accuracy is achieved.

## 3.5 Control Design on Aeroelastic System

In this work we are also interested in control synthesis on the nonlinear aeroelastic system for the purpose of disturbance rejection, dynamic stabilisation or controllability augmentation. Especially, the nonlinear modelling capabilities in this work will allow the exploration of the limits of using linear control methods on nonlinear systems, as will be done later in Section 7.5. The following section will describe the process of linearisation from the aeroelastic system (3.55) and the creation of a robust controller based on the linearised system dynamics, from which the performance of the nonlinear aircraft model will be evaluated.

### 3.5.1 System Linearisation

A linearisation on the nonlinear aeroelastic system of (3.55) is first sought for the purpose of control design. This assumes that a trim solution (i.e. static aeroelastic equilibrium) is found such that $\dot{\hat{\mathbf{q}}}_1 = \mathbf{0}$, $\dot{\hat{\mathbf{q}}}_2 = \mathbf{0}$ and $\dot{\hat{\mathbf{q}}}_a = \mathbf{0}$ is satisfied where we now use the hat symbol $\hat{\bullet}$ to represent equilibrium values, so that for example,

$$\mathbf{q}_1 = \hat{\mathbf{q}}_1 + \partial \mathbf{q}_1. \tag{3.57}$$

The linearisation on the variables $\mathbf{q}_1$, $\mathbf{q}_2$, $\mathbf{q}_a$ and $\mathbf{T}$ (i.e. excluding the displacement $\mathbf{r}$) is made using variations on the aforementioned equilibrium state. The rationale for the selection of these variables is that in linear aeroelastic and flight dynamic analysis, displacement information can be safely discarded as it is an integral of the velocity variables, however the same could not be done to rotations as the effect of gravity is directly dependent on local orientation. This linearisation results in a linear system containing the velocity and force structural modes, aerodynamic modes and nodal rotation variables.

We shall first present the linearisation of rotations represented by rotation matrices. A review of the various ways in which rotation can be linearised can be found in [5]. In the full system, the nodal rotations are stored as rotation matrices and a direct linearisation on this representation will result in redundant variables. Thus for linearisation purposes alone, infinitesimal rotation variables will be introduced that use three degrees of freedom per node to describe *infinitesimal* changes in orientation from a reference, loaded equilibrium condition at time $t = 0$. For example, from (3.46) at node $n$

$$\dot{\mathbf{T}}_n = \mathbf{T}_n \tilde{\boldsymbol{\omega}}_n. \tag{3.58}$$

As we are interested in small disturbance analysis, we assume $\dot{\mathbf{T}}_n$ and $\boldsymbol{\omega}_n$ are small,

$$\int_0^t \mathbf{T}_n(0) \tilde{\boldsymbol{\omega}}_n \, dt = \mathbf{T}_n(t) - \mathbf{T}_n(0). \tag{3.59}$$

It is easy to prove that for a finite rotation matrix $\mathbf{T}_n(0)$, $\mathbf{T}_n(0)\tilde{\boldsymbol{\omega}}_n = \widetilde{\mathbf{T}_n(0)\boldsymbol{\omega}_n}$. Thus we define the local (linear) rotation variable $\boldsymbol{\theta}_n$ so that

$$\boldsymbol{\theta}_n = \int_0^t \mathbf{T}_n(0) \boldsymbol{\omega}_n \, dt, \tag{3.60}$$

resulting in

$$\tilde{\boldsymbol{\theta}}_n(t) = \mathbf{T}_n(t) - \mathbf{T}_n(0). \tag{3.61}$$

We finally note that $\mathbf{T}_n(0)\boldsymbol{\omega}_n$ is the nodal angular velocity expressed in the global inertial frame, thus $\boldsymbol{\theta}_n$ is a vector of the three nodal rotation variables in the global frame.

Now that we can write changes in the nodal rotation matrix $\mathbf{T}$ as an infinitesimal rotation vector $\boldsymbol{\theta}$, we can proceed to linearise the full aeroelastic system (3.55). Therefore the state variable in the linearised system is now $\partial\mathbf{q} = [\ \mathbf{q}_1^\top \ \ \mathbf{q}_2^\top \ \ \mathbf{q}_a^\top \ \ \boldsymbol{\theta}^\top\ ]^\top$. The linearised aeroelastic system dynamics can be written as

$$\begin{aligned}
\partial\dot{\mathbf{q}}_1 =& \mathbf{A}_1^{-1}(\boldsymbol{\Lambda}_1\partial\mathbf{q}_2 - \boldsymbol{\Gamma}_1(\hat{\mathbf{q}}_1)\partial\mathbf{q}_1 - \boldsymbol{\Gamma}_2(\hat{\mathbf{q}}_2)\partial\mathbf{q}_2 - \boldsymbol{\Gamma}_1(\partial\mathbf{q}_1)\hat{\mathbf{q}}_1 - \boldsymbol{\Gamma}_2(\partial\mathbf{q}_2)\hat{\mathbf{q}}_2 \\
&+ (\mathbf{H}_1(\hat{\mathbf{q}}_1) + \mathbf{H}_{3,d}\hat{\delta}_d(\hat{\mathbf{q}}_1) + \hat{V}_\infty\mathbf{H}_2(\hat{\mathbf{q}}_a))(\partial\mathbf{q}_1 + \partial\mathbf{q}_{1g}) \\
&+ (\mathbf{H}_1(\partial\mathbf{q}_1 + \partial\mathbf{q}_{1g}) + \mathbf{H}_{3,d}\hat{\delta}_d(\partial\mathbf{q}_1 + \partial\mathbf{q}_{1g}) + \hat{V}_\infty\mathbf{H}_2(\partial\mathbf{q}_a))\hat{\mathbf{q}}_1 \\
&+ (\mathbf{H}_{3,d}\partial\delta_d(\hat{\mathbf{q}}_1) + \partial V_\infty\mathbf{H}_2(\hat{\mathbf{q}}_a))\hat{\mathbf{q}}_1 \\
&+ \mathbf{H}_g(\partial\mathbf{T}) + \mathbf{H}_T\partial\mathbf{f}_n), && \text{(3.62a)} \\
\partial\dot{\mathbf{q}}_2 =& \mathbf{A}_2^{-1}(\boldsymbol{\Lambda}_2\partial\mathbf{q}_1 + \boldsymbol{\Gamma}_3(\hat{\mathbf{q}}_1)\partial\mathbf{q}_2 + \boldsymbol{\Gamma}_3(\partial\mathbf{q}_1)\hat{\mathbf{q}}_2), && \text{(3.62b)} \\
\partial\dot{\mathbf{q}}_a =& \mathbf{P}_1(\partial\mathbf{q}_1 + \partial\mathbf{q}_{1g}) - \hat{V}_\infty\mathbf{P}_2\partial\mathbf{q}_a - \partial V_\infty\mathbf{P}_2\hat{\mathbf{q}}_a, && \text{(3.62c)} \\
\partial\dot{\tilde{\boldsymbol{\theta}}}_v =& \mathbf{N}_R\left(\partial\tilde{\boldsymbol{\theta}}\right)\hat{\mathbf{q}}_1 + \mathbf{N}_R\left(\hat{\mathbf{T}}\right)\partial\mathbf{q}_1. && \text{(3.62d)}
\end{aligned}$$

Note that the $\boldsymbol{\Gamma}$ and $\mathbf{H}$ functions, defined in Sections 3.1 and 3.2, are all linear functions of their respective variables. The eigenvalues and eigenvectors of this linearised system will also reveal the aerodynamic modes of the system including any unstable modes.

### 3.5.2 Open-Loop System Definition

In addition to linearisation on the states of the system described in Section 3.5.1, the system inputs and outputs must also be defined in order to construct an open-loop dynamic system suitable for linear dynamic simulations and control design, in the form of a continuous, linear, time-invariant system $\mathbf{S}$ containing states $\mathbf{q}$, with inputs $\mathbf{w}_d$, $\mathbf{u}_c$ and outputs $\mathbf{y}_c$, $\mathbf{y}_m$. The system $\mathbf{S}$ is defined as

$$\begin{pmatrix} \dot{\mathbf{q}} \\ \mathbf{y}_c \\ \mathbf{y}_m \end{pmatrix} = \begin{pmatrix} \mathbf{S}_A & \mathbf{S}_{B1} & \mathbf{S}_{B2} \\ \mathbf{S}_{C1} & \mathbf{S}_{D11} & \mathbf{S}_{D12} \\ \mathbf{S}_{C2} & \mathbf{S}_{D21} & \mathbf{S}_{D22} \end{pmatrix} \begin{pmatrix} \mathbf{q} \\ \mathbf{w}_d \\ \mathbf{u}_c \end{pmatrix}. \tag{3.63}$$

Here the system inputs include disturbance and control actions, whereas the outputs include sensor measurements and control objectives. For the linearised system, relevant terms will be identified from (3.62), whereas on the full nonlinear system (3.55) will be used.

The disturbance input to the flight dynamics in the aeroelastic system considered in this work will come from external forces on the airframe. In particular, external gust and its effect on the states will be linearised from $\mathbf{q}_{1g}$ in (3.54) and (3.62), other external forces, should they exist, will come from the $\boldsymbol{\eta}$ term in (3.55) and (3.62). Both these linearised effects can be summarised by the term $\mathbf{S}_{B1}\mathbf{w}_d$ in (3.63) where $\mathbf{w}_d$ contains the strengths of each disturbance at the current time.

An example of the control actions by the aircraft is control surface deflections, for which the equation describing control surface effects through the $\delta_d$ term in (3.55) (together with (3.56)) and (3.62). There can also be other forces directly acting on the airframe such as thrusters or shift in mass distributions, which are examples of forces applied in the local and global reference frame respectively. These follow the same form as the influence from thrust and gravity, which have already been discussed in Sections 3.3.3 and 3.3.2 respectively. For these terms only a linearisation on (3.52) and (3.51) is necessary, as is done in (3.62) in the $\mathbf{H}_g$ and $\mathbf{H}_T$ contributions. The linearised collective actions of these control actions will be summarised in the term $\mathbf{S}_{B2}\mathbf{u}_c$ in (3.63) where $\mathbf{u}_c$ contains the strengths of each control action (change from trim equilibrium condition) at the current time.

Sensor measurements involving either velocity measurements or force/strain measurements at particular locations can be computed by reconstructing the intrinsic variables from the state variables using (3.16). For example a velocity measurement at a particular location $s$ can be written as

$$\mathbf{x}_1(s,t) = \sum_{j=1}^{N_M} \boldsymbol{\phi}_{1j}(s) q_{1j}(t) = \mathbf{S}_{C2}\mathbf{q}_1. \tag{3.64}$$

Additionally, rotation measurements can be computed directly from the nodal rotation variables $\boldsymbol{\Psi}_n$ whereas displacement measurements can be integrated from the corresponding velocity variables. Despite the model using velocities as states, measurements of acceleration, if ever required, are still possible by taking time derivative on (3.16) and noting that the values of all $\dot{\mathbf{q}}_1$ can be replaced by the RHS of the first equation in (3.55). The linearised version of these measurements can be summarised by the measurement matrix $\mathbf{S}_{C2}$ and the collection of measurements $\mathbf{y}_m$ in (3.63).

Similarly, if a physical quantity is included in the control objective it would follow the same form as was defined in the sensor measurements. The control objective however can in fact contain any linear combination of states to suit the requirement of control design. This would produce the control objective matrix $\mathbf{S}_{C1}$ and the objective function (control goals) $\mathbf{y}_c$ in (3.63).

### 3.5.3 $\mathbf{H}_\infty$ Control Design on the Linearised System

The standard $\mathcal{H}_\infty$ control problem defines a state-space system with the form of (3.63) with the goal of designing a controller of the form

$$\begin{pmatrix} \dot{\mathbf{z}} \\ \mathbf{u}_c \end{pmatrix} = \begin{pmatrix} \mathbf{K}_A & \mathbf{K}_B \\ \mathbf{K}_C & \mathbf{K}_D \end{pmatrix} \begin{pmatrix} \mathbf{z} \\ \mathbf{y}_m \end{pmatrix} \tag{3.65}$$

in order to minimise the maximum value of the transfer function from any direction of $\mathbf{w}_d$ to $\mathbf{y}_c$ at any frequency [124]. This represents a control law that uses the measurements $\mathbf{y}_m$ to generate a control action $\mathbf{u}_c$ which minimises the absolute maximum gain of the control objective $\mathbf{y}_c$ from to the disturbance signal $\mathbf{w}_d$ at any frequency. The $\mathcal{H}_\infty$ control problem aims to solve the $\mathbf{K}$ matrices in (3.65) from an optimisation problem. The $\mathcal{H}_\infty$ method produces a control system that is of the same order as the system it is synthesised on. As the linearised model (3.62) from the aeroelastic system frequently contain thousands of states, it is thus necessary both from an efficiency and a reliability point of view that the state-space system be reduced in order before conducting the $\mathcal{H}_\infty$ synthesis. Thus the synthesis of a controller from the aforementioned state-space model would start from a balanced model truncation using Hankel singular values. The Hankel singular value describes the contribution of each independent singular value of the state-space system to the system's overall input-output behaviour. In a balanced model truncation procedure, only the most relevant singular values (i.e. those with the highest Hankel singular values) from a singular value decomposition are retained in the reduced model [133], which produces a reduced system that preserves the majority of the input-output behaviour of the system in terms of frequency response (more precisely, the $\infty$-norm of the difference between the original and reduced system is no more than twice the value of the largest singular value removed during reduction [134]). By default, any unstable states are retained by the procedure.

Subsequently the state-space system is augmented to include frequency-dependent weighting functions on the states, observers and control actions. This is performed to improve robustness of the resulting controller as well as providing tuning for the magnitude of control action for a given disturbance. It is part of a standard procedure for designing mixed-sensitivity robust controllers, a detailed review of how the method is carried out is described in Ref. [124].

As $\mathcal{H}_\infty$ is a linear controller, control saturation is a significant problem if encountered. The controller provides no guarantee of stability of the closed-loop system after control saturation occurs even after the disturbances have subsided. Thus in this work we make the best attempt to avoid control saturation by tuning the magnitude of the control action. The weighting functions are therefore selected so that the resulting controller applies a maximum allowed control action for the maximum strength of the anticipated disturbance. The definition of maximum anticipated disturbance is chosen on a case-by-case basis, for the model used in this work it is chosen as the gust strength that will induce an angle of attack which causes stall on any part of the aerofoil.

Finally, the control synthesis produces a set of $\mathbf{K}$ matrices in (3.65). In a time-domain simulation of the closed-loop system, the controller states $\mathbf{z}$ in (3.65) are treated as additional states in the ODE description of the aeroelastic system, with the control actions $\mathbf{u}_c$ obtained through the evaluation of (3.65) and coupled back onto the aeroelastic system.

We have thus arrived at a modal system of equations (3.55) which describes the aircraft dynamics with prescribed material properties and modes that are continuous in space. Chapter 5 will describe the process of obtaining such a system described in (3.55) without explicitly requiring information on sectional beam properties. Spatial discretisation on this system of equations will be discussed in Chapter 4 in order to develop a numerical scheme based on this intrinsic aeroelastic description. We also describe the procedures by which a robust controller of the dynamic system is obtained in this work briefly as MATLAB (under which the framework is implemented) provides an extensive toolbox for the functions and methods involved in control synthesis. Section 7.4 will demonstrate the design of such a controller on a full aircraft model.

# 4 Numerical Implementation

The coupled aeroelastic formulations presented in Chapters 2 and 3 provide the theoretical basis of the simulation framework used in this work. Here we will proceed to describe the numerical details in the implementation of the aeroelastic description into a simulation framework. Conservation laws of the system will first be scrutinised to evaluate if they provide any benefits to the numerical scheme, then the discretisation and time marching of the numerical scheme will be discussed, followed by some algorithmic optimisations to the basic numerical procedure.

## 4.1 Conservation Properties of the Nonlinear Structural Equations

The beam equations of motion enforce the total energy and momentum conservation laws of a mechanical system and this will first be proved in this section. As we are interested in the eventual use of reduced-order descriptions of the structural system, we will investigate next how well the conservation laws are satisfied on the reduced-order modal description of the system.

### 4.1.1 Energy Conservation

Define the "inner product" of two vector quantities distributed on the structure as the integral of their dot product over the entire structure, or

$$\langle \mathbf{y}, \mathbf{x} \rangle := \int_S \mathbf{y}^\top \mathbf{x}\, ds. \tag{4.1}$$

We define the total system energy $\mathcal{E}$ as the sum of total instantaneous system kinetic and potential energy, or expressed using intrinsic variables,

$$\mathcal{E} = \mathcal{K} + \mathcal{U} = \frac{1}{2}\langle \mathbf{x}_1, \mathbf{M}\mathbf{x}_1 \rangle + \frac{1}{2}\langle \mathbf{x}_2, \mathbf{C}\mathbf{x}_2 \rangle. \tag{4.2}$$

We now check that the intrinsic equations satisfy conservation of energy by showing that $\mathcal{E}$ is invariant with time when the external forcing $\mathbf{f}_A$ is zero, as the equations lack damping terms. The time derivative of system energy is, using the fact that any realistic $\mathbf{M}$ and $\mathbf{C}$ material properties should be inherently symmetrical,

$$\dot{\mathcal{E}} = \frac{1}{2}(\langle \dot{\mathbf{x}}_1, \mathbf{M}\mathbf{x}_1 \rangle + \langle \mathbf{x}_1, \mathbf{M}\dot{\mathbf{x}}_1 \rangle + \langle \dot{\mathbf{x}}_2, \mathbf{C}\mathbf{x}_2 \rangle + \langle \mathbf{x}_2, \mathbf{C}\dot{\mathbf{x}}_2 \rangle) = \langle \mathbf{x}_1, \mathbf{M}\dot{\mathbf{x}}_1 \rangle + \langle \mathbf{x}_2, \mathbf{C}\dot{\mathbf{x}}_2 \rangle. \tag{4.3}$$

Expanding the equation and substituting using (2.79) results in

$$\begin{aligned}\dot{\mathcal{E}} = \int_S \Big( &\mathbf{x}_1^\top \mathbf{x}_2' + \mathbf{x}_1^\top \mathbf{E}\mathbf{x}_2 - \mathbf{x}_1^\top \mathcal{L}_1(\mathbf{x}_1)\mathbf{M}\mathbf{x}_1 - \mathbf{x}_1^\top \mathcal{L}_2(\mathbf{x}_2)\mathbf{C}\mathbf{x}_2 \\ &+\mathbf{x}_2^\top \mathbf{x}_1' - \mathbf{x}_2^\top \mathbf{E}^\top \mathbf{x}_1 + \mathbf{x}_2^\top \mathcal{L}_1^\top(\mathbf{x}_1)\mathbf{C}\mathbf{x}_2 \Big)\, ds. \end{aligned} \tag{4.4}$$

First, by applying the natural boundary conditions (2.64) at the open ends of the beam structure we can show that

$$\int_S \left( \mathbf{x}_1^\top \mathbf{x}_2' + \mathbf{x}_2^\top \mathbf{x}_1' \right) ds = \int_S \left( \mathbf{x}_1^\top \mathbf{x}_2' + \mathbf{x}_1'^\top \mathbf{x}_2 \right) ds = \int_S (\mathbf{x}_1^\top \mathbf{x}_2)'\, ds = \Big[ \mathbf{x}_1^\top \mathbf{x}_2 \Big]_E = 0 \tag{4.5}$$

where $S$ indicates the integral across the entire structure and $E$ indicates boundary integral at the open ends of the beam assemblies. Then using the fact that a scalar is its own transpose,

$$\mathbf{x}_1^\top \mathbf{E}\mathbf{x}_2 = (\mathbf{x}_1^\top \mathbf{E}\mathbf{x}_2)^\top = \mathbf{x}_2^\top \mathbf{E}^\top \mathbf{x}_1. \tag{4.6}$$

Finally using the identities (2.82),

$$\mathbf{x}_1^\top \mathcal{L}_1(\mathbf{x}_1)\mathbf{M}\mathbf{x}_1 = -\mathbf{x}_1^\top \mathcal{L}_1(\mathbf{x}_1)\mathbf{M}\mathbf{x}_1 = 0 \tag{4.7}$$

and

$$\mathbf{x}_1^\top \mathcal{L}_2(\mathbf{x}_2)\mathbf{C}\mathbf{x}_2 = \mathbf{x}_2^\top \mathcal{L}_1^\top(\mathbf{x}_1)\mathbf{C}\mathbf{x}_2, \tag{4.8}$$

thus substituting (4.5) to (4.8) into (4.4) results in

$$\dot{\mathcal{E}} = 0. \tag{4.9}$$

This confirms that, as expected, the total energy of a system described by intrinsic beam equations (2.79) is invariant when there is no external forcing. In Section 4.1.3 we will prove the same result for a full-order system expressed in the modal formulation instead and investigate how mode truncation affects this result.

### 4.1.2 Structural Intensity

A second quantity of interest is the *structural intensity*, which in linear vibration analysis is a measure of the change of energy density in a given infinitesimal volume and a measure of the flow of vibration energy through various parts of the structure [135]. In a beam formulation the structural intensity only has one component and is defined by

$$i(s,t) = \mathbf{x}_1^\top \mathbf{x}_2. \tag{4.10}$$

It is common to consider the temporal integral of the structural intensity,

$$I_T := \int_0^T i \, dt, \tag{4.11}$$

which could be used in the analysis of periodic excitations. We again assume zero external forcing (no $\mathbf{f}_A$) and the spatial derivative of $I_T$ can be written as

$$\begin{aligned} I_T' &= \int_0^T \left( \mathbf{x}_2^\top \mathbf{x}_1' + \mathbf{x}_1^\top \mathbf{x}_2' \right) dt \\ &= \int_0^T \Big( \mathbf{x}_2^\top (\mathbf{C}\dot{\mathbf{x}}_2 + \mathbf{E}^\top \mathbf{x}_1 - \mathcal{L}_1^\top(\mathbf{x}_1)\mathbf{C}\mathbf{x}_2) \\ &\quad + \mathbf{x}_1^\top (\mathbf{M}\dot{\mathbf{x}}_1 - \mathbf{E}\mathbf{x}_2 + \mathcal{L}_1(\mathbf{x}_1)\mathbf{M}\mathbf{x}_1 + \mathcal{L}_2(\mathbf{x}_2)\mathbf{C}\mathbf{x}_2) \Big) \, dt. \end{aligned} \tag{4.12}$$

The elimination of terms using (4.6), (4.7) and (4.8) results in

$$I_T' = \int_0^T \left( \mathbf{x}_2^\top \mathbf{C}\dot{\mathbf{x}}_2 + \mathbf{x}_1^\top \mathbf{M}\dot{\mathbf{x}}_1 \right) dt. \tag{4.13}$$

We note that since the compliance matrix $\mathbf{C}$ is symmetrical,

$$\begin{aligned} \frac{\partial}{\partial t}(\mathbf{x}_2^\top \mathbf{C}\mathbf{x}_2) &= \mathbf{x}_2^\top \mathbf{C}\dot{\mathbf{x}}_2 + \dot{\mathbf{x}}_2^\top \mathbf{C}\mathbf{x}_2 \\ &= \mathbf{x}_2^\top (\mathbf{C} + \mathbf{C}^\top)\dot{\mathbf{x}}_2 \\ &= 2\mathbf{x}_2^\top \mathbf{C}\dot{\mathbf{x}}_2. \end{aligned} \tag{4.14}$$

Similarly

$$\frac{\partial}{\partial t}(\mathbf{x}_1^\top \mathbf{M}\mathbf{x}_1) = 2\mathbf{x}_1^\top \mathbf{M}\dot{\mathbf{x}}_1. \tag{4.15}$$

Therefore

$$\begin{aligned} I_T' =& \frac{1}{2} \int_0^T \left( \frac{\partial}{\partial t} \left( \mathbf{x}_2^\top \mathbf{C}\mathbf{x}_2 + \mathbf{x}_1^\top \mathbf{M}\mathbf{x}_1 \right) \right) dt \\ =& \frac{1}{2} \left( \mathbf{x}_2^\top \mathbf{C}\mathbf{x}_2 + \mathbf{x}_1^\top \mathbf{M}\mathbf{x}_1 \right) |_0^T. \end{aligned} \tag{4.16}$$

As noted above, Gavric [135] indicated that the temporal mean of $i_T$ indicates the energy flow through the structure under periodic excitations. Thus if $\mathbf{x}_1$ and $\mathbf{x}_2$ are periodic with period $T$, we have proved that $I_T' = 0$ for the un-damped and unforced system. We also define

$$J(s) := \lim_{T\to\infty} \frac{1}{T} I_T(s). \tag{4.17}$$

In the case where there is no external applied force ($\mathbf{f}_A = \mathbf{0}$, i.e. free vibrations), since $\mathbf{x}_1, \mathbf{x}_2 \in L^\infty(S \times \mathbb{R}_+)$,

$$|(\frac{1}{T} I_T(s))'| \leq \frac{1}{T}(\|\mathbf{x}_1\|_{L^\infty}^2 \|\mathbf{M}\| + \|\mathbf{x}_2\|_{L^\infty}^2 \|\mathbf{C}\|) \to 0, \tag{4.18}$$

thus $(\frac{1}{T} I_T(s))' \to 0$ uniformly in $s \in S$, implying $J$ is differentiable and

$$J'(s) = 0. \tag{4.19}$$

This indicates that with time, $J$ is a quantity that tends to distribute equally along the length of the entire beam structure.

### 4.1.3 Energy Conservation of Modal Equations

Since the intrinsic beam equations preserve total system energy, the full-mode (infinite number of dof) modal system described in (3.25) will also be energy-preserving naturally as it is simply a change of basis from the original system. However in practice it is interesting to investigate the the energy conservation properties of truncated systems, i.e. a modal system where only a finite number ($N_M$) of modes are retained. In preparation for this discussion we will modify the modal system (3.21) into a form that is easier to manipulate by defining

$$\mathbf{\Gamma}_{1,l} = \Gamma_{1,jkl}|_{jk}, \tag{4.20a}$$

$$\mathbf{\Gamma}_{2,l} = \Gamma_{2,jkl}|_{jk}, \tag{4.20b}$$

which results in (3.23) becoming

$$\mathbf{A}_1 \dot{\mathbf{q}}_1 = \mathbf{\Lambda}_1 \mathbf{q}_2 - q_{1,l} \mathbf{\Gamma}_{1,l} \mathbf{q}_1 - q_{2,l} \mathbf{\Gamma}_{2,l} \mathbf{q}_2 + \boldsymbol{\eta}_1, \tag{4.21a}$$

$$\mathbf{A}_2 \dot{\mathbf{q}}_2 = \mathbf{\Lambda}_2 \mathbf{q}_1 + q_{2,l} \mathbf{\Gamma}_{2,l}^\top \mathbf{q}_1, \tag{4.21b}$$

again with summation over repeated indices.

We now write the definition of total system energy $\mathcal{E}$ (equation (4.2)) in modal form, using the definition of the modal expansion (3.16). It is easy to see, using (3.18), that

$$\mathcal{E} = \frac{1}{2}(\mathbf{q}_1^\top \mathbf{A}_1 \mathbf{q}_1 + \mathbf{q}_2^\top \mathbf{A}_2 \mathbf{q}_2) \tag{4.22}$$

for any arbitrary set of space-spanning basis that are not necessarily natural modes nor required to be orthogonal. Furthermore, as the sectional mass and compliance matrices $\mathbf{M}$ and $\mathbf{C}$ matrices are always symmetric everywhere, it is also trivial to show that

$$\dot{\mathcal{E}} = \mathbf{q}_1^\top \mathbf{A}_1 \dot{\mathbf{q}}_1 + \mathbf{q}_2^\top \mathbf{A}_2 \dot{\mathbf{q}}_2. \tag{4.23}$$

Substitution using (4.21) and assuming zero external force ($\boldsymbol{\eta}_1$) gives

$$\dot{\mathcal{E}} = \mathbf{q}_1^\top (\boldsymbol{\Lambda}_1 + \boldsymbol{\Lambda}_2^\top)\mathbf{q}_2 - q_{1,l}\mathbf{q}_1^\top \boldsymbol{\Gamma}_{1,l}\mathbf{q}_1. \tag{4.24}$$

Owing to the form of the $\Gamma_1$ coefficients (equation (3.18)), each of the $\boldsymbol{\Gamma}_{1,l}$ matrices are anti-symmetric (as noted in (3.19)) and therefore each of the $\mathbf{q}_1^\top \boldsymbol{\Gamma}_{1,l}\mathbf{q}_1$ terms are zero and can thus be discarded, resulting in

$$\dot{\mathcal{E}} = \mathbf{q}_1^\top (\boldsymbol{\Lambda}_1 + \boldsymbol{\Lambda}_2^\top)\mathbf{q}_2. \tag{4.25}$$

If the modes $\boldsymbol{\phi}$ used in the projection are natural modes on the unloaded equilibrium of the structure, then we already have the result that $\boldsymbol{\Lambda}_1 = \mathbf{W}_D$ and $\boldsymbol{\Lambda}_2 = -\mathbf{W}_D$ as defined in Section 3.1.3. Therefore in this case $\boldsymbol{\Lambda}_1 + \boldsymbol{\Lambda}_2^\top = 0$, resulting in $\dot{\mathcal{E}} = 0$ which is the result we seek, that the total energy of the system is invariant if the external forcing $\boldsymbol{\eta}_1$ is zero. If, however, the modes used are arbitrarily defined modes around the unloaded equilibrium, in general the total energy is not conserved for a *finite-dimensional* system due to $\boldsymbol{\Lambda}_1 + \boldsymbol{\Lambda}_2^\top \neq 0$. It is important to note that even in this case, the full infinite-dimensional system must be energy-preserving as again it is simply a change of basis from the energy-preserving intrinsic equations (2.79).

Consider also the case where the modes are natural modes on a loaded initial equilibrium $\hat{\boldsymbol{\phi}}$ as defined in Section 3.1.2, with $\mathcal{E}$ defined the same way as (4.22). Importantly $\mathcal{E}$ no longer represents the total system energy as it does not include the contribution from the initial load $\hat{\mathbf{x}}_2$, nor does it even represent the change of the total system energy from the equilibrium value. Here again $\mathcal{E}$ is not invariant with time as for natural modes around the loaded equilibrium with $\hat{\mathbf{x}}_2 \neq \mathbf{0}$, $\boldsymbol{\Lambda}_1 + \boldsymbol{\Lambda}_2^\top \neq 0$. However in all cases considered here, the nonlinear term's contribution to $\mathcal{E}$ ($\boldsymbol{\Gamma}$ terms) is always conserved with time, regardless of whether the modal expansion is around the unloaded equilibrium or a loaded equilibrium, or whether the system is full- or reduced-order. These observations could potentially be of use in the analysis and control design of a structural system. However the aerodynamic model itself lacks such structure and symmetry found on the structural system and it will be very difficult to find a similar conservation law for the aerodynamic system or the coupled aeroelastic system. Therefore we will not attempt to apply the observations made in this section to developing time-marching schemes or control design.

### 4.1.4 Total Momentum Conservation of Modal Equations

Unlike total system energy, the total system momentum and angular momentum is a vector quantity dependent on not only the local velocities, but the local displacement and rotations as well. Their conservation is therefore much more complex than the system energy and in fact the first equation in the intrinsic structural equations (2.79) is, by nature, an equation describing the local momentum at a given point of the structure. Thus for local momentum to be conserved, the strong form of this equation, as in (2.79a), or the full modal form of which, as described in (3.25), must be satisfied. However, here we are instead concerned about the conservation of total momentum of the full system, which is the spatial integral of the local momentums at each point on the beam assembly. The total linear momentum vector of the structure at a given time is

$$\mathbf{p}_{total} = \int_S \mathbf{T}(\mathbf{M}\mathbf{x}_{1_{123}})\, ds \tag{4.26}$$

where the subscript indicates the retention of only the first three components out of a total of six. Similarly the total angular momentum vector of the structure is

$$\mathbf{h}_{total} = \int_S \mathbf{T}(\mathbf{M}\mathbf{x}_{1_{456}}) + (\tilde{\mathbf{r}} - \tilde{\mathbf{r}}_{CM})\mathbf{T}(\mathbf{M}\mathbf{x}_{1_{123}})\, ds \tag{4.27}$$

where $\mathbf{r}_{CM}$ is the spatial location of the centre-of-mass of the structure at the current time, about which point the angular momentum is evaluated. The evaluation of this integral is complicated by the fact that the orientation (rotation) of the local coordinate system, $\mathbf{T}$, is present in the integral. As local rotation is not a primary variable in the intrinsic description and is instead implied from the post-processing integration step itself using (2.86) or (2.88), it is difficult to investigate the properties of this integral analytically.

Later in Chapter 6 we will dedicate two test cases to investigate the conservation of linear momentum of the full- and reduced-order modal structural system. It will be seen that the momentum conservation of the reduced-order system is not guaranteed. Numerical schemes that preserve momentum have been investigated in a finite-element setting by e.g. [36, 136]. However, such schemes rely on FE-type discretisations and evaluating each element locally, so will be difficult to adapt to the use of natural modes as basis functions, which are non-trivial everywhere in the structure. Similarly, compatibility requires the strong form of the compatibility relation to be satisfied (2.79b); only satisfying the weak form in the reduced-order formulation may lead to integral errors in the tracking of locations and orientations of the nodes and will be described in more detail in Section 6.3. This problem is specific to the intrinsic description as it is a two-field description of the structural problem. In contrast, displacement- or strain-based methods describe other quantities using their sole primary variables (displacement and strain respectively) and the problem of integral errors between the two primary variables does not exist.

In summary, we have seen that while the full modal description satisfies conservation of total energy and momentum, a truncated modal description will only satisfy conservation of total energy when natural modes are used in the modal expansion. Additionally we have also found that the structural intensity is also conserved in periodic responses of the system.

## 4.2 Lumped Mass Approximation of Structural Problem

The system (3.55) describes a modal aeroelastic system whose coupling coefficients, described in (3.18) and (3.40), are computed from an airframe definition that is continuous in space. This is by nature infinite-dimensional and, thus, in order to arrive at a practical implementation of such a system, it is necessary to develop a suitable spatial discretisation to the airframe structure which we will use to compute the coefficients. For simplicity, in the current work we seek a low-order interpolation scheme and, if required, increase the number of nodes to reduce the errors associated with a low-order scheme.

As this will eventually be required by Guyan reduction as part of the condensation process from full 3D FE description to a beam-type model used in this work (a method that will be described later in Chapter 5), the discretised structural problem will be approximated by lumping of the structural inertia onto a series of discrete nodes that are joined via massless, flexible beams. This lumping of masses onto nodes is also commonly used in finite-element descriptions [49] but will require special treatment in the current method of projection onto global modes. The distributed external loads

$\mathbf{f}_A$ will also be integrated onto the nodes. Thus, we define an equivalent problem of a structure consisting a series of point masses on the $N_a$ nodes, linked by massless, flexible beams with external loads applied on the nodes only. We will now find a suitable spatial interpolation of the primary intrinsic variables (local velocities and sectional force resultants) on this modified structural problem.

We start by examining the governing intrinsic equations for which the interpolation schemes will be used. If, on the massless beam segment connecting the nodes, we assume that the intrinsic variables are small in magnitude, (i.e. remaining in the linear regime) and setting $\mathbf{M}$ to zero in (2.79a), obtaining

$$-\mathbf{x}_2' - \mathbf{E}\mathbf{x}_2 = \mathbf{0} \tag{4.28a}$$

as $\mathbf{f}_A$ is also zero on the beam segment. Expanding $\mathbf{x}_2$ into $\mathbf{f}$ and $\mathbf{m}$ gives

$$-\mathbf{f}' = \mathbf{0}, \tag{4.29a}$$

$$-\mathbf{m}' - \tilde{\mathbf{e}}\mathbf{f} = \mathbf{0}. \tag{4.29b}$$

As can be seen in the first equation, the sectional force $\mathbf{f}$ in a straight, massless beam segment between two nodes must be constant in the linear case as there is no external forces applied on the segment other than at the end points. The sectional moment $\mathbf{m}$ should also vary linearly with $s$, resulting from integrating the constant force along the length of the beam element in the second equation. Between adjacent elements however the sectional load $\mathbf{x}_2$ will not be continuous as our problem regards external load as lumped, concentrated loads applied on each node and also due to $\mathbf{M}$ not being zero at the nodes. If we further assume a constant but not necessarily diagonal $\mathbf{C}$ throughout the beam segment between two nodes, then $\mathbf{C}\mathbf{x}_2$ also varies linearly with $s$.

In contrast, the velocity field $\mathbf{x}_1$ must be continuous as can be shown via enforcing a finite $\mathbf{x}_2$ on the compatibility equation (2.79b). Again by assuming small magnitudes of variables in (2.79a), we obtain

$$\mathbf{C}\dot{\mathbf{x}}_2 - \mathbf{x}_1' + \mathbf{E}^T\mathbf{x}_1 = \mathbf{0}, \tag{4.30a}$$

or, expanding in individual components,

$$\dot{\boldsymbol{\gamma}} - \mathbf{v}' - \tilde{\mathbf{e}}\mathbf{v} = \mathbf{0}, \tag{4.31a}$$

$$\dot{\boldsymbol{\kappa}} - \boldsymbol{\omega}' = \mathbf{0}. \tag{4.31b}$$

It can be seen that, since components of $\mathbf{Cx}_2$, $\boldsymbol{\gamma}$ and $\boldsymbol{\kappa}$ vary linearly with $s$, the angular velocity $\boldsymbol{\omega}$ component in $\mathbf{x}_1$ must vary quadratically with $s$ whereas the linear velocity component varies with $s$ in a cubic manner. Note that such interpolation is very similar to that used in beam elements in commercial FE packages, e.g. CBEAM elements in NASTRAN [52] or B31 elements in ABAQUS [137]. As we have lumped the masses onto the nodes and made the beam segment massless, the momentum $\mathbf{Mx}_1$ is not continuous and is only non-zero at the nodes. We will refer to the lumped mass at node $i$ as $\mathbf{M}_{L,i}$ to differentiate this variable with the distributed mass (inertia)-per-unit-length $\mathbf{M}(s)$.

It will be shown in Section 5.2.3 that the Guyan reduction technique can result in slightly different values of $\mathbf{C}$ in each natural mode for the same beam segment. This means that similarly we could not compute the quadratic and cubic interpolation to $\mathbf{x}_1$ to a high precision using data from Guyan reduction. The use of a linear analysis with the assumption of a constant $\mathbf{C}$ matrix throughout further limits the accuracy advantage of the cubic interpolation over lower-order schemes to small deformations of each element, where geometric nonlinearities are insignificant, and material properties that do not vary along the length of the element. Particularly, the latter requirement is not likely to hold in a real-life situation, however the condensation method does not allow us to have a more detailed knowledge of the sub-element variations in $\mathbf{C}$. Therefore rather than attempting to use a physically accurate interpolation scheme based on a constant $\mathbf{C}$ assumption, we will instead simplify and reduce the order of the interpolation. If required, the node count can be increased to reduce the size of each beam segment, so that the error caused by using a low-order interpolation and geometrically nonlinear effects become far less significant.

In the interpolation used in this work we will therefore regard the sectional forces and moments $\mathbf{x}_2$, together with sectional force/moment strains $\mathbf{Cx}_2$, as piecewise constant, i.e. we discard the linear variation of the sectional moment with $s$ and assume it to be the midpoint value in the element, shown in the right image in Figure 6. As the velocity variables need to be continuous, the velocities and angular velocities $\mathbf{x}_1$ will be a linear interpolation between the nodal values at the end of each element as shown in the left image in Figure 6, again discarding higher-order variations.

We will now provide a mathematical description of the *interpolation* used in this work. Note that this is not a discussion of the basis functions used in the formulation but rather on the interpolation that the states, and the basis functions use. For simplicity and clarity of presentation, the following argument will be made with a beam with $N_a$ nodes and $N_a - 1$ elements between the nodes. It is easy to extend these arguments to a

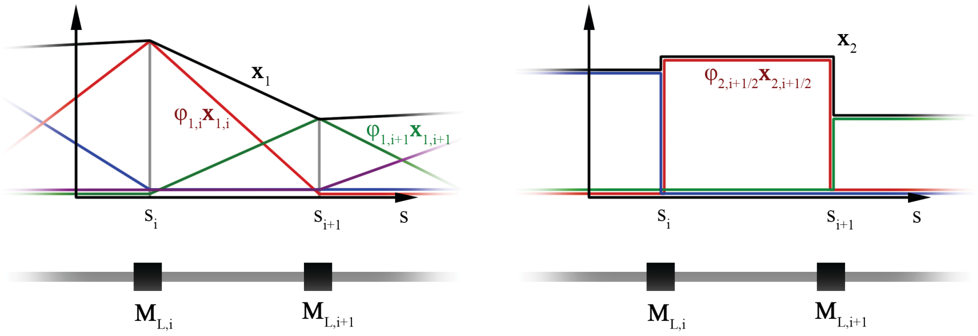

Figure 6: Interpolation scheme of velocity $\mathbf{x}_1$ and sectional force $\mathbf{x}_2$, with various contributions from interpolation functions coloured, used throughout the current work.

multi-beam problem in a practical implementation by taking account of the topology of the structure. The definition of $s$ in this case will be more complex but would not affect the arguments in this section.

If we define $\mathbf{x}_{1,i}$ as the discretised value of $\mathbf{x}_1$ defined at node $i$, that is, $\mathbf{x}_{1,i} = \mathbf{x}_1(s_i)$, linear interpolation results in the definition of the continuous $\mathbf{x}_1$ corresponding to the discretised values being

$$\mathbf{x}_1 \cong \sum_i \varphi_{1,i}\mathbf{x}_{1,i}, \tag{4.32}$$

with the shape function

$$\varphi_{1,i}(s) = \begin{cases} \frac{s-s_{i-1}}{s_i-s_{i-1}} & s_{i-1} < s < s_i \\ \frac{s-s_{i+1}}{s_i-s_{i+1}} & s_i < s < s_{i+1} \\ 0 & \text{otherwise} \end{cases} . \tag{4.33}$$

Similarly, the discretised $\mathbf{x}_2$, being piecewise constant between the nodes, can be represented as

$$\mathbf{x}_2 \cong \sum_i \varphi_{2,i+\frac{1}{2}}\mathbf{x}_{2,i+\frac{1}{2}} \tag{4.34}$$

with the variable being $\mathbf{x}_{2,i+\frac{1}{2}}$ and the shape function

$$\varphi_{2,i+\frac{1}{2}}(s) = \begin{cases} 1 & s_i < s < s_{i+1} \\ 0 & \text{otherwise} \end{cases} \tag{4.35}$$

This thus defines the interpolated version of the intrinsic states $\mathbf{x}_1$ and $\mathbf{x}_2$ at every point $s$ on the structure as a function of the collection of discretised intrinsic variables $\mathbf{x}_{1,i}$ and $\mathbf{x}_{2,i+\frac{1}{2}}$. These definitions form the basis on which we compute our modal system and the eventual aeroelastic model we will use in subsequent analysis and simulations. Similarly, the intrinsic modes $\boldsymbol{\phi}_1$ and $\boldsymbol{\phi}_2$ defined at every point $s$ will also follow this interpolation scheme and will be defined as

$$\boldsymbol{\phi}_{1j} \cong \sum_i \varphi_{1,i} \boldsymbol{\phi}_{1j,i}, \tag{4.36}$$

$$\boldsymbol{\phi}_{2j} \cong \sum_i \varphi_{2,i+\frac{1}{2}} \boldsymbol{\phi}_{2j,i+\frac{1}{2}}, \tag{4.37}$$

where $\boldsymbol{\phi}_{1j,i}$ and $\boldsymbol{\phi}_{2j,i+\frac{1}{2}}$ are the discretised values defined at the nodes and mid-points respectively. In the next section we will make use of these interpolations in computing the nonlinear coupling coefficients in the modal system.

## 4.3 Construction of Modal Intrinsic System from Lumped-Mass Approximation

### 4.3.1 Computation of Coupling Coefficients

Equations (3.18) and (3.40) express the necessary coefficients for the construction of the modal aeroelastic system as various integrals of the modal basis in space. As we have defined the interpolation used in the discretised system (equations (4.32) and (4.34)), these provide a basis for computing the coupling coefficients. Note here that this section assumes knowledge of $\boldsymbol{\phi}_{1j}$ and $\boldsymbol{\phi}_{2j}$, as well as explicit knowledge of $\mathbf{M}$ and $\mathbf{C}$ matrices. However the methods described in this section can be applied equally to a situation where we only have explicit knowledge of $\boldsymbol{\phi}_{1j}$, $\boldsymbol{\phi}_{2j}$, $\mathbf{M}\boldsymbol{\phi}_{1j}$ and $\mathbf{C}\boldsymbol{\phi}_{2j}$ instead, as will be done in Chapter 5.

We start by assuming that an arbitrary complete set of space-spanning modes $\boldsymbol{\phi}_1$ and $\boldsymbol{\phi}_2$ are specified, either as natural modes or otherwise. The linear coupling coefficients

$\mathbf{A}$ can be computed from (3.18a) and (3.18f) as

$$\begin{aligned} A_{1,jk} &= \sum_i \boldsymbol{\phi}_{1j,i}^\top \mathbf{M}_{L,i} \boldsymbol{\phi}_{1k,i}, \\ A_{2,jk} &= \sum_i (s_{i+1} - s_i) \boldsymbol{\phi}_{2j,i+\frac{1}{2}}^\top \mathbf{C}_{i+\frac{1}{2}} \boldsymbol{\phi}_{1k,i+\frac{1}{2}} \end{aligned} \tag{4.38}$$

Here $\boldsymbol{\phi}_{1j,i}$ could be expressed in *any* frame of reference as long as $\mathbf{M}_{L,i}\boldsymbol{\phi}_{1k,i}$ is expressed in the same frame of reference, as the integral is a scalar. The same requirement follows for all other equations in this section.

The nonlinear coupling coefficients $\boldsymbol{\Gamma}_1, \boldsymbol{\Gamma}_2$ in (3.23) can also be computed by direct application of (3.18c) and (3.18d)

$$\begin{aligned} \Gamma_{1,jkl} &= \sum_i \boldsymbol{\phi}_{1j,i}^\top \mathcal{L}_1\left(\boldsymbol{\phi}_{1k,i}\right) \mathbf{M}_{L,i} \boldsymbol{\phi}_{1\ell,i}, \\ \Gamma_{2,jkl} &= \sum_i (s_{i+1} - s_i) \boldsymbol{\phi}_{1j,i+\frac{1}{2}}^\top \mathcal{L}_2(\boldsymbol{\phi}_{2k,i+\frac{1}{2}}) \mathbf{C}_{i+\frac{1}{2}} \boldsymbol{\phi}_{2\ell,i+\frac{1}{2}} \end{aligned} \tag{4.39}$$

where $\boldsymbol{\phi}_{1j,i+\frac{1}{2}} = \frac{1}{2}(\boldsymbol{\phi}_{1j,i} + \boldsymbol{\phi}_{1j,i+1})$, all expressed in the (straight) beam element's local frame of reference, are the interpolated values of $\boldsymbol{\phi}_{1j}$ at the mid-points of each beam element. $\mathbf{C}_{i+\frac{1}{2}}$ is the compliance of the beam segment between node $s_i$ to $s_{i+1}$ which is assumed constant throughout the element. Note that if the starting point is a beam-type description, $\mathbf{C}_{i+\frac{1}{2}}$ would be already known. Otherwise the product $\mathbf{C}_{i+\frac{1}{2}}\boldsymbol{\phi}_{1k,i+\frac{1}{2}}$ can be computed from the method described in Section 5.2.3.

The computation of the $\boldsymbol{\Lambda}$ coefficients in (3.18) however is more involved. As both $\boldsymbol{\phi}_1$, $\boldsymbol{\phi}_1'$ and $\boldsymbol{\phi}_2$ are bounded, the $\boldsymbol{\Lambda}_2$ coefficients are evaluated along the lengths of each beam element from (3.18g) as

$$\Lambda_{2,jk} = \sum_i \boldsymbol{\phi}_{2j,i+\frac{1}{2}}^\top (\boldsymbol{\phi}_{1k,i+1} - \boldsymbol{\phi}_{1k,i} - (s_{i+1} - s_i)\mathbf{E}^\top \boldsymbol{\phi}_{1k,i+\frac{1}{2}}). \tag{4.40}$$

In contrast, the force component of the mode shape $\boldsymbol{\phi}_2$ is not differentiable everywhere due to discontinuities in the interpolation scheme at nodes and also because multiple connectivity at a node in a multi-beam assembly will prevent this quantity from even being defined there. Therefore (3.18b) can not be applied directly to compute $\boldsymbol{\Lambda}_1$. However we note that we could split the contributions to $\boldsymbol{\Lambda}_1$ into two parts,

$$\Lambda_{1,jk} = \int_S \boldsymbol{\phi}_{1j}^\top \boldsymbol{\phi}_{2k}' \, ds + \int_S \boldsymbol{\phi}_{1j}^\top \mathbf{E} \boldsymbol{\phi}_{2k} \, ds. \tag{4.41}$$

The term $\boldsymbol{\phi}_{1j}^{\top}\mathbf{E}\boldsymbol{\phi}_{2k}$ is bounded and thus only needs to be evaluated on each of the elements, ignoring the nodes which have infinitesimal size. This contribution produces

$$\int_S \boldsymbol{\phi}_{1j}^{\top}\mathbf{E}\boldsymbol{\phi}_{2k}\, ds = \sum_i (s_{i+1} - s_i)\boldsymbol{\phi}_{1j,i+\frac{1}{2}}^{\top}\mathbf{E}^{\top}\boldsymbol{\phi}_{2k,i+\frac{1}{2}}. \tag{4.42}$$

Since we have assumed $\boldsymbol{\phi}_2$ to be constant along each element, $\boldsymbol{\phi}_2'$ is zero everywhere on the element. Thus the $\boldsymbol{\phi}_{1j}^{\top}\boldsymbol{\phi}_{2k}'$ term only need to be evaluated on the nodes themselves. Note that this time the nodes could not be ignored as $\boldsymbol{\phi}_{2k}'$ approaches infinity at each node. Here we will denote an integration only in the infinitesimal part around every node $s_i$ by the symbol $S_N$. Thus from the previous argument,

$$\int_S \boldsymbol{\phi}_{1j}^{\top}\boldsymbol{\phi}_{2k}'\, ds = \int_{S_N} \boldsymbol{\phi}_{1j}^{\top}\boldsymbol{\phi}_{2k}'\, ds. \tag{4.43}$$

We further note that integration by parts gives

$$\int_{S_N} \boldsymbol{\phi}_{1j}^{\top}\boldsymbol{\phi}_{2k}'\, ds = \left[\boldsymbol{\phi}_{1j}^{\top}\boldsymbol{\phi}_{2k}\right]_C - \int_{S_N} \boldsymbol{\phi}_{1j}'^{\top}\boldsymbol{\phi}_{2k}\, ds, \tag{4.44}$$

where here the symbol $C$ indicates an evaluation around the immediate boundary surrounding $S_N$, or each of the lumped-mass nodes. As noted previously, we are only interested in the infinitesimal region $S_N$ around the lumped-mass nodes. Thus the second term on the RHS disappears due to $\boldsymbol{\phi}_{1j}'$ and $\boldsymbol{\phi}_{2k}$ both being finite everywhere. We are therefore interested in evaluating the value of the boundary values $\left[\boldsymbol{\phi}_{1j}^{\top}\boldsymbol{\phi}_{2k}\right]_{C_i}$ at each node $i$ where $C_i$ indicates an evaluation around the boundary immediately surrounding node $i$. This can be completed by a simple sum over all beam segments connecting to the node $i$ as

$$\left[\boldsymbol{\phi}_{1j}^{\top}\boldsymbol{\phi}_{2k}\right]_{C_i} = \sum_{c_i} \boldsymbol{\phi}_{1j,c_i}^{\top}\boldsymbol{\phi}_{2k,c_i}\epsilon_{c_i} \tag{4.45}$$

where $\boldsymbol{\phi}_{1j,c_i}$ is the value of $\boldsymbol{\phi}_{1j}$ expressed in the local frame of reference of beam element $c_i$ connecting to node $i$, $\boldsymbol{\phi}_{2k,c_i}$ is the value of $\boldsymbol{\phi}_{2k}$ throughout the beam element $c_i$ and $\epsilon_{c_i}$ takes the value of 1 if the direction of increasing $s$ points away from the node in the segment $c_i$, or the value of $-1$ otherwise. Combining (4.42) and (4.45) gives the expression for $\boldsymbol{\Lambda}_1$ as

$$\Lambda_{1,jk} = \sum_i \left( (s_{i+1} - s_i)\boldsymbol{\phi}_{1j,i+\frac{1}{2}}^{\top}\mathbf{E}^{\top}\boldsymbol{\phi}_{2k,i+\frac{1}{2}} + \sum_{c_i} \boldsymbol{\phi}_{1j,c_i}^{\top}\boldsymbol{\phi}_{2k,c_i}\epsilon_{c_i} \right). \tag{4.46}$$

In Section 5.2.3, it will be seen that this method is equivalent to the summation-of-force method described in [138].

The coefficients $\mathbf{A}$, $\mathbf{\Lambda}$ and $\mathbf{\Gamma}$ in (3.23) provide all the information required for the nonlinear structural equations of motion (3.23). Additionally the aerodynamic coefficients $\mathbf{H}$ can be computed in the same form as $\mathbf{\Gamma}$ coefficients and will allow the aerodynamic coupling terms to be computed from the modes as well.

### 4.3.2 Eigenvector and Eigenvalue Solution

In order to obtain the natural modes of the discretised system, we note that (3.23), when linearised about the unloaded equilibrium and removing external forcing, becomes

$$\begin{aligned} \dot{\mathbf{q}}_1 &= \mathbf{A}_1^{-1}\mathbf{\Lambda}_1\mathbf{q}_2, \\ \dot{\mathbf{q}}_2 &= \mathbf{A}_2^{-1}\mathbf{\Lambda}_2\mathbf{q}_1. \end{aligned} \tag{4.47}$$

Substituting the second equation into the first results in

$$\ddot{\mathbf{q}}_1 = \mathbf{A}_1^{-1}\mathbf{\Lambda}_1\mathbf{A}_2^{-1}\mathbf{\Lambda}_2\mathbf{q}_1. \tag{4.48}$$

Similarly

$$\ddot{\mathbf{q}}_2 = \mathbf{A}_2^{-1}\mathbf{\Lambda}_2\mathbf{A}_1^{-1}\mathbf{\Lambda}_1\mathbf{q}_2. \tag{4.49}$$

Thus we could obtain the set of natural modes of the system from an arbitrary, full set of space-spanning basis, for example the local modes that will be described later in Section 4.6.3 which will be very easy to construct. The eigenvalues of the system will be the square root of the eigenvalues of $\mathbf{A}_1^{-1}\mathbf{\Lambda}_1\mathbf{A}_2^{-1}\mathbf{\Lambda}_2$ or $\mathbf{A}_2^{-1}\mathbf{\Lambda}_2\mathbf{A}_1^{-1}\mathbf{\Lambda}_1$. As a low-order interpolation is used, the eigenvalues of the two matrices are not guaranteed to be the same, but they will be extremely close especially at the low-frequency end where the error from the interpolation is small. Furthermore, if (4.48) and (4.49) has eigenvectors $\overline{q}_{1i}$ and $\overline{q}_{2i}$ respectively, then the eigenvectors of the discretised structural system will be

$$\overline{\mathbf{q}}_{1i} = \sum_j q^*_{1i,j}\boldsymbol{\phi}_{1j}, \tag{4.50}$$

$$\overline{\mathbf{q}}_{2i} = \sum_j q^*_{2i,j}\boldsymbol{\phi}_{2j}. \tag{4.51}$$

## 4.4 Nonlinear Static Equilibrium Solution in Modal Coordinates

In this work, the modes of the system are expanded about the undeformed configuration of the structure due to the more desirable properties of the basis as described in Section 4.1. There are, however, situations in which we are interested in solutions to the static problem where $\mathbf{x}_1 = \dot{\mathbf{x}}_1 = \mathbf{0}$ and $\dot{\mathbf{x}}_2 = \mathbf{0}$, i.e. the solution to $\hat{\mathbf{x}}_2$ in (3.12) given an external static load $\mathbf{f}_A$. Rather than solving (3.12) directly, we apply a modified version of the existing modal structural equations (3.23) to arrive at the static solution to the external forcing that is consistent with the lumped mass discretisation.

We assume that a set of modal equations in the form of (3.23) has been previously obtained on the unloaded system using any compete set of modes (i.e. a full-order modal system). Then we cast the static equilibrium problem by enforcing $\mathbf{q}_1 = \mathbf{0}$, $\dot{\mathbf{q}}_1 = \mathbf{0}$ and $\dot{\mathbf{q}}_2 = \mathbf{0}$ and project the external load $\mathbf{f}_A$ onto the modal system as $\boldsymbol{\eta}_1$ using (3.18e), resulting in the static modal equation

$$\boldsymbol{\Lambda}_1\hat{\mathbf{q}}_2 - \boldsymbol{\Gamma}_2(\hat{\mathbf{q}}_2)\hat{\mathbf{q}}_2 + \boldsymbol{\eta}_1 = \mathbf{0} \tag{4.52}$$

As the static equation (4.52) is nonlinear, a Newton-Raphson method will be used to arrive at the solution iteratively. However in a nonlinear problem, Newton-Raphson iteration is not guaranteed to converge when the starting conditions are far from the solution. Therefore the external force is applied in ‘steps’, starting from $\mathbf{0}$ and subsequently taking the value of $\boldsymbol{\eta}_{1,n} = n\boldsymbol{\eta}_1/N_{steps}$ at each step, with the solution being $\hat{\mathbf{q}}_{2,n}$. Eventually the external load reaches $\boldsymbol{\eta}_1$ after $N_{steps}$ loading steps and the solution $\hat{\mathbf{q}}_{2,N_{steps}} = \hat{\mathbf{q}}_2$ is reached. The equation describing the static solution at step $n$ and $n+1$ respectively are

$$\boldsymbol{\Lambda}_1\hat{\mathbf{q}}_{2,n} - \boldsymbol{\Gamma}_2(\hat{\mathbf{q}}_{2,n})\hat{\mathbf{q}}_{2,n} + \boldsymbol{\eta}_{1,n} = \mathbf{0}, \tag{4.53a}$$

$$\boldsymbol{\Lambda}_1\hat{\mathbf{q}}_{2,n+1} - \boldsymbol{\Gamma}_2(\hat{\mathbf{q}}_{2,n+1})\hat{\mathbf{q}}_{2,n+1} + \boldsymbol{\eta}_{1,n+1} = \mathbf{0}. \tag{4.53b}$$

Assuming that at step $n$, the solution $\hat{\mathbf{q}}_{2,n}$ to the external load $\boldsymbol{\eta}_{1,n}$ is known to a sufficient accuracy from prior computations, subtracting (4.53a) from (4.53b) produces

$$\boldsymbol{\Lambda}_1(\hat{\mathbf{q}}_{2,n+1} - \hat{\mathbf{q}}_{2,n}) - (\boldsymbol{\Gamma}_2(\hat{\mathbf{q}}_{2,n+1})\hat{\mathbf{q}}_{2,n+1} - \boldsymbol{\Gamma}_2(\hat{\mathbf{q}}_{2,n})\hat{\mathbf{q}}_{2,n}) + \boldsymbol{\eta}_{1,n+1} - \boldsymbol{\eta}_{1,n} = \mathbf{0}. \tag{4.54}$$

We then define $\delta\hat{\mathbf{q}}_{2,n+1} = \hat{\mathbf{q}}_{2,n+1} - \hat{\mathbf{q}}_{2,n}$ and $\delta\boldsymbol{\eta}_{1,n+1} = \boldsymbol{\eta}_{1,n+1} - \boldsymbol{\eta}_{1,n}$, substituting these variables into (4.54) results in

$$\mathbf{\Lambda}_1\delta\hat{\mathbf{q}}_{2,n+1} - (\mathbf{\Gamma}_2(\hat{\mathbf{q}}_{2,n})\delta\hat{\mathbf{q}}_{2,n+1} + \mathbf{\Gamma}_2(\delta\hat{\mathbf{q}}_{2,n+1})\delta\hat{\mathbf{q}}_{2,n+1} + \mathbf{\Gamma}_2(\delta\hat{\mathbf{q}}_{2,n+1})\hat{\mathbf{q}}_{2,n}) + \delta\boldsymbol{\eta}_{1,n+1} = \mathbf{0}. \tag{4.55}$$

This equation describes the relation of $\delta\hat{\mathbf{q}}_{2,n+1}$ with the known $\hat{\mathbf{q}}_{2,n}$. Although this is merely a change of variable from (4.54), we note that the unknown $\delta\hat{\mathbf{q}}_{2,n}$ can now be as small as required (by varying $N_{steps}$) for the Newton-Raphson method to operate on (4.55) reliably. Thus by starting from an unloaded configuration and gradually increasing the external load, finding the equilibrium solution at each load, one will be able to arrive at the full load static equilibrium solution. However if the loading condition produces singularities such as snap-through, a more reliable option would be to introduce artificial damping on a dynamic simulation rather than using the static relaxation approach described here, constantly removing kinetic energy from the system until convergence towards the static equilibrium.

## 4.5 Modal Time Marching and Integration

In the previous section we have described the solution to the static loading problem using a modal basis. Here we will describe the time-marching of the modal equations in a dynamic solution. To simplify the analysis, time marching in this work uses the classical explicit fourth-order Runge-Kutta (RK4) integrator (built-in in Matlab) on the modal aero(servo)elastic system of (3.55). The selection of the RK4 time integration scheme is due to its ease of implementation, control of stability and reliability through automatic timestep selections. Forwards and backwards Euler schemes were also attempted but found to offer no benefit in computational efficiency for the same level of accuracy, and in the backwards (implicit) case, convergence of iteration was very difficult on the nonlinear modal system. However the efficiency of the RK4 scheme is limited by a maximum stable timestep that is on the order of the period of the highest frequency mode of the linear system ($\omega_{max}^{-1}$, where $\omega_{max}$ is the square root of the largest eigenvalue in $\mathbf{A}_1^{-1}\mathbf{\Lambda}_1\mathbf{A}_2^{-1}\mathbf{\Lambda}_2$ in the structural problem, or its equivalent in the aeroelastic problem), as a result of RK4's finite stability boundary. If the modal system is stiff, that is, the ratio between the smallest and largest eigenvalues are large, this maximum stable timestep limit produces unnecessarily small timesteps and makes it very expensive to compute the low-frequency dynamics for such a system. A way to circumvent this limit is described in Section 4.6.1.

Improvements to the general-purpose integration scheme were not sought as accuracy of the numerical scheme was deemed sufficient for the current work and will be demonstrated in Chapters 6 and 7. The results show that numerical integration scheme is not the primary source of error in the aeroelastic problem. In fact, the modal aerodynamic model described in Chapter 3 makes a number of simplifications and assumptions that introduce far more significant errors than that caused by the RK4 numerical integration used in this work, such as the lack of tip effects and a constant $V_\infty$ everywhere on the wing.

### 4.5.1 Displacement and Rotation Integration

The nodal displacement and rotation at each subsequent instant can be easily tracked by re-assembling the local velocity from the velocity modes and applying (3.46), i.e. by integrating in time. The displacements and rotations in the beam segment between each node, if required, could be computed in a similar way to the nodal displacements by using the interpolation in (4.32). However, as described in Section 4.1.4, only satisfying the weak form of the structural compatibility equation (as found in the modal form of the intrinsic equations (3.23)) with a reduced-order model might introduce integral errors in tracking the shape of the deformed structure. This means that without explicitly enforcing the relative displacements and rotations between nodes, the integral error will not only give rise to deviations in the overall spatial location of the structure but also errors in the relative distances between nodes on the structure, i.e. the structure could "fly apart" without the numerical solution acknowledging this fact due to each node being tracked individually. As this arises from the use of a reduced-order formulation, a more accurate time-marching scheme would not alleviate this problem. Therefore, to prevent this scenario from taking place, a regularisation step of integration in the $s$-direction along each element, or along the beam structure, is performed by applying an RK4 integration on (3.47) at regular time intervals selected during use. Thus, during a normal timestep at node $s_i$ and time $t_j$, $\mathbf{r}_{i,t}$ (and similarly $\mathbf{T}_{i,j}$) is computed from knowledge of the spatial position at the previous time $\mathbf{r}_{i,j-1}$ and the velocities of the current node $\mathbf{x}_{1,i,j}$. However during regularisation, at regular intervals in time, a step is carried out so that $\mathbf{r}_{i,j}$ is computed from the spatial position of its adjacent node at the current time $\mathbf{r}_{i-1,j}$ and the strains in the beam segment between the two nodes at the current time $\mathbf{x}_{2,i,j}$ using (3.47). The exact frequency that this needs to be carried out at depends on the extent of the modal reduction: if more structural modes are retained (thus bearing a better approximation to the full-mode system), this operation would be required infrequently and vice versa.

So far in this work all calculations regarding rotations or orientations are conducted using rotation matrices, for example in (3.46) and (3.47). These equations integrate each of the nine elements of a rotation matrix separately without trying to satisfy the constraints placed on the elements in a rotation matrix. Storing rotations as cartesian rotation vectors and converting them into the rotation matrices during computation is possible, however in practice it was found that with the automatic error control of the RK4 algorithm set to the level described above, the rotation matrices remain orthonormal to a high degree and little loss of accuracy is seen by storing rotation matrices directly, although re-orthogonalisation of the stored rotation matrices, by transforming them into the closest rotation vector and then back, is performed at regular time intervals for added reliability.

## 4.6 Numerical Scheme Optimisation

This section will discuss various methods in which improvements were made to the efficiency of time-marching algorithms of the modal system. Although computational time is not critical in most numerical cases investigated in this work, algorithm optimisation is still very necessary if the method is to be applied to problems of practical importance.

### 4.6.1 Residualisation

As described in Section 4.5, the largest permissible time-step for stable time marching of the system (3.23) or (3.55) using the RK4 scheme is determined by the period of the highest frequency mode in the linear system (a discussion of the stability boundaries of various ODE time marching schemes is found in textbooks such as [139]). As will be demonstrated by simulations in Section 6.3, the structural model requires the inclusion of high-frequency modes in order to conserve system momentum. As a result the permissible time-step becomes very small compared to the typical timescale of the low-frequency dynamics, increasing the computational cost required to compute a given length of time in the simulation.

The problem of stiffness in ODEs has been extensively studied in the literature on numerical methods [139]. For displacement-based formulations in particular, damping is added to the Newmark method [1]. The time-stepping scheme will thus be able to march at a larger timestep than the highest eigenvalue permits without becoming unstable, while retaining good accuracy for low-frequency responses that are typically of interest. However the method relies on using the structure of the generalised equations of motion which is difficult to translate into the intrinsic modal formulation where a different set of primary variables is used. As described previously, other integration schemes that include numerical damping are either too limited in their applicability or caused convergence problems in the implicit iterations.

In the aeroelastic system in which we are interested in this work however, we are primarily interested in the low-frequency behaviour. The use of a beam-type description of a slender structure becomes less accurate at wavelengths comparable to the typical section size of the structure, furthermore the strength of aerodynamic damping in an aeroelastic system increases with frequency and will remove any high frequency dynamics very quickly. Thus we are only interested in the inclusion of high-frequency modes as a *nonlinear correction term* to the low-frequency modes in the structural model. This philosophy is the same as the residualisation method used in linear model reduction [124] where rather than reducing the size of a system by simply truncating parts of the dynamics altogether (balanced truncation), the truncated dynamics are instead solved as algebraic equations and coupled back to the retained parts of the dynamics, which also ensure that the solution to the static problem is preserved. In linear model reduction, the truncation method is normally used to remove low-frequency modes, whereas residualisation is used for high-frequency ones as is the case here. There exists a difference between the balanced residualisation technique and the method used currently, where balanced residualisation operates on linear systems, the current method seeks to retain the coupling in nonlinear dynamics.

We will now describe the algebraic procedure by which the residualisation is carried out in this work. First, we take the structural modal equations (3.28) as the starting point of this analysis. It is thus implied that a finite number of natural modes of the system are used resulting in a diagonal $\mathbf{W}_D$ matrix that is diagonal by definition. If this is not the case it will be straightforward to orthogonalise the modes until this is achieved, using the method in Section 4.3.2. The aerodynamic and flight dynamic couplings are not considered part of the residualisation process and are computed after residualisation is performed. We now define a pair of modes $\boldsymbol{\phi}_{1,j}$ and $\boldsymbol{\phi}_{2,j}$ as being high-frequency when their associated eigenvalue, $\omega_j$, is higher than a specified cut-off frequency, $\omega_C$. Otherwise it is regarded as being low-frequency. We now split $\mathbf{q}$ into two parts containing the low- and high-frequency modes, $\mathbf{q}_L$ and $\mathbf{q}_H$, respectively, that is, $\mathbf{q} = \begin{bmatrix} \mathbf{q}_L^\top & \mathbf{q}_H^\top \end{bmatrix}^\top$. Using this, (3.28) can be split into

$$\dot{\mathbf{q}}_L = \mathbf{W}_L \mathbf{q}_L + \boldsymbol{\Gamma}_L(\mathbf{q})\mathbf{q} + \boldsymbol{\eta}_L, \tag{4.56a}$$

$$\dot{\mathbf{q}}_H = \mathbf{W}_H \mathbf{q}_H + \boldsymbol{\Gamma}_H(\mathbf{q})\mathbf{q} + \boldsymbol{\eta}_H \tag{4.56b}$$

Under a slow external forcing, the linear part of the second equation, which defines a set of high-frequency harmonic oscillators, operates at a very different frequency to the quadratic part of the equation, which contains contributions from geometric nonlinear couplings, and to the external forcing. Therefore if only the low-frequency dynamics are of interest, the system can be approximated by regarding a time-averaged $\overline{\mathbf{q}}_H$ that reacts instantaneously to excitations from the $\mathbf{\Gamma}_H(\mathbf{q})\mathbf{q}$ and $\boldsymbol{\eta}_H$ terms. This approximation effectively removes the high-frequency dynamics from the $\mathbf{q}_H$ states and converts (4.56) into a set of differential-algebraic equations (DAE), or

$$\overline{\mathbf{q}}_H = -\mathbf{W}_H^{-1}(\mathbf{\Gamma}_H(\overline{\mathbf{q}})\overline{\mathbf{q}} + \boldsymbol{\eta}_H), \tag{4.57a}$$

$$\dot{\mathbf{q}}_L = \mathbf{W}_L\mathbf{q}_L + \mathbf{\Gamma}_L(\overline{\mathbf{q}})\overline{\mathbf{q}} + \boldsymbol{\eta}_L, \tag{4.57b}$$

with $\overline{\mathbf{q}} = \begin{bmatrix} \mathbf{q}_L^\top & \overline{\mathbf{q}}_H^\top \end{bmatrix}^\top$. This set of equations is marched by first iterating the value of $\overline{\mathbf{q}}_H$ using the currently known values of system states $\mathbf{q}_L$ with the first equation of (4.57), then computing the value of $\dot{\mathbf{q}}_L$ using the second equation to obtain the time derivatives for time marching. The iteration of $\overline{\mathbf{q}}_H$ can be carried out as

$$\overline{\mathbf{q}}_{H,k+1} = -\mathbf{W}_H^{-1}(\mathbf{\Gamma}_H(\overline{\mathbf{q}_k})\overline{\mathbf{q}_k} + \boldsymbol{\eta}_H) \tag{4.58}$$

which converges quickly provided the eigenvalues in $\mathbf{W}_H$ are large. More elaborate iteration schemes such as Newton-Raphson can also be used for faster convergence but were not necessary in the results shown in this work.

In practice, the residualisation method was able to significantly speed up the computation by providing an increase in maximum stable timestep, a result that a truncation of high-frequency also achieves. However residualisation of high-frequency components provides the benefit of being much more accurate in predicting the low-frequency response of the structure than a truncation can achieve. This is because it retains coupling interactions from high-frequency modes that occur at a far slower rate than their natural frequencies. The effectiveness of this method will be demonstrated in Section 6.3 and compared against full mode simulation using (3.28).

### 4.6.2 Algorithm Optimisation

In simulations, it was found that the overwhelming majority of the computation time was spent computing the quadratic nonlinear coupling terms in the modal ODE in each time-step in the form of $\Gamma_{1,jkl}q_{1,k}q_{1,l}$, for example. In general, $\mathbf{\Gamma}_1$ is fully populated. If we assume that we have included $N_M + 6$ velocity modes ($\boldsymbol{\phi}_1$), computing $\Gamma_{1,jkl}q_{1,k}q_{1,l}$ directly requires $2(N_M + 6)^3$ multiplications, with a similar number on the other structural and aerodynamic coupling terms. Optimisation to the algorithm is sought in order to speed up this step in the simulation (time-marching) process. For clarity, the following discussion uses the $\Gamma_{1,jkl}q_{1,k}q_{1,l}$ term only, with similar extensions to other terms of the same nature.

First we note that by pre-computing a matrix $Q_{1,kl} = q_{1,k}q_{1,l}$ before computing the quadratic coupling as $\Gamma_{1,jkl}q_{1,k}q_{1,l} = \Gamma_{1,jkl}Q_{1,kl}$, one almost halves the number of multiplications required to $(N_M+6)^3+(N_M+6)^2$. Then by realising $Q_{1,kl} = Q_{1,lk}$, one could further pre-compute $\hat{\Gamma}_{1,jkl}\big|_{k\neq l} = \Gamma_{1,jkl} + \Gamma_{1,jlk}$, giving $\Gamma_{1,jkl}Q_{1,kl} = \hat{\Gamma}^*_{1,jkl}Q_{1,kl}\big|_{j\leq k}$ which now requires only $(N_M+6)(N_M+6)(N_M+7)/2+(N_M+6)(N_M+7)/2$ multiplications. At large values of $N_M$ this represents only a quarter of the original number of multiplications required, or quadrupling the speed of time-marching. However it is worth noting that the latter reduction could not be applied to terms of the form $\Gamma_{2,jkl}q_{1,k}q_{2,l}$, on these terms only a two-fold reduction can be achieved.

### 4.6.3 Local Mode Projection

In the above paragraph we have described optimising the computation of nonlinear coupling terms purely by reducing and grouping redundant multiplications. The nonlinear coupling coefficients $\mathbf{\Gamma}$ and $\mathbf{H}$ themselves however are still fully populated due to the use of global modes, modes that are not confined in a particular region or element in space and will thus produce a non-zero coupling with every other mode. This is in contrast to a finite-element type approach, where each mode is only non-zero in its local element and will thus only couple with other modes that are non-zero in the same element, producing very sparsely populated coupling coefficients. The conventional wisdom in linear modal analysis is that one would need less modes than the number of degrees of freedoms in the system. However in Section 6.3 we will discuss how this is not necessarily the case for conservation of momentum in nonlinear problems, i.e. any degree of truncation would introduce significant integral errors in momentum. We thus seek to project the *coupling* between the global modes into local modes and obtain a sparse coupling coefficient matrix, which would result in a far more significant improvement in computational speed.

We make the lumped mass model defined in Section 4.2 as our starting point and limit the discussion to the structural model (the aerodynamic coupling coefficients follow the same process and will not be discussed separately). The local modes in this model will be the component-wise shape functions (as $\mathbf{x}_1$ and $\mathbf{x}_2$ both contain six components) which we have already used to define the interpolation of the intrinsic variables $\mathbf{x}_1$ and

$\mathbf{x}_2$ in (4.32) and (4.34). We thus define the set of local modes as

$$\boldsymbol{\varphi}_{1,6n+p} = \mathbf{c}_p \varphi_{1,n}, \tag{4.59a}$$

$$\boldsymbol{\varphi}_{2,6n+p} = \mathbf{c}_p \varphi_{1,n+\frac{1}{2}}, \tag{4.59b}$$

where $\mathbf{c}_p$ is a 6-element unit vector with the $p$-th element being unity and $\varphi$ is the interpolation shape function defined in Section 4.2. The associated modal expansion using this basis is written as

$$\mathbf{x}_1 = \sum_{j=1}^{6N} \boldsymbol{\varphi}_{1j}(s)\mu_{1j}(t), \tag{4.60a}$$

$$\mathbf{x}_2 = \sum_{j=1}^{6(N-1)} \boldsymbol{\varphi}_{2j}(s)\mu_{2j}(t). \tag{4.60b}$$

Projecting onto this basis will result in a set of modal equations with an identical form to (3.22), or

$$\mathbf{A}_1^* \dot{\boldsymbol{\mu}}_1 = \boldsymbol{\Lambda}_1^* \boldsymbol{\mu}_2 - \boldsymbol{\Gamma}_1^*(\boldsymbol{\mu}_1)\boldsymbol{\mu}_1 - \boldsymbol{\Gamma}_2^*(\boldsymbol{\mu}_2)\boldsymbol{\mu}_2 + \boldsymbol{\eta}_1^*, \tag{4.61a}$$

$$\mathbf{A}_2^* \dot{\boldsymbol{\mu}}_2 = \boldsymbol{\Lambda}_2^* \boldsymbol{\mu}_1 + \boldsymbol{\Gamma}_3^*(\boldsymbol{\mu}_1)\boldsymbol{\mu}_2, \tag{4.61b}$$

with the $\mathbf{A}^*$, $\boldsymbol{\Lambda}^*$, $\boldsymbol{\Gamma}^*$ and $\boldsymbol{\eta}^*$ defined identically to those in (3.22). It is also worth noting that with the use of local, finite-element discretisation, this becomes effectively a nonlinear *finite-element* description of the structural system.

If (3.22) uses a full set of modes (of a finite number) in the structural model (not necessarily natural modes) then (3.22) and (4.61) are different but completely equivalent representations of the same system. A transformation between the two bases can be defined by noting that

$$\mathbf{x}_1 = \sum_{j=1}^{6N_a} \boldsymbol{\varphi}_{1j}\mu_{1j} = \sum_{j=1}^{6N_a} \boldsymbol{\phi}_{1j}^* q_{1j}, \tag{4.62}$$

then performing a Galerkin projection on both, resulting in

$$\langle \mathbf{x}_1, \boldsymbol{\varphi}_{1k} \rangle = \sum_{j=1}^{6N_a} \langle \boldsymbol{\varphi}_{1j}, \boldsymbol{\varphi}_{1k} \rangle \mu_{1j} = \sum_{j=1}^{6N_a} \langle \boldsymbol{\phi}_{1j}^*, \boldsymbol{\varphi}_{1k} \rangle q_{1j}. \tag{4.63}$$

We can thus define

$$Y_{1,jk} = \langle \boldsymbol{\varphi}_{1k}, \boldsymbol{\varphi}_{1j} \rangle, \tag{4.64a}$$

$$Z_{1,jk} = \langle \boldsymbol{\phi}^*_{1j}, \boldsymbol{\varphi}_{1j} \rangle \tag{4.64b}$$

which results in $\mathbf{Y}_1 \boldsymbol{\mu}_1 = \mathbf{Z}_1 \mathbf{q}_1$ or if we define $\mathbf{N}_1 = \mathbf{Z}_1^{-1} \mathbf{Y}_1$,

$$\mathbf{q}_1 = \mathbf{N}_1 \boldsymbol{\mu}_1, \tag{4.65a}$$

$$\boldsymbol{\mu}_1 = \mathbf{N}_1^{-1} \mathbf{q}_1. \tag{4.65b}$$

The transformation $\mathbf{N}_2$ between $\mathbf{q}_2$ and $\boldsymbol{\mu}_2$ can be defined in the same manner.

The local modal system of (4.61) can now be written using global modes as

$$\mathbf{A}_1^* \mathbf{N}_1^{-1} \dot{\mathbf{q}}_1 = \boldsymbol{\Lambda}_1^* \mathbf{N}_2^{-1} \mathbf{q}_2 - \boldsymbol{\Gamma}_1^* (\mathbf{N}_1^{-1} \mathbf{q}_1) \mathbf{N}_1^{-1} \mathbf{q}_1 - \boldsymbol{\Gamma}_2^* (\mathbf{N}_2^{-1} \mathbf{q}_2) \mathbf{N}_2^{-1} \mathbf{q}_2 + \boldsymbol{\eta}_1^*, \tag{4.66a}$$

$$\mathbf{A}_2^* \mathbf{N}_2^{-1} \dot{\mathbf{q}}_2 = \boldsymbol{\Lambda}_2^* \mathbf{N}_1^{-1} \mathbf{q}_1 + \boldsymbol{\Gamma}_3^* (\mathbf{N}_1^{-1} \mathbf{q}_1) \mathbf{N}_2^{-1} \mathbf{q}_2, \tag{4.66b}$$

or

$$\dot{\mathbf{q}}_1 = \mathbf{A}_1^{*-1} \mathbf{N}_1 (\boldsymbol{\Lambda}_1^* \mathbf{N}_1^{-1} \mathbf{q}_2 - \boldsymbol{\Gamma}_1^* (\mathbf{N}_1^{-1} \mathbf{q}_1) \mathbf{N}_1^{-1} \mathbf{q}_1 - \boldsymbol{\Gamma}_2^* (\mathbf{N}_1^{-1} \mathbf{q}_2) \mathbf{N}_1^{-1} \mathbf{q}_2 + \boldsymbol{\eta}_1^*), \tag{4.67a}$$

$$\dot{\mathbf{q}}_2 = \mathbf{A}_2^{*-1} \mathbf{N}_2 (\boldsymbol{\Lambda}_2^* \mathbf{N}_1^{-1} \mathbf{q}_1 + \boldsymbol{\Gamma}_3^* (\mathbf{N}_1^{-1} \mathbf{q}_1) \mathbf{N}_1^{-1} \mathbf{q}_2). \tag{4.67b}$$

Importantly, this system is completely equivalent to (3.23), it follows that the linear and nonlinear part of the dynamics should separately be equal to their respective counterparts, i.e.

$$\mathbf{A}_1^{-1} \boldsymbol{\Gamma}_1 (\mathbf{q}_1) \mathbf{q}_1 = \mathbf{A}_1^{*-1} \mathbf{N}_1 \boldsymbol{\Gamma}_1^* (\mathbf{N}_1^{-1} \mathbf{q}_1) \mathbf{N}_1^{-1} \mathbf{q}_1, \tag{4.68a}$$

$$\mathbf{A}_2^{-1} \boldsymbol{\Gamma}_2 (\mathbf{q}_2) \mathbf{q}_2 = \mathbf{A}_1^{*-1} \mathbf{N}_1 \boldsymbol{\Gamma}_2^* (\mathbf{N}_1^{-1} \mathbf{q}_2) \mathbf{N}_1^{-1} \mathbf{q}_2, \tag{4.68b}$$

$$\mathbf{A}_2^{-1} \boldsymbol{\Gamma}_3 (\mathbf{q}_1) \mathbf{q}_2 = \mathbf{A}_2^{*-1} \mathbf{N}_2 \boldsymbol{\Gamma}_3^* (\mathbf{N}_1^{-1} \mathbf{q}_1) \mathbf{N}_1^{-1} \mathbf{q}_2. \tag{4.68c}$$

We can thus replace the multiplications involving $\boldsymbol{\Gamma}$ by those involving $\boldsymbol{\Gamma}^*$ and pre-multiplications with $\mathbf{N}$ or $\mathbf{N}^{-1}$. As noted at the start of this section, the nonlinear coupling coefficients $\boldsymbol{\Gamma}^*$ involving local modes are very sparse. Therefore although the latter expressions carry additional pre-multiplication computations that are on the order of $\mathcal{O}(N_a^2)$, it reduces the $\mathcal{O}(N_a^3)$ multiplications of the original coupling coefficient computation using $\boldsymbol{\Gamma}$ into $\mathcal{O}(N_a)$ multiplications using the sparse $\boldsymbol{\Gamma}^*$. The result is a significant reduction from an overall $\mathcal{O}(N_a^3)$ into $\mathcal{O}(N_a^2)$ multiplications with the use of a local mode basis.

When the original system in question is reduced-order however, a problem with this method will arise. As the full set of local modes must always be used, the **Z** matrices cease to be square. It is, however, still possible to make this transformation by *including* the truncated modes only when computing the **Z** matrices, resulting in square **N** and $\mathbf{N}^{-1}$ matrices which can then be truncated to the appropriate dimensions. Thus the method is not limited to a full-mode system. It is worth noting that modal truncation of the original system will result in a complexity of $\mathcal{O}(N_M^3)$ where $N_M \leq 6N_a$ is the number of retained modes, however the local mode projection remains at a complexity of $\mathcal{O}(N_a^2)$. Thus for values of $N_M$ less than a certain threshold, the use of FE-space projection no longer offers a computational saving.

# 5 Generation of 1D Intrinsic System from Condensation of 3D Model

The previous chapter described a numerical procedure to obtain a nonlinear modal structure/aeroelastic system. There we have assumed that we have explicit knowledge of the material properties, $\mathbf{M}$ and $\mathbf{C}$ of the structure. As described previously, the sectional compliance properties are typically obtained via structural homogenisation or using variational asymptotic principles. However in this chapter we propose a method of obtaining a nonlinear intrinsic description of a 3D structure via a direct condensation from a high-fidelity 3D FE model, without requiring the typical section to be regular or periodic, or explicit knowledge of the sectional compliance matrix in a beam-type description. First we will make a short review of Guyan reduction, a method for the condensation of degrees of freedom that will play an important part in our approach. We will then define the suitable form of structural problem to which we can apply this approach and describe the process of generating a modal structural or aeroelastic system from this starting point. The application of this method will be demonstrated in Chapter 6.

## 5.1 Guyan reduction

The Guyan reduction [140] is one of several reduction methods which aims to reduce the number of degrees of freedoms in a structural problem by condensing the entire system dynamics onto a specific set of dofs. A detailed review of the different reduction techniques can be found in standard textbooks such as that by Preumont [141].

Consider a forced, finite-dimensional linear structural system without damping, where the inertia is lumped onto a set of dofs, with associated infinitesimal displacement vectors $\mathbf{u}_i$ and, in general, rotation vectors $\boldsymbol{\theta}_i$ at every node $i$ collected into a vector $\mathbf{x}_a$, whereas the remaining set $\mathbf{x}_r$ has no inertia and receives no external excitation. Then the linear equations of motion describing $\mathbf{x}_g = \left[\begin{array}{cc} \mathbf{x}_a^\top & \mathbf{x}_r^\top \end{array}\right]^\top$ can be written as

$$\mathbf{M}_g \ddot{\mathbf{x}}_g + \mathbf{K}_g \mathbf{x}_g = \mathbf{f}_g, \tag{5.1}$$

which can be split according to the analysis degrees of freedom,

$$\begin{pmatrix} \mathbf{M}_{g,11} & \mathbf{0} \\ \mathbf{0} & \mathbf{0} \end{pmatrix} \begin{pmatrix} \ddot{\mathbf{x}}_a \\ \ddot{\mathbf{x}}_r \end{pmatrix} + \begin{pmatrix} \mathbf{K}_{g,11} & \mathbf{K}_{g,12} \\ \mathbf{K}_{g,21} & \mathbf{K}_{g,22} \end{pmatrix} \begin{pmatrix} \mathbf{x}_a \\ \mathbf{x}_r \end{pmatrix} = \begin{pmatrix} \mathbf{f}_a \\ \mathbf{f}_r \end{pmatrix} \tag{5.2}$$

where $\mathbf{f}_a$ and $\mathbf{f}_r$ are the external forcing terms. We assume that there is no associated forcing on $\mathbf{x}_r$, or $\mathbf{f}_r = \mathbf{0}$. The second equation in equation (5.2) now becomes an algebraic equation that links the "slave" states $\mathbf{x}_r$ to the "master" dofs $\mathbf{x}_a$ by

$$\mathbf{x}_r = -\mathbf{K}_{g,22}^{-1}\mathbf{K}_{g,21}\mathbf{x}_a \tag{5.3}$$

and by making this substitution into the original equation, the structural dynamics become

$$\mathbf{M}_{g,11}\ddot{\mathbf{x}}_a + (\mathbf{K}_{g,11} - \mathbf{K}_{g,12}\mathbf{K}_{g,22}^{-1}\mathbf{K}_{g,21})\mathbf{x}_a = \mathbf{f}_a \tag{5.4}$$

Although this is strictly accurate only when there are no inertia associated with the slave dofs, Guyan reduction nonetheless assumes this transformation to be valid and applies the same process even when $\mathbf{M}_{g,22} \neq \mathbf{0}$, transforming the system as

$$\begin{aligned}(\mathbf{M}_{g,11} + \mathbf{K}_{g,12}\mathbf{K}_{g,22}^{-1\top}\mathbf{M}_{g,22}\mathbf{K}_{g,22}^{-1}\mathbf{K}_{g,21})\ddot{\mathbf{x}}_a + (\mathbf{K}_{g,11} - \mathbf{K}_{g,12}\mathbf{K}_{g,22}^{-1}\mathbf{K}_{g,21})\mathbf{x}_a & \quad (5.5)\\ = \mathbf{f}_a - \mathbf{K}_{g,12}\mathbf{K}_{g,22}^{-1}\mathbf{f}_r & \quad (5.6)\end{aligned}$$

which again condenses the system onto the $\mathbf{x}_a$ dofs. Note that this process is very similar to the residualisation method described in Section 4.6.1, thus the error associated with the natural mode shapes of this condensed system becomes significant at frequencies beyond the lowest eigenvalue of the system $\mathbf{M}_{g,22}\ddot{\mathbf{x}}_r + \mathbf{K}_{g,22}\mathbf{x}_r = \mathbf{0}$ [141], i.e. the cut-off frequency. Additionally even with such generalisation, a restriction still applies that the inertias of $\mathbf{x}_a$ and $\mathbf{x}_r$ sets of dofs should not be coupled. We finally define the mass $\mathbf{M}_a$ and stiffness $\mathbf{K}_a$ matrices of the reduced system as

$$\mathbf{M}_a = \mathbf{M}_{g,11} + \mathbf{K}_{g,12}\mathbf{K}_{g,22}^{-1\top}\mathbf{M}_{g,22}\mathbf{K}_{g,22}^{-1}\mathbf{K}_{g,21}, \tag{5.7a}$$

$$\mathbf{K}_a = \mathbf{K}_{g,11} - \mathbf{K}_{g,12}\mathbf{K}_{g,22}^{-1}\mathbf{K}_{g,21}. \tag{5.7b}$$

This allows us to write the reduced system, for the case of $\mathbf{f}_r = \mathbf{0}$, as

$$\mathbf{M}_a\ddot{\mathbf{x}}_a + \mathbf{K}_a\mathbf{x}_a = \mathbf{f}_a. \tag{5.8}$$

## 5.2 Computation of Intrinsic Modes from Condensation

In this section, we aim to obtain intrinsic modes of a beam-type description of a structure from a 3D FE model describing the full structure, with which we can then apply the method described in Section 4.3.1 to construct a nonlinear modal system. To outline the process by which we reduce a structure into a 1D beam-type description using an existing linear 3D FE model, we first make our starting point a complex-geometry (linear) finite-element model of a structure with slender sub-components built using any combination of 1D, 2D or 3D elements (Step I in Figure 7). In order to cast the problem into a form compatible with the Guyan reduction technique, we will lump the inertia of the structure as point masses at a set of $N_a$ analysis nodes along the main load paths $S$ of the structure. From now on we will treat these $N_a$ analysis nodes as the nodes in the spatial discretisation described in Section 4.2. Such nodes can be either part of the structure, e.g., along the wing spar in an aircraft model, or floating nodes along the main load paths. In the latter case, they are linked to the local structural nodes by means of interpolation elements (e.g., RBE3 elements in NASTRAN [52] or kinematic coupling constraints in ABAQUS [137]).

We then perform the Guyan reduction on the original structure and obtain the $\mathbf{M}_a \in \mathbb{R}^{N_a \times N_a}$ and $\mathbf{K}_a \in \mathbb{R}^{N_a \times N_a}$ matrices on each of the six degrees of freedom (three displacements and three rotations) at $N_a$ analysis nodes. We define this collection of displacement and rotations in the global frame as a six-component vector $\mathbf{x}_0 = \begin{bmatrix} \mathbf{r}^\top & \boldsymbol{\theta}^\top \end{bmatrix}^\top$ and the corresponding discrete version $\mathbf{x}_{a,i} = \mathbf{x}_0(s_i)$. At this stage the $\mathbf{M}_a$ and $\mathbf{K}_a$ matrices still describe the linear dynamics between this set of $N_a$ nodes without any explicit knowledge of the beam-like connectivity between them. Due to mass lumping, the reduced matrix $\mathbf{M}_a$ is a block diagonal matrix. The reduced stiffness matrix $\mathbf{K}_a$ is symmetric and can be fully populated. The number of degrees of freedom in the reduced, *linear* problem is $6N_a$ and consists of the displacements $\mathbf{r}(s_i, t)$ and rotations $\boldsymbol{\Psi}(s_i, t)$ of the individual analysis nodes in the global frame of reference (a-frame, defined in Section 2.1). Then by defining an open network of beams (i.e. a tree structure without any closed loops) linking the analysis nodes, we introduce the information regarding connectivity between the analysis nodes, where by doing this we effectively regard the linear elastic behaviour described by the $\mathbf{K}_a$ matrix as arising from massless beams that connect nodes on the load paths. The discrete linear system defined in the form of (5.8) will eventually be used to obtain the interpolated, continuous intrinsic modes in velocities, $\boldsymbol{\phi}_{1j}$, and stress resultants $\boldsymbol{\phi}_{2j}$, as well as the corresponding momenta $\mathbf{M}\boldsymbol{\phi}_{1j}$ and sectional strains $\mathbf{C}\boldsymbol{\phi}_{2j}$.

Our aim is to utilise the information obtained above to identify a model of the form (3.23) by the use of the intrinsic modes using the method described in Section 4.3.1, which will additionally capture the *geometrically-nonlinear* dynamics of the structure. We identify the coefficients in the nonlinear equations through structural and inertial information from mass $\mathbf{M}_a$ and stiffness $\mathbf{K}_a$ matrices and geometrical nonlinear effects from the location of the nodes along load paths.

For the purpose of model reduction we intend to describe the modal system using natural modes. In view of (3.18), this will involve computing the linear natural mode shapes $\boldsymbol{\phi}_{1j}(s)$ and $\boldsymbol{\phi}_{2j}(s)$, which are defined at every point point $s$. However, the reduction from a 3D FE model only provides information at the location of the discrete analysis nodes $s_i \in S$, as shown in Step II in Figure 7. Our goal is thus to construct interpolated (natural) mode shapes $\boldsymbol{\phi}_{1j}$, $\boldsymbol{\phi}_{2j}$ and the associated momentums $\mathbf{M}\boldsymbol{\phi}_{1j}$ and strains $\mathbf{C}\boldsymbol{\phi}_{2j}$ from the discrete natural modes of the stiffness and mass matrices $\mathbf{K}_a$ and $\mathbf{M}_a$ described in global displacement and rotations. For ease of discussion we will also define $\boldsymbol{\psi}_{1j} = \mathbf{M}\boldsymbol{\phi}_{1j}$ and $\boldsymbol{\psi}_{2j} = \mathbf{C}\boldsymbol{\phi}_{2j}$.

### 5.2.1 Displacement and Rotation Modes

We now define $\boldsymbol{\Phi}_{0j}$ to be the discrete mode shapes in these displacement/rotation degrees of freedom (Step III in Figure 7), with corresponding natural angular frequencies $\omega_{a,j}$, which are obtained from the eigenvalue problem corresponding to (5.8) as

$$\left(-\omega_j^2 \mathbf{M}_a + \mathbf{K}_a\right) \boldsymbol{\Phi}_{0j} = \mathbf{0}. \tag{5.9}$$

These are the mode shapes and frequencies of a standard linear vibration analysis. The mode shape $\boldsymbol{\Phi}_{0j}$ of the reduced system, defined by (5.9), exists only at each of the $N_a$ condensation nodes $s_i$. These correspond to the natural mode shapes of the original full FE system given by

$$\left(-\omega_j^2 \mathbf{M}_g + \mathbf{K}_g\right) \boldsymbol{\Phi}_{gj} = \mathbf{0} \tag{5.10}$$

where $\boldsymbol{\Phi}_{gj} = \begin{bmatrix} \boldsymbol{\Phi}_{0j}^\top & \boldsymbol{\Phi}_{rj}^\top \end{bmatrix}^\top$ and $\boldsymbol{\Phi}_{rj}$ contains the removed degrees of freedom from the FE model. As masses are only lumped onto the analysis degrees of freedoms, $\mathbf{M}_{g,22} = \mathbf{0}$. This means that for (5.10) to hold,

$$-\omega_j^2 \mathbf{M}_{g,11} \boldsymbol{\Phi}_{0j} + \mathbf{K}_{g,11} \boldsymbol{\Phi}_{0j} + \mathbf{K}_{g,12} \boldsymbol{\Phi}_{rj} = \mathbf{0}, \tag{5.11a}$$

$$\mathbf{K}_{g,21} \boldsymbol{\Phi}_{0j} + \mathbf{K}_{g,22} \boldsymbol{\Phi}_{rj} = \mathbf{0}. \tag{5.11b}$$

The second equation can be rearranged as

$$\boldsymbol{\Phi}_{rj} = \mathbf{K}_{g,22}^{-1} \mathbf{K}_{g,21} \boldsymbol{\Phi}_{0j}, \tag{5.12}$$

substitution into the first equation gives

$$-\omega_j^2 \mathbf{M}_{g,11} \boldsymbol{\Phi}_{0j} + (\mathbf{K}_{g,11} - \mathbf{K}_{g,12} \mathbf{K}_{g,22}^{-1} \mathbf{K}_{g,21}) \boldsymbol{\Phi}_{0j} = \mathbf{0}, \tag{5.13}$$

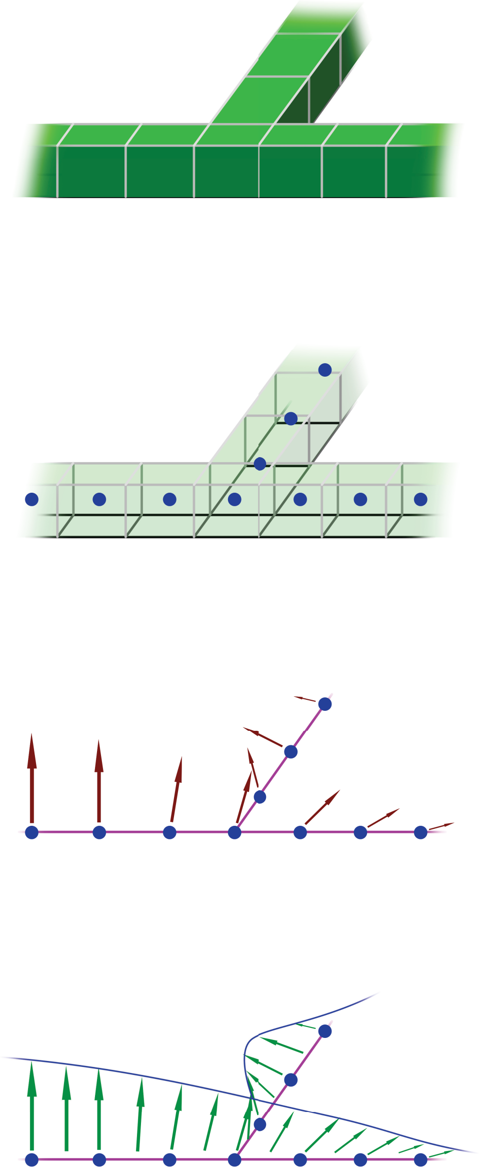

**Step I** A 3D FE model of the structure is provided.

**Step II** A set of nodes are selected as analysis degrees of freedoms.

**Step III** Discrete natural modes in displacements and rotations are obtained on the analysis dofs, load paths are also defined between nodes.

**Step IV** Continuous intrinsic modes are interpolated from displacement and rotation modes.

Figure 7: The process of obtaining intrinsic modes from a 3D FE model showing each step of the method.

which is identical to (5.9). Thus the values of the mode shapes on the corresponding degrees of freedom (i.e. those on the $N_a$ analysis nodes), as well as eigenvalues of the two systems must be identical.

We then prescribe the load paths between the analysis nodes and regard these interconnections as a set of beams that would provide the system with stiffness instead of the original FE structure, as in Step III in Figure 7. This thus defines an equivalent problem in which a set of point masses with mass described by the lumped masses are linked by a set of massless beams described by the load path, consistent with that described in Section 4.2. Since we regard this beam problem and the FE problem as equivalent, their linear natural modes must also correspond with each other. We thus take the set of natural modes from the FE reduced problem and use it to obtain the linear natural modes in the beam problem in the intrinsic description.

We now define each continuous displacement-rotation mode shape $\boldsymbol{\phi}_{0j}$ as taking the value of the discrete mode shapes from the Guyan reduction $\boldsymbol{\Phi}_{0j}$ at each node, shown in Step III in Figure 7, and their corresponding $\omega_j$ by the relation

$$\boldsymbol{\phi}_{0j}(s_i) = \boldsymbol{\Phi}_{0j,i}, \qquad i = 1, \ldots, N_a. \tag{5.14}$$

Following this, we consider intrinsic natural modes of the beam problem described earlier in this section, $\boldsymbol{\phi}_{1j}(s)$ and $\boldsymbol{\phi}_{2j}(s)$, which are solutions to the intrinsic eigenvalue equation (3.1) with eigenvalues $\omega_j$. Since the linear intrinsic description and the FE description are different formulations of the same (linear) problem, their eigenvalues and eigenvectors must correspond to each other exactly. Based on this argument, we will obtain the intrinsic modes $\boldsymbol{\phi}_{1j}$ and $\boldsymbol{\phi}_{2j}$ using the modes in displacement and rotations $\boldsymbol{\phi}_{0j}$. Here we consider these intrinsic modes to be consistent with the interpolation scheme described in (4.32) and (4.34), i.e. linear velocity and constant load between nodes. To facilitate the discussion we will first define the inverse of the transformation matrix at each point on the undeformed beam from the global inertial frame ($a$-frame) to the local frame (0-frame), $\mathbf{R}^{0a}$, as

$$\mathbf{T}_L = (\mathbf{R}^{0a})^{-1}. \tag{5.15}$$

The matrix $\mathbf{T}_L$ only describes the unloaded geometrical configuration of the beam in space and is not a variable of time. As velocity is the time derivative of displacement, the continuous velocity intrinsic modes will correspond to eigenvectors described in terms of displacement and rotation of the beam problem, which we refer to as $\boldsymbol{\phi}_{0j}(s)$, by the simple relation

$$\boldsymbol{\phi}_{1j}(s) = \omega_j \mathcal{R}(\mathbf{T}_L(s)) \boldsymbol{\phi}_{0j}(s), \tag{5.16}$$

where $\mathcal{R}$ rotates the pair of 3-element vectors in a 6-element variable $\boldsymbol{\phi}_{0j}$ using the same rotation matrix $\mathbf{T}_L$, as previously defined in (3.33). In order for this relation to be consistent with the definition of $\boldsymbol{\phi}_{1j}(s)$ in (3.2), we prescribe the linear displacement/rotation field $\mathbf{x}_0(s,t)$ of the eigenvalue solution to the beam model as harmonic solutions to (5.8) that varies in time with

$$\mathbf{x}_{0j}(s,t) = -\cos(\omega_j t)\boldsymbol{\phi}_{0j}(s) \tag{5.17}$$

and the discrete version as

$$\mathbf{x}_{aj,i}(t) = -\cos(\omega_j t)\boldsymbol{\Phi}_{0j,i}. \tag{5.18}$$

Note here that since the displacement/rotation mode is defined in the global $a$-frame while the local velocity mode is defined in the local $t$-frame, the transformation matrix $\mathbf{T}_L$ from the global to the local reference frame of the particular beam element is thus included in the transformation from the global-frame $\boldsymbol{\phi}_{0j}$ to the local-frame $\boldsymbol{\phi}_{1j}$. By using (5.14) and (5.16) we finally obtain a relation where we can relate the natural modes of the intrinsic beam problem, shown in Step IV in Figure 7, with the natural modes of the reduced FE system.

### 5.2.2 Velocity Modes

As described in the previous section, the linear velocity mode $\boldsymbol{\phi}_{1j}$ will be obtained directly from the linear displacement mode $\boldsymbol{\phi}_{0j}$ using (5.16). As the displacement mode is interpolated linearly between nodes, the velocity mode will also use such interpolation, consistent with (4.32).

The non-zero $\mathbf{M}\boldsymbol{\phi}_{1j}$ is obtained by simply multiplying the nodal lumped mass $\mathbf{M}_{L,i}$ with the nodal values of the velocity mode as

$$\int_{s_i-\delta s}^{s_i+\delta s} \boldsymbol{\psi}_{1j}(s)\,ds = \mathbf{M}_{L,i}\boldsymbol{\phi}_{1j}(s_i), \qquad \delta s \to 0 \tag{5.19}$$

Note that due to the different units between lumped mass and distributed mass, an integral sign is used. As described previously in Section 4.3.1 the value of $\boldsymbol{\psi}_{1j}$ is only non-zero at the node points, the reference frame of $\boldsymbol{\psi}_{1j}(s_i)$ can be the local reference frames of any beam segment connecting to it. This is only used to compute the coupling coefficients $\mathbf{A}_1$ and $\boldsymbol{\Gamma}_1$, the computation would be valid as long as $\boldsymbol{\psi}_{1j,i}$ and $\boldsymbol{\phi}_{1j,i}$ use the same reference frames.

### 5.2.3 Force Modes

We will now proceed to describe how the information from $\boldsymbol{\phi}_{0j}$ is used to construct the intrinsic mode shape in sectional forces $\boldsymbol{\phi}_{2j}$ in the beam problem. Note that we also require knowledge of the corresponding modes in momentum $\boldsymbol{\psi}_{1j}$ and sectional curvature strains $\boldsymbol{\psi}_{2j}$. As described previously, the problem is set up as a set of massless beams connecting lumped masses, the sectional mass $\mathbf{M}$ are collocated and only non-zero at the nodes themselves ($\mathbf{M}_{L,i}$). However the sectional stiffness $\mathbf{C}$ is not well-defined, which arises from the fact that the $\mathbf{K}_a$ matrix can be fully populated as a result of the Guyan reduction process (and is found to be so). The fully populated stiffness matrix $\mathbf{K}_a$ indicates that the force-strain relations are not perfectly local as would have been expected by a beam-type description, implying the localised displacement of one node while keeping all other nodes fixed will generate internal forces across the entire structure (and not just its adjacent elements), or vice versa. In contrast, under the assumptions of localised stress-strain relationships, which the sectional $\mathbf{C}$ matrices describe, a local strain would only generate stresses in its immediate vicinity. The $\mathbf{K}_a$ matrix of a model that uses actual beam elements between nodes will be sparsely populated with the non-zero elements related directly to the connectivity between nodes. In fact, the deviation of the actual $\mathbf{K}_a$ matrix from this expected sparse form of a beam problem (i.e. the magnitude of the entries that should have been zero) would provide a valuable metric on the suitability of using a beam-type description of the structure in question. Due to this problem with the definition of $\mathbf{C}$ matrix, in this work we seek to obtain $\boldsymbol{\psi}_{2j}$, or $\mathbf{C}\boldsymbol{\phi}_{2j}$ directly from $\boldsymbol{\phi}_{0j}$ without explicit knowledge of $\mathbf{C}$.

We compute $\boldsymbol{\psi}_{2j}$ from $\boldsymbol{\phi}_{1j}$ by applying the linearised intrinsic equations. From (3.1b) we can obtain,

$$\omega_j \boldsymbol{\psi}_{2j}(s) = -\boldsymbol{\phi}_{1j}'(s) + \mathbf{E}^\top \boldsymbol{\phi}_{1j}(s), \tag{5.20}$$

where subject to the linear interpolation in $\boldsymbol{\phi}_{1j}$ and piecewise constant $\boldsymbol{\psi}_{2j}$, we can also write in discrete form that for each beam element between two nodes,

$$\boldsymbol{\psi}_{2j,i+\frac{1}{2}} = \omega_j^{-1} \Big( -(\boldsymbol{\phi}_{1j,i+1} - \boldsymbol{\phi}_{1j,i})/(s_{i+1} - s_i) + \mathbf{E}^\top (\boldsymbol{\phi}_{1j,i} + \boldsymbol{\phi}_{1j,i+1})/2 \Big), \tag{5.21}$$

with $\boldsymbol{\psi}_{2j}(s) = \boldsymbol{\psi}_{2j,i+\frac{1}{2}}$ for $s_i < s < s_{i+1}$.

Lastly the sectional force modes $\boldsymbol{\phi}_{2j}$ will also be computed *directly* from $\boldsymbol{\phi}_{0j}$, i.e. there is no need for explicit knowledge of the sectional $\mathbf{C}$ matrix in this method. Similar to $\boldsymbol{\psi}_{2j}$, we can rewrite (3.1a) and obtain

$$\boldsymbol{\phi}_{2j}'(s) + \mathbf{E}\boldsymbol{\phi}_{2j}(s) = \omega_j \mathbf{M}\boldsymbol{\phi}_{1j}(s). \tag{5.22}$$

However for a lumped-mass model, this equation encounters issues with geometry and is difficult to apply, as previously described in Section 4.2. In order to clarify the method used in our approach, we seek an alternative but equivalent description to $\boldsymbol{\phi}_{2j}$. We first note that the term $\mathbf{K}_a\mathbf{x}_a$ in (5.8) describes the elastic forces and moments experienced on each of the $6N_a$ degrees of freedoms on the analysis nodes of the system caused by the distribution of displacements/rotations $x_0$. Thus at each node $i$,

$$\begin{pmatrix} \mathbf{f}_{K,i} \\ \mathbf{m}_{K,i} \end{pmatrix} = (\mathbf{K}_a\mathbf{x}_a)|_i. \tag{5.23}$$

We also note that this elastic force can equally be described by an imbalance of sectional (internal) forces, i.e. there is a one-to-one relation between the distribution of $\mathbf{x}_2$ and the distribution of $\mathbf{f}_K$ and $\mathbf{m}_K$ (thus $\mathbf{x}_a$). In order to obtain the relation, we consider the linear static problem where the structure experiences an internal stress distribution $\mathbf{x}_2$ which arises from the application of $\mathbf{f}_K$ and $\mathbf{m}_K$. We observe that for node $i$ in Figure 8, the relation between the forces described by the $\mathbf{K}_a$ matrix, and internal sectional forces, is

$$\mathbf{f}_{K,i} = \mathbf{T}_L(s_{i+\frac{1}{2}})\mathbf{x}_2(s_{i+\frac{1}{2}})\big|_{123} - \mathbf{T}_L(s_{i-\frac{1}{2}})\mathbf{x}_2(s_{i-\frac{1}{2}})\big|_{123}, \tag{5.24a}$$

$$\begin{aligned} \mathbf{m}_{K,i} = &\mathbf{T}_L(s_{i+\frac{1}{2}})\mathbf{x}_2(s_{i+\frac{1}{2}})\big|_{456} + (\tilde{\mathbf{r}}_{i+\frac{1}{2}} - \tilde{\mathbf{r}}_i)\mathbf{T}_L(s_{i+\frac{1}{2}})\mathbf{x}_2(s_{i+\frac{1}{2}})\big|_{123} \\ &- (\mathbf{T}_L(s_{i-\frac{1}{2}})\mathbf{x}_2(s_{i-\frac{1}{2}})\big|_{456} + (\tilde{\mathbf{r}}_{i-\frac{1}{2}} - \tilde{\mathbf{r}}_i)\mathbf{T}_L(s_{i-\frac{1}{2}})\mathbf{x}_2(s_{i-\frac{1}{2}})\big|_{123}). \end{aligned} \tag{5.24b}$$

Due to the piecewise-constant interpolation of $\mathbf{x}_2$ within each beam element, it is natural to evaluate the value of $\mathbf{x}_2$ at the midpoint of each element, i.e. $s_{i+\frac{1}{2}}$ and $s_{i-\frac{1}{2}}$. The sign in front of each sectional force term is dependent on the direction of increasing $s$, as reversing this direction reverses the definition of sectional force and thus reverses the sign. We finally note that in the eigenvalue problem we have defined via (3.1) and (5.9) that $\mathbf{x}_2 = \cos(\omega_j t)\boldsymbol{\phi}_{2j}$ and $\mathbf{x}_a = -\cos(\omega_j t)\Phi_{0j}$, thus we obtain the relation between

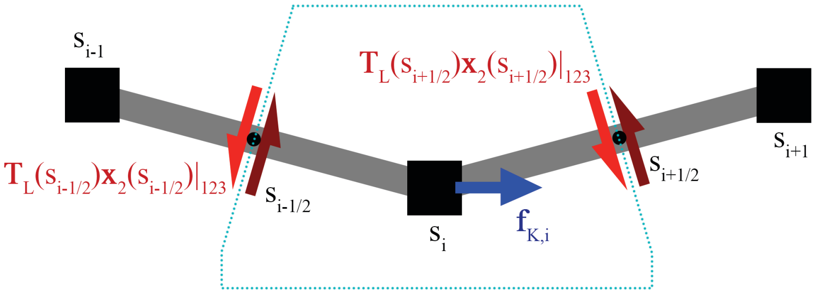

Figure 8: Illustration of the beam internal forces $\mathbf{T}_L\mathbf{x}_2$ (red) and the equivalent nodal applied force $\mathbf{f}_{K,i}$ (blue) at node $i$ for the region outlined by dotted line. The negative sign in one of the internal force terms is due to the definition of the integration direction (in this case equivalent to increasing $i$).

$\boldsymbol{\phi}_{0j}$, obtained from $\boldsymbol{\Phi}_{0j}$ and $\boldsymbol{\phi}_{2j}$ at node $s_i$ as

$$-(\mathbf{K}_a\Phi_0)\big|_{i,123} = \mathbf{T}_L(s_{i+\frac{1}{2}})\boldsymbol{\phi}_{2j}(s_{i+\frac{1}{2}})\big|_{123} - \mathbf{T}_L(s_{i-\frac{1}{2}})\boldsymbol{\phi}_{2j}(s_{i-\frac{1}{2}})\big|_{123}, \tag{5.25a}$$

$$\begin{aligned} -(\mathbf{K}_a\Phi_0)\big|_{i,456} = {} & \mathbf{T}_L(s_{i+\frac{1}{2}})\boldsymbol{\phi}_{2j}(s_{i+\frac{1}{2}})\big|_{456} + (\tilde{\mathbf{r}}_{i+\frac{1}{2}} - \tilde{\mathbf{r}}_i)\mathbf{T}_L(s_{i+\frac{1}{2}})\boldsymbol{\phi}_{2j}(s_{i+\frac{1}{2}})\big|_{123} \\ & - (\mathbf{T}_L(s_{i-\frac{1}{2}})\boldsymbol{\phi}_{2j}(s_{i-\frac{1}{2}})\big|_{456} + (\tilde{\mathbf{r}}_{i-\frac{1}{2}} - \tilde{\mathbf{r}}_i)\mathbf{T}_L(s_{i-\frac{1}{2}})\boldsymbol{\phi}_{2j}(s_{i-\frac{1}{2}})\big|_{123}). \end{aligned} \tag{5.25b}$$

This equation can be easily extended to nodes that contain multiple connectivity between beam elements. The equation can be inverted to obtain $\boldsymbol{\phi}_{2j}$ from a knowledge of $\boldsymbol{\Phi}_{0j}$ and $\omega_j$, by starting from any end point on the beam assembly and computing $\boldsymbol{\phi}_{2j}$ at each subsequent beam segment from the value of $\boldsymbol{\phi}_{2j}$ at the previous segment and $\mathbf{K}_a\boldsymbol{\Phi}_0$ at the node. Note that this method is completely equivalent to that described in Section 4.2. For a single beam without any branching structures, the method can be written as

$$\boldsymbol{\phi}_{2j}(s_{i+\frac{1}{2}}) = \left( \begin{array}{c} \sum\limits_{k>i} (\mathbf{K}_a\boldsymbol{\Phi}_0)|_{k,123} \\ \sum\limits_{k>i} \Big( (\mathbf{K}_a\boldsymbol{\Phi}_0)|_{k,456} + (\tilde{\mathbf{r}}_k - \tilde{\mathbf{r}}_{i+\frac{1}{2}})(\mathbf{K}_a\boldsymbol{\Phi}_0)|_{k,123} \Big) \end{array} \right). \tag{5.26}$$

From this complete knowledge of $\boldsymbol{\phi}_1$, $\boldsymbol{\phi}_2$, $\boldsymbol{\psi}_1$ and $\boldsymbol{\psi}_2$, we can compute the coefficients $\mathbf{A}$ and $\boldsymbol{\Gamma}$ in the nonlinear modal form of the structural equations, as well as the

**H** coefficients for any aerodynamic forces with the necessary aerodynamic definitions, according to the method described in Section 4.3.1. Thus this method allows as to arrive at a complete modal description of the aeroelastic system by using data from the static condensation on a full 3D FE model to generate the structural model.

To summarise, the condensation method described in this work is carried out as follows,

**Step I**, the starting point is a 3D FE model of the structure with the requirement that inertia is lumped onto a set of analysis nodes along load paths.

**Step II**, we carry out the Guyan reduction on the 3D model, arriving at the reduced mass and stiffness matrices describing the linear dynamics of the discrete reduced degrees of freedoms in displacement and rotations $\mathbf{x}_a$ and a linear system described by (5.8).

**Step III**, the natural modes described in discrete global displacements and rotations of the analysis nodes $\mathbf{\Phi}_{0j}$ are obtained from the mass and stiffness matrices.

**Step IV**, we obtain the equivalent, continuous intrinsic modes $\boldsymbol{\phi}_1$, $\boldsymbol{\phi}_2$, $\boldsymbol{\psi}_1$ and $\boldsymbol{\psi}_2$ from the discrete natural modes $\mathbf{\Phi}_{0j}$.

**Step V**, the nonlinear intrinsic modal system (3.23) is obtained by computing the coupling coefficients from the continuous intrinsic modes.

Thus, we have developed a method of arriving at a geometrically nonlinear, modal description of a slender structure from a linear 3D FE model of the structure. Chapter 6 will demonstrate the application of this method to an actual FE model.

# 6 Numerical Results of Structural Model

In this chapter, the implementation of the structural solution method of the proposed simulation framework will be verified against established test cases. The chapter will also demonstrate some numerical aspects of the modal intrinsic formulation in Sections 6.3 and 6.4. First, large, geometrically nonlinear static response of a cantilever beam under external load will be compared against published results. Then the static condensation procedure described in Section 5.2 will be used to create a modal intrinsic system of a cantilever beam modelled in FE using shell elements, which will subsequently be used to validate its dynamic response. Subsequently, a free-flying beam undergoing large rotations as well as elastic deformations will be used to demonstrate various aspects of convergence and momentum conservation of the intrinsic modal formulation. Lastly a similar test will be applied to another model obtained via the condensation process. Combined, all these test cases will provide confidence in the proposed method and its implementation, and also a good understanding of the numerical issues.

## 6.1 Static Deformation of an Initially Curved Beam

This section described a static test case to test the geometrically nonlinear static solution of the structural solver. The test case, initially described by Geradin and Cardona [1], as well as Simo *et al.* [2], specifies a cantilever beam with a constant initial curvature in the unloaded configuration so that the reference axis spans a 45° arc of a circle with radius of 100m in the (horizontal) $xy$-plane. The beam has a constant cross-section of $1 \times 1$ m, a Young's modulus of $10^7$ Pa and negligible Poisson's ratio. A follower force (one that rotates with the local frame of reference) is applied to the tip of the beam in the $z$-axis up to 3000 N and the equilibrium tip displacement is then tracked.

In the current model, the cantilever beam is discretised into 100 elements and the full set of natural modes is used to compute the static equilibrium. Owing to the large deflections involved, the load is applied in increments as specified in Section 4.4 to facilitate convergence. The initial shape of the beam, as well as the resulting deflections under the follower tip load can be seen in Figure 9. A comparison of the results with Simo's as well as those by Palacios *et al.* [43] is shown in Figure 10. The results match closely with published data. It is difficult to comment on the exact source of the difference with Simo *et al.*, however the current results agree very well with those by Palacios *et al.*, which was computed using both displacement-based and intrinsic descriptions and therefore the discrepancy might be due to a coarse discretisation arising from the limited computation power available at Simo's time (1986).

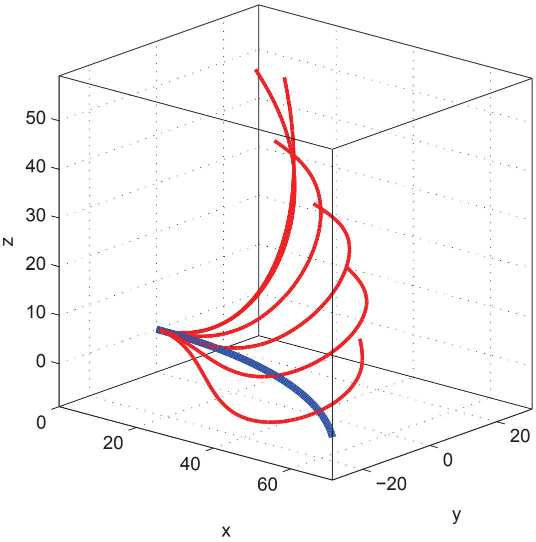

Figure 9: The initial shape of the curved beam (thick blue) and the deflection under follower tip loads in 500 N increments, up to 3000 N.

## 6.2 Static Condensation and Dynamic Response of Cantilever Beam

In this section, we consider a simple prismatic thin-walled cantilever structure with constant dimensionless properties ($E = 10^6$, $\nu = 0.3$, $\rho_m = 1$) and a rectangular cross section. The box beam has length $L = 20$, width $w = 1$, height $h = 0.1$, and walls of thickness $t = 0.01$. MSC NASTRAN (v2012.1.0) is then used to build 3D FE models using 4-noded shell elements. The model has 1600 shell elements, which are reduced to 40 condensation nodes along the centre line. These nodes are free to move in all six degrees freedom.

This problem is also well approximated as a constant-section Euler-Bernoulli beam. In this case, the sectional mass and compliance matrices are

$$\mathbf{M} = \operatorname{diag}\left\{\rho_m A, \rho_m A, \rho_m A, \rho_m I_1, 0, 0\right\}, \tag{6.1}$$

and

$$\mathbf{C}^{-1} = \operatorname{diag}\left\{EA, \infty, \infty, GJ, EI_2, EI_3\right\}, \tag{6.2}$$

where we have used the usual definitions for the stiffness and inertia constants.

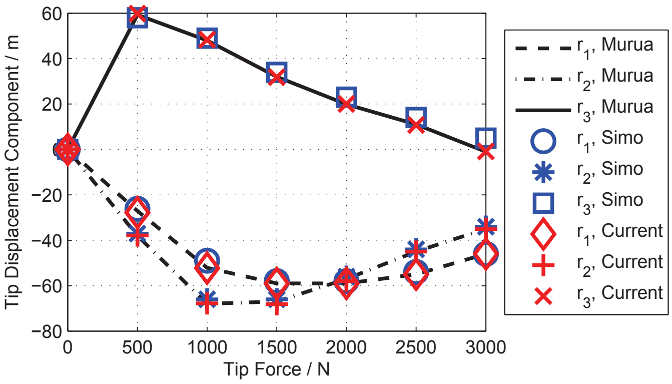

Figure 10: Tip displacements in three axes for the initially curved beam under various tip follower loads and compared against Ref. [1, 2].

### 6.2.1 Comparison of natural frequencies and mode shapes.

The LNMs in intrinsic variables can in this case be solved analytically as in [9]. We can therefore compare the LNMs obtained from the condensation process with the analytical ones. This will serve to verify details of implementation, but also to highlight some characteristics, and advantages, of the condensation approach. Table 1 shows the lowest natural frequencies of the different types of natural modes.

The comparison showed that the bending and axial modes agree very well between the condensation method and the theoretical value from using sectional properties. A lack of warping restraint (4-th order effect not captured by the intrinsic beam theory, as reviewed in Section 1.2.1) near the ends of the beam contributed to the small differences between theoretical and computed frequencies on the torsional modes. It is important to emphasise that the constant-section beam solution is included here only as a reference: The nonlinear model obtained by the condensation method is calculated in terms of mode shapes and frequencies directly obtained from the 3D FE. As a result, the present method, being based on an actual built-up geometrically-accurate model of the structure, naturally includes end effects due to kinematic restrictions along the longitudinal dimension.

### 6.2.2 Geometrically-nonlinear beam dynamics

We subsequently investigate the dynamic response of the modal intrinsic system computed using the method described in Chapter 5, using modes obtained in the previous section. The cantilever is given an initial velocity distribution with the form of

| Mode type | $N_{\text{condensed}}$ | $\omega_{\text{beam}}$ | $\omega_{\text{condensed}}$ |
|---|---|---|---|
| 1st $x$-$z$ bending | 1 | 0.426 | 0.427 |
| 2nd $x$-$z$ bending | 2 | 2.67 | 2.65 |
| 3rd $x$-$z$ bending | 4 | 7.47 | 7.34 |
| 1st $x$-$y$ bending | 3 | 2.76 | 2.75 |
| 2nd $x$-$y$ bending | 7 | 17.29 | 17.05 |
| 3rd $x$-$y$ bending | 13 | 48.41 | 48.48 |
| 1st torsion | 5 | 13.95 | 13.90 |
| 2nd torsion | 10 | 41.83 | 39.13 |
| 1st axial | 98 | 78.54 | 78.60 |
| 2nd axial | 134 | 235.62 | 235.55 |

Table 1: Selected natural angular frequencies from static condensation of the 3-D FEM and 1-D analytical solution.

$\mathbf{x}_1(s,0) = \mathbf{x}_{1,0}\,(s/L)^2$, where $\mathbf{x}_{1,0} = \begin{bmatrix} 0 & 2 & 2 & 0 & 0 & 0 \end{bmatrix}^\top$, i.e. a parabolic velocity distribution in both transverse directions. The RK4 integration has automatic timestep control with relative error bound of $10^{-3}$ and absolute error bound of $10^{-6}$, as will also be the case in all problems presented in this work.

The resulting response is large enough (tip displacement of 25% total beam length) to observe geometrically-nonlinear effects on the system. Figure 11 compares the displacement at the centroid of the free end obtained from condensation with 50 LNMs with those obtained from 1) the constant-section intrinsic beam equations, 2) constant-section beam models in Abaqus, and 3) full 3D FE in Abaqus. The constant section intrinsic modal solution uses also 50 modes on a 200-node beam with the same time marching settings. The Abaqus constant section finite-element beam solution is a converged geometrically-nonlinear solution (2000 B31 Abaqus elements and time step $\Delta t = 0.01$), whereas the Abaqus finite-element 3D solution uses 4500 S4 shell elements with a time step $\Delta t = 0.02$ and geometrically-nonlinear deformations. On the full 3D FE model, massless cross-sectional reinforcements are added to prevent wrinkling that would appear at large deflections due to the warping of the thin shell. Such skin warping is not captured by the linear sectional compliance matrix and leads to significant differences with that predicted by the beam theory. Very good agreement can be observed between both constant section beam models, which verify our implementation of the nonlinear intrinsic beam solver. Equally, the nonlinear solution on the full 3D FEM and that based on the static condensation also agree with each other. The difference between the two

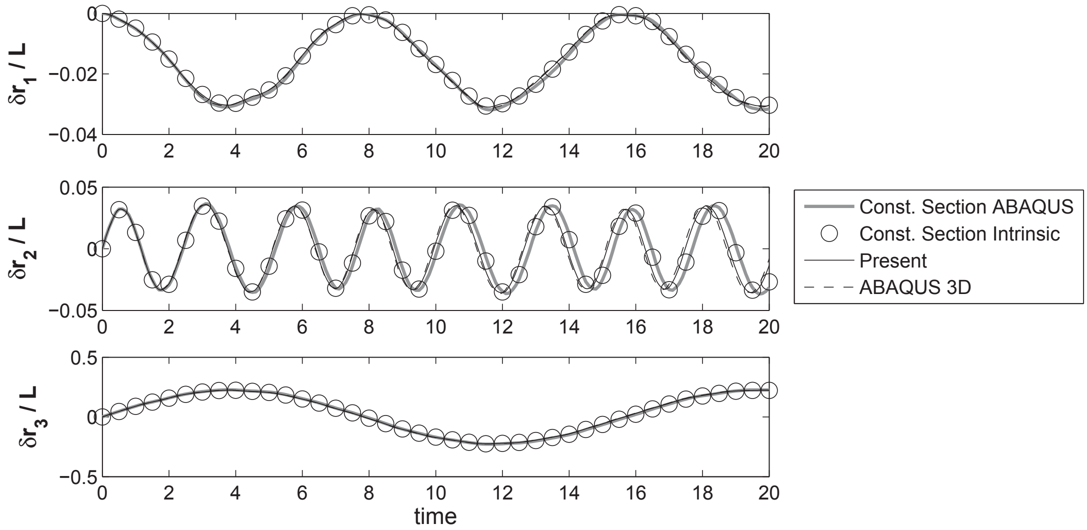

Figure 11: Components of the displacements (in the global frame) at $s = L$ for an initial parabolic excitation.

sets of results can be seen in the $\delta r_2$ response and the results show the improvement obtained when deriving the beam equations directly from the 3D model, which are mostly due to the poor approximation to the torsional modes in the constant-section models.

Table 2 shows the norm of the displacement vector error of tip displacement as a fraction of the maximum tip displacement between the full 3D model and the present method with 50 modes for different amplitudes of initial velocity with amplitude of $\mathbf{x}_{1,0} = \begin{bmatrix} 0 & \lambda & \lambda & 0 & 0 & 0 \end{bmatrix}$. The error shows that as the maximum tip displacement $\delta r_{3,max}$ increases, the normalised error eventually increases due to the increasing effects of section warping not captured in the condensation model. It should be also noted that the error arises mostly from a difference in frequency of the response while amplitude is very well captured, as can be seen in Figure 11.

### 6.3 Dynamic Response of a Free-Flying Beam

A flexible, free-flying beam (FFB) testcase is used to test convergence the accuracy of momentum conservation using the intrinsic modal formulation. This case was previously used in works by Simo *et al.* [2], Hsiao *et al.* [4] and Hesse *et al.* [3], and consists of a initially still beam with properties listed in Figure 12 and Table 6.3 subjected to time-

| $\lambda$ | $p_{z,max}$ | $\epsilon_{RMS}/p_{z,max}$ |
|---|---|---|
| 0.002 | 0.004216 | 0.0306 |
| 0.2 | 0.4221 | 0.0303 |
| 1 | 2.1622 | 0.0242 |
| 2 | 4.5644 | 0.0131 |
| 3 | 7.2270 | 0.0105 |
| 4 | 10.0135 | 0.0205 |
| 5 | 12.4721 | 0.0410 |

Table 2: RMS error between 3D FEM and present method of the vertical displacement $p_z$ (in the global frame) at $x = L$, for $\mathbf{x}_{10} = (0; \lambda; \lambda; 0; 0; 0)$, normalised using maximum tip displacement.

varying dead (fixed w.r.t. global reference frame, as opposed to follower force that rotates with the local frame) forces and moments. As the position of the centre-of-mass of the free-flying structure can be computed by rigid body analysis analytically, it offers a good test to assess the conservation of total momentum of the structure.

| | | |
|---|---|---|
| extensional stiffness | $EA$ | $10^4$ |
| shear stiffness | $GA_s$ | $10^4$ |
| bending stiffness | $EI_y$, $EI_z$ | 500 |
| torsion stiffness | $GJ$ | 500 |
| mass density | $\rho_m A$ | 1 |
| axial moment of inertia | $\rho_m J_x$ | 20 |
| transverse moment of inertia | $\rho_m J_y$, $\rho_m J_z$ | 10 |

Table 3: Dimensionless properties of the isotropic free-flying beam testcase. [3].

First, 1-D beam models of the structure are constructed using $N_a$ =5, 10, 15, 20, 25, 30, 50 and 80 nodes with masses lumped at the nodes. A reduction is then performed on the structures in the same way as one would on a 3-D model, following the methods outlined in Section 5. The node at the midpoint of the beam, or the one closest to the midpoint, is used as the sole tracking node between timesteps. Using these models, full-mode simulations are performed in order to verify convergence, with the corresponding number of elastic modes $N_M = 6(N_a - 1)$ from each of the spatial discretisations. The test case uses the load profile provided in Figure 13 with the applied dead loads in Figure 12 being $F_x = 20f$, $M_y = 200f$ and $M_z = 100f$ fixed in the global frame.

It was found in practice that the relative and absolute error bound settings of the

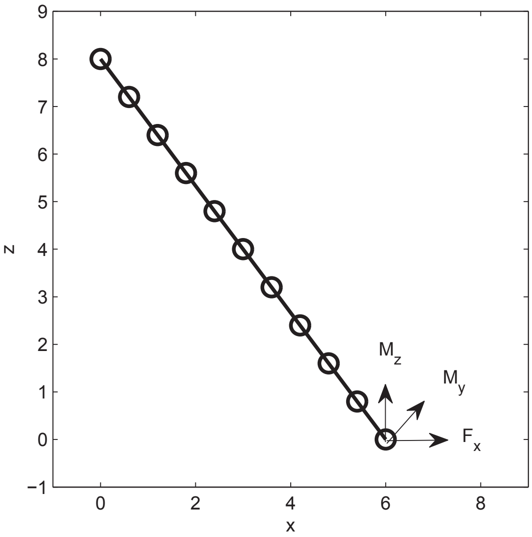

Figure 12: Initial configuration of the free-flying beam, shown with 10 elements. The applied forces and moments are also indicated. Reproduced from [3].

RK4 integration ($10^{-3}$ and $10^{-6}$ respectively) are high enough to ensure that the nodal rotation matrices remain orthonormal to the necessary degree of accuracy (a typical error of $10^{-6}$ over a timescale typical of the lowest-frequency dynamics of the system), and that the total system energy conservation on the structural system is also observed (an error of less than $10^{-6}$ over a timescale typical of the lowest-frequency dynamics of the system) even though the integration scheme does not implicitly guarantee the accuracy of either quantities.

The numerical simulation results showed good convergence of centre-of-mass (c.m.) location $\mathbf{u}_{CM}$ with element count as can be seen in the plot of error in c.m. location in Figure 14, with the error scaling quadratically with element size (shown as the slope on the log-log plot) as expected with discretisation errors. As the time-step size is automatically controlled by error estimates in the RK4 numerical scheme, the errors seen here are due to spatial discretisation errors and are expected to converge quadratically with element size. In this test case such errors arise due to the linear velocity and piecewise-constant stress interpolations used in the model. This interpolation is no longer accurate when there is significant bending of an individual element that induces geometrically nonlinear couplings. Reducing the element size limits this error and improves accuracy. Finally, the shape of the beam as it moves in space also match very

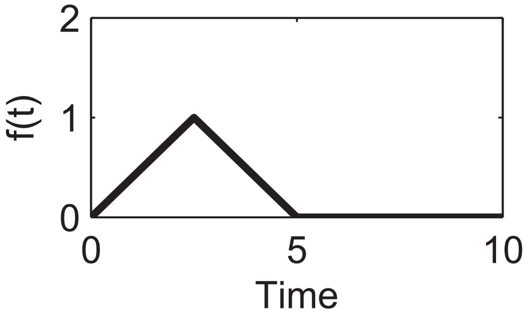

Figure 13: Time-varying load profile $f(t)$ applied as forces and moments on the free-flying beam test case.

well with previously published results and is shown in Figure 15.

In order to test the impact of mode truncation on the accuracy of the global momentum conservation, the 80-element model is truncated from $N_M$ =480 to 300 lowest-frequency elastic modes in $\mathbf{q}_1$ and $\mathbf{q}_2$, then simulated with the same conditions as before, shown in Figure 16. The cut-off frequency in this case is 620 $rad/s$ and corresponds to a reduction of the maximum eigenvalue of the linear system from 1600 to 612.2 $rad/s$, which also allows an almost 3-fold increase in maximum stable timestep. Although this model contained the same number of modes as the 50-segment full model, and even more than that of the lower-fidelity discretisations, the figure showed that the momentum conservation properties of this system are very poor, that is, on par with that of the 5-segment discretisation. However if elastic modes beyond 300 are residualised instead using the method described in Section 4.6.1, their contribution to compatibility between low-frequency modes are retained. The total momentum in this case is again accurate to a high degree while still allowing for a larger timestep to be used as in the truncated model. Additionally we also track the position difference between the two ends of the beam in space as $\mathbf{u}_R = \mathbf{u}_{end} - \mathbf{u}_1$ as a measure of the angular orientation accuracy. Table 6.3 lists the r.m.s. deviation of the c.m. location $\mathbf{r}_{CM}$ and the orientation vector $\mathbf{r}_R$ over a simulation time of 50 s against the $N_M$ = 480 full mode solution which we regard here as converged. Again the residualisation produces far better results than a total truncation of high-frequency dynamics. We have thus determined that the full mode solution and the residualised solution both achieves high simulation accuracy, with the additional benefit that the residualised solution allows the use of a far larger time-step than the full mode solution ($1/\omega_{300}$ as compared to $1/\omega_{480}$) making the improved timestep 2.31× that of the original.

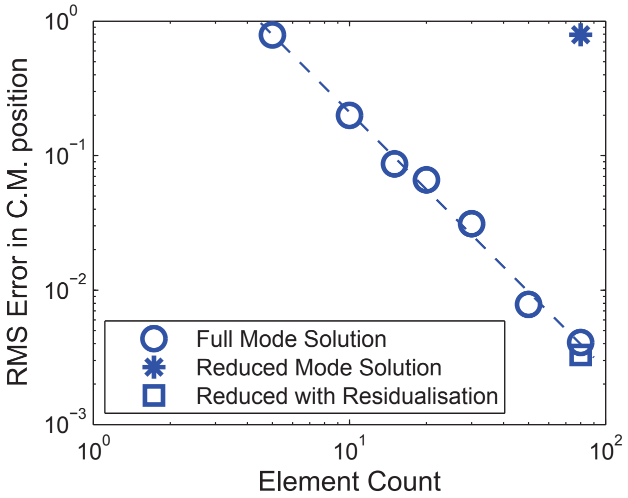

Figure 14: Convergence of time-varying c.m. location (distance to theoretical value) with element count. Also shown are the data for a total truncation from full 480 to 300 lowest-frequency modes, compared with a residualisation of modes 301-480, i.e. removing only their linear dynamics. The truncation introduces significant errors while retaining the quasi-steady coupling through residualisation alleviates the problem.

This example illustrates the importance of retaining full modal information in enforcing momentum conservation on the nonlinear system and correct displacement tracking in the structural model, either by using the full mode system or by residualising the full mode system into a reduced-order system with the residualised modes serving as correction terms. In contrast, truncating higher-order modes could bring significant errors. This effect is made apparent by the large geometrical nonlinearities present in this test case. It should be noted that HALE aircraft are not designed to undergo such degrees of rotations as demonstrated in this example and the appropriate level of truncation could be determined by a convergence study.

### 6.4 Static Condensation and Dynamic Response of a U-shaped Beam

This test case is a U-shaped beam that was originally defined by Hesse [5]. It consists of a free-flying U-shaped beam assembly with solid rectangular cross-sections subject to external loads. The shape of the structure is shown in Figure 17(a) with isotropic sectional properties listed in Table 5. The applied forces and moments in Figure 17(a) are $F_z = 1000f$, $F_y = 100f$, $F_{y2} = 250f$ and $M_y = 100L_x f$, where the load profile $f(t)$ is shown in Figure 17(b). All applied forces are dead loads while the applied moments are

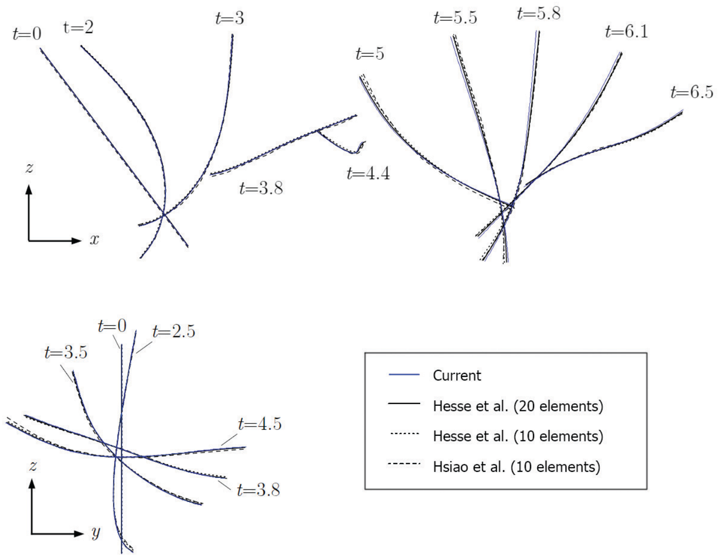

Figure 15: A comparison of the dynamic response of the current model using 80 elements and full modes ($N_M = 480$), compared to that by Hsiao *et al.* [4] and Hesse *et al.*. [3].

| rms difference at $t$ =50 in | $\lvert\mathbf{u}_{CM}\rvert$ | $\lvert\mathbf{u}_R\rvert$ |
|---|---|---|
| truncated to 300 modes | 0.7878 | 0.2498 |
| full modes, residualised beyond 300 | 0.0008456 | 0.0012 |

Table 4: A comparison of residualisation against truncation on a system with $N_M = 480$ (i.e. 480 modes in $\mathbf{q}_2$ and 486 modes in $\mathbf{q}_1$), compared against a full-mode simulation using $N_M = 480$. The truncated system truncates $\mathbf{q}_1$ and $\mathbf{q}_2$ both to 300 lowest frequency modes, similarly for the residualised system where modes beyond 300 are residualised.

follower loads that move with the local reference frame. As the position of the centre-of-mass of the free-flying structure under the influence of dead loads can be computed analytically, it offers a good test to assess the convergence requirements to preserve total momentum in the structure.

A finite-element model is constructed using a commercial FE analysis package (MSC NASTRAN v2012.1.0), shown in Figure 18(a). This model contains 4752 3D solid elements and 1-5 lumped mass condensation nodes per 5-metre span (i.e. models with total model sizes of 7, 13, 19, 25 and 31 lumped mass nodes respectively). Lumped mass elements are connected to the massless structure using NASTRAN's RBE3 interpolation elements, so that the spatial location of the lumped mass nodes are expressed as a linear

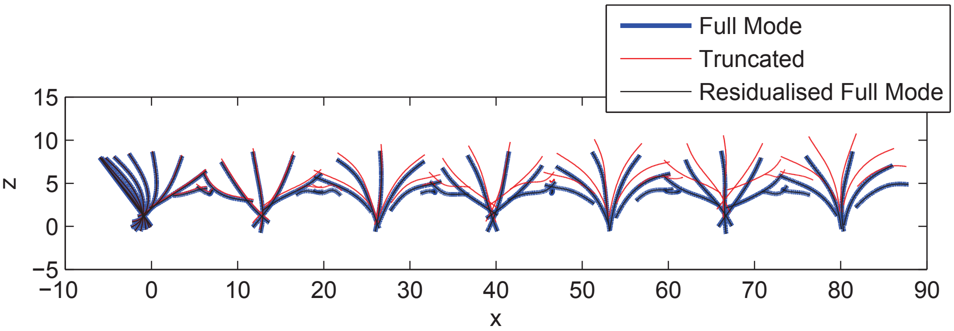

Figure 16: A comparison of the spatial shape of the free-flying beam test case simulated using $N_M = 480$ full mode system, $N_M = 300$ truncated system and $N_M = 480$, $N_C = 300$ residualised system. The full and residualised system are almost indistinguishable.

combination of the closest nodes on the structure. Static condensation is then used to reduce the stiffness matrix to the degrees of freedom associated with the lumped mass nodes. For comparison, beam models using equivalent 1-D sectional property definitions (Table 5) were constructed with the same number of nodes and the modal system is obtained in the same way as in the condensed model.

Figure 19 shows the non-zero entries in the stiffness matrices of the beam model and the condensed model. It can be seen from the Figure that the stiffness matrix obtained from the condensation of the 3D FE model in the 31-node case is fully populated with significant non-zero entries far from the diagonal, whereas that from a beam model is

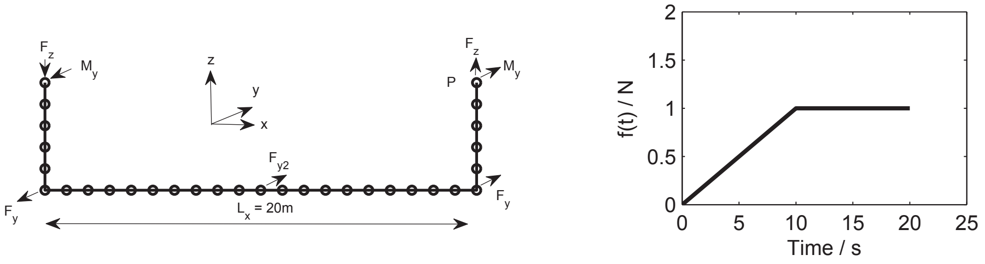

(a) Initial configuration of the structure shown with 31 nodes. Applied forces and moments are also indicated.

(b) Time-varying load profile $f(t)$ applied as forces and moments on the structure.

Figure 17: Three-bar structure and applied loads (after Hesse *et al.* [5]).

| | |
|---|---|
| Cross Section | $0.1 \times 0.05$ m rectangular |
| $E$ | 70 GPa |
| $\nu$ | 0.3 |
| $\rho$ | 2700 kg/m$^3$ |
| $EA$ | 3.5e8 N |
| $GJ$ | 140224.3 Nm$^2$ |
| $EI_2$ | 291666.7 Nm$^2$ |
| $EI_3$ | 72916.7 Nm$^2$ |
| $\rho A$ | 13.5 kg/m |
| $\rho_m I_1$ | 0.0140625 kg·m |
| $\rho_m I_2$ | 0.01125 kg·m |
| $\rho_m I_3$ | 0.0028125 kg·m |

Table 5: Table of properties and equivalent sectional properties of the isotropic free-flying structure [5].

banded with a very small bandwidth. The maximum magnitude of entries in the fully populated stiffness matrix that are zero in the beam-based stiffness matrix is about 1% of the magnitude of entries within the banded matrix. Figure 20 shows the difference between the lowest 40 structural eigenvalues of the condensed model and the beam-element model for the 31-node problem.

The numerical results show that the r.m.s. difference of c.m. location vector with theory for models both built from prescribed beam elements and constructed using the condensation method (simulated with full modal basis). The error scales, in this case, quadratically with element size (shown as the slope on the log-log plot in Figure 21). Thus the application of condensation in creating the nonlinear modal system can achieve a similar level of conservation to the beam-element model. In this test case these are mainly discretisation errors that arise due to the linear velocity and piecewise-constant stress interpolations used in the model.

The effect of truncation and residualisation on the accuracy of the simulation is also studied with momentum conservation. Here the 31-node full-order model (total structural mode number $N_M = 180$) is either truncated to $N_C$ lowest-frequency modes by removing the remaining modes from the system, or residualised to $N_C$ lowest-frequency modes by only removing the linear dynamics of the remaining modes. Their effect on the accuracy of system momentum conservation is shown in Figure 22(a). The maximum stable timesteps for the truncated and residualised system relative to the full-order system are the same and is shown in Figure 22(b). It can be seen that residualisation provides significantly better results compared to truncation for any given $N_C$, while

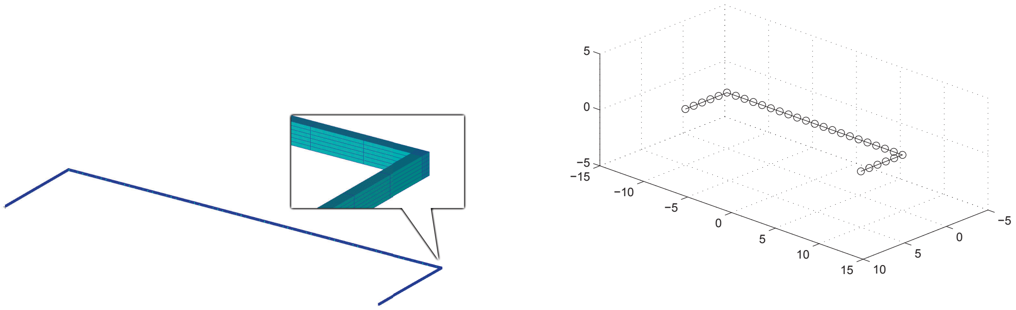

(a) The 4752-element FE model constructed according to the material definitions in Table 5.

(b) The 31 analysis nodes in Figure 18(a) with the interconnecting load path also shown.

Figure 18: The 3D solid-element and corresponding 1D model of the U-shaped beam.

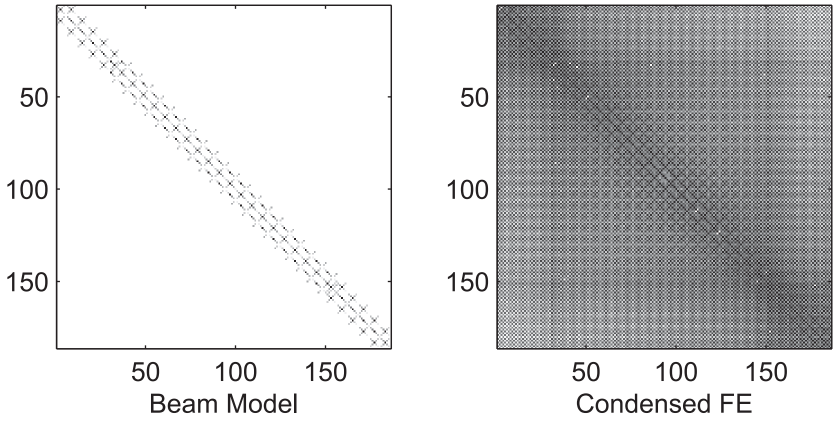

Figure 19: A comparison of sparsity of stiffness matrix $\mathbf{K}_a$ computed from beam elements and a Guyan reduction on 3-D FE model. Both models contain 31 nodes. Dark dots indicate a non-zero entry where shading implies higher magnitude.

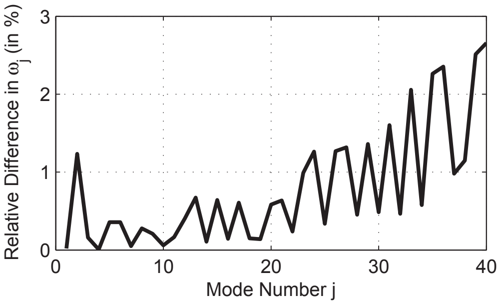

Figure 20: Relative difference in the lowest structural eigenvalues between the condensed system and the beam-element solution for the 31-node model.

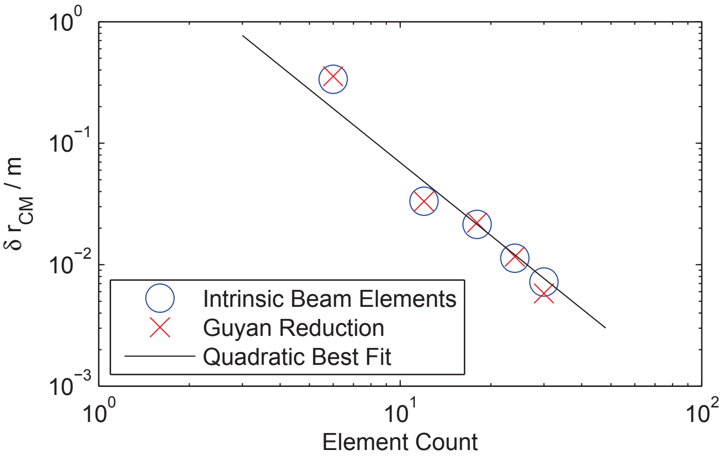

Figure 21: Error in c.m. location between computed and analytical results over a simulation period of 20 $s$. Both the condensed model and the beam-element model are shown. The line for cubic error reduction with element number is also indicated.

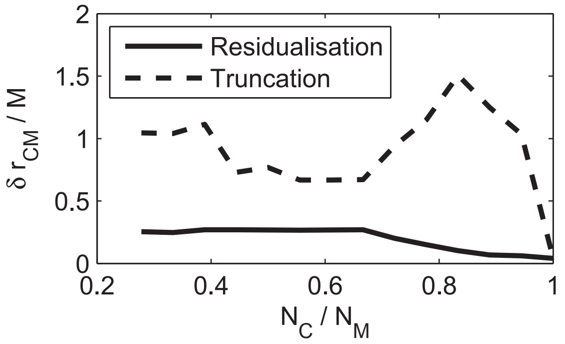

(a) Effect of truncation and residualisation on the accuracy of c.m. location over a simulation period of 20 $s$.

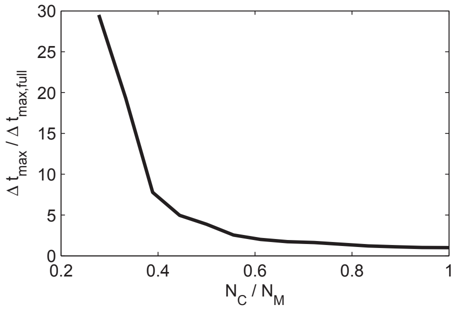

(b) The maximum stable timestep $\Delta t_{max}$ for the truncated / residualised system, relative to the full-order system.

Figure 22: Effects of truncation and residualisation.

allowing for the same increase in maximum permissible timestep $\Delta t_{max}$ as truncation, an increase that can be very significant.

Snapshots of the shapes of the deformed beam during the first 15 seconds of time-marching simulation using the condensed and beam element approach, both with 31 nodes, are shown in Figure 23. Although the two models are arrived by completely different processes, their responses are still very similar. As can be seen in Figure 20, the difference in the lowest structural eigenvalues between the condensed model and the beam-element model for the 31-node problem is small. For longer time integrations the small differences between models (as seen in the eigenvalues in Figure 20) accumulate to give slowly diverging trajectories. Figure 24 plots the response of the 31-node, statically condensed model together with data from a converged solution using beam elements from SAMCEF Mecano (from [5]), the comparison demonstrates that the response is captured

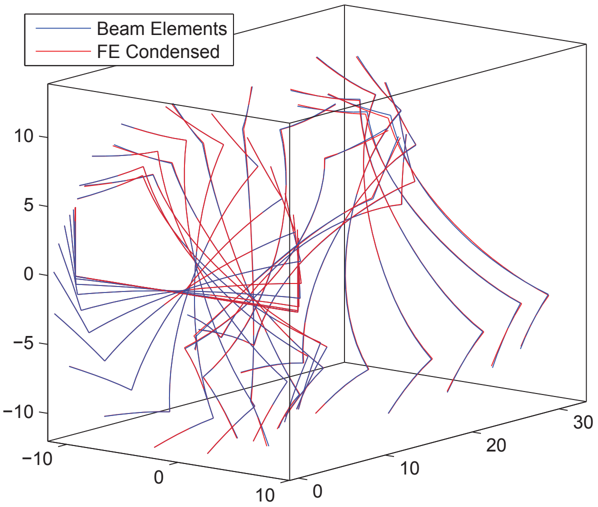

Figure 23: Dynamic response of the structure in the first 15 seconds when subjected to the prescribed forces and moments shown in Figure 17(a). This figure shows the difference between that of a system computed from 1-D beam property definitions and that of a model from a static condensation of 3-D FE buildup.

to a good degree of accuracy by the condensation technique. The difference between them arises due to the differences present in the linear normal modes between the methods, in particular the capturing of end effects by the reduction method, which is then amplified by the large, geometrically nonlinear motions that the structure underwent.

To summarise, the numerical cases in this chapter demonstrated the capabilities of an intrinsic modal formulation of beams. Static and dynamic results were verified against literature and the momentum conservation properties of the modal formulation have been investigated. The next chapter will couple the structural model with aerodynamic interactions and demonstrate static and dynamic aeroelastic analysis of wings and full airframes.

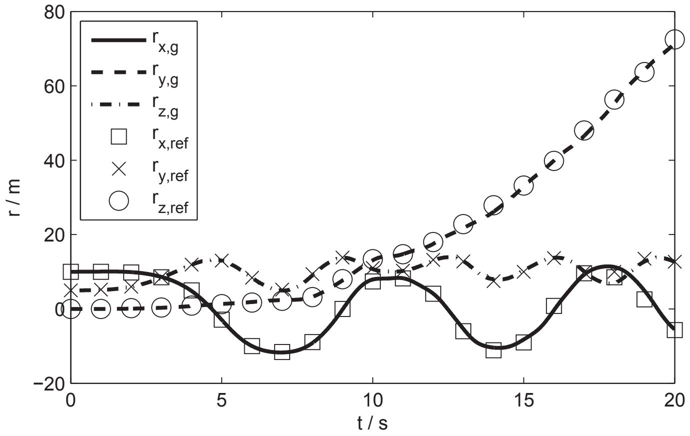

Figure 24: Comparison of the response in Figure 23 for the spatial location of point P in Figure 17(a) for the reduced model from static condensation ($\mathbf{r}_g$) and converged solution from SAMCEF Mecano ($\mathbf{r}_{ref}$).

# 7 Numerical Results of Aeroservoelastic Model

In this section, the fully coupled dynamic aeroelastic implementation of the framework will be demonstrated. A linear test case concerning flutter on a cantilever wing will be investigated first and compared to published data to verify the implementation of the unsteady aerodynamic model. Subsequently a model of a full aircraft with a flexible, flying wing configuration similar to that of AeroVironment's Helios will be constructed. Trim and dynamic stability analysis will be performed on the uncontrolled (open-loop) configuration under a number of payloads, then an $\mathcal{H}_\infty$ control design with the objective being dynamic stabilisation will also be demonstrated on the system, followed by a closed-loop simulation of the flight dynamics of the aircraft.

## 7.1 Linear Stability Analysis of the Goland Cantilever Wing

In this section, the Goland wing model [142] is used to validate the coupling between structural and aerodynamic forces in the model. The Goland wing is a low aspect ratio wing in a cantilever configuration and is a well-studied benchmark numerical test case for aeroelastic simulations, in which the structural model is based on beam elements. Properties of the beam can be found in Table 6.

| | | | |
|---|---|---|---|
| Chord, $2b$ | 1.8288m | Mass per unit length, $\rho_m A$ | 35.71kg/m |
| Semi-span, $L$ | 6.096m | Moment of inertia around e.a., $\rho_m I_1$ | 8.64 kg·m |
| Elastic axis (from l.e.) | $0.66b$ | Torsional stiffness, $GJ$ | $0.99\times10^6$N·$m^2$ |
| C.G. (from l.e.) | $0.86b$ | Bending stiffness, $EI_2$ | $9.77\times10^6$N·$m^2$ |

Table 6: Relevant properties of the Goland wing [9]

The airspeed at which flutter occurs on the Goland wing is computed by a linearisation of the dynamics over a range of increasing airspeeds. An unstable eigenvalue in the linearised dynamics indicates that flutter has occurred. The current study uses 11 bending modes and 1 axial mode which produced results (Figure 25, Table 7) that match well with previous studies using 2D aerodynamic approximations, whereas 3D aerodynamic methods such as UVLM more accurately reflect tip effects which have a noticeable impact on the computed flutter speed [9].

Time-domain simulation showed that structural nonlinearities do not give rise to any limit-cycle oscillations on the Goland wing at post-flutter speeds. Patil et al [96] also confirmed that structural nonlinearities in themselves are unable to create limit-cycle oscillations post-flutter. Instead they observed that in general stall and other nonlinear aerodynamic effects will set in well before significant structural nonlinearity is observed.

| Author | Model | $V_f$, $ms^{-1}$ | $\omega_f$, $rad\,s^{-1}$ |
|---|---|---|---|
| Current | Intrinsic / 2D aero (Modal) | 139 | 70.0 |
| Palacios et al [9] | Intrinsic / 2D aero (Modal) | 141 | 69.8 |
| Sotoudeh et al [143] | Intrinsic / 2D aero (FD) | 137 | 70.1 |
| Wang et al [29] | Intrinsic / UVLM | 164 | - |
| Murua et al [25] | Displacement / UVLM | 165 | 69 |

Table 7: Flutter velocity and frequency for the Goland wing at $\rho_\infty = 1.02\,kg\,m^{-3}$

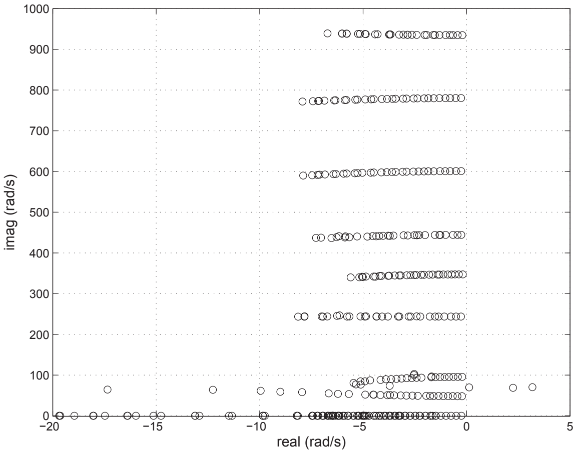

Figure 25: Pole plot of the linearised aeroelastic system of the Goland wing with 11 bending modes, 1 axial mode and 24 aerodynamic modes used, $V_\infty$ varied from 0 to $150ms^{-1}$.

## 7.2 Trim and Stability of High Aspect Ratio Flying Wing

### 7.2.1 Test case description

For the remainder of this chapter, we consider the 72m-span high-aspect-ratio flying wing model originally created by Patil et al. [8] and subsequently used by Su et al. [7] and Dillsaver et al. [6] , shown in Figure 26. Its properties are shown in Table 8. The airframe has a flat, straight midsection and an outer section with 10° dihedral. Three vertical fins are placed below the midsection and thrust is provided by five propellers mounted forward of the midsection. The payload is placed in the central pod and is variable between 0 (0 %) and 227 kg (100 %).

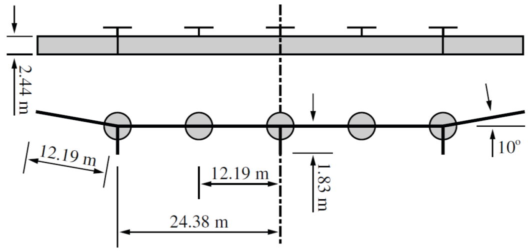

Figure 26: Configuration of the flying wing [6]. Properties are listed in Table 8.

| | |
|---|---|
| Elastic/reference axis | 25% chord |
| Aerodynamic centre | 25% chord |
| Centre of gravity | 25% chord |
| $GJ$ | $1.65 \times 10^5$Nm$^2$ |
| $EI_2$ | $1.03 \times 10^6$Nm$^2$ |
| $EI_3$ | $1.24 \times 10^7$Nm$^2$ |
| $m$ | 8.93kg/m |
| $I_{11}$ | 4.15 kg m |
| $I_{22}$ | 0.69 kg m |
| $I_{33}$ | 3.46 kg m |
| Wing $c_{l\alpha}$ | $2\pi$ |
| Wing $c_{l\delta}$ | 1 |
| Wing $c_{d0}$ | 0.01 |
| Wing $c_{m0}$ | 0.025 |
| Wing $c_{m\delta}$ | -0.25 |
| Pod $c_{l\alpha}$ | 5 |
| Pod $c_{d0}$ | 0.02 |
| Pod $c_{m0}$ | 0 |

Table 8: Relevant properties of the flying wing [7].

The structural model of the aircraft is created using a separate in-house finite-element beam code [3], with 40 elements for each side of the central section, 20 elements for the outer section and 1 rigid element each for each of the 3 fins under the wing. Eigenvalue analysis was then performed on the structure, obtaining the structural displacement modes and their corresponding eigenvalues defined on the 124 nodes on the airframe. Guyan reduction from a 3D structure is not needed in this case as the airframe is already defined using beams, however the starting point for our analysis is equally the displacement description of the modes and the masses at the nodes. Those are post-processed using the method as before. The payload is considered part of the model, thus varying the payload requires re-computing the modes, it is worth noting that Moulin *et al.* [144] demonstrated a method in which this is avoided. Applying the method described in Chapter 3 to the modes and frequency information leads to the $\mathbf{A}$, $\mathbf{\Lambda}$ matrices and $\mathbf{\Gamma}$ coefficients. Additional wing section definitions lead to the $\mathbf{H}$ coefficients for aerodynamic influences.

The lowest frequency mode shapes in velocity vector ($\mathbf{\Phi}_1|_{123}$) and the sectional moment vectors ($\mathbf{\Phi}_2|_{456}$) in the corresponding force modes are shown in Figure 27. The angular velocity and sectional force vectors are not shown. Note here that the velocity vector, when plotted in global coordinates, scales directly with displacement vectors. While the definition of force and moment are dependent on the beam direction and the local coordinates of the beam segment.

In this work we are interested in the symmetric response of the airframe and thus define four possible *symmetric* control actions available on this flying wing: a simultaneous flap deflection by a fixed angle on the entire wing (simultaneous flap $\delta$), a simultaneous change in the thrust in each engine pod (simultaneous thrust $F_S$), a differential flap deflection by deflecting the flaps on the outboard section (the section with dihedral) in the other direction from the inboard flaps (symmetric differential flap $\delta_D$), a differential thrust by increasing output from the two outboard pods and reducing output in the central pod (symmetric differential thrust $F_D$). The differential flap and thrust inputs are designed to provide better control on the degree of bending exhibited on the wing. For trimming the airframe however only the simultaneous flap and thrust controls are used with the other two control inputs set to zero. Figure 28 illustrates the flap deflections for symmetric and differential actions.

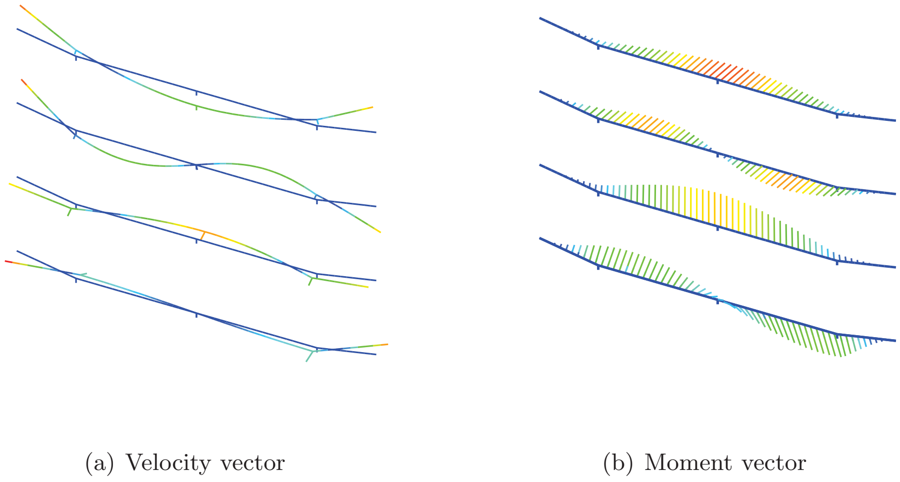

(a) Velocity vector (b) Moment vector

Figure 27: Field plots of local sectional velocity and sectional moment vectors for the first four structural modes of the 0-payload airframe obtained through the condensation. These corresponds to (from above) first symmetric out-of-plane bending, first antisymmetric out-of-plane bending, first symmetric in-plane bending and first antisymmetric in-plane bending.

### 7.2.2 Trim Solution Validation

The vehicle, as prescribed by the original work describing it, is flown at 12.2 m/s at sea level and its trim condition is computed for various central pod payloads and for both rigid airframe and the fully flexible airframe. The rigid case uses six rigid body velocity modes only, whereas the flexible case uses 294 symmetric flexible structural velocity modes together with the six rigid body velocity modes selected based on lowest eigenvalue frequency. It was found that such number of modes is required for convergence of the flexible trim solution. Note that the number of force modes ($\mathbf{q}_2$) needed is equal to the number of flexible velocity modes, whereas the number of aerodynamic modes ($\mathbf{q}_a$) is equal to the total number of velocity modes, multiplied by the total number of aerodynamic lags ($N_{AE}$) used to approximate Wagner's function. As throughout this work $N_{AE} = 2$, the rigid model contains 18 modes in total (6 rigid body velocities and 12 aerodynamic modes associated) and the flexible model contains 1194 structural and aerodynamic modes ($N_M = 294$ velocity and force modes, 6 rigid body and 600 associated aerodynamic modes). Both models contain the same additional $\mathbf{T}$ and $\mathbf{r}$ states used to integrally track displacements and rotations for each node.

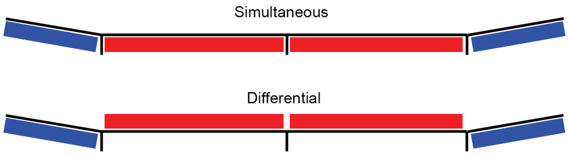

Figure 28: Flap deflections on the flying wing for symmetric and differential actions.

The process of trimming the airframe includes first prescribing an angle of attack $\alpha$ at the centre node of the flying wing, then computing the aerodynamic loads on a starting configuration (zero deformation) under such conditions. These aerodynamic forces are then regarded as constant follower forces applied on the structure, and the correct amount of structural deformation, thrust force, flap deflection and gravity are computed to exactly balance this aerodynamic force and keep the airframe flying level at the fixed velocity. The solver then iterates the aerodynamic force by computing it under this new deformed configuration and repeats the process until convergence. By picking different angles of attack through the method of bisection, the solver eventually finds the correct angle of attack (with the converged thrust and flap deflection) that requires a gravity of $1g$ for level flight.

The trim angle of attack (computed at the centre node of the airframe), thrust and flap deflection for varying centre pod payload is shown in Figure 29, with comparison against Su [7] and Patil [8]. The comparison is found to be very good although the current method uses a reduced modal description for aerodynamic forces, the associated approximations made in order to pose it into such a form have contributed to the differences seen in the results. The structural deformations at the trim conditions of the six different payloads are shown in Figure 30.

### 7.2.3 Trim Stability Validation

A linearized eigenvalue analysis of the system around the trim configuration is performed for each payload of the rigid/flexible case (Figure 31). Again comparison is made for the phugoid eigenvalue between the current method and previous works by Su [7] and Patil [8].

Here it is seen that as well as increasing in frequency, the phugoid mode becomes unstable in the flexible case after 50% payload, while in the rigid airframe the phugoid mode is always stable. This highlights the contribution of structural flexibility to the

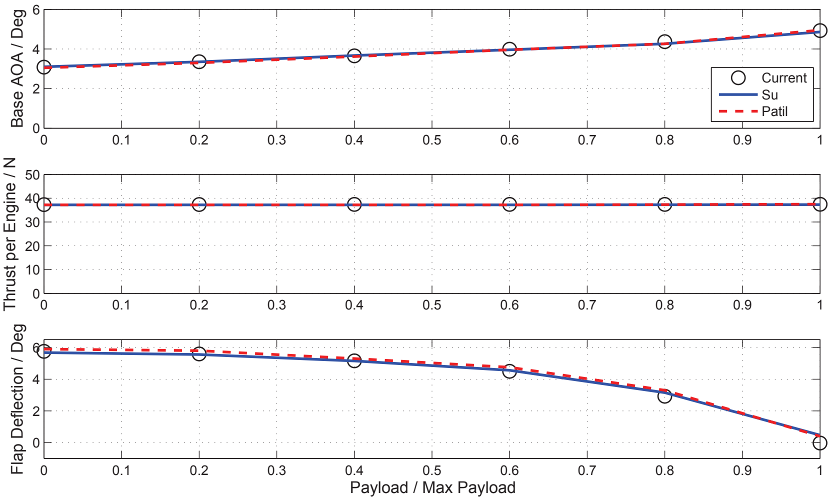

Figure 29: Angle of attack, engine thrust and flap deflection at trim condition for payload varying from 0 to 100%, compared against previous results by Su *et al.* [7] and Patil *et al.* [8]

dynamic stability of this airframe and in particular a decreased level of stability in this model is associated with an increased bending deformation on the wing, as shown in Figure 30. The phugoid frequency and damping for different payloads matches very well with Patil's results (while Su's frequency tends to be lower). However the damping of the phugoid mode lies closer to Su's results for the low-payload cases. Given the difference between the two referenced results, the current result is deemed to be in good agreement with them. The flexible phugoid becomes unstable soon after the payload reaches 50% of maximum, again agreeing well with both Patil's (51%) and Su's (61%).

## 7.3 Open-Loop Dynamic Simulation of Flying Wing

First, nonlinear dynamic simulation is performed using the trimmed airframe model of 100% payload with an excitation caused by transient, simultaneous flap deflections of the form shown in Figure 32. This test case has previously been investigated by Patil [8] and the resulting response and comparison is shown in Figure 33. It is seen that the results compare very well with differences in results primarily attributed to the use of modal aerodynamic solution, which is limited by small-angle approximations and the assumption of constant freestream velocity at any given time [145]. As the setup is dynamically unstable, the airframe reaches large angles of attack after 20 seconds.

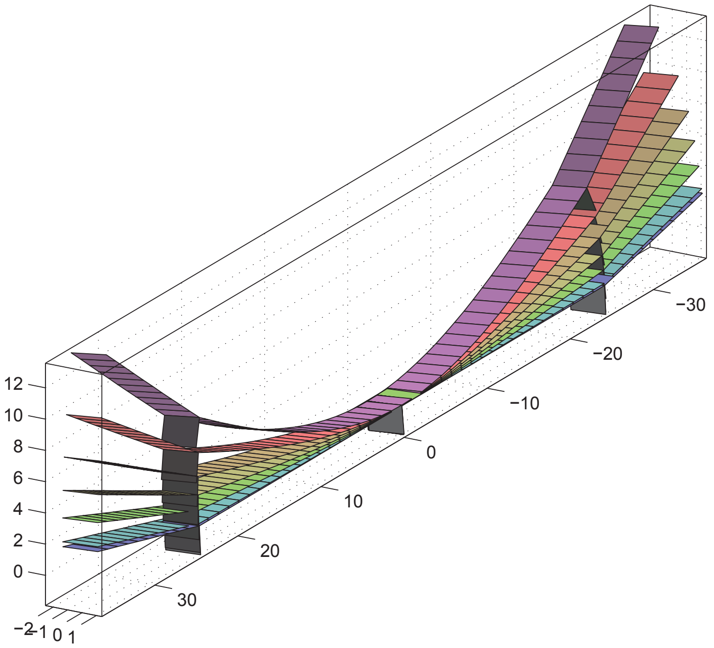

Figure 30: Static deformation at trim condition compared to undeformed shape (bottom) for increasing payloads of (0,20%,40%,60%,80%,100%), with the 100% configuration being on the top.

Therefore the response after this time exceeded the operating range for the assumptions made in the numerical model to be valid, since both models being presented lack a stall model.

## 7.4 Control Design of Flying Wing System

Here we will describe the process of control design on the unstable open-loop 100%-payload model using the process outlined in Section 3.5, with the objective being stabilisation of the unstable system. We first define the input and output of the dynamic system in order to define the state-space system on which we perform the control design. The control action input ($\mathbf{u}_c$ in (3.63)) are the four controls (symmetric and differential flap and thrust) described in Section 7.2.1 written in state-space form using the method in Section 3.5.1. The disturbance input ($\mathbf{w}_d$ in (3.63)) includes two channels, one being a $1-\cos$ vertical force distribution in space, centred on the midpoint of the airframe,

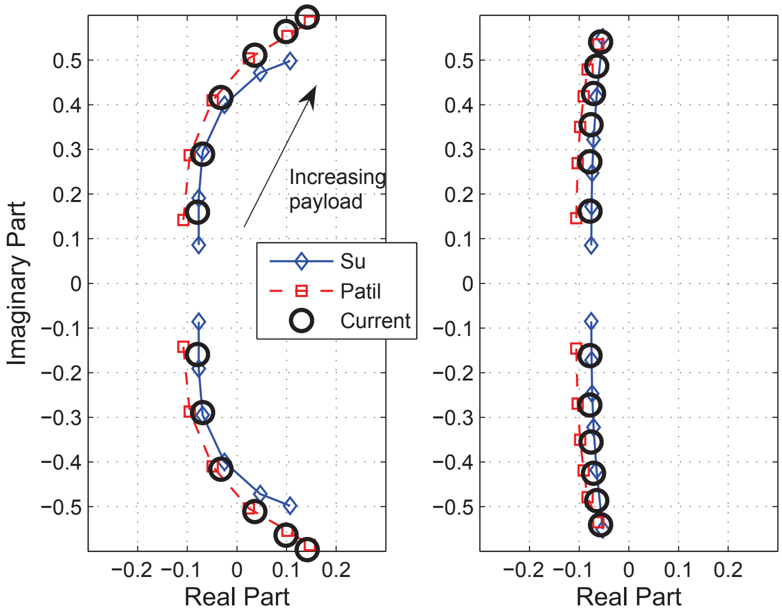

Figure 31: Root locus of the phugoid mode of the flexible (left) and rigid (right) airframe computed with payloads varying from 0 to 100%, compared against previous results by Su [7] and Patil [8]

to simulate a worst-case gust distribution that causes bending of the airframe, the other one being a constant force distribution in space designed to simulate a gust without spatial variations. Four measurements ($\mathbf{y}_m$ in (3.63)) are defined, all taken at midpoint of the airframe, while also serving as the control objective function ($\mathbf{y}_c$ in (3.63)) with the appropriate weightings. The first and second measurements are the local velocities in the chordwise and normal directions, a third measurement is the local out-of-plane bending stress measurement with the fourth and final measurement being the global pitching rotation. These four measurements are designed to provide information both on the flight dynamics and the bending deformation of the airframe. These definitions of inputs and outputs thus yield a state-space description with $4 + 2$ inputs including controls and disturbances and $4 + 4$ outputs including control objective functions and measurements. The control goal in this control design exercise is defined to be dynamic stabilisation.

The 100% payload model is first linearised according to the method described in Section 3.5.1. The 1566-state linearised system is then reduced by balanced model

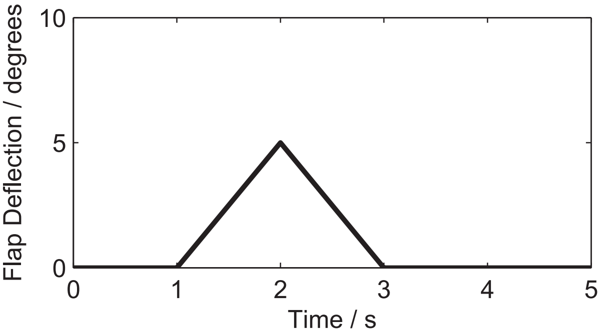

Figure 32: The initial flap input on the open-loop airframe test case.

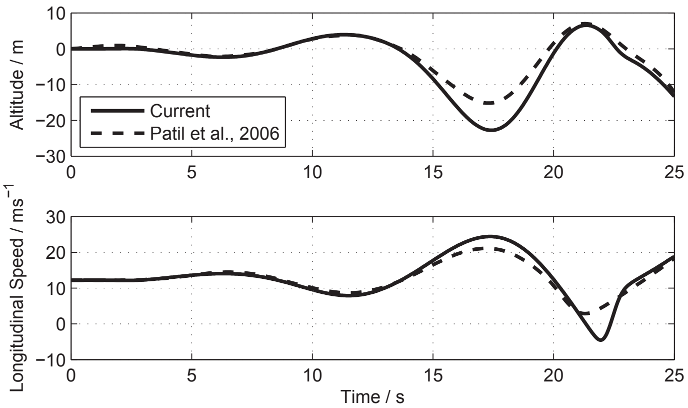

Figure 33: Dynamic open-loop response to the flap deflection of Figure 32.

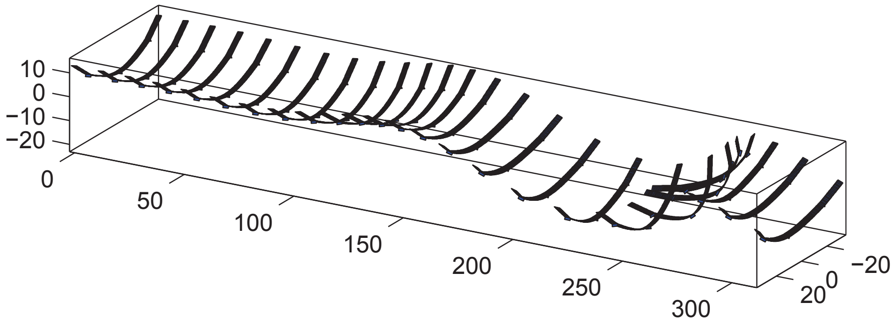

Figure 34: 25-second flight of the flying wing after being subjected to the flap deflection of Figure 32.

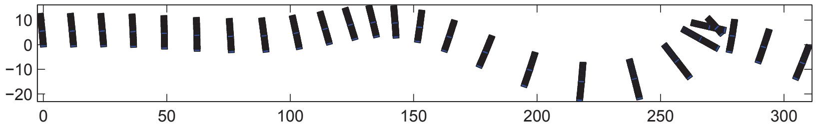

Figure 35: 25-second flight of the flying wing after being subjected to the flap deflection of Figure 32.

Figure 36: A plot of Hankel singular values in the linearised aeroelastic system showing the distribution of stable and unstable modes that contribute to the input-output dynamics. Only the most contributing modes out of a total of 1566 are shown.

reduction prior to control design. Figure 36 is a plot of Hankel singular values in the linearised aeroelastic system and it can be seen from the singular value plot that only a few states out of the full 1566 contribute significantly to the overall input-output behaviour of the system. These modes include the pair of poles corresponding to the unstable flexible phugoid mode shown previously, these are shown in blue on the singular value plot. All remaining poles are either stable or are pure integrators (located at the origin).

State-space simulations of both the full- and reduced-order systems reveal that the low-frequency input-output characteristics of the system could be described by as low as 20 low-frequency modes. The full system is thus reduced by balanced model reduction and a 20-mode reduced system is obtained. We then apply appropriate frequency-based weightings on each part of the control objective function, with a higher weighting at low frequency on the root bending moment measurement and a higher weighting at high

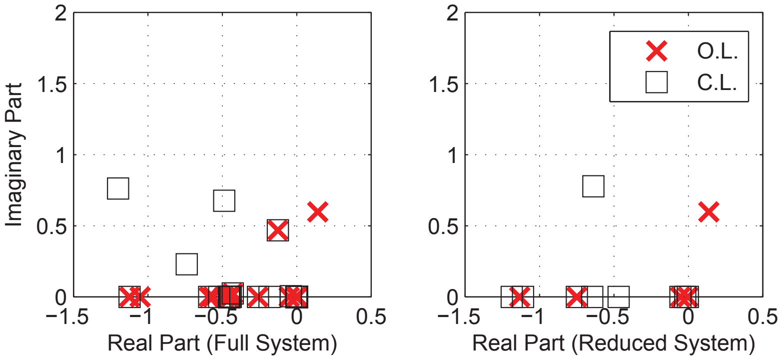

Figure 37: Low-frequency poles in the flying-wing testcase, showing the poles in the full- and reduced-order system, both in open loop and in closed loop. The open-loop pole on the full-state system that is not moved by the controller is an antisymmetric mode.

frequency for the control action. An $\mathcal{H}_\infty$ control system is synthesised according to the method in Section 3.5, that will apply the maximum possible control action within the control saturation range for each control channel (a range of ±10 degrees for symmetric and differential flap and ±15 N maximum for symmetric and differential thrust). The tuning is such that the maximum possible control action will correspond to the maximum admissible gust encounter, i.e. the maximum possible gust without instantly stalling the airframe. As the aircraft travels as 12.2 m/s, the load corresponding to a maximum vertical gust of 5 m/s is considered to be an extreme and selected as the maximum possible gust velocity. With a controller applied, the poles of the closed-loop system is shown in Figure 37. It can be seen in the figure that the unstable phugoid mode in both reduced- and full-order system is moved to the LHS half-plane, indicating the controller achieved stabilisation.

## 7.5 Closed-Loop Flight of Flying Wing

Finally, we apply the stabilising control system developed above to the full-payload flying wing. The excitation used is a DARPA gust, which is a transient vertical gust with a spatial distribution. The vertical gust velocity $\mathbf{v}_{g,3}$ at a location $\mathbf{u}$ is defined as

$$\mathbf{v}_{g,3} = -\frac{1}{2}(1 - \cos(2\pi t/t_g))\frac{1}{2}\cos(\pi(u_2 - u_{2,0})/L_y)u_g \qquad (7.1)$$

for the duration of $0 < t < t_g$. Here $u_g$ indicates the strength of the gust, whereas $\tau$ indicates gust length. $u_{2,0}$ is the current location of the reference point, for the flying wing it is defined as the wing's mid point. $u_2$ is the $y$-component of $\mathbf{u}$, assuming a global coordinate in which the aircraft flies along the $x$-direction and the $z$-axis points up. $L_y$ is the characteristic size of the spatial variation of the gust, for this problem a value of 72m (span of the aircraft) is used.

Figures 38 and 39 illustrates the responses and control actions applied for variable gust durations and a fixed gust strength of 0.2m/s. The closed-loop simulations confirmed that the controller stabilises the open-loop unstable aeroelastic system using control actions that are well within saturation range. Figures 40 and 41 illustrates those for an airframe experiencing the above mentioned DARPA gust starting at $t$ =0, for a fixed gust duration of 0.5s and variable strengths. In the latter two figures, the response to larger gusts shows clear differences to that of smaller gusts, illustrating the geometrically nonlinear effects observed for larger deflections. In particular, the largest gust size requires the control input to be held high for considerably longer. In all cases the controller applies almost no control action to the engine thrust ($10^{-4}$ N), the engine thrust is thus not shown. It is also interesting to note that the controller applies almost opposite inputs to simultaneous and differential flap deflections, showing that the outboard flaps are deflected much more than the inboard ones, with the maximum inboard flap deflection being only 38% of the maximum on the outboard flaps. Under the current implementation in MATLAB, the simulation time for the 50 second closed-loop nonlinear response is 20 hours on one desktop machine.

However, if the closed-loop system experiences a much longer gust with relatively high strength, the geometrically nonlinear effects would eventually render the system unstable, showing the limited authority the controller has on a nonlinear system. This is demonstrated with a maximum gust strength of 2 m/s and a duration of 5s in 42 and 43 where an initial increase in dihedral due to the gust can be seen clearly and the airframe then enters a divergent dive. It is worth relating to the fact that the linear trim results also associate a higher dihedral with a less stable phugoid mode. As part of the control objective function, the controller will always try to correct the change in dihedral to remove any change in the measured root bending moment. However in this case it is not done fast enough before the now-unstable system enters a dive. Figure 44 illustrates the range of gust intensity and length in which the response is stable, a boundary between gust excitations resulting in stable and unstable responses can be seen in the figure with a large gust intensity and length both associated with less stable closed-loop behaviour.

To summarise, this chapter demonstrated the effectiveness of the coupled aeroelastic

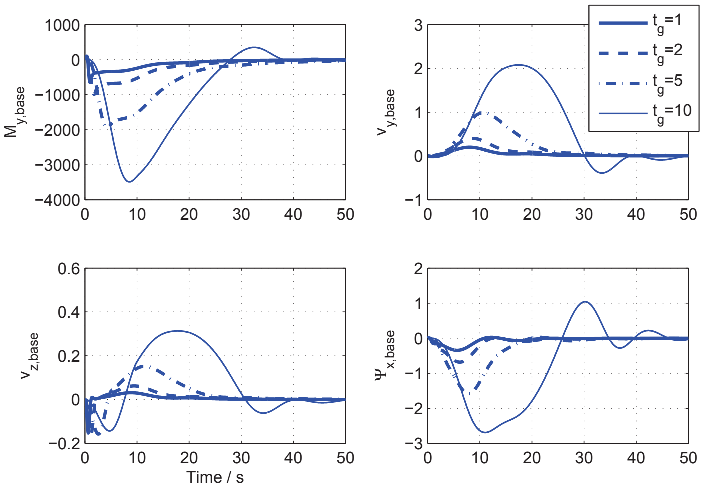

Figure 38: Airframe responses for different DARPA gust durations at a maximum gust strength of 0.2m/s.

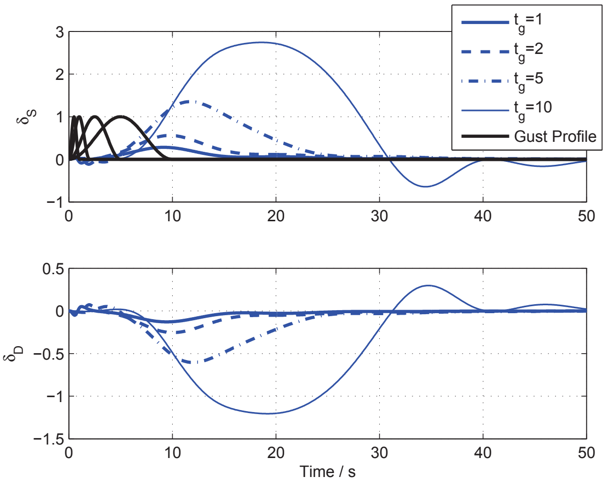

Figure 39: Control actions for different DARPA gust durations at a maximum gust strength of 0.2m/s. Also plotted is the variation of gust velocity with time. Here $\bullet_S$ indicates simultaneous inboard and outboard control actions while $\bullet_D$ indicates differential actions.

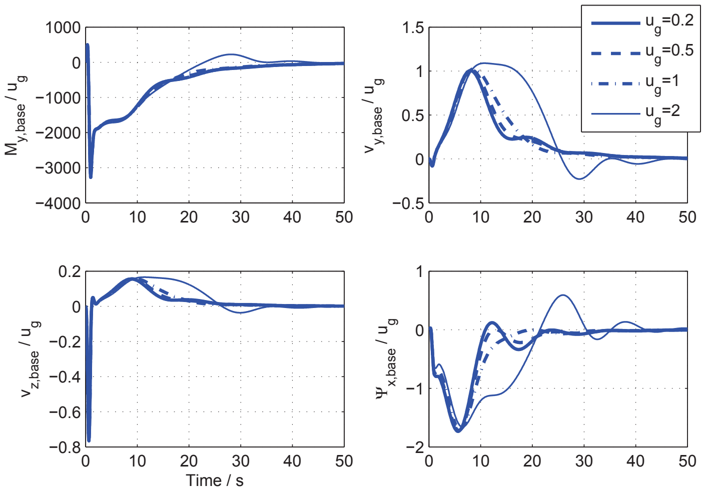

Figure 40: Airframe responses for different DARPA gust strengths at a total gust duration of 0.5s. Normalised with gust strength $u_g$ in m/s.

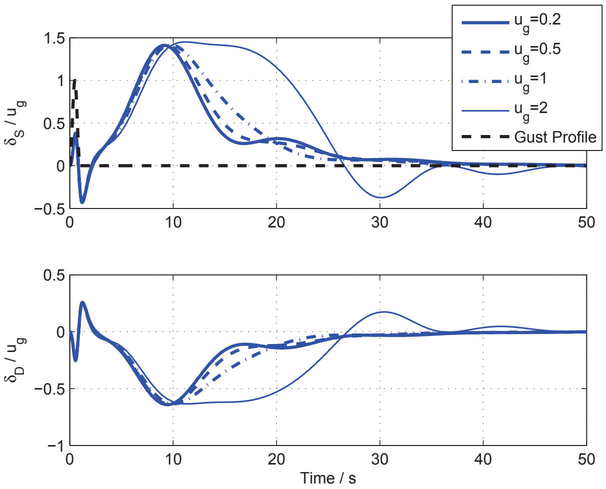

Figure 41: Control actions for different DARPA gust strengths at a total gust duration of 0.5s. Units in degrees and normalised with gust strength $u_g$ in m/s. Also plotted is the variation of gust velocity with time. Here $\bullet_S$ indicates simultaneous inboard and outboard control actions while $\bullet_D$ indicates differential actions.

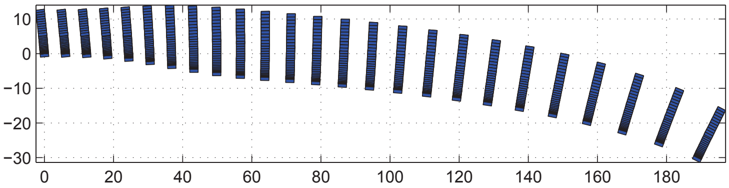

Figure 42: Divergent response to a DARPA gust with maximum strength of 2 m/s and a duration of 5s. Airframe moving from left to right side of image.

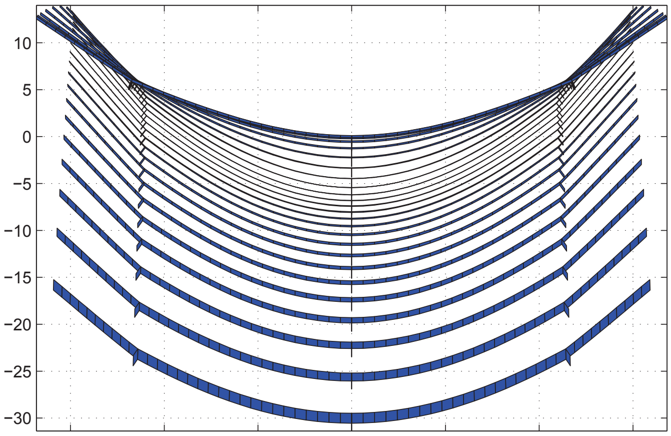

Figure 43: Divergent response to a DARPA gust with maximum strength of 2 m/s and a duration of 5s.

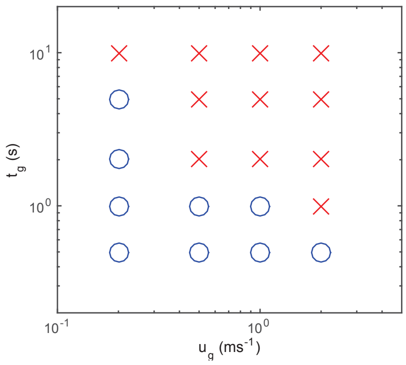

Figure 44: A plot of stability nonlinear response to DARPA gusts of varying lengths $t_g$ and intensities $u_g$. Circles indicate eventual return to trim conditions whereas cross indicates a divergent response.

simulation framework in analysing and simulating the unsteady nonlinear dynamics of an aeroelastic system, as well as in assisting control design on such a system.

# 8 Conclusions and Future Work

## 8.1 Summary

In this work, we have developed a modal formulation of a geometrically-nonlinear structural dynamics problem using intrinsic beam theory. By coupling this with a 2D unsteady strip theory, we were able to arrive at a closed-form aeroelastic description for the dynamics of slender airframes. In the choice of modelling fidelities, we have focused on being able to carry out model reduction on the coupled aeroelastic system. As a result, the intrinsic beam theory and the 2D strip theory were selected as they can both be cast into modal forms with ease.

We have developed a numerical scheme to implement the modal aeroelastic system with the prior assumption of a lumped mass model. The spatial interpolation scheme in this work is linear for velocity states and piecewise constant for sectional force states. The time-marching is carried out using the adaptive timestep RK4 method with automatic error norm control, with the displacement and rotation states integrated from velocity states in time and, during a structural regularisation step, integrated from strain states in space. The set of natural modes on the unloaded structure is used as the modal basis in most of the cases while other bases have also been investigated.

The coupled description has the advantage of using a second-order exact description of geometrical nonlinearities that occur during large rotations and can be linearised easily. The modal formulation was developed and model reduction using a reduced-order description is investigated and we have found that a reduced-order description using the modal formulation retains geometrical nonlinearities to an accuracy adequate for aeroelastic and flight dynamic simulations. The reduced-order description in its nonlinear modal form also preserves total system energy, however we found that order reduction by truncation tended to break the conservation of total momentum of the system.

In identifying a suitable basis for model reduction, we found that a selection of natural modes of the linear dynamic system are the natural choice of basis as it allows the removal of dynamics according to frequency. However as natural modes have non-zero magnitude across the span the entire structure, the coupling between any pair of modes is non-zero, resulting in costly computation of the nonlinear couplings. We have thus developed a technique to transform states into a local basis before the computation of the now sparse nonlinear couplings, leading to significant computational savings. A residualisation technique was also developed to retain coupling information from modes whose linear dynamics were truncated, so that the errors due to mode truncation could be reduced.

A technique was also developed, in which a nonlinear modal description of a slender structure can be obtained through a reduction from a linear 3D FE model of the structure. The method makes use of Guyan reduction on a set of reduced degrees of freedom of the FE model defined using displacements and rotations, intrinsic modes are then obtained from the resulting linear reduced system and the nonlinear modal system computed from the intrinsic modes.

The theoretical developments are demonstrated and validated with numerical findings. This work selected a range of numerical test cases to verify the implementation of the structural and aerodynamic modelling frameworks. Other test cases were selected to demonstrate the process of static condensation from a linear FE model with the subsequent nonlinear dynamic results matching those computed by direct simulations on the FE model and an equivalent beam description. The simulation environment was then used in the reduced-order modelling of a flying wing configuration and was able to carry out static and eigenvalue analysis as well as nonlinear dynamic simulations. We further demonstrated the intended application of this approach in a realistic analysis of control design based on the reduced-order model and the simulation of closed-loop responses of the airframe.

## 8.2 Key Contributions

The key contributions from this work can be summarised as follows:

### Nonlinear Modal Intrinsic Beam Formulation Development

Nonlinear model order reduction is one of the primary objectives of this work. In the order reduction of nonlinear structural models, the existence of finite rotations complicates the modal projection of nonlinear structural dynamics in a displacement-based formulation. We have seen that the intrinsic formulation avoids the infinite-dimensional nonlinearities associated with rotations by choosing a different set of primary variables and can be projected into a compact modal description of the geometrically-nonlinear dynamics of beams. The intrinsic beam formulation was thus cast in a modal form in this work to facilitate a reduced-order description of the structural problem.

The nonlinear modal beam formulation developed in this work is general and we have not limited the method to a particular choice of projection basis, which could range from normal modes to finite-element discretisation. In fact, we subsequently used different bases to their respective advantages. The use of linear natural mode basis allowed the removal of all (truncation) or the linear (residualisation) high-frequency content of the dynamics. In the truncation case, this allows a direct reduction in the number of variables (modes) in the system as model reduction is one of the primary objectives of this work, while in the residualisation case it enables an increase in maximum stable timestep, also allowing savings in computational time. In contrast, the use of localised basis lead to an extremely sparse nonlinear system and significantly reduces the number of multiplications required in nonlinear time-marching.

### Energy/Momentum Conservation Properties of the Nonlinear Modal Beam Formulation

Following the development of the nonlinear modal beam formulation, we investigated whether conservation laws are satisfied on a reduced-order description of the nonlinear modal system. We have demonstrated the conservation of total system energy in free responses of the intrinsic beam description in time, both in its original form and when cast in a modal form. We were also able to show that a reduced-order nonlinear description using a subset of linear natural modes as a basis still preserves total system energy, and if the basis is not of natural modes, the nonlinear part of the dynamics is still energy-preserving. We subsequently showed that the time-averaged value of structural intensity under periodic responses is constant across the structure.

In contrast, we showed that the total momentum measure of a reduced-order structural system is, in general, not conserved under a global modal basis, which was indeed confirmed in the numerical results. The results also showed that the residualisation technique could alleviate this problem numerically, even when significant geometric nonlinearities are encountered.

### A Nonlinear Modal Aeroelastic and Flight Dynamic Formulation Development that Seamlessly Integrates with Existing Linear Aeroelastic Analysis Methods

A modal aerodynamic formulation was developed that tightly integrates with the modal structural formulation to construct a coupled aeroelastic model. The aerodynamic forces are expressed in terms of the local velocities of the aerofoil section using a 2D inflow model written in state-space form. Subsequently, the projection of aerodynamic states onto structural modes enables the aeroelastic system to be cast in a closely coupled form.

The flight dynamic model was constructed by the incorporation of displacement / rotation tracking, gravity, thrust, gust and control actions into the aeroelastic model.

The displacement and rotation information were known through direct integration of velocities in time or strains in space, where the velocities and strains are known from projecting the states back to the intrinsic variables. Once such information is known, effects due to gravity were computed by transforming the gravity force vector into the local coordinates of each point. The thrust was similarly modelled as forces applied on the structure that rotates with the local reference frame. Gust effects were included by modelling their induced change in the velocity of local airflow on each aerofoil section, whereas control surfaces are modelled as changes in the aerofoil section's aerodynamic coefficients. We were thus able to formulate a nonlinear modal aeroelastic and flight dynamic formulation which was subsequently implemented numerically.

### Nonlinear Modal Aeroelastic Simulation Environment Development

This work developed an nonlinear aeroelastic simulation environment that is based on a modal formulation for the structure and aerodynamics. The modes used in the model can be the same as those used in standard linear aeroelastic analysis and link directly to existing methods and software. Numerical discretisation and time-marching schemes were developed for the numerical implementation of the coupled aeroelastic and flight dynamic simulation framework. The spatial discretisation investigated in this work is based on the assumption of a structure with lumped masses at nodes connected by massless flexible beams. A low-order spatial interpolation scheme for intrinsic variables is then developed, based on a linear interpolation for velocity states and a piecewise constant interpolation for force states, so that intrinsic variables are defined at each and every point along the beam structure. We justified this choice of interpolation by noting the difficulty of defining a higher-order interpolation based on existing information and the limited benefits that higher-order schemes will bring. For time-marching, an explicit 4th order Runge-Kutta scheme with adaptive timestep and automatic error control was selected as the time-marching scheme used in this work.

The two-field solution provided by the intrinsic beam equations requires regularisation steps during time-marching to enforce the strong form of the compatibility equation. The regularisation involves spatial integration of displacement and rotation variables along a beam structure's running direction and were also carried out using the explicit RK4 scheme as their governing equations share a very similar form to the time integration of these variables.

Although the first implementation of the simulation environment uses methods that are numerically inefficient, efforts were made to streamline the numerical procedure and study the potential improvements that can be made to speed up nonlinear dynamic simulations. These involve making use of the inherent structure and symmetry in the dynamic system to reduce the number of computations in each timestep, and the use of the aforementioned residualisation technique to increase maximum timestep. The numerical cases demonstrated that despite being written implemented in the relatively inefficient MATLAB environment, a nonlinear full aircraft dynamic simulation using the current approach takes only hours to run on a desktop processor.

### Development of a Condensation Method to Obtain Nonlinear Structural System from Linear FE Model

One of the most important contributions from this work is to provide a way of directly linking 3D modelling fidelity with a geometrical nonlinear 1D description. The formation of an equivalent beam description from a 3D solid involves extracting the sectional mass and stiffness properties. The inertia is easy to approximate via mass lumping from the solid model or section definition, however as reviewed previously obtaining the sectional stiffness matrices at each location requires analysis from the 2D cross-section or periodic 3D FE models.

In this work, the process is approached differently. The sectional stiffness is not computed explicitly, rather, the stresses and strains associated with intrinsic natural modes are each computed separately from natural modes expressed in a reduced set of displacement degrees of freedom. This method makes use of the FE stiffness matrix between the reduced set of dofs and also connectivity information describing the running directions of the beam structures and has the advantage of being compatible with an arbitrary FE model.

This approach was demonstrated using a condensation from a solid element FE model of both a cantilever beam and a free-flying structure under external load. It was seen that the resulting large, geometrically-nonlinear dynamic response is very similar to one that is computed with an equivalent beam description and also matches very well with 3D FE simulation.

### Nonlinear Aeroelastic Simulation and Control Design of a High Aspect-Ratio Flying Wing

The aeroelastic simulation environment was applied on a Helios-type flying wing configuration. The flying wing carries a variable payload and its dynamics and stability characteristics are modified by the payload. The modal formulation used in this work enables a linearised state-space system of the airframe to be created easily and was then used to develop a linear robust controller. The control goal was defined as suppression of bending deformations of the wing and stabilisation of a dynamically unstable payload configuration. The control was effected by inboard and outboard flap inputs and changes in engine thrust, with the feedback provided by measurements of velocities, spatial orientation and bending strain at the centre of the flying wing. The closed-loop aircraft model was then tested under a vertical gust profile that is designed to excite its primary bending mode. The time-domain results show that the dynamically unstable open-loop system is now stabilised by the robust control system against a variety of gust intensities and lengths. It was also seen that at the longest and most severe disturbances, the linear robust controller was no longer able to suppress the resulting excitation which leads to a divergent response of the airframe.

## 8.3 Recommendations for Future Work

### Algorithm Optimisations

A direction of potential work is the practically relevant problem of nonlinear model reduction and optimisation of the solver. The ability to simulate the nonlinear aeroelastic response of HALE UAVs to an adequate accuracy in real-time would be crucial in the design of nonlinear MPC controllers as a potential improvement beyond the use of linear robust control schemes, and would also benefit flight simulations and pilot training of HALE UAVs that will enable the technology to move forward. The modal approach used in this work allows for reduction in a number of ways and have the potential to achieve this goal. The implementation of a nonlinear model-based controller will rest upon the success of this development.

Improvements to the time marching scheme could also be sought. As described above, the current adaptive explicit RK4 scheme is used due to its reliability during prototyping. In a practical implementation, fixed-timestep RK4 or more advanced, implicit schemes could be better choices due to either stability or efficiency considerations.

Similarly, although MATLAB is a powerful environment for code prototyping, MATLAB implementations are known to be significantly slower than C or FORTRAN. The migration of the current code to another language will help reduce the computational time further.

### Model Reduction Based on Intrinsic Formulation

This work only tentatively explored the relation between the extent of reduction (in this case, the number of retained modes) on the accuracy of the dynamic simulations, as part of its convergence studies. In practice it would be very beneficial to understand and tailor the fidelity of the reduced-order model to different requirements. For example, a reduced-order system for full aircraft dynamic simulations and a system model used in an MPC present very different requirements for simulation speed and accuracy. Selecting the appropriate fidelity requires understanding factors affecting the level of accuracy can be achieved with a given amount of computational power and speed requirement in the current modal approach.

In the current formulation, the unsteady aerodynamic model is projected onto the entire structural basis. This however is not a requirement of the formulation and it is completely possible to use different fidelities for both parts of the model so that the number of states could be reduced further.

### 3D FE Stress Recovery

The condensation method described in this work only provides a one-way link between a 3D FE model and the equivalent 1D beam description. It would be interesting to investigate if the method could conversely be used to apply results from the nonlinear 1D simulation back to the 3D FE model to recover displacements and stresses in the 3D structure, and how well these information could be reconstructed using this approach.

### Improvement to Aerodynamic Model

As reviewed previously, [96, 97] indicated that dynamic stall is a significant contributor to nonlinear behaviour on flexible wings. The current aerodynamic formulation is based on a 2D potential flow model and does not include the effects of stall. However as the aerodynamic model is cast as a state-space form, the potential flow model could be replaced by state-space formulations of other models, such as a model based on Leishman-Beddoes dynamic stall model [93].

### Control Design

This work only lightly touched on the control design for nonlinear aeroelastic systems by demonstrating the design of a linear robust controller on a nonlinear aeroelastic system. As we complete the nonlinear aeroelastic simulation framework for flexible aircraft, it will allow us to have a better understanding of the severity and nature of system nonlinearities, which could in turn make robust control designs more reliable by making better informed choices of robustness margins. It is also worth mentioning that although guaranteed stability margins in robust control methods allows some degree of deviation from the ideal linear dynamics used to create the controller, either due to model differences in the actual system or nonlinear behaviour. A nonlinear controller can provide better reliability compared to linear robust controllers when applied to a nonlinear system.

# References

[1] Michel Geradin and Alberto Cardona. *Flexible Multibody Dynamics: A Finite Element Approach*. Wiley, 2001.

[2] Juan C Simo and Loc Vu-Quoc. A three-dimensional finite-strain rod model. part ii: Computational aspects. *Computer Methods in Applied Mechanics and Engineering*, 58(1):79–116, 1986.

[3] Henrik Hesse and Rafael Palacios. Consistent structural linearisation in flexible-body dynamics with large rigid-body motion. *Computers & Structures*, 110:1–14, 2012.

[4] Kuo-Mo Hsiao and Jing-Yuh Jang. Dynamic analysis of planar flexible mechanisms by co-rotational formulation. *Computer Methods in Applied Mechanics and Engineering*, 87(1):1–14, 1991.

[5] Henrik Hesse. *Consistent Aeroelastic Linearisation and Reduced-Order Modelling in the Dynamics of Manoeuvring Flexible Aircraft*. PhD thesis, Imperial College London, 2013.

[6] Matthew Dillsaver, Carlos Cesnik, and Ilya Kolmanovsky. Gust response sensitivity characteristics of very flexible aircraft. In *AIAA Atmospheric Flight Mechanics Conference*, Minneapolis, Minnesota, 2012. American Institute of Aeronautics and Astronautics.

[7] Weihua Su and Carlos ES Cesnik. Dynamic response of highly flexible flying wings. In *Proceedings of the 47th AIAA/ASME/ASCE/AHS/ASC Structural, Structural Dynamics and Materials Conference*, Newport, Rhode Island, 2006.

[8] Mayuresh J Patil and Dewey H Hodges. Flight dynamics of highly flexible flying wings. *Journal of Aircraft*, 43(6):1790–1799, 2006.

[9] Rafael Palacios and Bogdan I Epureanu. An intrinsic description of the nonlinear aeroelasticity of very flexible wings. In *52th AIAA/ASME/ASCE/AHS/ASC Structures, Structural Dynamics, and Materials Conference*, Denver, Colorado, USA, April 2011.

[10] Christopher M Shearer and Carlos ES Cesnik. Nonlinear flight dynamics of very flexible aircraft. *Journal of Aircraft*, 44(5):1528–1545, 2007.

[11] William P Henderson and Bruce J Holmes. Induced drag-historical perspective. Technical report, SAE Technical Paper, 1989.

[12] Daniel P Raymer. *Aircraft Design: A conceptual Approach*. AIAA, 4th edition, 2006.

[13] Laurence Joseph Clancy. *Aerodynamics*. Pitman, London, 1975.

[14] Eli Livne and Terrence A Weisshaar. Aeroelasticity of nonconventional airplane configurations-past and future. *Journal of Aircraft*, 40(6):1047–1065, 2003.

[15] Andre Noth, Roland Siegwart, and Walter Engel. *Design of solar powered airplanes for continuous flight*. PhD thesis, ETH, 2008.

[16] Peter Thiede. Aerodynamic drag reduction technologies. In *Proceedings of the CEAS/DragNet European Drag Reduction Conference*, volume 76, Potsdam, Germany, 2000. Springer.

[17] Thomas E Noll, John M Brown, et al. Investigation of the helios prototype aircraft mishap. Technical report, NASA, 2004.

[18] Wei Shyy, Hikaru Aono, Satish Kumar Chimakurthi, P Trizila, C-K Kang, Carlos ES Cesnik, and Hao Liu. Recent progress in flapping wing aerodynamics and aeroelasticity. *Progress in Aerospace Sciences*, 46(7):284–327, 2010.

[19] Maximilian Richter and Mayuresh Patil. Influence of wing flexibility on the stability of flapping flight. In *AIAA Atmospheric Flight Mechanics Conference*, Toronto, Ontario, 2010.

[20] Bing F Ng, Rafael Palacios, Michael R Graham, and Eric C Kerrigan. Robust control synthesis for gust load alleviation from large aeroelastic models with relaxation of spatial discretisation. In *EWEA 2012*, Copenhagen, Denmark, 2012.

[21] Vitali V Volovoi, Dewey H Hodges, Carlos ES Cesnik, and Bogdan Popescu. Assessment of beam modeling methods for rotor blade applications. *Mathematical and Computer Modelling*, 33(10):1099–1112, 2001.

[22] Ted Belytschko, Wing Kam Liu, Brian Moran, and Khalil Elkhodary. *Nonlinear Finite Elements for Continua and Structures*. John Wiley & Sons, 2013.

[23] P Frank Pai. *Highly Flexible Structures: Modeling, Computation, and Experimentation*. AIAA, 2007.

[24] Carlos ES Cesnik and Weihua Su. Nonlinear aeroelastic simulation of x-hale: a very flexible uav. In *49th AIAA Aerospace Sciences Meeting including the New Horizons Forum and Aerospace Exposition, Orlando, Florida*, 2011.

[25] Joseba Murua, Rafael Palacios, and J Michael R Graham. Assessment of wake-tail interference effects on the dynamics of flexible aircraft. *AIAA Journal*, 50(7):1575–1585, 2012.

[26] Brijesh Raghavan and Mayuresh J Patil. Flight control for flexible, high-aspect-ratio flying wings. *Journal of Guidance, Control, and Dynamics*, 33(1):64–74, 2010.

[27] Weihua Su and Carlos ES Cesnik. Strain-based geometrically nonlinear beam formulation for modeling very flexible aircraft. *International Journal of Solids and Structures*, 48(16):2349–2360, 2011.

[28] Mark Drela. Integrated simulation model for preliminary aerodynamic, structural, and control-law design of aircraft. *40th AIAA SDM Conference*, 99:1394, 1999.

[29] Zhicun Wang, Ping C Chen, Danny D Liu, and Dean T Mook. Nonlinear-aerodynamics/nonlinear-structure interaction methodology for a high-altitude long-endurance wing. *Journal of Aircraft*, 47(2):556–566, 2010.

[30] Zhenjun Zhao and Gexue Ren. Multibody dynamic approach of flight dynamics and nonlinear aeroelasticity of flexible aircraft. *AIAA Journal*, 49(1):41–54, 2011.

[31] Leonard Meirovitch and Ilhan Tuzcu. Unified theory for the dynamics and control of maneuvering flexible aircraft. *AIAA Journal*, 42(4):714–727, 2004.

[32] Martin Otto Laver Hansen, Jens Nørkær Sørensen, S Voutsinas, Niels Sørensen, and H Aa Madsen. State of the art in wind turbine aerodynamics and aeroelasticity. *Progress in Aerospace Sciences*, 42(4):285–330, 2006.

[33] Kei Senda, Takuya Obara, Masahiko Kitamura, Naoto Yokoyama, Norio Hirai, and Makoto Iima. Effects of structural flexibility of wings in flapping flight of butterfly. *Bioinspiration & Biomimetics*, 7(2):025002, 2012.

[34] Bret Stanford, Philip Beran, Richard Snyder, and Mayuresh Patil. Stability and power optimality in time-periodic flapping wing structures. *Journal of Fluids and Structures*, 38:238–254, 2013.

[35] Donald A Danielson and Dewey H Hodges. Nonlinear beam kinematics by decomposition of the rotation tensor. *Journal of Applied Mechanics*, 54(2):258–262, 1987.

[36] Olivier Andre Bauchau. *Flexible Multibody Dynamics*, volume 176. Springer, 2010.

[37] Dewey H Hodges. Nonlinear composite beam theory. *Progress in Astronautics and Aeronautics*, 213, 2006.

[38] Eugène Cosserat and François Cosserat. Théorie des corps déformables. *Paris*, 1909.

[39] A. E. H. Love. *A Treatise on the Mathematical Theory of Elasticity.* Dover Publications Inc, New York, NY, USA, 4th edition, 1944. (First published in 1927 by Cambridge University Press).

[40] Eric Reissner. On one-dimensional large-displacement finite-strain beam theory. *Studies in Applied Mathematics*, 52(2):87–95, 1973.

[41] Juan C Simo. A finite strain beam formulation. the three-dimensional dynamic problem. part i. *Computer Methods in Applied Mechanics and Engineering*, 49(1):55–70, 1985.

[42] John Argyris. An excursion into large rotations. *Computer Methods in Applied Mechanics and Engineering*, 32(1):85–155, 1982.

[43] Rafael Palacios, Joseba Murua, and Robert G Cook. Structural and aerodynamic models in nonlinear flight dynamics of very flexible aircraft. *AIAA Journal*, 48(11):2648–2659, 2010.

[44] Joseba Murua, Henrik Hesse, Rafael Palacios, and J Michael R Graham. Stability and open-loop dynamics of very flexible aircraft including free-wake effects. In *52nd AIAA/ASME/ASCE/AHS/ASC Structures, Structural Dynamics and Materials Conference*, Denver, Colorado, 2011.

[45] Dewey H Hodges. A mixed variational formulation based on exact intrinsic equations for dynamics of moving beams* 1. *International Journal of Solids and Structures*, 26(11):1253–1273, 1990.

[46] Michael A Crisfield and Gordan Jelenić. Objectivity of strain measures in the geometrically exact three-dimensional beam theory and its finite-element implementation. *Proceedings of the Royal Society of London. Series A: Mathematical, Physical and Engineering Sciences*, 455(1983):1125–1147, 1999.

[47] Dewey H Hodges. Geometrically exact, intrinsic theory for dynamics of curved and twisted anisotropic beams. *AIAA Journal*, 41(6):1131–1137, 2003.

[48] Alessandro Macchelli and Claudio Melchiorri. Modeling and control of the timoshenko beam. the distributed port hamiltonian approach. *SIAM Journal on Control and Optimization*, 43(2):743–767, 2004.

[49] Olek C Zienkiewicz and Robert L Taylor. *The Finite Element Method for Solid and Structural Mechanics.* Butterworth-heinemann, 2005.

[50] George Papadakis. A novel pressure–velocity formulation and solution method for fluid–structure interaction problems. *Journal of Computational Physics*, 227(6):3383–3404, 2008.

[51] Agostino Antonio Cannarozzi and Francesco Ubertini. A mixed variational method for linear coupled thermoelastic analysis. *International Journal of Solids and Structures*, 38(4):717–739, 2001.

[52] M Reymond RS Lahey, MP Miller. *MSC/NASTRAN Reference Manual.* MSC.

[53] Atle Gjelsvik. *The Theory of Thin Walled Bars.* Wiley New York, 1981.

[54] Nathan Mortimore Newmark. A method of computation for structural dynamics. In *Proc. ASCE*, volume 85, pages 67–94, 1959.

[55] Michel Géradin and Daniel Rixen. *Mechanical Vibrations.* John Wiley, 1997.

[56] TC Fung. Numerical dissipation in time-step integration algorithms for structural dynamic analysis. *Progress in Structural Engineering and Materials*, 5(3):167–180, 2003.

[57] Wenbin Yu, Dewey H Hodges, and Jimmy C Ho. Variational asymptotic beam sectional analysis–an updated version. *International Journal of Engineering Science*, 59:40–64, 2012.

[58] C.E.S. Cesnik and D.H. Hodges. VABS: A new concept for composite rotor blade cross-sectional modeling. *Journal of the American Helicopter Society*, 42(1):27–38, 1997.

[59] Wenbin Yu, Dewey H Hodges, Vitali Volovoi, and Carlos ES Cesnik. On timoshenko-like modeling of initially curved and twisted composite beams. *International Journal of Solids and Structures*, 39(19):5101–5121, 2002.

[60] Rafael Palacios. *Asymptotic models of integrally-strained slender structures for high-fidelity nonlinear aeroelastic analysis*. PhD thesis, University of Michigan, 2005.

[61] Ahmed K Noor, Melvin S Anderson, and William H Greene. Continuum models for beam-and platelike lattice structures. *AIAA Journal*, 16(12):1219–1228, 1978.

[62] H Tollenaere and D Caillerie. Continuous modeling of lattice structures by homogenization. *Advances in Engineering Software*, 29(7-9):699–705, 1998.

[63] Patrice Cartraud and Tanguy Messager. Computational homogenization of periodic beam-like structures. *International Journal of Solids and Structures*, 43(3):686–696, 2006.

[64] Julian Dizy, Rafael Palacios, and Sylvestre T Pinho. Homogenisation of slender periodic composite structures. *Journal of Solids and Structures*, 50(9):1473–1481, May 2013.

[65] Marilyn J Smith, Mayuresh J Patil, and Dewey H Hodges. CFD-based analysis of nonlinear aeroelastic behavior of high-aspect ratio wings. In *19th AIAA Applied Aerodynamics Conference*, volume 1582, page 2001, 2001.

[66] Jack J McNamara and Peretz P Friedmann. Flutter boundary identification for time-domain computational aeroelasticity. *AIAA Journal*, 45(7):1546–1555, 2007.

[67] Rafael Palacios and Carlos ES Cesnik. Static nonlinear aeroelasticity of flexible slender wings in compressible flow. In *Proc. 46th AIAA/ASME/ASCE/AHS/ASC Structures, Structural Dynamics and Materials Conference, AIAA Paper*, 2005.

[68] Joseph A Garcia. Numerical investigation of nonlinear aeroelastic effects on flexible high-aspect-ratio wings. *Journal of Aircraft*, 42(4):1025–1036, 2005.

[69] Joseph Katz and Allen Plotkin. *Low-Speed Aerodynamics*. Cambridge University Press, 2001.

[70] John David Anderson Jr. *Fundamentals of Aerodynamics.* Tata McGraw-Hill Education, 1985.

[71] Jack Moran. *An Introduction to Theoretical and Computational Aerodynamics.* Courier Dover Publications, 1984.

[72] John L Hess and AMO Smith. Calculation of potential flow about arbitrary bodies. *Progress in Aerospace Sciences*, 8:1–138, 1967.

[73] Edward Albano and William P Rodden. A doublet-lattice method for calculating lift distributions on oscillating surfaces in subsonic flows. *AIAA Journal*, 7(2):279–285, 1969.

[74] William P Rodden, Paul F Taylor, and Samuel C McIntosh. Further refinement of the subsonic doublet-lattice method. *Journal of Aircraft*, 35(5):720–727, 1998.

[75] Joseba Murua, Pablo Martínez, Hector Climent, Louw Van Zyl, and Rafael Palacios. T-tail flutter: potential-flow modelling and experimental validation. In *International Forum on Aeroelasticity and Structural Dynamics*, Bristol, UK, 2012.

[76] Max Blair. A compilation of the mathematics leading to the doublet lattice method. Technical report, DTIC Document, 1992.

[77] William P Rodden. The development of the doublet-lattice method. In *Proceedings of the International Forum on Aeroelasticity and Structure Dynamics*, Rome, 1997.

[78] Jamal M Elzebda, Dean T Mook, and Ali H Nayfeh. Numerical simulation of steady and unsteady, vorticity-dominated aerodynamic interference. *Journal of Aircraft*, 31(5):1031–1036, 1994.

[79] Zhicun Wang and Dean T Mook. Numerical aerodynamic analysis of formation flight. In *41st Aerospace Sciences Meeting and Exhibit*, pages 2003–610, 2003.

[80] Spyros G Voutsinas. Vortex methods in aeronautics: how to make things work. *International Journal of Computational Fluid Dynamics*, 20(1):3–18, 2006.

[81] David J Willis, Jaime Peraire, and Jacob K White. A combined pfft-multipole tree code, unsteady panel method with vortex particle wakes. *International Journal for Numerical Methods in Fluids*, 53(8):1399–1422, 2007.

[82] EC James. Lifting-line theory for an unsteady wing as a singular perturbation problem. *Journal of Fluid Mechanics*, 70(04):753–771, 1975.

[83] Ali R Ahmadi and Sheila E Widnall. Unsteady lifting-line theory as a singular perturbation problem. *Journal of Fluid Mechanics*, 153:59–81, 1985.

[84] Herbert Wagner. Über die entstehung des dynamischen auftriebes von tragflügeln. *ZAMM-Journal of Applied Mathematics and Mechanics/Zeitschrift für Angewandte Mathematik und Mechanik*, 5(1):17–35, 1925.

[85] Theodore Theodorsen and WH Mutchler. General theory of aerodynamic instability and the mechanism of flutter. 1935.

[86] Walter Eversman and Ashish Tewari. A reduced cost rational-function approximation for unsteady aerodynamics. In *AIAA/ASME/ASCE/AHS/ASC Structures, Structural Dynamics and Materials Conference*, Long Beach, CA, 1990.

[87] Mordechay Karpel. Design for active flutter suppression and gust alleviation using state-space aeroelastic modeling. *Journal of Aircraft*, 19(3):221–227, 1982.

[88] David A Peters and Ninh HaQuang. Dynamic inflow for practical applications. *American Helicopter Society*, 33:64–68, 1988.

[89] David A Peters, Swaminathan Karunamoorthy, and Wen-Ming Cao. Finite state induced flow models. i-two-dimensional thin airfoil. *Journal of Aircraft*, 32(2):313–322, 1995.

[90] David A Peters. Two-dimensional incompressible unsteady airfoil theory–an overview. *Journal of Fluids and Structures*, 24(3):295–312, 2008.

[91] David A Peters. Toward a unified lift model for use in rotor blade stability analyses. *Journal of the American Helicopter Society*, 30(3):32–42, 1985.

[92] Didier Petot. Differential equation modeling of dynamic stall. *La Recherche Aerospatiale (English Edition)*, (5):59–72, 1989.

[93] J Gordon Leishman and TS Beddoes. A semi-empirical model for dynamic stall. *Journal of the American Helicopter Society*, 34(3):3–17, 1989.

[94] A Da Ronch, KJ Badcock, Y Wang, A Wynn, and R Palacios. Nonlinear model reduction for flexible aircraft control design. In *AIAA Atmospheric Flight Mechanics Conference*, pages 13–16, 2012.

[95] Marthinus C Van Schoor and Andreas H von Flotow. Aeroelastic characteristics of a highly flexible aircraft. *Journal of Aircraft*, 27(10):901–908, 1990.

[96] Mayuresh J Patil, Dewey H Hodges, and Carlos ES Cesnik. Limit-cycle oscillations in high-aspect-ratio wings. *Journal of Fluids and Structures*, 15(1):107–132, 2001.

[97] Mayuresh J Patil, Dewey H Hodges, and Carlos ES Cesnik. Nonlinear aeroelasticity and flight dynamics of high-altitude long-endurance aircraft. *Journal of Aircraft*, 38(1):88–94, 2001.

[98] Matthew Dillsaver, Carlos Cesnik, and Ilya V Kolmanovsky. Gust load alleviation control for very flexible aircraft. In *AIAA Atmospheric Flight Mechanics Conference*, 2011.

[99] Weihua Su and Carlos E S. Cesnik. Dynamic response of highly flexible flying wings. *AIAA Journal*, 49(2):324–339, 2011.

[100] Carlos ES Cesnik, Patrick J Senatore, Weihua Su, Ella M Atkins, Christopher M Shearer, and Nathan A Pitcher. X-hale: a very flexible uav for nonlinear aeroelastic tests. In *51st AIAA/ASME/ASCE/AHS/ASC Structures, Structural Dynamics, and Materials Conference*, Orlando, Florida, 2010.

[101] Joseba Murua. *Flexible Aircraft Dynamics with a Geometrically-Nonlinear Description of the Unsteady Aerodynamics*. PhD thesis, Imperial College London, 2012.

[102] Robert JS Simpson and Rafael Palacios. Numerical aspects of nonlinear flexible aircraft flight dynamics modeling. In *54TH AIAA/ASME/ASCE/AHS/ASC Structures, Structural Dynamics, and Materials Conference*, Boston, Massachusetts, 2013.

[103] Joseba Murua, Rafael Palacios, and J Michael R Graham. A discrete-time state-space model with wake interference for stability analysis of flexible aircraft. In *International Forum of Aeroelasticity and Structural Dynamics*, Paris, 2011.

[104] Michael H Love, P Scott Zink, Paul A Wieselmann, and Harold Youngren. Body freedom flutter of high aspect ratio flying wings. In *Proceedings of the 46th AIAA/ASME/ASCE/AHS/ASC Structures, Structural Dynamics and Materials Conference*, Austin, Texas, 2005.

[105] Deman Tang, H Yamamoto, and E H Dowell. Flutter and limit cycle oscillations of two-dimensional panels in three-dimensional axial flow. *Journal of Fluids and Structures*, 17(2):225–242, 2003.

[106] Luciano Demasi and Eli Livne. Dynamic aeroelasticity of structurally nonlinear configurations using linear modally reduced aerodynamic generalized forces. *AIAA Journal*, 47(1):70–90, 2009.

[107] Luciano Demasi and Eli Livne. Aeroelastic coupling of geometrically nonlinear structures and linear unsteady aerodynamics: two formulations. *Journal of Fluids and Structures*, 25(5):918–935, 2009.

[108] Bruce Moore. Principal component analysis in linear systems: Controllability, observability, and model reduction. *IEEE Transactions on Automatic Control*, 26(1):17–32, 1981.

[109] Zhaojun Bai. Krylov subspace techniques for reduced-order modeling of large-scale dynamical systems. *Applied Numerical Mathematics*, 43(1):9–44, 2002.

[110] Philip S Beran, David J Lucia, and Chris L Pettit. Reduced-order modelling of limit-cycle oscillation for aeroelastic systems. *Journal of Fluids and Structures*, 19(5):575–590, 2004.

[111] Kenneth C Hall, Jeffrey P Thomas, and Earl H Dowell. Proper orthogonal decomposition technique for transonic unsteady aerodynamic flows. *AIAA journal*, 38(10):1853–1862, 2000.

[112] Jeffrey P Thomas, Earl H Dowell, and Kenneth C Hall. Three-dimensional transonic aeroelasticity using proper orthogonal decomposition-based reduced-order models. *Journal of Aircraft*, 40(3):544–551, 2003.

[113] Sanjay Lall, Jerrold E Marsden, and Sonja Glavaški. Empirical model reduction of controlled nonlinear systems. In *Proceedings of the IFAC World Congress*, Beijing, 1999. International Federation of Automatic Control.

[114] Jacquelien MA Scherpen. Balancing for nonlinear systems. *Systems & Control Letters*, 21(2):143–153, 1993.

[115] Juergen Hahn and Thomas F Edgar. An improved method for nonlinear model reduction using balancing of empirical gramians. *Computers & Chemical Engineering*, 26(10):1379–1397, 2002.

[116] Andrea Da Ronch, Nikolaos D Tantaroudas, Sebastian Timme, and Ken J Badcock. Model reduction for linear and nonlinear gust loads analysis. In *54th*

*AIAA/ASME/ASCE/AHS/ASC Structures, Structural Dynamics, and Materials Conference*, Boston, Massachusettes, 2013.

[117] Fritz Adrian Lülf, Duc-Minh Tran, and Roger Ohayon. Reduced bases for nonlinear structural dynamic systems: A comparative study. *Journal of Sound and Vibration*, 332(15):3897–3921, 2013.

[118] Marc P Mignolet, Adam Przekop, Stephen A Rizzi, and S Michael Spottswood. A review of indirect/non-intrusive reduced order modeling of nonlinear geometric structures. *Journal of Sound and Vibration*, 332(10):2437–2460, 2013.

[119] David Amsallem and Charbel Farhat. Interpolation method for adapting reduced-order models and application to aeroelasticity. *AIAA Journal*, 46(7):1803–1813, 2008.

[120] Kenneth D Frampton, Robert L Clark, and Earl H Dowell. Active control of panel flutter with piezoelectric transducers. *Journal of Aircraft*, 33(4):768–774, 1996.

[121] Banu Korbahti. Specially orthotropic panel flutter control using PID controller. *Acta Mechanica*, 212(3-4):191–197, 2010.

[122] Mario Andrighettoni and Paolo Mantegazza. Multi-input/multi-output adaptive active flutter suppression for a wing model. *Journal of Aircraft*, 35(3):462–469, 1998.

[123] J Rocha, P Moniz, and A Suleman. Aeroelastic control of a wing with active skins using piezoelectric patches. *Mechanics of Advanced Materials and Structures*, 14(1):23–32, 2007.

[124] Sigurd Skogestad and Ian Postlethwaite. *Multivariable Feedback Control: Analysis and Design*, volume 2. Wiley New York, 2007.

[125] Flávio J Silvestre and Pedro Paglione. Dynamics and control of a flexible aircraft. In *Proceedings of the AIAA Atmospheric Flight Mechanics Conference and Exhibit, Honolulu, Hawaii, USA*, 2008.

[126] Robert G Cook, Rafael Palacios, and Paul Goulart. Robust gust alleviation and stabilization of very flexible aircraft. *AIAA Journal*, 51(2):330–340, February 2013.

[127] John C Doyle. Guaranteed margins for lqg regulators. *IEEE Transactions on Automatic Control*, 23(4):756–757, August 1978.

[128] Jean-Jacques E Slotine, Weiping Li, et al. *Applied Nonlinear Control*. Prentice-Hall Englewood Cliffs, NJ, 1991.

[129] David Wagg and Simon Neild. *Nonlinear Vibration with Control: for Flexible and Adaptive Structures*. Springer, 2009.

[130] Robert JS Simpson, Rafael Palacios, Henrik Hesse, and PJ Goulart. Predictive control for alleviation of gust loads on very flexible aircraft. In *55TH AIAA/ASME/ASCE/AHS/ASC Structures, Structural Dynamics, and Materials Conference*, 2014.

[131] H-G Giesseler, M Kopf, P Varutti, T Faulwasser, and R Findeisen. Model predictive control for gust load alleviation. In *4th IFAC Nonlinear Model Predictive Control Conference International Federation of Automatic Control*, Noordwijkerhout, NL., August 23-27 2012.

[132] Rafael Palacios. Nonlinear normal modes in an intrinsic theory of anisotropic beams. *Journal of Sound and Vibration*, 330(8):1772–1792, April 2011.

[133] Michael G Safonov and RY Chiang. A schur method for balanced-truncation model reduction. *IEEE Transactions on Automatic Control*, 34(7):729–733, 1989.

[134] Geir Dullerud and Fernando Paganini. *A Course in Robust Control Theory*. Springer-Verlag New York, 2000.

[135] L Gavrić and G Pavić. A finite element method for computation of structural intensity by the normal mode approach. *Journal of Sound and Vibration*, 164(1):29–43, 1993.

[136] Juan C Simo, N Tarnow, and KK Wong. Exact energy-momentum conserving algorithms and symplectic schemes for nonlinear dynamics. *Computer Methods in Applied Mechanics and Engineering*, 100(1):63–116, 1992.

[137] P Sorenson D Hibbit, B Karlsson. *ABAQUS Reference Manual*. Dassault Systemes.

[138] M. Karpel, B. Moulin, E. Presente, L. Anguita, C. Maderuelo, and H. Climent. Dynamic gust loads analysis for transport aircraft with nonlinear control effects. In *49th AIAA/ASME/ASCE/AHS/ASC Structures, Structural Dynamics, and Materials*. Schaumburg, Illinois, USA, April 2008. AIAA Paper 2008-1994.

[139] Arieh Iserles. *A first course in the numerical analysis of differential equations*. Cambridge University Press, 2009.

[140] Robert J Guyan. Reduction of stiffness and mass matrices. *AIAA Journal*, 3(2):380–380, 1965.

[141] André Preumont. *Vibration Control of Active Structures.* Kluwer academic publishers, Dordrecht, 1997.

[142] M Goland. The flutter of a cantilever wing. *Journal of Applied Mechanics*, 12(4):197–208, 1945.

[143] Z. Sotoudeh, D.H. Hodges, and C.S. Chang. Validation studies for aeroelastic trim and stability analysis of highly flexible aircraft. *Journal of Aircraft*, 47(4):1240–1247, 2010.

[144] Boris Moulin, Moshe Idan, and Mordechay Karpel. Aeroservoelastic structural and control optimization using robust design schemes. *Journal of Guidance Control and Dynamics*, 25(1):152–159, 2002.

[145] Yinan Wang, Andrew Wynn, and Rafael Palacios. Nonlinear model reduction and aeroelastic control of flexible aircraft described by large finite-element models. In *AIAA SciTech 2014*, Washington, DC, January 2014.